

**DAHLGREN DIVISION**  
**NAVAL SURFACE WARFARE CENTER**

Dahlgren, Virginia 22448-5100

---



**NSWCDD/TR-08/127**

**REVERBERANT MICROWAVE PROPAGATION**

**DR. ROBERT E. RICHARDSON**

**ELECTROMAGNETIC & SENSOR SYSTEMS DEPARTMENT (Q)**

**OCTOBER 2008**



REPORT DOCUMENTATION PAGE			Form Approved OMB No. 074-0188	
Public reporting burden for this collection of information is estimated to average 1 hour per response, including the time for reviewing instructions, searching existing data sources, gathering and maintaining the data needed, and completing and reviewing this collection of information. Send comments regarding this burden estimate or any other aspect of this collection of information, including suggestions for reducing this burden to Washington Headquarters Services, Directorate for Information Operations and Reports, 1215 Jefferson Davis Highway, Suite 1204, Arlington, VA 22202-4302, and to the Office of Management and Budget, Paperwork Reduction Project (0704-0188), Washington, DC 20503				
1. AGENCY USE ONLY (Leave blank)	2. REPORT DATE October 2008	3. REPORT TYPE AND DATES COVERED Technical Report spanning 2000 to 2008		
4. TITLE AND SUBTITLE <i>Reverberant Microwave Propagation</i>			5. FUNDING NUMBERS	
6. AUTHOR(S) Dr. Robert E. Richardson				
7. PERFORMING ORGANIZATION NAME(S) AND ADDRESS(ES) Attn: Electromagnetic Environmental Effects (E3) Systems Engineering and Technology Development Branch (Q51) Naval Surface Warfare Center, Dahlgren Division 5493 Marple Road, Suite 156 Dahlgren, VA 22448-5153			8. PERFORMING ORGANIZATION REPORT NUMBER NSWCDD/TR-08/127	
9. SPONSORING / MONITORING AGENCY NAME(S) AND ADDRESS(ES)			10. SPONSORING / MONITORING AGENCY REPORT NUMBER	
11. SUPPLEMENTARY NOTES None				
12a. DISTRIBUTION / AVAILABILITY STATEMENT Approved for public release; distribution is unlimited.			12b. DISTRIBUTION CODE A	
13. ABSTRACT (117 words) The purposes of this Reverberant Microwave Propagation work were, first, to expand measurement capabilities by an extensive investigation of short pulse excitation of empty, partially filled, and coupled cavities, and second, to improve our understanding of microwave propagation in moderately reverberant spaces, such as ship and aircraft compartments and in metal buildings. Understanding propagation in these types of spaces is increasingly important to the U.S. Navy. Various Electromagnetic Compatibility (EMC) issues relate to the proliferation of high-powered microwave emitters in these spaces. Also, reverberant/multipath propagation has a limiting effect on the rate at which data may be sent in digital wireless communication links. The document contains 82 figures, 6 tables, and 7 appendices and references 41 different sources.				
14. SUBJECT TERMS Complex Cavity, Electromagnetic Compatibility (EMC), Insertion Loss (IL), Isotropic Field, Microwave Propagation, Microwave Reverberation, Mode-Stirred Chamber, Multipath Propagation, Over-Moded Cavity, Power Delay Profile, Reverberant Field, Reverberant Propagation, Reverberation Chamber, Short-Pulse Radar			15. NUMBER OF PAGES 246	
			16. PRICE CODE	
17. SECURITY CLASSIFICATION OF REPORT UNCLASSIFIED	18. SECURITY CLASSIFICATION OF THIS PAGE UNCLASSIFIED	19. SECURITY CLASSIFI- CATION OF ABSTRACT UNCLASSIFIED	20. LIMITATION OF ABSTRACT UL	

This page is intentionally blank.

## FOREWORD

The purposes of this *Reverberant Microwave Propagation* work were, first, to expand measurement capabilities by an extensive investigation of short pulse excitation of empty, partially filled, and coupled cavities, and second, to improve our understanding of microwave propagation in moderately reverberant spaces, such as ship and aircraft compartments and in metal buildings. Understanding propagation in these types of spaces is increasingly important to the U.S. Navy. Various electromagnetic compatibility (EMC) issues relate to the proliferation of high-powered microwave emitters in these spaces. Also, reverberant/multipath propagation has a limiting effect on the rate at which data may be sent in digital wireless communication links.

Funding for this work was provided by the Naval Surface Warfare Center, Dahlgren Division (NSWCDD) Independent Laboratory In-house Research (ILIR) and Self-Sponsored Scientific & Technical Initiative (S3TI) sources. Funds were also provided by the Office of Naval Research (ONR)–334 (P. Potter) and by the Directed Energy Technology Office (DETO).

Dr. Gustav Freyer (G.J.F. Consulting) reviewed this report. The author would like to thank Gus for his thoughtful and probing questions and discussion.

Approved by:

A handwritten signature in black ink, reading "Virginia S. Hudson". The signature is fluid and cursive, with the first name "Virginia" being more prominent and the last name "Hudson" following in a similar style.

VIRGINIA S. HUDSON, Department Head  
Electromagnetic & Sensor Systems Department  
NSWCDD

## ACKNOWLEDGEMENTS

The author is indebted to Michael Hatfield (NSWCDD Q51), Michael Slocum (NSWCDD Q52), David M. Johnson (NAVSEA 05W43), and Mark Katrancha (NSWCDD Q51) for many thoughtful discussions and suggestions and for help in designing and assembling many of the experiments that were performed. Development of the two-cavity-coupling analysis problem described in Section 3 arose from discussions between the author and Mike Hatfield during analysis of microwave coupling between sections of a Boeing 747 fuel tank. This analysis was a small part of a much larger study performed by engineers from the National Aeronautics and Space Administration (NASA), NSWCDD, and other organizations examining the Flight 800 disaster of 1996.

This work was performed over a period of about eight years, so identifying the sources of all the ideas in this report may be difficult. Some certainly originated from discussions between the author and engineers from the 818.02 Division at the National Institute of Standards & Technology (NIST). The following NIST staff contributed documents that were particularly useful: David Hill, Christopher Holloway, John Ladbury, Bob Johnk, and Galen Koepke.

The author is pleased to acknowledge significant contributions by Theodore Lehman (T. H. Lehman Consultants) and Blaise Corbett (NSWCDD Q51), particularly in the area of statistical behavior of fields and interpretation of measurement results. Additionally, Blaise made significant improvements to the design of one of several “home-built” radar sets used to perform measurements in this work.

The author would like to thank Dr. Barton Billard (NSWCDD Q23) for significant help in clarifying the discussion in Appendix C, concerning diffraction and scattering by objects within a chamber.

Technical editing was performed by Ms. Dorothy Summers from Lockheed Martin. The author would like to acknowledge not only her sharp eye for detail, but also her unerring ability to capture a nearly hidden idea and restate it with extreme precision and clarity. Surely her diligence has made the reader’s task easier.

Most importantly, the author would like to thank his wife, Jeannine M. H. Richardson, for her patience and encouragement. Without her continued support, this report could not have been finished.

## CONTENTS

<u>Section</u>	<u>Page</u>
<b>1.0 INTRODUCTION.....</b>	<b>1-1</b>
1.1 Background.....	1-1
1.1.1 Overview of Reverberant Fields and Spaces.....	1-1
1.1.2 Field Properties .....	1-2
1.1.3 Analytical Approach .....	1-4
1.1.4 Radar-Based Instrumentation.....	1-6
1.2 Organization and Purpose of This Report.....	1-7
1.3 Summary: Microwave Energy Processes and Measurement.....	1-8
<b>2.0 REVERBERANT FIELD FORMATION AND PROPERTIES .....</b>	<b>2-1</b>
2.1 Introduction.....	2-1
2.2 Measurement Setup and Observations.....	2-1
2.2.1 Instrumentation Measurement and Analysis Overview .....	2-1
2.2.1.1 Radar Settings and A-scope Display Features .....	2-3
2.2.1.2 Antenna Positioning.....	2-5
2.2.1.3 Line-of-Sight (LOS) Antenna Positioning.....	2-5
2.2.1.4 Non-LOS Antenna Positioning.....	2-7
2.2.1.5 Ensemble Averaging.....	2-9
2.2.1.6 General Approach .....	2-9
2.3 Characteristic Wall-Scattering Time .....	2-10
2.4 Statistical View of Reverberant Field Development .....	2-11
2.4.1 Reverberant Field Formation Time .....	2-12
2.4.2 Measurement Setup and Measurement Results.....	2-12
2.4.3 Time Development of Decorrelation .....	2-14
2.4.4 Comparison of Measured Data Cumulative Distribution Function (CDF) with Exponential CDF.....	2-17
2.5 Paddle Wheel Performance.....	2-19
2.5.1 Stirring During Propagation.....	2-20
2.5.2 Stirring/Scattering at Transmission.....	2-24
2.5.3 Additional Paddle Wheel Experiments .....	2-27

**CONTENTS (CONTINUED)**

<u>Section</u>	<u>Page</u>
2.6 Transient Behavior from a Cavity Mode Viewpoint .....	2-27
2.7 Summary: Reverberant Field Formation and Measurement.....	2-29
<b>3.0 REVERBERANT FIELD BEHAVIOR AND PRIMARY MEASUREMENTS.....</b>	<b>3-1</b>
3.1 Introduction.....	3-1
3.2 Idealized Chamber Response to Delta Function Excitation .....	3-2
3.2.1 Fundamental Differential Equation.....	3-2
3.2.2 Insertion Loss .....	3-3
3.2.2.1 Example of Received and Transmitted Energy Ratio Measurement: Tent Experiment .....	3-4
3.2.2.2 Antenna Efficiency Factor Estimate .....	3-7
3.2.2.3 Comparison of Continuous Wave (CW) and Time-Domain Insertion Loss Data.....	3-7
3.3 Nested Chamber Shielding Effectiveness Measurement .....	3-9
3.3.1 Coupled (Nested) Cavities .....	3-10
3.3.2 Definition of $\Lambda$ -Rate Coefficients and Discussion of Differential Equations for $u(t)$ .....	3-11
3.3.3 Comparison of Calculations and Measurement Data for Nested Chambers .....	3-13
3.3.4 Nested Cavity Shielding Effectiveness in Terms of Rate Coefficients..	3-16
3.4 Cavity Perturbation Measurements.....	3-18
3.4.1 Perturbation Measurements and Losses .....	3-19
3.4.1.1 Tuner Loss .....	3-20
3.4.1.2 Antenna Loss Coefficient $\Lambda_{ant}$ .....	3-21
3.4.1.3 Gasket Losses.....	3-22
3.4.2 Material Sheet Resistivity Evaluation.....	3-23
3.4.3 Low-Frequency Measurement Limitations .....	3-24
3.4.3.1 Localized Losses from Antennas .....	3-25
3.4.3.2 Cavity Mode Overlap Factor .....	3-26
3.4.4 Application of CW Technique for Cavity Perturbation Studies .....	3-27
3.5 Additional Measurements and Sample Calculations .....	3-27
3.5.1 Losses Due to People Present in a Test Chamber .....	3-28



**CONTENTS (CONTINUED)**

<u>Section</u>	<u>Page</u>
3.5.1.1 Perturbation Measurement .....	3-28
3.5.1.2 Independent Calculation of Loss Rate Coefficient for a Person in a Reverberant Field .....	3-30
3.5.2 Shielding Effectiveness of an Aircraft Passenger Compartment .....	3-31
3.5.2.1 Leakage Through Windows .....	3-32
3.5.2.2 Internal Cabin Losses .....	3-33
3.5.2.3 Losses Due to Passengers .....	3-33
3.5.2.4 Losses Due to Leakage Out the Cabin Window .....	3-34
3.5.2.5 Combined Internal Losses .....	3-34
3.5.2.6 Internal E Field and Power Emitted from an Internal Emitter Within an Aircraft Cabin .....	3-34
3.6 Antenna Cross Talk Estimate: Direct Versus Reverberant Response .....	3-35
3.6.1 Direct and Reverberant Coupling .....	3-35
3.6.2 Implication for Digital Wireless Communication .....	3-36
3.7 Summary: Reverberant Field Behavior and Primary Measurements .....	3-36
<b>4.0 MEASUREMENT IN MODERATELY REVERBERANT SPACES .....</b>	<b>4-1</b>
4.1 Introduction .....	4-1
4.2 Measurement in Pre-Engineered Building (PEB) .....	4-3
4.2.1 Building Description .....	4-3
4.2.2 Basic Characterization: 1/e Time and Insertion Loss .....	4-4
4.2.2.1 1/e Time Measurement .....	4-5
4.2.2.2 Fabry-Perot Mode .....	4-10
4.2.2.3 Insertion Loss Measurement .....	4-11
4.2.2.4 Data Reduction to Extract Insertion Loss .....	4-13
4.2.3 Measurement of Overhead Roll-up Door Leakage Area .....	4-15
4.2.3.1 Excitation .....	4-16
4.2.3.2 Typical Measured Response .....	4-17
4.2.3.3 Open-Door Loss Mechanism .....	4-18
4.2.4 General Features of Propagation in Poorly Reverberant Spaces .....	4-20
4.2.5 Other Kinds of Measurements: Mapping Hot and Cold Regions in a Space .....	4-21

**CONTENTS (CONTINUED)**

<u>Section</u>	<u>Page</u>
4.2.6 Overview of Localized Field Measurements in an Automobile .....	4-22
4.3 Summary: Measurement in Moderately Reverberant Spaces .....	4-25
<b>5.0 LOSS STUDY AND CHAMBER DESIGN SCALING LAWS .....</b>	<b>5-1</b>
5.1 Introduction .....	5-1
5.2 Building Overview .....	5-1
5.3 Cavity Perturbation Measurement Technique .....	5-4
5.3.1 Concrete Floor Reflectivity Calculation from Perturbation Experiment .	5-6
5.3.2 Theoretical Estimate of Floor Reflectivity .....	5-7
5.3.3 Preferred Technique for Reverberation Measurement .....	5-9
5.4 Other Losses .....	5-9
5.4.1 Wall, Floor, and Ceiling Losses .....	5-10
5.4.2 Nonconductive Overlap in Wall Insulation .....	5-10
5.4.3 Loss Through Overhead Doors .....	5-13
5.4.4 Semitransparent Door .....	5-13
5.4.5 Leaky Gap Model .....	5-13
5.4.6 Loss from Exposed Steel .....	5-14
5.4.7 Loss from Bare Floor Walk-Around Test Area .....	5-15
5.4.8 Innumerable Losses and Loss Audit .....	5-15
5.5 Scaling Calculations for New Chamber Design .....	5-16
5.5.1 Characteristic Wall-Scattering Time .....	5-18
5.5.2 1/e Time Estimate .....	5-18
5.5.2.1 Wall and Floor Losses .....	5-18
5.5.2.2 Overhead Door and Other Losses .....	5-19
5.5.3 Low-Frequency Operating Range Estimate .....	5-19
5.5.4 Chamber Calibration Factor (CF) and Loading Effects .....	5-20
5.6 Summary: Loss Study and Chamber Design Scaling Laws .....	5-21
<b>6.0 GENERAL OVERVIEW AND CONCLUSIONS .....</b>	<b>6-1</b>
6.1 Reverberant Propagation .....	6-1
6.2 General Features of Time-Domain (TD) Measurement and Analysis .....	6-2
6.3 Key Features and Application of TD Measurement .....	6-3

## CONTENTS (CONTINUED)

<u>Section</u>	<u>Page</u>
<b>7.0 REFERENCES.....</b>	<b>7-1</b>
<b>DISTRIBUTION.....</b>	<b>(1)</b>

## APPENDIXES

<u>Appendix</u>	<u>Page</u>
<b>A    RADAR-BASED INSTRUMENTATION .....</b>	<b>A-i</b>
A.1    Introduction.....	A-1
A.2    Direct Time-Domain (TD) Instrumentation.....	A-1
A.3    Synthetic TD Measurement and Systems .....	A-3
A.4    Vector Network Analyzer (VNA) Operation and Typical Results .....	A-13
A.5    Summary: Radar-Based Instrumentation.....	A-19
A.6    References.....	A-20
<b>B    EQUIVALENT REVERBERATION CHAMBER FROM       THE METHOD OF IMAGES .....</b>	<b>B-i</b>
B.1    Introduction.....	B-1
B.2    Application of Image Method.....	B-1
B.3    Fields Within Chamber .....	B-2
B.4    Wall Reflections and Losses.....	B-4
B.5    Summary: Equivalent Reverberation Chamber from the Method of Images .....	B-4
B.6    References.....	B-5
<b>C    SCATTERING PROPERTIES OF A REVERBERANT FIELD .....</b>	<b>C-i</b>
C.1    Introduction.....	C-1
C.2    Scalar Power Density .....	C-1
C.3    Leakage and Scattering at a Chamber Wall.....	C-2
C.4    Scattering from Objects Within a Chamber.....	C-4
C.4.1    Projected Area.....	C-4
C.4.2    Scattering, Diffraction, and the Extinction Paradox .....	C-5
C.4.3    Wall Leakage Calculations .....	C-7
C.5    Summary: Scattering Properties of a Reverberant Field.....	C-7
C.6    References.....	C-7

**APPENDIXES (CONTINUED)**

<u>Appendix</u>	<u>Page</u>
<b>D WIRE CURRENT IN A REVERBERANT FIELD ..... D-i</b>	
D.1 Introduction.....	D-1
D.2 Dipole in a Planewave Field .....	D-1
D.3 Application of the Dipole Model in a Stochastic Field.....	D-2
D.4 Experimental Results .....	D-3
D.5 Discussion .....	D-5
D.6 Summary: Wire Current in a Reverberant Field .....	D-6
D.7 References.....	D-6
<b>E CAVITY PERTURBATION MEASUREMENTS ..... E-i</b>	
E.1 Introduction.....	E-1
E.2 Wall Surface Resistivity .....	E-1
E.2.1 Relationship Between Cavity Energy and Wall Losses.....	E-2
E.2.2 Cavity $Q$ and 1/e Time in Terms of Wall Surface Resistivity .....	E-2
E.2.3 Prototype Panel Surface Resistivity Measurement .....	E-3
E.3 Summary: Cavity Perturbation Measurements .....	E-5
<b>F ANTENNA RESPONSE AND FIELD MEASUREMENTS IN A REVERBERANT SPACE..... F-i</b>	
F.1 Introduction.....	F-1
F.2 Localized Measurements in a Poorly Reverberant Space.....	F-1
F.3 Apparent Antenna Gain in a Highly Reverberant Field.....	F-5
F.4 Summary: Antenna Response and Field Measurements in a Reverberant Space.....	F-7
F.5 References.....	F-7
<b>G FIELDS AT CHAMBER WALLS ..... G-i</b>	
G.1 Introduction.....	G-1
G.2 Fields in Terms of Chamber Modes.....	G-1
G.3 Volume Integrals.....	G-2
G.4 Surface Integrals and Averaging.....	G-2
G.5 Summary: Fields at Chamber Walls .....	G-4
G.6 References.....	G-4

## ILLUSTRATIONS

<u>Figure</u>		<u>Page</u>
1-1	Reverberation Index for Various Reverberant Spaces.....	1-4
1-2	Schematic of Reverberation Test Chamber or Other Test Space with Radar Test Instrumentation.....	1-7
2-1	Typical Reverberation Chamber Setup.....	2-2
2-2	Schematic Diagram of Reverberation Chamber Measurement Setup .....	2-3
2-3	A-scope Display Showing Typical Variation of Received Power Versus Time with LOS Antenna Arrangement.....	2-4
2-4	Typical Variation of Received Power Versus Time with Non-LOS Antenna Arrangement .....	2-8
2-5	Reverberation Chamber with Discone Rx and Tx Antennas and Paddle Wheel .....	2-13
2-6	Received Power Versus Time with Discone Antennas in Chamber.....	2-14
2-7	Decay of Pearson Correlation Coefficient Between Individual Transient Response Pair Segments with Time.....	2-16
2-8	Growth of Standard Deviation During Formation of a Reverberant Field ..	2-17
2-9	Fit of Measured Data to an Exponential CDF .....	2-18
2-10	Unstirred Fraction of Energy Versus Reflection Number .....	2-21
2-11	Received Power Versus Normalized Time .....	2-22
2-12	Root Mean Square (RMS) Deviation (Decibel) of Received Power from Exponential Trend Versus Normalized Time .....	2-24
2-13	RMS Deviation from Exponential Trend Line Versus Normalized Time...	2-26
2-14	Measured E Field Response of an Over-Moded Cavity to Pulsed Excitation .....	2-28
3-1	Excitation Pulse and Received Power Versus Time for Antennas in a Tent Chamber.....	3-5
3-2	Integrated $P_r(t)$ Responses from Tent Chamber .....	3-6
3-3	Insertion Loss (IL) Measurement Results for Large NSWCDD Reverberation Chamber .....	3-8
3-4	Pair of Nested Cavities.....	3-10
3-5	Transient Energy Density Response in a Pair of Coupled Cavities.....	3-13
3-6	Transient Response $u_1(t)$ (L) and $u_2(t)$ (S) Applying Pulse to Chamber L ..	3-14
3-7	Transient Response $u_1(t)$ (S) and $u_2(t)$ (L) Applying Pulse to Chamber S ..	3-15
3-8	NSWCDD “Coffin” Chamber Fitted with Removable Top Plate .....	3-19
3-9	Measured Chamber 1/e Time With and Without Tuner .....	3-21
3-10	Variation in Decay Rate ( $1/\tau$ ) as a Function of Bolt Torque .....	3-22
3-11	Measured Ensemble-Averaged Transient Response with Silver (Ag) Reference Plate and Mild (1010 Alloy) Steel Test Plate .....	3-23
3-12	Measured Sheet Resistivity ( $\Delta R_S$ ) for Mild (1010) Steel Versus Frequency.....	3-24

**ILLUSTRATIONS (CONTINUED)**

<u>Figure</u>		<u>Page</u>
3-13	Transient Response Comparison at 1.5 GHz .....	3-26
3-14	Ensemble-Averaged Chamber Response Showing Loading Effects .....	3-29
3-15	Model for Aircraft Passenger Cabin .....	3-32
4-1	Reflectivity of Various Spaces.....	4-2
4-2	South End of Building 1427 Showing the West Overhead Roll-up Door .....	4-4
4-3	Interior of South End of Building 1427 .....	4-5
4-4	Building 1427 Floor Plan.....	4-6
4-5	Typical Reverberant Transient Response .....	4-7
4-6	Occasional Reverberant Transient Response.....	4-8
4-7	Measured 1/e Time Versus Frequency in Building 1427 .....	4-9
4-8	Transient Response Showing Fabry-Perot Mode in Building 1427 .....	4-10
4-9	Antenna Arrangement for Excitation of Fabry-Perot Mode in Building 1427 .....	4-11
4-10	Antenna Positioning and Movement Locus for IL Measurement.....	4-11
4-11	Measured IL Versus Frequency for Building 1427 .....	4-12
4-12	Reverberation Response Measured in Zones 1 and 3 .....	4-14
4-13	Integrated Responses from Figure 4-12 .....	4-14
4-14	Diagram of Antenna Positioning for Door Leakage Measurement .....	4-16
4-15	Received Power Versus Time from Discone Antenna with Open Door and Closed Door.....	4-17
4-16	Leakage Area of Overhead Roll-up Door .....	4-18
4-17	Measured Open-Door Leakage Rate in Building 1427.....	4-20
4-18	Vehicle Irradiation Scenario .....	4-23
4-19	Three Orthogonal Positions of a Discone Measurement Antenna.....	4-23
4-20	Transmitted and Received Power and Energy in Vehicle Irradiation Experiment.....	4-24
5-1	External View of Electric Railgun (ERG) Building .....	5-2
5-2	Internal View of ERG Building .....	5-2
5-3	View of Measurement Instrumentation and Bare “Walk-Around” Area.....	5-3
5-4	ERG Building Interior with Covered Floor .....	5-3
5-5	Floor Plan and Diagram of Antenna Positioning for 1/e Time Measurements in the ERG Building .....	5-4
5-6	Typical Measured Decay Responses with Bare and Conductive Cloth-Covered Floor .....	5-5
5-7	Variation of Building 1/e Time with Bare and Cloth-Covered Floor .....	5-6
5-8	Noncontacting Overlap Between Insulation Sheets.....	5-11
5-9	Prototype Building: Sample Demonstrating Scaling Calculations .....	5-17
A-1	Schematic of a Simple Direct Pulse-Synthesis Short-Pulse Radar .....	A-2
A-2	Block Diagram of Frequency Modulation–Continuous Wave (FM–CW) Radar Measurement System .....	A-4

**ILLUSTRATIONS (CONTINUED)**

<u>Figure</u>		<u>Page</u>
A-3	Variation of Microwave Frequency in Reverberation Chamber over Time .....	A-4
A-4	Relationship Among Fast Fourier Transformation (FFT) Block Size, Sweep Rate, and Measurement Bandwidth .....	A-5
A-5	Time Behavior of a 3-GHz-Center Frequency Pulse with 200-MHz Bandwidth (BW) .....	A-7
A-6	Simplified Schematic of a Heterodyne Swept CW Short-Pulse Radar System .....	A-9
A-7	Heterodyne Swept CW Short-Pulse System .....	A-10
A-8	Portable Two-Band Swept CW Short-Pulse Radar System.....	A-11
A-9	Simplified Low-Band Architecture of a Swept CW Short-Pulse Radar System .....	A-12
A-10	Windowed and Unwindowed Excitation Pulses .....	A-14
A-11	Vector Network Analyzer (VNA) Connection to Test Chamber.....	A-15
A-12	Raw and Corrected CW Insertion Loss (IL) for NSWCDD “Coffin” Test Chamber .....	A-16
A-13	TD-Decay Response Observed for Fields in the Test Chamber .....	A-17
A-14	Integrated Pulse and Response Calculation to Determine IL from Time-Domain (TD) Data .....	A-18
A-15	Comparison of Time and Frequency Domain-Calculated Values of IL .....	A-19
B-1	Two-Dimensional Representation of a Three-Dimensional Lattice of Image Sources.....	B-2
C-1	Diffraction Pattern Observed for a Conductive Strip at Two Ranges .....	C-5
D-1	Equivalent Circuits for a Dipole Receiving Antenna and a Dipole Element Scatterer .....	D-2
D-2	Current in Wires Placed in 10 Volts/Meter (V/m) (Peak) Field in a Reverberation Chamber .....	D-4
E-1	Time Constant Decrease due to Chamber Loading with a 4-ft by 8-ft Panel .....	E-4
E-2	Increase in Reverberation Chamber $1/\tau$ with Increased Loading Panel Area.....	E-5
F-1	Incident Electric Field on Three Orthogonally Placed Dipole Antennas .....	F-2



**TABLES**

<u>Table</u>		<u>Page</u>
1-1	Summary of Properties of Free-Space and Reverberant Propagation .....	1-3
5-1	ERG Building Physical Parameters Used in Scaling.....	5-4
5-2	Audit of Losses in ERG Building with Covered Floor.....	5-15
5-3	Prototype Building: Physical Constants.....	5-17
5-4	Prototype Building: Inner Surface Resistivity .....	5-18
F-1	Directivity Factors for Short Dipole (SD) and Half-Wave Dipole (HWD)...	F-3

## ABBREVIATIONS AND ACRONYMS

A-D	Analog-to-Digital
A-scope	A display of signal amplitude (or power) versus time
Ag	Silver
BW	Bandwidth
CDF	Cumulative Distribution Function
CF	Calibration Factor ( $\text{W}/\text{m}^2/\text{W}$ )
CW	Continuous Wave
dB	Decibel(s)
dBv	Decibels referred to one volt
E field	Electric field component of electromagnetic wave
DE	Differential Equation
DETO	Directed Energy Technology Office
DOF	Degree(s) of Freedom
E field	Electric Field component of electromagnetic wave
E3	Electromagnetic Environmental Effects
EM	Electromagnetic
EMC	Electromagnetic Compatibility
EME	Electromagnetic Environment
ERG	Electric Railgun (building)
<i>F</i>	Frequency
FFT	Fast Fourier Transformation
FM	Frequency Modulation
ft	Foot (feet)
FWHM	Full-Width Half-Maximum
GEMACS	General Electromagnetic Model for the Analysis of Complex Systems
GHz	Gigahertz
H field	Magnetic field component of electromagnetic wave
HERO	Hazards of Electromagnetic Radiation to Ordnance
HP	Hewlett Packard
HWD	Half-Wave Dipole
IEC	International Electrotechnical Commission
IEE	Institution of Electrical Engineers
IEEE	Institute of Electrical & Electronics Engineers

**ABBREVIATIONS AND ACRONYMS (CONTINUED)**

IF	Intermediate Frequency
IL	Insertion Loss
ILIR	Independent Laboratory In-house Research
LOS	Line of Sight
m	Meter(s)
mho	Conductance unit (1/ohm)
MHz	Megahertz
MOM	Method of Moments
μsec	Microsecond(s)
mW	Milliwatt(s)
n. pag.	No pagination (used with references)
NASA	National Aeronautics and Space Administration
NEC	Numerical Electromagnetic Code
NIST	National Institute of Standards & Technology
no.	Number (issue number used with references)
nsec	Nanosecond(s)
NSWC	Naval Surface Warfare Center
NSWCDD	Naval Surface Warfare Center, Dahlgren Division
ohm/sq	Ohm(s) per square (i.e., sheet resistivity)
O/H	Overhead
ONR	Office of Naval Research
PC	Personal Computer
PEB	Pre-Engineered Building
PW	Paddle Wheel
<i>Q</i>	Quality Factor
<i>R</i>	Reflectivity (factor)
RC	Resistance Capacitance
RF	Radio Frequency
RFI	Radio Frequency Interference
RMS	Root Mean Square
Rx	Receiver
<i>S</i>	Surface area or isotropic power density
S21	Transfer function S-parameter measurement
S3TI	Self-Sponsored Scientific & Technical Initiative
SD	Short Dipole
SE	Shielding Effectiveness

**ABBREVIATIONS AND ACRONYMS (CONTINUED)**

sq ft	Square Foot (feet)
s.v.	<i>Sub Verbo</i> (Latin for “under the word,” used with references)
T <sub>C</sub>	Characteristic Wall-Scattering Time
TD	Time Domain
TE	Transverse Electric
TE <sub>101</sub>	Dominant Transverse Electric Mode
TEM	Transverse Electromagnetic
T <sub>x</sub>	Transmitter
U.S.	United States
USE	Un-Scattered Energy
UHF	Ultra High Frequency
V	Volume
VHF	Very High Frequency
VNA	Vector Network Analyzer
vol.	Volume (used with references)
VSWR	Voltage Standing Wave Ratio
W	Watt(s)
$\delta(t)$	Delta function, a mathematical function with 0 width, infinite height, and unit area
$\tau$	1/e time, where e represents 2.71828
$\Psi$	Fluence, joule/meter squared (J/m <sup>2</sup> )

## 1.0 INTRODUCTION

### 1.1 BACKGROUND

U.S. Navy electromagnetic compatibility (EMC) and ship design engineers are encountering an increasing number of challenges concerning electromagnetic environments (EMEs) in reverberant spaces. Below-deck ship compartments, aircraft compartments, and metal buildings are good examples of reverberant spaces where an EMC engineer may be called upon to determine shielding factors from external fields or, perhaps, to determine how rapidly fields build up within a space from internal emitters or how well digital wireless signals could propagate. These kinds of tasks can only become more important as the U.S. Navy employs higher-powered shipboard radars and designs ship structures with composite materials.

The emphasis in this report is on reverberant field behavior and how to examine it. The report is written for engineers tasked with solving EMC and newly emerging ship electromagnetic (EM) design problems. Its intent is to provide an intuitive picture of reverberant field behavior that suggests techniques for performing measurements and analysis. It assumes that the reader has some familiarity with reverberation chamber measurement technique, which has been an increasingly important tool for solving EMC problems. While the emphasis is on studying reverberant field behavior rather than on examining equipment radio frequency interference (RFI) response, which is the usual task of reverberation chamber operation, several measurements that provide useful supplementary backup information to corroborate results from the usual continuous wave (CW)-based calibration techniques used during RFI testing are also discussed.

A short-pulse radar with radar-based measurement technique is introduced as a measurement approach. The radar A-scope display, which shows received power versus time, is a powerful, information-rich tool for investigation of the fields in a reverberant space. Time-domain (TD) measurement provides complementary information beyond that which is usually gained from CW-based measurement—the mainstay of day-to-day test-oriented chamber operation. Additionally, it is particularly well suited for examining propagation in moderately reverberant spaces, such as ship and aircraft compartments. Note that the terms “time-domain-based” and “radar-based” measurement may be used synonymously.

#### 1.1.1 Overview of Reverberant Fields and Spaces

The term reverberant is used in this report to describe a space where significant reflection of microwave energy from the walls occurs. At any point within the space, the field components from waves reflected from the walls may be much greater than the field that is directly incident from some internal emitting source or from some aperture or wire penetration in the walls where fields leak in from outside. The field in this environment

consists of a large number of individual wave components, such that, statistically, no net direction of propagation or polarization occurs. When this is the case, familiar planewave-based ideas, such as antenna gain and space loss, cannot be directly applied. Other analytical tools and measurement techniques must be found.

Fortunately, a number of useful theoretical relationships and measurement techniques do exist for this type of environment. They have been developed experimentally and theoretically over the last 25 years, largely from research and development experience with reverberation chambers. This report draws significantly on that experience but emphasizes some of the more recent results that have been obtained from radar-based measurement.

In addition to the information obtained directly from reverberation chamber operation and experiments, significant insight may be borrowed from theoretical concepts conceived by engineers studying acoustic reverberation in cathedrals and opera halls in the late 19<sup>th</sup> and early 20<sup>th</sup> centuries.

Two requirements are necessary for a space to be reverberant:

- a. The space must be large in terms of the wavelength of the EM waves being considered.
- b. The space must be suitably reflective.

The first requirement is based on the notion that enough cavity modes can exist to generate a random field with proper stirring. This means that reverberation response, as described here, is a phenomenon that occurs at microwave frequencies or, perhaps, very high frequency (VHF)/ultra high frequency (UHF) for larger spaces. The second and more obvious requirement is that waves make many bounces from the walls and contents of the space before energy in the space inevitably decays. A large number of available waves can generate a random field that is statistically uniform and isotropic. The time-domain-based measurement and analysis techniques emphasized in this report are particularly useful for examining reverberant behavior from this perspective.

### **1.1.2 Field Properties**

Table 1–1 summarizes the properties of free-space and highly reverberant fields. In a highly reverberant space, the direct transmission path signal from one antenna to another is usually very small compared to the components from multiple reflective paths off the walls. In this environment, the familiar space-loss-propagation relationship, with received power set deterministically by antenna separation and gain, is replaced by chamber insertion loss (also referred to as IL). Received power has a 2-degree-of-freedom (DOF) Chi-squared,  $\chi_2^2$  (exponential) statistical behavior rather than

deterministic behavior.<sup>1</sup> Antennas retain directivity in a reverberant space; however, directivity or gain loses much of its usual significance. Effective gain of any efficient antenna, regardless of its directivity, is unity with a 3-decibel (dB) polarization mismatch loss. The gain and polarization losses arise from a general inability to match the antenna orientation deterministically to the field.

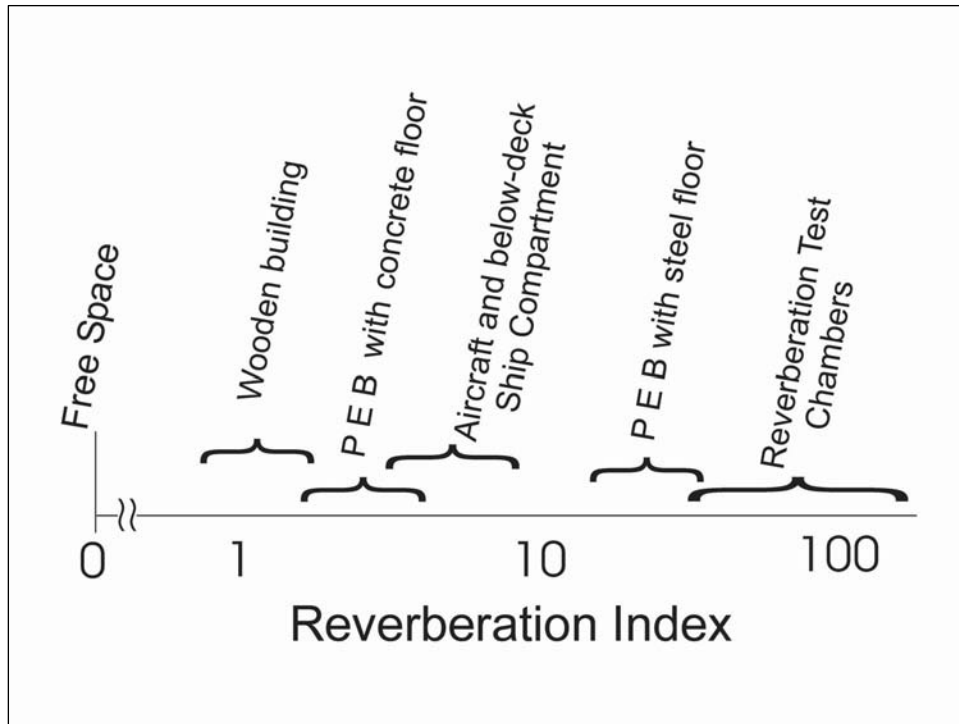
**Table 1–1. Summary of Properties of Free-Space and Reverberant Propagation**

<b>Comparison of Theoretical Principles for Free-Space and Reverberant Fields</b>		
<b>Characteristic or Quantity</b>	<b>Free-Space</b>	<b>Reverberant</b>
Power Density	Poynting Vector $S = E \times H$	Scalar $S = c u$
	Plane-wave Unidirectional Propagation	Isotropic – No Net Direction of Propagation
Tx and Rx Coupling	Deterministic	Statistical
	Space Loss $(\lambda/4\pi R)^2$	Insertion Loss
	Friis Free-Space or Radar-Range Equation	Conservation of Energy, Chi-squared $\chi^2$ Statistics
Antenna Gain and Directivity	Free-Space Gain and Directivity	Effective Unity Gain 3-dB Polarization Loss

Reverberant spaces can be rated according to their reverberance by defining a reverberation index. The index is basically the ratio of the exponential decay 1/e time (alternatively referred to as  $\tau$ ) to the characteristic wall-scattering time ( $T_C$ ), that is, the average time between bounces off the walls that wavefronts undergo in the space.<sup>2</sup> Loosely described, the index is the average number of reflections that waves make off the walls in the time required for 1/e decay of energy in the chamber. Figure 1–1 illustrates reverberation index ranges for typical spaces of interest.

<sup>1</sup> Insertion loss is defined as the ratio of received to transmitted power in a chamber, and for TD measurements, the ratio of received to transmitted energy. Insertion loss will be discussed in more detail in Section 3.2.2.

<sup>2</sup> In this report, 1/e time and  $\tau$  are used interchangeably.



Note: Pre-engineered buildings are also referred to as PEBs.

**Figure 1–1. Reverberation Index for Various Reverberant Spaces**

Reverberation test chambers with an index typically between 50 and 300 are the most reflective spaces an EMC engineer is likely to encounter. Ship and aircraft compartments with an index ranging between 2 and 10 are much less reflective. Propagation in these intermediate spaces exhibits mixed-mode features, characteristic of highly reverberant chambers and also of free space. Behavior in highly reverberant spaces is a useful paradigm to consider when analyzing propagation in intermediate spaces. By applying calculations from both the free-space and reverberant limit, an EMC engineer can construct a reasonable “worst case” estimate of field behavior.

### **1.1.3 Analytical Approach**

In analyzing a reverberant space, three basic questions are addressed about the rates of major processes occurring to the fields:

- a. How rapidly is energy scattered from the walls of a space?
- b. How rapidly is energy lost ohmically?
- c. How rapidly does energy leak into or out of the space?

Additionally, EMC engineers are often interested in whether or not “hot” (i.e., abnormally high fields) or “cold” (i.e., abnormally low fields) regions exist within the



space. If these questions can be answered quantitatively, then propagation is understood in that space. The time-domain-based measurement and analysis techniques to be discussed in this report are well suited for answering these questions.

A major component of this analytical approach in studying reverberant fields is to make use of the fact that in a confined reverberant space, conservation of energy can be applied to describe field behavior. Using a free-space-based analytical approach, an EMC engineer can make only a few coarse estimates about how fields behave in a reflective space. More than one or two wall reflections rapidly make problems intractable. However, by applying conservation of energy and the analytical procedures described in this report, the bulk properties of a reverberant environment are considered rather than individual planewaves. In this approach, “more reflections are better.” The more reverberant the space is, the more accurate the calculation and measurement results are.

In a highly reverberant space, the spatially averaged energy density closely follows a simple first-order differential equation (also referred to as DE) based on conservation of energy. This approach makes analytical procedures straightforward. The highly reverberant environment is discussed in some detail in this report because of its direct applicability to reverberation chamber technique.

In moderately reverberant spaces, such as ship and aircraft compartments where the reverberation index is lower, the high-reverberation-limit analytical approach becomes softer and more difficult to apply. It is surprisingly useful as a starting point, however, due to its uncluttered view of the processes at work in the space. In any case, while some of the high-reverberation-limit behaviors become less exact as the reverberation index decreases, the basic TD measurement approach, using a short-pulse radar, is still quantitatively correct. It is particularly useful for examining hot or cold regions in such a space. Such regions, by definition, do not exist in a highly reverberant space.

In the work described here, analysis is performed on the transient response of fields within a chamber rather than on the steady-state response that is available with the CW technique. Access to additional information is available in this way, because information can be examined and derived from the field response over a time interval rather than from a single number at the end of the response. Much of the analysis in this work is derived from received energy or the ratio of received-to-transmitted energy rather than power.

The transient-response analysis is generally performed, not on individual responses, but on an ensemble of responses. Generally, average response (i.e., ensemble average, not time average) rather than peak response is studied; however, CW-based analysis is generally done on peak response. Despite the significant differences in the transient-response-based and CW-based analytical approaches, results from each approach can be usefully compared for quantitative consistency. Time-domain-based results are useful for verifying various assumptions made about the environment used for CW-based measurements.

Results from this kind of analysis are quite broad based. They provide useful points of departure for performing a variety of tasks involving reverberant propagation. These

include questions referring specifically to reverberation chamber operation, shielding analysis, evaluation of materials and structures, such as composite panels used in new ship design; Hazards of Electromagnetic Radiation to Ordnance (HERO) analyses; and digital wireless system performance prediction and analysis.

#### **1.1.4 Radar-Based Instrumentation**

This report emphasizes time-domain-based measurement of fields with a small short-pulse radar, instead of the more common CW-based instrumentation. The radar A-scope display (i.e., received power versus time) “time tags” the chamber field response so that the development of reverberant fields and their subsequent decay can be observed directly. The major difference between radar-based and CW-based experiments is simply the use of radar instrumentation and transient-based analytical techniques rather than the CW instrumentation and analysis. The remainder of chamber hardware and its setup is generally similar.<sup>3</sup>

Figure 1–2 depicts a measurement test setup using a small radar set in a reverberation chamber with a paddle wheel (also referred to as PW). In many experiments, the paddle wheel mode stirrer is not used, but the antennas are repositioned, changing both their location and pointing angle during measurement.

---

<sup>3</sup> Antenna positioning with time-domain-based measurement is more versatile than with CW-based measurement.

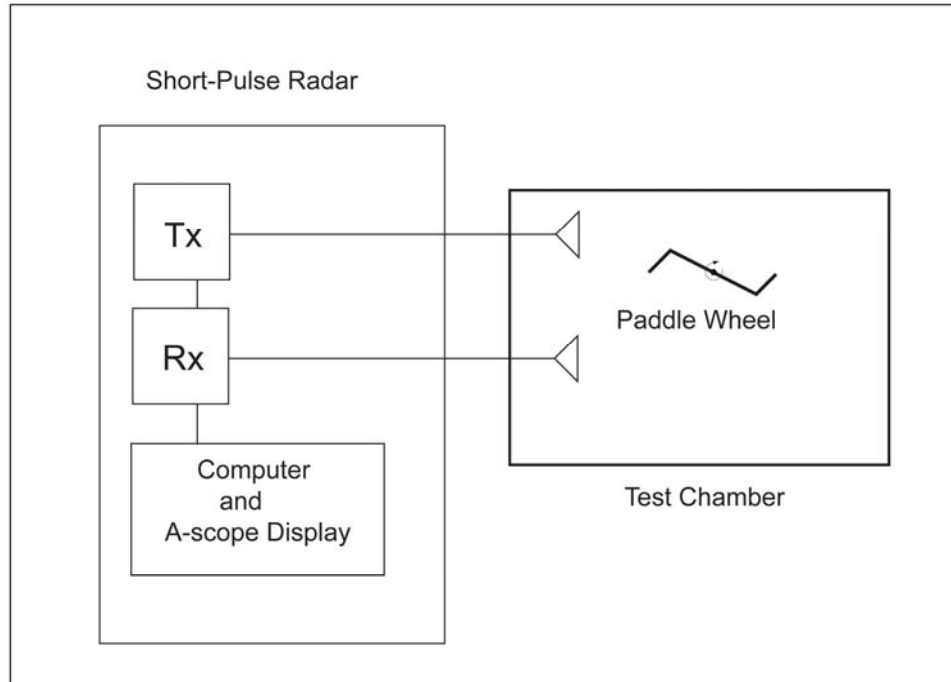


**Figure 1–2. Schematic of Reverberation Test Chamber or Other Test Space with Radar Test Instrumentation**

Several different radar test instrumentation packages were used to collect data shown in this report. One approach in radar design has been to pulse modulate and amplify a CW signal and then coherently detect the received signal from the chamber with a simple double-balanced mixer. The signal is then squared to observe received power. Another approach has been to use simple frequency modulation (FM)-CW radars, which are similar in operation to the synthetic pulse scheme used in vector network analyzers (VNAs) with time-domain capability. A few of the measurements described in this report were made with a precision VNA. Most were made with homemade radars. Instrumentation is discussed in more detail in Appendix A.

## 1.2 ORGANIZATION AND PURPOSE OF THIS REPORT

This report is intended to shed insight into reverberation phenomena and also to provide a description and examples of measurement and analytical techniques that are useful in analyzing and solving reverberant EM problems. Additionally, it is intended specifically to explore and demonstrate radar-based technique to make it more accessible to U.S. Navy EMC engineers tasked with solving EM problems in reverberant spaces. This technical report is intended to provide scientific explanation; it is not a procedural manual. Some of the experimental results presented here are still incomplete. The hope is that enough detail is provided to suggest ideas for future research.

Section 2.0 examines the process of how a reverberant field is formed and how its statistical properties develop. Measurement results obtained with a short-pulse radar are

emphasized. The radar A-scope display provides a particularly intuitive and information-rich view of the reverberant field ring-up process.

Section 3.0 considers idealized reverberant field behavior, characterized by exponential decay and field uniformity within the space. In this regime, the energy density in a chamber follows a simple first-order differential equation with a simple exponential solution. Coupled cavities, which may be used to study shielding effectiveness (also referred to as SE), may be described by a pair of first-order coupled differential equations. The transient energy density behavior is observed by performing an ensemble average of transient response measurements; thus, rate coefficients can be evaluated for energy loss in each cavity and transfer of energy between cavities. This provides a clear analysis of shielding effectiveness, either in a nested cavity reverberation chamber measurement or in other practical scenarios, such as between compartments of a ship or aircraft. Several additional measurement examples are included to demonstrate specifically how TD measurement results are analyzed and applied.

Section 4.0 provides a study of specific results from experiments in moderately reverberant spaces. When a space is only moderately reverberant, measurement results typically depart from predictions, based on conservation of energy where field uniformity is assumed. Even though the behavior of the reverberant environment changes somewhat in the less reflective space, the fundamental time-domain-based measurement approach is still quantitatively correct and highly useful for characterizing field behavior.

Section 5.0 presents a case study of losses in a pre-engineered steel building. This section illustrates how to apply scaling laws and to predict operating characteristics of such a structure if it were to be used as a reverberation chamber for testing large items.

Section 6.0 summarizes reverberant microwave propagation and features of the time-domain-based measurement and analysis approach.

Section 7.0 lists all of the references cited in this technical report.

Appendixes A through G provide useful adjunct information to this technical report.

### **1.3 SUMMARY: MICROWAVE ENERGY PROCESSES AND MEASUREMENT**

This technical report is about microwave field behavior in reverberant spaces, such as ship and aircraft compartments, metal buildings, and reverberation test chambers. Both theoretical ideas and measurement techniques are discussed. A time-domain-based measurement technique is described where a short pulse of microwave energy is injected into the space(s) under study, and the ensemble-averaged, energy density transient response is examined.

The three important processes that microwave energy can undergo in a space or in two or more coupled spaces follow:

- a. Energy is scattered and/or reflected from the walls and contents of the space(s).
- b. Energy is lost ohmically during the scattering process.
- c. Energy is transferred or coupled by an aperture or other mechanism between spaces.

These processes, together with studies of field uniformity, can be specifically identified and quantified with the measurement and analysis approach described in this technical report.

In applying the radar-based measurement approach, the primary measurement tool is a small short-pulse radar set that injects short microwave pulses into a reverberant space and then records received power versus time. With this technique, individual reflections in a poorly reverberant space may be observed directly. In a moderately or highly reverberant space, one observes the behavior of the reverberant field as a whole. The analysis procedure applicable to data from highly or moderately reverberant spaces is a statistical mechanics technique applied to an ensemble average of transient field responses to the injected pulses. Analysis is based on conservation of energy and the observed Chi statistical behavior of the fields. Behavior of fields in a single cavity, or in two or more coupled cavities where energy is transferred from cavity to cavity, can be analyzed.

The time-domain-based measurement technique described in this report yields results that are directly comparable with traditional CW measurement results. More importantly, the time-domain-based technique is largely independent of CW technique. Thus, the time-domain technique provides an independent avenue of verifying or explaining results that have been obtained through the usual CW approach.

This page is intentionally blank.

## **2.0 REVERBERANT FIELD FORMATION AND PROPERTIES**

### **2.1 INTRODUCTION**

The starting point for a discussion of reverberant field formation and behavior is with a description of a measurement setup and approach in a highly reverberant space, i.e., a reverberation chamber, where the idealized properties of a reverberant field can be most closely realized. This approach is applicable to other situations because, even in a moderately reverberant space where typical measurement results begin to depart from the idealized behavior, the behavior in the high-reverberation limit offers a practical and intuitive way of designing an experiment and analyzing results.

A reverberant field environment begins as a single-plane or spherical wavefront and is transformed, usually within a few tens of nanoseconds, to a stochastic environment. This environment has many wavefronts that have many polarizations and directions of propagation. One refers to a pre-reverberant phase, during which this transformation occurs, and a subsequent reverberant phase during which the field decays exponentially. With single-pulse excitation, the two processes are separated in time. With CW excitation both pre-reverberant and reverberant field components exist simultaneously in a space.

In a poorly reverberant space, such as a wooden or cinder block building, only the pre-reverberant phase exists. The reverberant phase is never realized because too few reflections bounce from the walls. In a highly reverberant space, such as a reverberation test chamber, the reverberant phase is dominant. The pre-reverberant phase is very short by comparison and is usually neglected. Finally, there are many moderately reverberant spaces of interest to the U.S. Navy, such as ship and aircraft compartments, for which both phases are important.

### **2.2 MEASUREMENT SETUP AND OBSERVATIONS**

The primary purpose of this subsection is to describe field behavior. At the same time, descriptions of some measurement instrumentation, signal processing, and antenna placement techniques are necessary because they are an integral part of how field behavior is studied and understood.

#### **2.2.1 Instrumentation Measurement and Analysis Overview**

Figure 2–1 is a snapshot of a typical chamber. A test antenna illuminates a large paddle wheel tuner. A second smaller chamber is depicted within the large chamber. The “chamber within a chamber” setup is frequently used for radio frequency (RF) gasket and materials testing. Figure 2–2 schematically shows a typical single-chamber measurement

setup. For CW measurements, the transmitter (Tx) would typically be a microwave sweeper and a power amplifier. The receiver (Rx) could be a spectrum analyzer, a power meter, or possibly even a simple crystal detector.



**Figure 2–1. Typical Reverberation Chamber Setup**

For TD measurement, one uses a short-pulse radar.



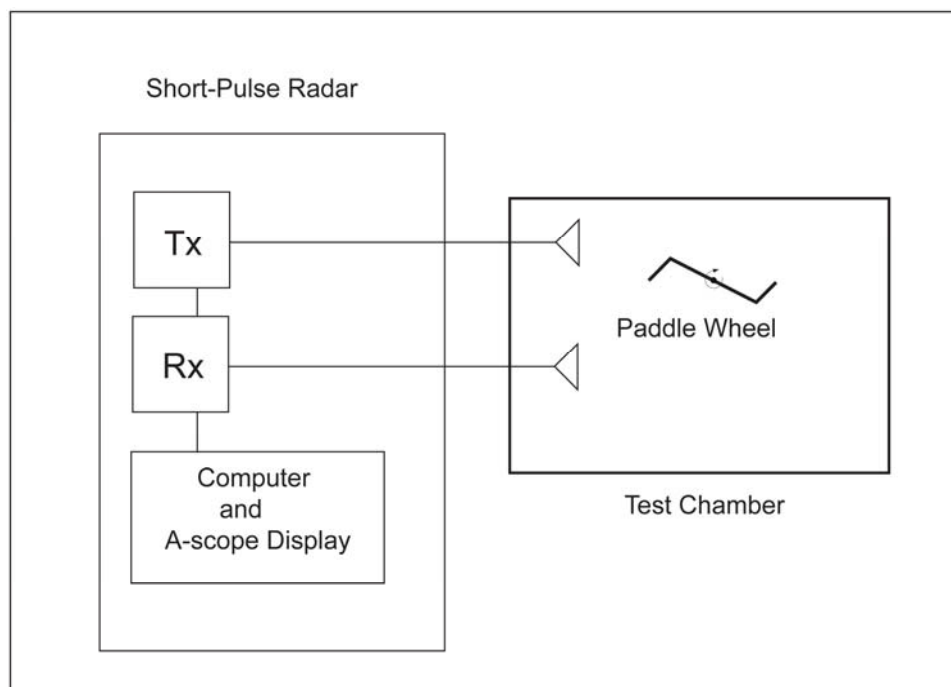
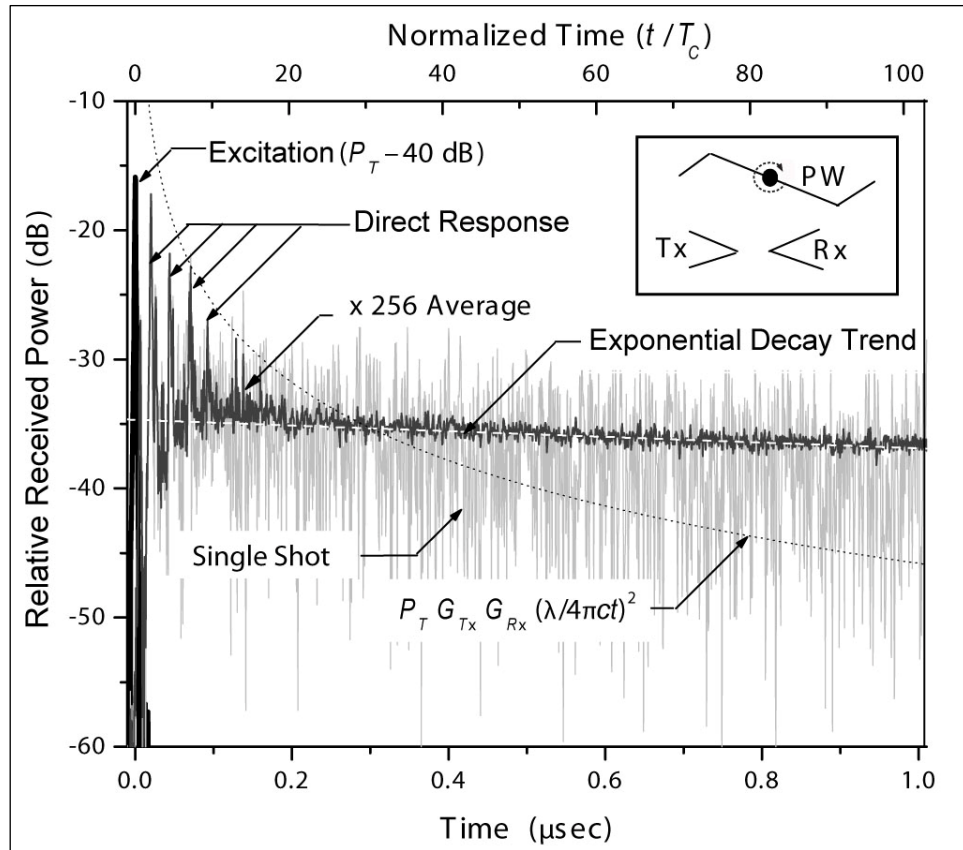


**Figure 2–2. Schematic Diagram of Reverberation Chamber Measurement Setup**

#### 2.2.1.1 Radar Settings and A-scope Display Features

When initiated with a single pulse, reverberant field generation and decay is a transient process. A radar A-scope display, as depicted in Figure 2–3, is an ideal tool for observation. Figure 2–3 shows a rather detailed chamber response. The response and how it relates to chamber physics will be discussed in more detail throughout Section 2, as well as in other sections of this report. Initial discussion here is primarily meant to describe various display features.



Note:  $T_p = 1$  nsec and  $F_0 = 3.6$  GHz.  
 $G_{Tx}$  is used interchangeably with  $G_t$ , and  $G_{Rx}$  is used interchangeably with  $G_r$ .  
 Antenna positioning is shown schematically.

**Figure 2-3. A-scope Display Showing Typical Variation of Received Power Versus Time with LOS Antenna Arrangement**

An A-scope display shows the received signal power amplitude versus time. The horizontal axis extends in this case out to 1 microsecond ( $\mu\text{sec}$ ). A second normalized time scale is also shown and will be discussed in more detail in Section 2.3. The vertical axis is a logarithmic or decibel scale that is convenient for displaying the large dynamic range of signals frequently observed. Exponential decay is observed ubiquitously in chamber response. Exponential decay appears as a straight line on a logarithmic scale, and decay rate is determined simply from its slope.

Several signals are displayed in Figure 2-3. The radar-transmit or chamber-excitation pulse labeled as  $P_T - 40$  dB was measured in the receiver by disconnecting the Rx and Tx antennas at their bases and directly connecting the Rx and Tx transmission lines together through an attenuator. In this case, a 40-dB attenuator was used. This direct-connection measurement provides a convenient calibration reference, which includes the delay and losses of the transmission lines. The vertical scale of the display is relative rather than absolute. Typically, the signal level entering the analog-to-digital (A-D) converter in the radar receiver processor is used as a signal-level indicator. For quantitative analysis, the

difference in vertical positions of chamber response and excitation signals (or their integrals) yields all required information.

Generally, the required excitation pulse is short compared with natural chamber time constants. Frequently, this means that the original pulse is confined in space over a distance that is comparable with or even much smaller than chamber dimensions. By suitable adjustments of the radar, this objective can usually be met while also maintaining a definable pulse carrier frequency. Measurement results can then be readily compared with CW results taken at a specific frequency. The short excitation pulse ( $P_T$ ) generated for the data of Figure 2–3 is synthesized from a CW signal swept from 2.6 to 4.6 gigahertz (GHz); thus, the pulse has a 3.6-GHz center frequency and a 2-GHz bandwidth (BW). According to pulse synthesis techniques used within the radar processor, this yields an equivalent pulse width ( $T_p$ , defined as  $T_p = 2/BW$ ) of a little over 1 nsec after Fast Fourier Transformation (FFT) and windowing. A pulsed wave packet with a pulse length of 1 nsec has a spatial extent (defined as  $c \times T_p$ ) of about 1 foot (ft).

#### 2.2.1.2 Antenna Positioning

Measurement results in a reverberant space may be strongly dependent upon antenna positioning and on antenna beam pattern directivity. With the radar-based technique described here, antenna positioning is much more flexible than with CW technique. With CW, direct antenna cross-talk or pre-reverberant field components must be avoided to prevent contaminating the reverberant field component data. With radar-based technique, pre-reverberant responses can be identified by their horizontal position on the display. They can then be studied or discarded. Antennas are generally deployed bistatically.<sup>4</sup> Several measurement cases that are combinations of how the Rx and Tx antennas view each other and how they view the chamber paddle wheel(s) are considered here. These cases provide significant insight into how a reverberant field environment is developed.

#### 2.2.1.3 Line-of-Sight (LOS) Antenna Positioning

First, an antenna alignment where the Tx and Rx antenna are facing each other in the chamber in a line-of-sight (LOS) fashion is considered. The Rx antenna “sees” the direct Tx wave and mirrored wall reflections from image sources along the beam axis. To provide the data in Figure 2–3, the antennas were aligned parallel to each other and had the same polarization.<sup>5</sup> Thus, these antennas directly see each other multiple times because a pulse from the transmitting antenna is reflected off opposing parallel chamber walls in mirror-like fashion. A mode-mixing paddle wheel is present in the chamber, but

---

<sup>4</sup> Due to special requirements of in-situ ship and aircraft compartment measurements, the author has occasionally used a single-antenna monostatic configuration, where received power was derived from the return port of a directional coupler in the Tx line. Chamber response could be separated from antenna mismatch signals by its horizontal position on the A-scope display. This arrangement inherently has lower dynamic range than a two-antenna arrangement.

<sup>5</sup> The antennas were 10-dB dual-ridge waveguide horns with nominal 50-degree “full-width, half-maximum” (FWHM) beam width.

as shown schematically in Figure 2–3, the antennas are positioned and aimed to avoid illuminating or viewing it. Fields reflected from the walls eventually interact with the paddle wheel, however, as the reverberant field is formed.

Measurement data for Figure 2–3 are taken by injecting a  $P_T$  pulse and measuring a transient response signal at a given paddle wheel position. This process is repeated many times at different paddle wheel positions.

An individual transient signal labeled as a “single shot” is shown in light grey in Figure 2–3. For further processing, individual responses are ensemble averaged. One can visualize the ensemble averaging process of transients as aligning them in time, one beneath the other, and performing a “vertical average” at each time point. The average is performed on received power, not E field. It is an average of mean square field behavior, not a vector or phasor average.

Both pre-reverberant and reverberant phase signals can be observed in Figure 2–3. The early pre-reverberant phase of the response can be analyzed in terms of free-space ideas. The Friis free-space transmission relation states that when two antennas are facing each other in free space and separated by a distance  $r$ , then the received power  $P_r$  is given in Equation (2–1):

$$P_r = P_t \cdot \frac{\lambda^2}{4\pi} \frac{G_r \cdot G_t}{4\pi r^2} \quad (2-1)$$

where

$G_r$  and  $G_t$  are the receive and transmitting antenna gains.

$P_r$  and  $P_t$  are the received and transmitted powers.

For observing the short pulse in the chamber, the separation distance  $r$  is set to equal  $ct$ .

Free-space propagation behavior is observed repeatedly in the early part of the response, shown in Figure 2–3, because of the successive reflections of the transmitted pulse from the parallel walls.

The receiver can clearly discern the first few reflections, which appear as spikes with amplitude that roughly follows the envelope  $[P_t G_t G_r (\lambda/4\pi ct)^2]$ , given in Equation (2–1). These spikes are labeled as “Direct Response” in Figure 2–3 because they occur from mirror-like reflection off the walls opposing the Rx and Tx antennas. This arrangement of antennas is effectively LOS, even though the antennas are looking away from each other.

After about 0.3  $\mu\text{sec}$ , the individual direct illumination spikes that vary with time roughly as  $t^{-2}$  are overshadowed by wave components from other wall reflections as the reverberant field builds up. More detailed analysis described in Appendix B shows that the total number of individual wavefronts present in the chamber at any time  $t$  grows approximately as  $t^2$ . With intensity in each wavefront varying as  $t^{-2}$  and the total number

of wavefronts varying as  $t^{+2}$ , the energy in the chamber remains constant except for slow exponential decay.

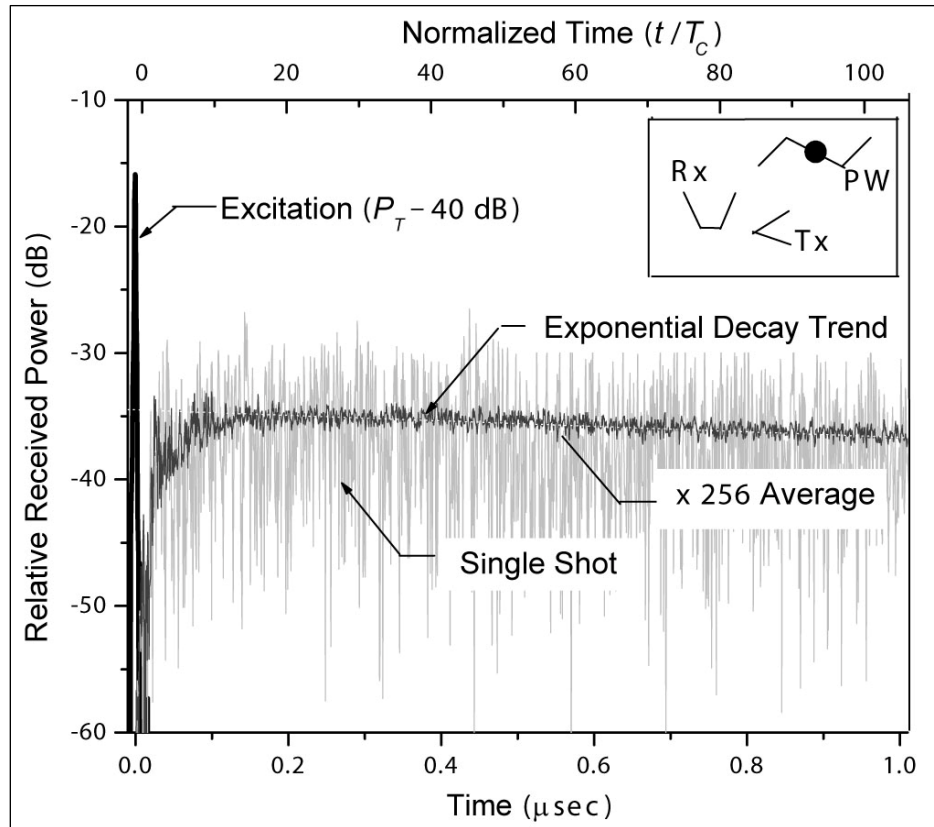
With the number of individual wavefronts continually increasing, the radar soon loses its ability to distinguish between them. Instead, it responds to the sum of an increasingly ( $t^2$ ) large number of vanishingly ( $t^{-2}$ ) small wavefronts.<sup>6</sup> Statistically, this response, in terms of received power, is that of electromagnetic energy density in the chamber, and it leads naturally to an analytical approach based on conservation of energy. In this approach, attention is directed toward behavior of the field as a whole. Individual wavefronts are meaningless.

#### 2.2.1.4 Non-LOS Antenna Positioning

The second case under consideration is a non-LOS measurement where the transmit and receive antennas (10-dB horns and 50-degree beam width) are cross polarized and aimed 90 degrees away from each other. Antenna arrangement is depicted schematically in Figure 2-4. This case specifically illustrates reverberant field buildup. The receive antenna is aimed and positioned to respond to field components that originate from the regions to the side of the transmit antenna. Further, the polarization of the received components is orthogonal to that which was originally transmitted. These components that are part of the reverberant field exist only as a result of scattering from the walls, paddle wheel, and other chamber objects. They require time to build up.

---

<sup>6</sup> Note that acoustics engineers frequently refer to a reverberant sound field as a “diffuse field”; however, the term “diffuse” has not yet become widely used in the EMC community.



Note:  $T_p = 1$  nsec, and  $F_0 = 3.6$  GHz.

**Figure 2-4. Typical Variation of Received Power Versus Time with Non-LOS Antenna Arrangement**

Observed response in this non-LOS measurement builds up more slowly initially than in the LOS case, but eventually transitions over to simple exponential decay behavior that is statistically identical to that observed in the later part of the LOS measurement.

EMC engineers interpret the simple exponential decay, which is observable after the short pre-reverberant “ring-up” phase, as indicating the presence of a fully reverberant field environment.

The transient response of the fields in an ideal chamber immediately after a short pulse has been injected, thus, consists of two components: a short pre-reverberant ring-up phase<sup>7</sup> and a subsequent reverberant phase. The pre-reverberant phase is best described in terms of a few free-space spherical wavefronts being scattered. The reverberant phase is characterized not by individual wavefronts, but from the environment as a whole.

<sup>7</sup> Christopher L. Holloway, Michael G. Cotton, and Paul McKenna, “A Model for Predicting the Power Delay Profile Characteristics Inside a Room,” *IEEE Transactions on Vehicular Technology*, vol. 48, no. 4 (July 1999): 112.

Clearly, the character of the reverberant phase is much different from that of individual wavefronts, which necessarily have  $t^{-2}$  behavior as described by the Friis Equation (2-1). Individual wavefronts are indistinguishable in the reverberant environment, and the environment as a whole has simple exponential decay behavior.

#### 2.2.1.5 Ensemble Averaging

Chamber reverberant response is stochastic and analysis relies heavily on ensemble-averaged measurement results. The individual, single-shot, transient responses in Figures 2-3 and 2-4, though noisy, clearly suggest exponential decay. However, the average response, formed as an ensemble average of 256 individual transient responses, is much smoother and yields exponential decay trend lines with a high correlation coefficient.

The average performed with CW measurement is an ensemble average of steady-state responses while the average performed with the time domain technique is an ensemble average of transient responses. Both are often interpreted as spatial averages.

Typically in chamber measurements, the field level is desired not only at a single point but at multiple points within the chamber. If the reverberant field is sufficiently formed, the field level at one point is statistically equivalent to that at another point. This can be verified by taking measurement data at many different chamber locations. Equivalently, in a chamber equipped with paddle wheels, multiple paddle wheel positions can be used to form an ensemble average of responses. An underlying assumption is that the ensemble average of responses with different paddle wheel positions is equivalent to a spatial average of responses taken at many chamber locations. This is usually a good approximation in a highly reverberant environment.

#### 2.2.1.6 General Approach

The reference to a reverberant field or reverberant field environment is usually not to a single field configuration within a chamber (i.e., from a single paddle wheel position) but, more specifically, to an ensemble of statistically independent field configurations from which an ensemble average is formed. Field behavior is observed in an ensemble-averaged sense. This analytical approach, which relies heavily on observation of average behavior, is much like the use of gas laws and other statistical mechanics procedures that consider average behavior, such as determination of temperature and pressure rather than the velocity and position of individual gas molecules. The average behavior together with statistical relations provides a powerful description of field behavior.

Fully reverberant field environments are characterized by all of the following:

- a. Exponential decay

- b. Statistically uniform distribution of energy, propagation direction, and polarization within the chamber (as desired for proper test item measurements)
- c. Chi (for the E field) or Chi-squared (for received power) statistical behavior

The transient reverberation response analysis procedure described in this report replaces the usual free-space wave analysis procedure [provided in Equation (2–1)] with a statistical mechanics procedure. This procedure relies on conservation of energy and Chi or Chi-squared statistics, where the behavior of the reverberant EME is viewed as a whole, rather than analyzing the behavior of individual wavefronts. These ideas will be described in more detail in Sections 2.3 through 2.6.

### 2.3 CHARACTERISTIC WALL-SCATTERING TIME

The reverberant field is formed from scattering from the chamber walls and contents. In describing acoustic reverberation, Sabine and others<sup>8</sup> have derived a quantity loosely termed here as characteristic wall-scattering length ( $L_C$ ).<sup>9</sup> A characteristic scattering time ( $T_C = L_C/c$ ) for a room is given as Equation (2–2). [For a simple derivation of Equation (2–2), see Appendix C.]

$$T_C = \frac{4V}{Sc} \quad (2-2)$$

where

$V$  is the volume of the chamber and  $S$  is the wall surface area.

The quantity  $W/T_C$ , where  $W$  is the total EM energy in the chamber, is interpreted as the rate (power) at which energy scatters off the walls. In time  $T_C$ , an “average” photon in the reverberant field strikes the walls exactly once.

In a highly reverberant environment, the scattering rate is dominant. All other rates such as loss and leakage are much smaller. The  $1/e$  time of the chamber used to generate the data of Figures 2–3 and 2–4, for example, is 1.9  $\mu\text{sec}$ . The characteristic wall-scattering time given by Equation (2–2) is only 9.7 nsec. Consistent with the requirement that the scattering rate is much greater than the loss rate, the chamber is highly reverberant.

<sup>8</sup> Three sources confirm this finding:

Robert W. Young, “Sabine Reverberation Equation and Sound Power Calculations,” *Journal of the Acoustical Society of America*, vol. 31, no. 7 (July 1959): 912;

F. V. Hunt, “Remarks on the Mean Free Path Problem,” *Journal of the Acoustical Society of America*, vol. 36, no. 3 (March 1964): 536–564;

C. W. Kosten, “The Mean Free Path in Room Acoustics,” *Acoustica*, vol. 10 (1960): 245.

<sup>9</sup> The exact definition of  $L_C$  is subtle; it is sometimes referred to as “the reciprocal of the mean free reciprocal path length.”



Intuitively, EMC engineers envision the scattering process with rate  $(1/T_C)$  as an “engine” that produces an isotropic field from a single wavefront injected into the chamber. Motion of paddle wheels or test antennas within a chamber provides variation in chamber geometry. This allows the formation of an ensemble average of statistically identical but independent chamber responses.

If the energy loss and leakage rates are much lower than the reverberant field formation rate<sup>10</sup> (i.e., the wall-scattering rate), then EMC engineers can assume that these processes, which determine insertion loss, shielding effectiveness,<sup>11</sup> and other quantities of interest, happen in the presence of a good reverberant field.<sup>12</sup> Thus, they are well defined. They can be unambiguously measured and often can be modeled with a high degree of fidelity. In a space that is moderately or poorly reverberant, some of the calculations to be presented that are based on the idealized situation become less exact, though still highly useful. Even though some of the analysis procedures and results based on the high reverberation limit become less exact, the basic TD measurement approach itself remains exact and perfectly correct. It provides a clear picture of just how reverberant a space is and thus gives the EMC engineer an idea of just what assumptions and analytical approaches are applicable to his measurement situation.

## 2.4 STATISTICAL VIEW OF REVERBERANT FIELD DEVELOPMENT

Lehman has shown that field quantities in a reverberant space demonstrate well defined statistical behavior.<sup>13</sup> The E field follows a Chi distribution. The power received from an antenna placed in a reverberant environment follows a 2-DOF Chi-squared  $\chi^2_2$  distribution. This is equivalent to an exponential distribution. Beginning with a single spherical wavefront, the statistical properties develop during the pre-reverberant phase and appear as its average behavior approaches the exponential decay limit. In fact, it is the statistical properties—with lack of correlation between individual field distributions—that allow the smooth exponentially decaying average to be formed during the ensemble averaging process.

The remainder of this section describes several experiments that are designed to provide insight into how the reverberant field is formed and how the statistical properties develop.

---

<sup>10</sup> This is normally true in a good reverberation chamber, for example.

<sup>11</sup> These terms will be discussed in more detail throughout this technical report.

<sup>12</sup> For more details about wire current in a reverberant field, see Appendix D.

<sup>13</sup> Two sources confirm this finding:

Theodore H. Lehman, “A Statistical Theory of Electromagnetic Fields in Complex Cavities,” U.S. Air Force, Phillips Laboratory Interaction, Technical Note 494 (May 1993): n. pag.

David A. Hill, “Section 3.3: Probability Density Functions,” *Electromagnetic Theory of Reverberation Chambers*, National Institute of Standards and Technology (NIST) Technical Note 1506

(December 1998): 17–21.

### 2.4.1 Reverberant Field Formation Time

Referring to the normalized time scale ( $t/T_C$ ) in Figures 2–3 and 2–4, the measured response approaches the exponential decay trend in approximately 8-to-10 characteristic scattering times. This result is consistent with results from studies of development of acoustic reverberant fields.<sup>14</sup>

The nominal 8-to-10  $T_C$  period for reverberant field formation has been defined only qualitatively here; in fact, the 8-to-10  $T_C$  period is not a unique quantity. Further, the term reverberant field generally refers not to a single field pattern, but to an ensemble of statistically independent field patterns. EMC engineers are not interested in how long it takes to form a field pattern, but how long it takes to form a “new” field pattern independent of previous patterns in the chamber. This is true not just for the TD measurements referenced here, but also for general reverberation test chamber operations where test items are evaluated with CW fields. When test items are examined in a reverberation test chamber, EMC engineers rely on proper paddle wheel operation or antenna repositioning to construct a large number of statistically equivalent, but independent, chamber geometries. These independent geometries create independent, uncorrelated surface current patterns to uncover test item leakage points.

### 2.4.2 Measurement Setup and Measurement Results

Figure 2–5 diagrams a chamber with discone Rx and Tx antennas. A discone antenna pattern is dipole-like and, thus, nearly omnidirectional, allowing the Rx antenna to sample all field components—pre-reverberant and reverberant—with roughly equal weighting.

---

<sup>14</sup> E. K. Dunens and R. F. Lambert, “Impulsive Sound Response Statistics in a Reverberant Enclosure,” *Journal of the Acoustical Society of America*, vol. 6, no. 6 (June 1977): 1524–1532.

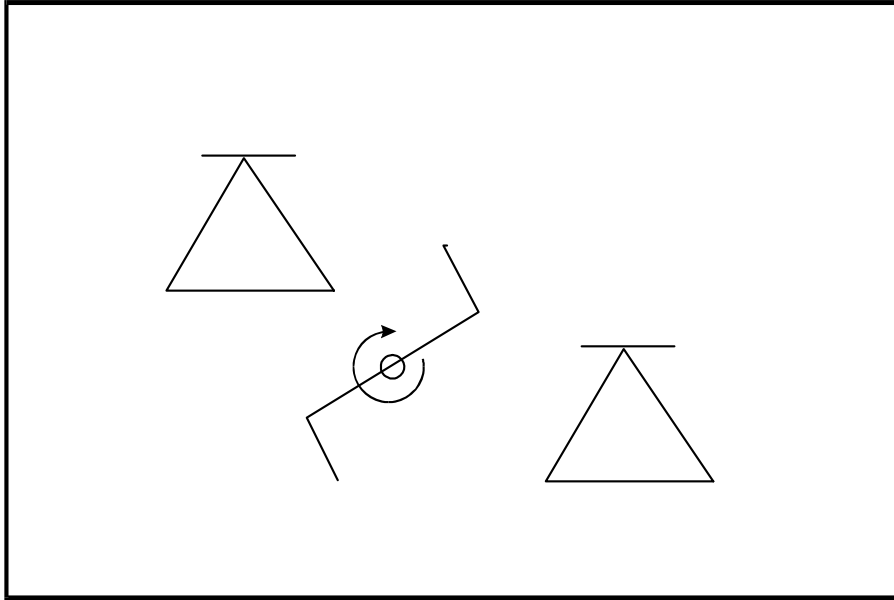
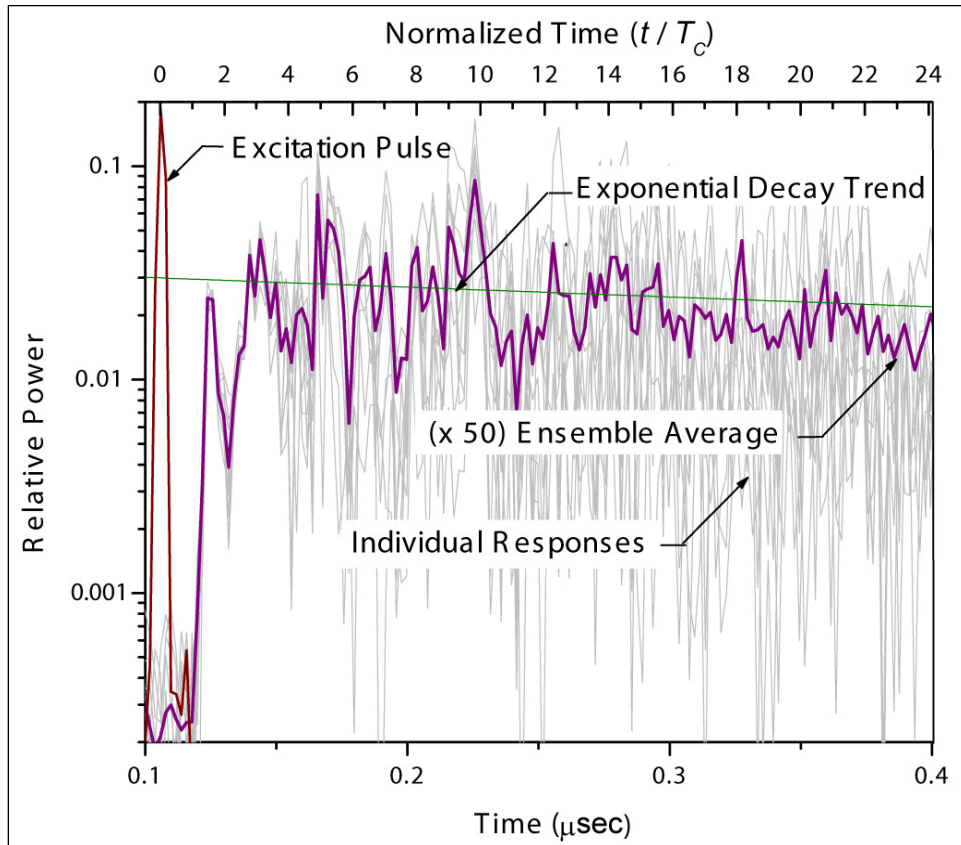


**Figure 2–5. Reverberation Chamber with Discone Rx and Tx Antennas and Paddle Wheel**

The Rx and Tx antennas for the data in Figure 2–6 were held in a fixed position, and individual transient responses were recorded for different paddle wheel positions. The excitation pulse for the following data set was derived from a chirp signal with a 5.25-GHz center frequency and a 0.5-GHz BW; thus, it has a nominal 4-nsec pulse width.



Note: The figure shows excitation, 8 individual single shots, and an ensemble average constructed from 50 shots.

**Figure 2–6. Received Power Versus Time with Discone Antennas in Chamber**

The initial behavior of each transient signal in Figure 2–6 is nearly identical and consists of “direct cross talk” between the Tx and Rx antennas. In this case, the initial part of the response is always the same because the antennas are not moved. Only after several bounces (i.e.,  $T_C$  periods), where wavefronts have had time to reflect off the walls and interact with the paddle wheels, do the individual transients become unique and uncorrelated with each other.

### **2.4.3 Time Development of Decorrelation**

One can watch the decorrelation between individual transients unfold with time by calculating the correlation coefficient of short segments from pairs of individual transient responses and then “sliding” the segment or “aperture” along in the responses. Calculated correlation results depicted in Figure 2–7 were formed from a 13-nsec ( $1 \times T_C$ ) aperture. That is, the correlation coefficient from data points in corresponding 13-nsec segments centered at time  $t$  between random pairs of responses is

calculated.<sup>15</sup> The variable  $t$  is the time following chamber excitation with the short pulse. As the center of the aperture is moved along in time  $t$  following excitation, the average correlation between each segment decreases. Each transient response has had more time to interact with its unique chamber geometry.

Figure 2–7 shows the averaged Pearson Correlation coefficient<sup>16</sup> calculated from data points in the aperture in each response as a function of the position ( $t$ ) of the center of the aperture. Consistent with visual observation of the data in Figure 2–6, which shows nearly identical behavior in the initial response of each transient, the correlation is high at the beginning of the transient ( $t/T_C \sim 1.5$ ). Initially, this transient consists only of direct cross talk between antennas. The correlation “noisily” approaches zero after about  $10 T_C$ . The small drop in correlation at  $t/T_C \sim 2$  is clearly due to the lack of signal<sup>17</sup> at that point, as seen in Figure 2–6. The signal from the first wall reflection does not begin until  $t/T_C \sim 2.5$ . The drop in correlation at  $t/T_C \sim 3.5$  and the spike at 10 do not have such an obvious interpretation, but they are consistent with the individual transient response signals, as shown in Figure 2–6. Averaged correlation remains low after  $t/T_C \sim 10$ . In Figure 2–7, individual correlation coefficient calculations are noisy and vary rapidly between plus or minus (+/-) 1 with the narrow aperture width.<sup>18</sup>

---

<sup>15</sup> This calculation was performed in Microsoft Excel using the CORREL function. The application of correlation coefficients is described in the following source: “Correlation Coefficients,” *International Electrotechnical Commission (IEC)*, 61000–4–21 (Draft), Annex A: 15.

<sup>16</sup> Ibid., 15.

<sup>17</sup> Correlation, at that point, is on system noise, not signal.

<sup>18</sup> When a wider aperture is used, individual correlation coefficients at  $t/T_C > 10$  are lower and much less noisy. When an aperture width of  $6 T_C$  is chosen, for example, the maximum amplitude of any individual coefficient for  $t/T_C > 10$  is within +/-0.3.

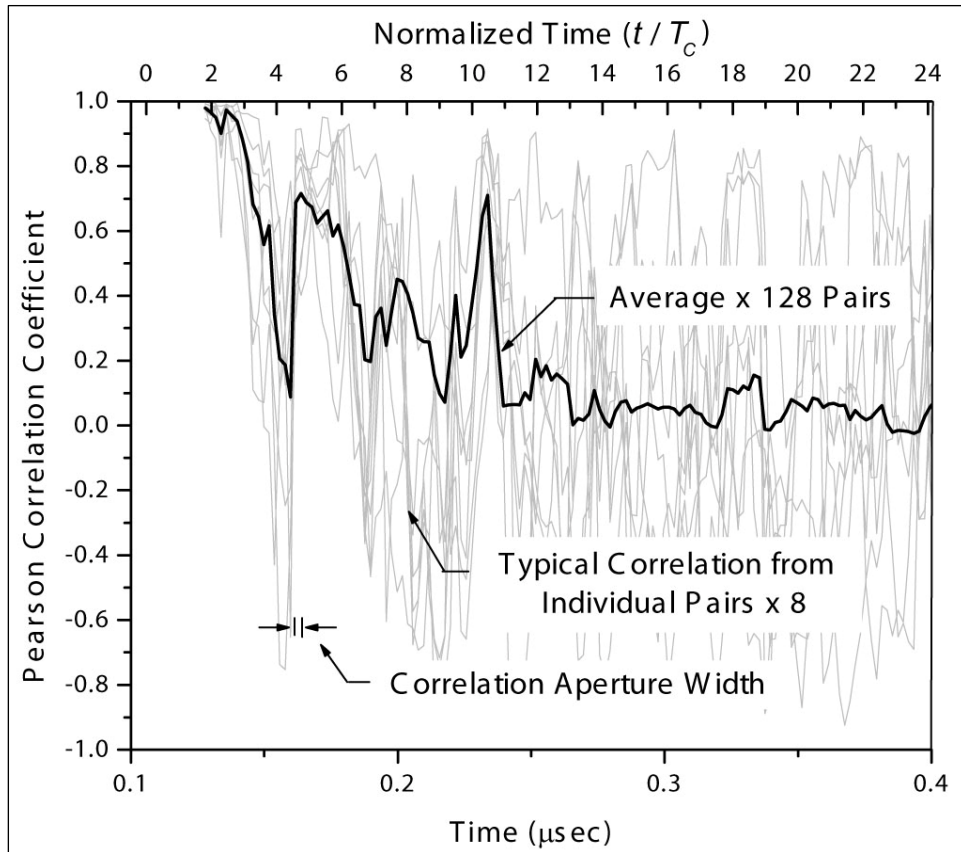


**Figure 2-7. Decay of Pearson Correlation Coefficient  
Between Individual Transient Response Pair Segments with Time**

Figure 2-8 shows the instantaneous normalized standard deviation for the data calculated at each instant of time from the ensemble population of 50 individual responses. The standard deviation grows nearly monotonically with time for about the first 8-to-10  $T_C$  periods until it equals the mean value of the received power. At this point, the normalized standard deviation is approximately unity, which is a feature of the 2-DOF Chi-squared,  $\chi_2^2$  (exponential) distribution. Development of statistical fluctuation in the signal—with loss of correlation between individual transients—allows formation of the smooth exponentially decaying average. Smooth exponential decay is observed ubiquitously in reverberant field behavior. This behavior is central to analytical procedures that will be used to determine shielding effectiveness and other quantities of interest to an EMC engineer.

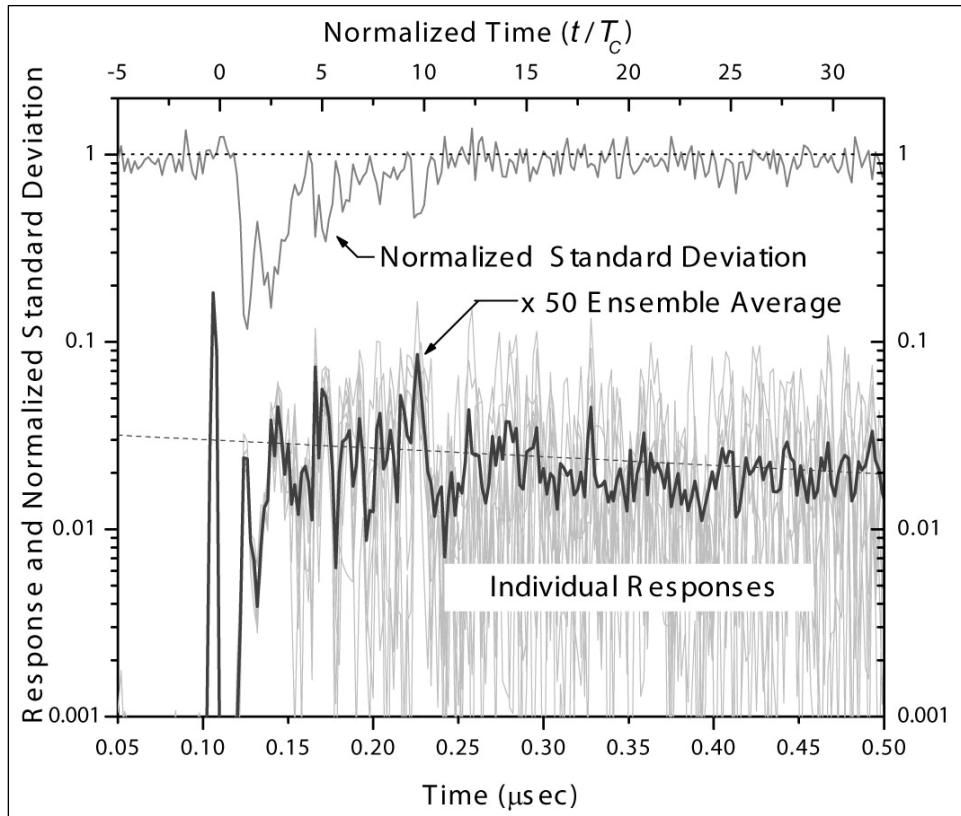


**Figure 2-8. Growth of Standard Deviation  
During Formation of a Reverberant Field**

#### **2.4.4 Comparison of Measured Data Cumulative Distribution Function (CDF) with Exponential CDF**

The received power from an antenna in a fully formed reverberant environment exhibits Chi-squared statistics with 2 degrees of freedom ( $\chi^2_2$ ). The Chi-squared behavior can be observed in several ways. With CW data, for example, data points at a particular frequency but with different paddle wheel positions are used to form an ensemble. Equivalently, the frequency can be stepped in a frequency stirring approach.

After the reverberant field is formed, measurement data taken at any instant of time in a transient response should fit the Chi-squared-exponential Cumulative Distribution Function (CDF). That is, at some time point ( $t \gg 8\text{-to-}10 T_C$ ), data points from the ensemble members should fit a Chi-squared CDF.

Further, Corbett, Richardson, and Lehman have shown that if the data are corrected for exponential decay, then multiple individual data points from a single response should

also fit a single Chi-squared CDF.<sup>19</sup> Additionally, Lehman has suggested that the number of independent points available from a single record can be derived as Equation (2-3):

$$\#indep\ pts \approx \frac{BW_{sweep}}{Mode\ Line\ Width} \approx \frac{\pi\tau}{T_p} \quad (2-3)$$

Several individual responses, similar to those shown in Figure 2-6, were corrected for decay. That is, data were normalized by dividing the response value at each time point by the best fit exponential trend line value at that point. 4500 points were chosen from the time region 1.5 to 2.0  $\mu$ sec of the response. In this region, the reverberant field was well established (i.e.,  $t/T_C = 100$  to 150). Figure 2-9 depicts the CDF for these data, where an ideal exponential probability CDF is also displayed.

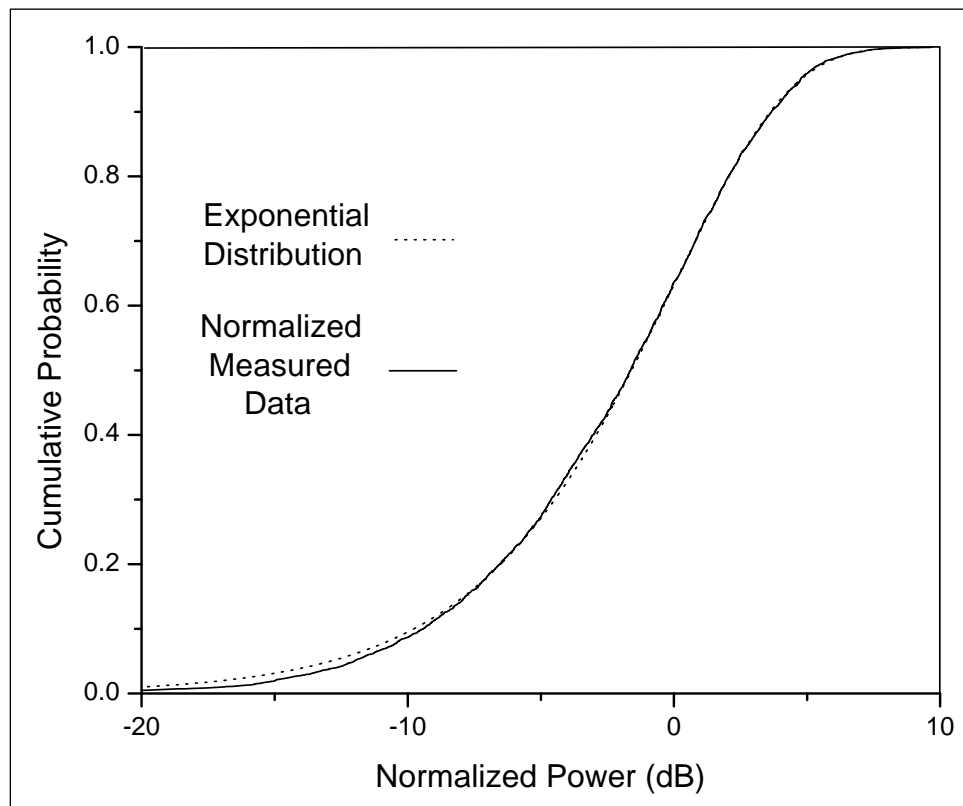


**Figure 2-9. Fit of Measured Data to an Exponential CDF**

Clearly a close fit exists between the distribution of measurement data and the ideal exponential function CDF. Close examination uncovers a break between theory and experiment at somewhat less than 0.1 on the CDF curve; however, at such a low value, it is of little practical importance for operational chamber measurements. This fit is

<sup>19</sup> B. L. Corbett, R. E. Richardson, and T. H. Lehman, "Statistical Characterization of Reverberant Chamber Transient Response Using Common CW-Analysis Tools and Methods." Topical Meeting on Reverberation Chambers, Zurich, Switzerland, 13-18 February 2005. EMC Zurich, [www.emczurich.ch](http://www.emczurich.ch).



considered good for reverberation chamber data. CW data generally show a break at higher probability values on the CDF.

The poorer fit of CW data that has been reported in CW experiments is attributed to the fact that with CW excitation, the chamber is driven during the measurement. The presence of the nonisotropic, pre-reverberant CW beam contaminates the reverberant environment. This is not an issue with TD data because after 8-to-10  $T_C$  periods, the original pulse has been converted to many isotropically propagating wavelets, and the excitation is no longer in its original form. See Appendix B for further discussion of method of images.

For either CW or transient excitation, direct cross talk from the original excitation is a smaller component of the total observed signal when the reverberation index of the chamber is high. Thus, better CDF fits should be observed from data taken in chambers with higher reverberation index.

## 2.5 PADDLE WHEEL PERFORMANCE

The operational definition of a reverberant field refers not to a single reverberant field configuration, but to an ensemble of equivalent, uncorrelated, statistically identical field configurations that one can use to form a good ensemble average.<sup>20</sup> The averaged response yields information about energy decay and leakage. Specifically, an EMC engineer can determine chamber insertion loss, shielding effectiveness, and other quantities of interest.

Paddle wheel design and performance is a key element of chamber and test/experimental design. The function of the paddle wheel is to change the geometry of the chamber so that at each position, a new, independent, uncorrelated field configuration can be obtained. A particular paddle wheel design is assumed to be good for CW measurements when it produces proper field uniformity and field statistics within the chamber.

Observation of pulsed-excitation ring-up responses provides insight about how paddle wheels perform and how paddle wheel designs may be studied and rated. Specifically, paddle wheel “goodness” should be correlated with the speed at which it converts the pre-reverberant nonisotropic field into a new, reverberant, isotropic field configuration that is statistically independent of other configurations produced in the chamber with the paddle wheel in other positions.

Wavefronts in the chamber can be stirred or scattered at transmission if the paddle wheel is irradiated by the transmitting antenna, as is usually done in CW chamber measurements. Irradiating the paddle wheel changes the excitation; additionally, waves are scattered further by the paddle wheel during subsequent reverberant propagation in the chamber. Experimentally, these two processes may be isolated for study by either

---

<sup>20</sup> Often in test operations where various test items are evaluated for performance in a specific EM environment, the maximum rather than average value of the field is considered.

directly irradiating or intentionally not irradiating the paddle wheels by the Tx and Rx antennas.

### 2.5.1 Stirring During Propagation

Energy is scattered by the paddle wheel during reverberant propagation in the chamber. The fraction of energy, which is scattered due to this assumed random interaction with the paddle wheel during reverberation, may be estimated as follows. Note that Equation (2-4) was defined earlier by Equation (2-2):

$$T_C = \frac{4V}{Sc} \quad (2-4)$$

where

$T_C$  is the characteristic time.

$S$  is the wall surface area in a chamber.

$V$  is volume.

The rate of wall scattering by energy  $W$  in the chamber is calculated in Equation (2-5):

$$P_{WallScat} = \frac{W}{T_C} = \frac{W}{V} \cdot \frac{c}{4} \cdot S \quad (2-5)$$

In time  $T_C$ , each photon in the chamber has scattered off the walls exactly once. This is shown explicitly by Equation (2-6):

$$P_{WallScat} \cdot T_C = W \quad (2-6)$$

By analogy, in this same time period  $T_C$ , the energy scattered from the paddle wheel  $P_{PWScat}$  is given by Equation (2-7):

$$P_{PWScat} = \frac{W}{V} \cdot c \cdot \Sigma_{PW} \quad (2-7)$$

where

$\Sigma_{PW}$  is the scattering cross section of the paddle wheel in an isotropic reverberant field;  $\Sigma_{PW}$  is the average (over  $4\pi$  steradians) projected area of the paddle wheel in the reverberant field multiplied by 2. (See Appendix C for a more detailed discussion.)

Dividing Equation (2-7) by Equation (2-6) shows that in time  $T_C$ , the fraction  $4\Sigma_{PW}/S$  of energy  $W$  in the chamber is scattered by the paddle wheel. In this interval the fraction  $(1 - 4\Sigma_{PW}/S)$  remains unscattered or unstirred. After  $n$  scattering  $T_C$  periods, the fraction  $(1 - 4\Sigma_{PW}/S)^n$  remains unscattered at least once. Equation (2-8) defines the fraction of un-scattered energy (USE):

$$USE_n = (1 - \frac{4\Sigma_{PW}}{S})^n \quad (2-8)$$

where

$USE_n$  is the fraction of energy in the chamber that has been unscattered or unstirred at least once after  $n$  characteristic  $T_C$  periods.

In Figure 2-10, Equation (2-8) is plotted as a function of  $n$  for several different values of  $\Sigma_{PW}$ . The wall surface area  $S$  is assumed to be 128 meters (m)<sup>2</sup>, which is the area of the chamber. The adage “bigger is better” is true for paddle wheels. Note, however, that in Equation (2-8)  $\Sigma_{PW}$  appears as a ratio with the chamber wall surface area. Thus, for stirring effects that occur during propagation, a given-size paddle wheel is less effective if it is placed in a larger chamber. The plots of Figure 2-10 show further that highly reverberant chambers permit better stirring of energy because higher  $n$  values lead to a lower unstirred energy fraction in Equation (2-8).

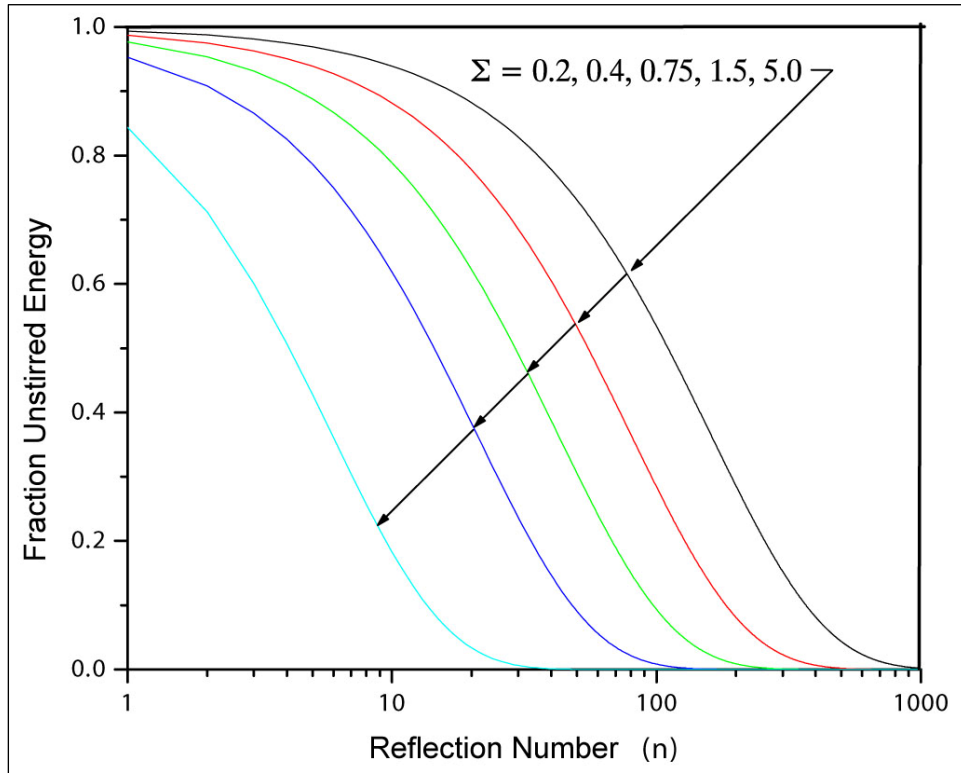


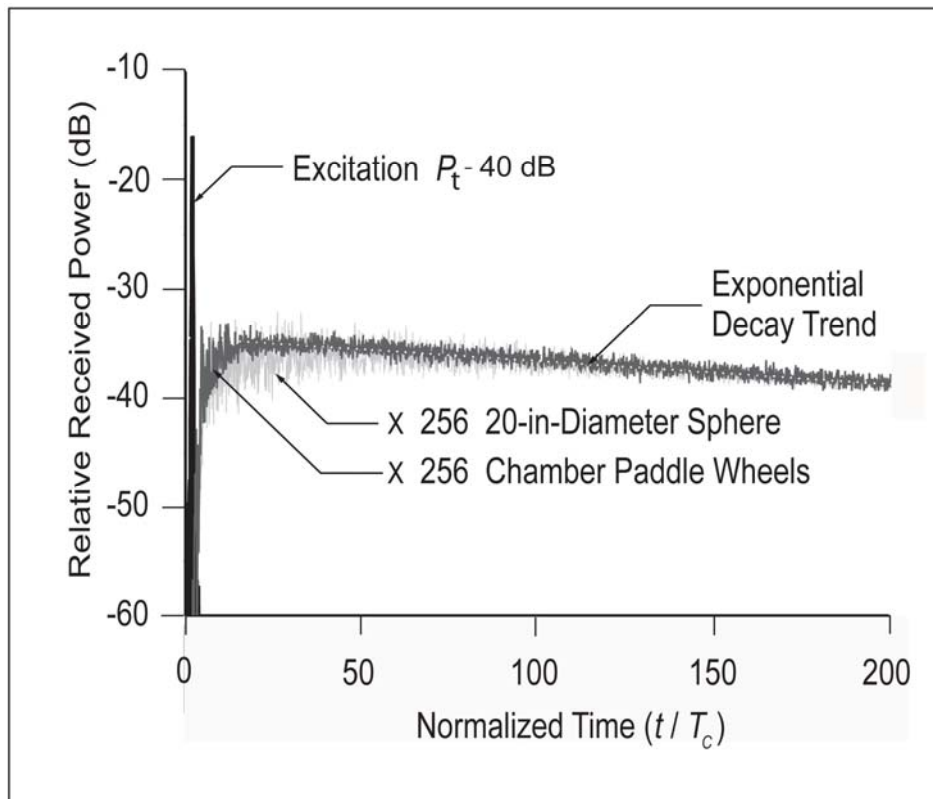
**Figure 2-10. Unstirred Fraction of Energy Versus Reflection Number**

The existence of uncorrelated field patterns permits the formation of a smooth exponentially decaying average, which is characteristic of good reverberant field behavior.

Similar to the ring-up response in Figure 2–4, Figure 2–11 depicts cases where the energy is stirred by either one of these stirring devices:

- a. Large chamber paddle wheels normally used in chamber operation
- or
- b. One 20-inch-diameter sphere that is revolved in the chamber about a 4-foot moment arm radius<sup>21</sup>

Ensemble-averaged received power approaches the exponential trend, indicating that the field patterns become independent much more rapidly with the larger paddle wheel.<sup>22</sup>



Note: Stirring was done with a large paddlewheel and a 20-inch-(in)-diameter sphere.

**Figure 2–11. Received Power Versus Normalized Time**

<sup>21</sup> Directional antennas in non-LOS configuration were used.

<sup>22</sup> The large paddle wheel has a Z-fold design with a one-sided area of approximately 6.5 m<sup>2</sup>.

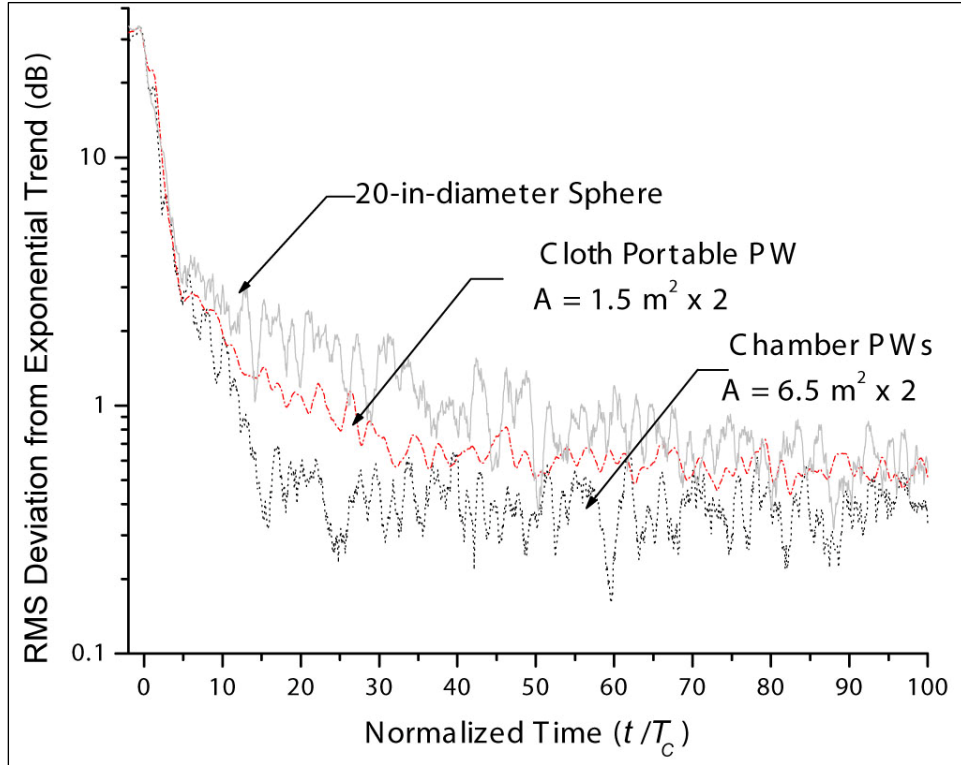
Figure 2–11 demonstrates that for the sphere, about 100 scattering times are required before the averaged response closely approaches the smooth exponential trend, indicating the formation of a new independent field configuration.<sup>23</sup>

A 20-inch-diameter sphere has a scattering cross section of only about  $0.4 \text{ m}^2$  (see Appendix C). In time  $T_C$ , the sphere scatters only about 1.27 percent of the energy present in a chamber with a  $128\text{-m}^2$  wall surface area. Figure 2–10 indicates that for  $n = 100$  and  $\Sigma_{PW} = 0.4 \text{ m}^2$  about 27 percent of the energy remains unstirred. The actual scattering cross section of the stirring arrangement with the 20-inch-diameter sphere may have been somewhat larger than  $0.4 \text{ m}^2$  because of scattering from the sphere support arm and counterbalance structure. For  $\Sigma_{PW} = 0.5 \text{ m}^2$ , approximately 20 percent of the energy remains unstirred at  $n = 100$ , and 11 percent remains at  $n = 140$ .

Further, Figure 2–12 depicts the calculated root mean square (RMS) deviation from the exponential trend ( $P_{RdB}(t) - P_{Trend \text{ dB}}$ ) versus time ( $t$ ) for several sphere measurements and for several measurements with a larger conductive cloth paddle wheel, referred to as a flat-plate paddle wheel. The one-sided geometrical area of the cloth paddle wheel was  $1.5 \text{ m}^2$ . The RMS deviation data from these cases were further smoothed by averaging over a 10-nsec interval. Averaged received power approaches the trend line behavior more rapidly with larger scattering area, as predicted by the calculation appearing in Figure 2–10. According to the results shown in Figure 2–12, the averaged response approaches the smooth trend in about  $50 T_C$  periods for the cloth paddle wheel. For  $\Sigma_{PW} = 1.5 \text{ m}^2$  in a chamber with  $S = 128 \text{ m}^2$ , 23 percent of the power remains unscattered at  $n = 30$ , and 9 percent remains at  $n = 50$ .

---

<sup>23</sup> The Lindgren Chamber has a characteristic wall scattering time of 9.7 nsec and a  $1/e$  time of about 2  $\mu\text{sec}$ . Thus, energy reverberates off the walls about 200 times in the time required for  $1/e$  energy decay.



Note: Three different stirring devices were employed.

**Figure 2-12. Root Mean Square (RMS) Deviation (Decibel) of Received Power from Exponential Trend Versus Normalized Time**

These results suggest that an EM environment begins to look reverberant with 10 to 20 percent of its total energy left unscattered at least once. On the other hand, the reduction technique, which has been employed here, is subjective, and analysis was based on a limited data set. A clear definition of just when the response reached true exponential decay was not stated. All of the curves are noisy, suggesting insufficient data. Additional experiments and a more detailed reduction approach are suggested as a topic of further investigation.

### **2.5.2 Stirring/Scattering at Transmission**

If the transmitting antenna illuminates the paddle wheel,<sup>24</sup> power scattered at transmission is given by Equation (2-9):

$$P_{PWScat} = \frac{P_{Tx} G_{Tx}}{4\pi R^2} \cdot \sigma_{PW} \quad (2-9)$$

<sup>24</sup> For consistency in this equation,  $T_x$  has been used as a subscript; elsewhere in this document, transmitting gain has been referred to as  $G_t$ .

The fraction of power scattered on transmission (i.e.,  $P_{PWScat}/P_{Tx}$ ) is typically about 29 percent. For example, the following typical values apply:

- a.  $R = 2 \text{ m}$
- b.  $\sigma_{PW} = 1.5 \text{ m}^2$   
(Note that for a paddle wheel that rotates,  $\sigma_{PW}$  is defined differently from  $\Sigma_{PW}$ . It is the average projected area over a 360-degree paddle wheel rotation.)
- c.  $G_{Tx} = 10 \text{ dB}$

In a calculation similar to that which was performed for reflection number, one can consider the energy that remains unscattered after some number of independent paddle wheel positions. After one position of the paddle wheel described above, the fraction 0.71 remains unscattered. For 10 independent paddle wheel positions, the amount of energy left unscattered (i.e., the percentage USE) from the paddle wheel is expressed in Equation (2–10):

$$\%USE_{10} = 100 \times 0.71^{10} \approx 3.25\% \quad (2-10)$$

The data for Figures 2–11 and 2–12 were generated with an antenna arrangement in which the Tx and Rx antennas did not directly illuminate or view the scattering objects, so they measure the scattering during propagation. EMC engineers have demonstrated in regular CW chamber operation that by irradiating a paddle wheel with the Tx antenna, more uniform fields are achieved over a greater frequency range. The data of Figure 2–13 show that the observed transient behavior approaches the ideal exponential trend most rapidly if the Tx and Rx antennas irradiate and view chamber paddle wheels. In this best case, response approaches the exponential trend to within 1 dB in approximately 4 to 5  $T_C$  periods. About 10  $T_C$  periods are required for the nonilluminate/nonview case, where stirring occurs only during propagation.

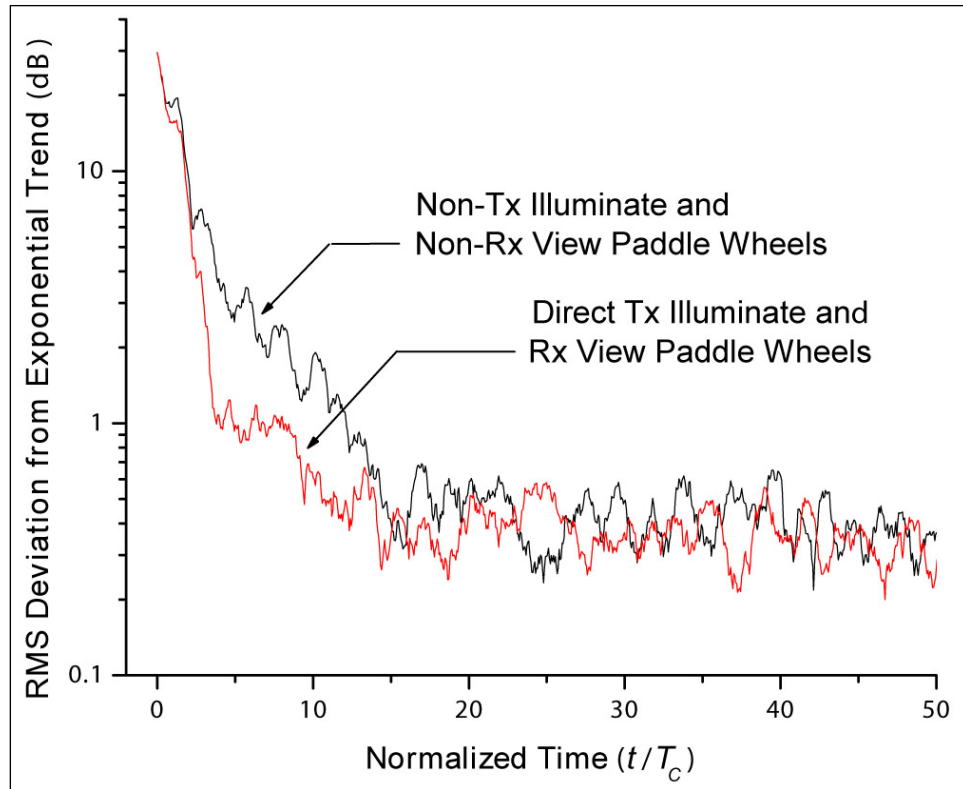


**Figure 2-13. RMS Deviation from Exponential Trend Line Versus Normalized Time**

When the Tx and Rx<sup>25</sup> antennas view the paddle wheels, maximum randomization of the chamber excitation and field sampling is achieved, which “immediately” causes statistical variation in the measured response before the field has had time to randomize from the usual propagation process.<sup>26</sup> During normal chamber operation in measurements of a test item, neither the test item nor the Rx antenna views the paddle wheel.

Equation (2-9) shows that to maximize the fraction of energy that is scattered by the paddle wheel during transmission, one should maximize the quantity  $(G_t \sigma_{PW}/R^2)$ . Thus, a high-gain transmit antenna, a large paddle wheel, and the placement of the antenna as close as possible to the paddle wheel all lead to maximal stirring at transmission.

Illumination of the paddle wheel is a powerful technique. One may guess that the only improvement to this technique would be to move the Tx antenna itself to a new

<sup>25</sup> Rx antenna viewing of the paddle wheel is not characteristic of normal test chamber operation with an item under test.

<sup>26</sup> Recall that for the measurement data displayed in Figures 2-6 through 2-8, the Rx and Tx antennas were fixed. While the antennas did view the paddle wheels, they had nearly omnidirectional gain ( $G \sim 1$ ) and were intentionally not deployed near the paddle wheels. These factors tended to minimize  $G_t \sigma_{PW}/R^2$ .



independent position at each step. Given this arrangement, 100 percent of the injected power, rather than only 29 percent as in Equation (2–9), would be randomized. Hatfield has shown that even in poorly reverberant spaces, useful reverberation chamber-type measurements can be performed by “aggressive” antenna repositioning between data collection sequences.<sup>27</sup>

The data displayed in Figures 2–11 through 2–13 were all taken with a pulse that had a 3.6-GHz-carrier center frequency and a nominal 1-nsec-equivalent pulse width. The 3.6-GHz frequency is well within the good chamber operating frequency range.

### **2.5.3 Additional Paddle Wheel Experiments**

The results of Section 2.5.2 suggest that a field begins to look reverberant while between 10 to 20 percent of its total energy remains unscattered or unstirred. Intuitively, this is a high percentage; however, the reduction technique was somewhat subjective. Analysis was based on a limited data set. Additional data, additional experiments, and a more precise reduction approach are suggested to examine this result further. In any case, time-domain-based experiments appear to be particularly well suited to paddle wheel performance and design study, since they offer a direct view of reverberant field development.

These experiments demonstrate that paddle wheel performance is inextricably linked to chamber size and reverberation index, as well as whether the paddle wheel is illuminated or not illuminated by the excitation. Further, additional work is required to study paddle wheel effectiveness at lower frequencies at which chamber and paddle wheel performance begin to degrade.

A fundamental question about paddle wheel performance arises: How many statistically independent paddle wheel positions are available from a particular paddle wheel design at a particular frequency? If paddle wheel positions are independent, the correlation between individual transient responses should decay with time, as is demonstrated in Figure 2–7. An enlightening experiment would be to study how rapidly and/or how much the correlation between two transient signals from adjacent paddle wheel positions decays as a function of how many degrees a paddle wheel is rotated between steps. Results from this type of experiment could be compared with and may provide additional insight into experimental results that have been obtained with CW technique.

## **2.6 TRANSIENT BEHAVIOR FROM A CAVITY MODE VIEWPOINT**

The preceding discussion in all of Section 2 has been cast in terms of planewaves scattering off chamber walls and paddle wheels. An alternative, yet equivalent and equally compelling viewpoint is to consider the fields in terms of cavity modes rather than planewaves.

---

<sup>27</sup> M.O. Hatfield, in. situ, *Shielding Effectiveness Measurements of a Transport Aircraft*. NSWCDD/TR-03/107: n. pag.

Figure 2–14 shows relative E field response of a chamber after pulse excitation. The antenna setup is similar to that of Figure 2–4.

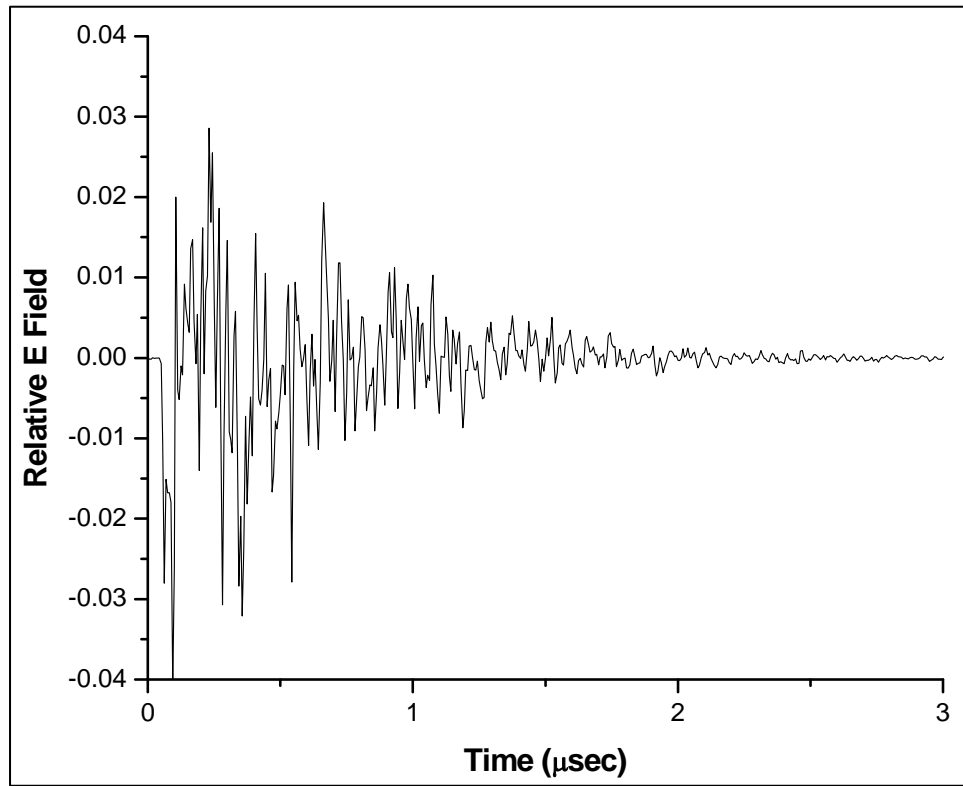


**Figure 2–14. Measured E Field Response of an Over-Moded Cavity to Pulsed Excitation**

Data that have been considered thus far have been squared and ensemble averaged to indicate  $E^2$  or received power versus time. The single-shot data of Figure 2–14 are unsquared and unaveraged. This response indicates relative E field rather than received power versus time.<sup>28</sup> The data of Figure 2–14 are highly suggestive of individual modes beating together while decaying. Individual modes decay exponentially, but due to beating between modes, the decay is nonmonotonic.<sup>29</sup> Smooth exponential decay is observed only from squared, ensemble-averaged data. Analysis of an ensemble of responses from the experiment, in which these data were generated, shows that the 1/e time for the data of Figure 2–14 is about 0.3 μsec. This kind of signal is available at the output of the final mixer in a radar receiver, as further explained in Appendix A.

The kind of behavior shown in Figure 2–14 was first reported by Lamb in 1946. He observed it in large (and thus highly overmoded) cavities that he had constructed to study

<sup>28</sup> This kind of signal is available at the output of the final mixer in a radar receiver.

<sup>29</sup> Robert E. Richardson, “Mode-Stirred Chamber Calibration Factor, Relaxation Time and Scaling Laws,” *IEEE Transactions on Instrumentation Measurement*, vol. IM-34 (December 1985): 573–580.

molecular absorption of microwave energy by various gasses. He referred to this cavity behavior as “gurgling.”<sup>30</sup>

## 2.7 SUMMARY: REVERBERANT FIELD FORMATION AND MEASUREMENT

In this report, a short-pulse radar is used as a measurement tool to study reverberant field formation and behavior. This is done by examining ensemble-averaged transient responses to short pulses that the radar has injected into the chamber under study.

Beginning with a single spherical wavefront, many individual wavefronts are created by reflections off chamber walls and internal contents. After a short time, individual wavefronts become indistinguishable. Measurements and analysis are performed on the environment as a whole.

Depending on context, the definition of reverberant field generally refers not just to a single field configuration, but to an ensemble of field configurations within the space under study. New field configurations are formed by changing the chamber geometry or excitation. This is done either by antenna relocation or the use of mode stirring paddle wheels.

The fundamental and dominant process, which occurs in reverberant field behavior, is that of EM energy in the space scattering or reflecting from the walls. This is the process whereby a reverberant field is created. A natural wall-scattering rate ( $1/T_C$ ) has been defined by acoustic reverberation scientists early in the 20th century as Equation (2–11), previously Equations (2–2) and (2–4):

$$T_C = \frac{4V}{Sc} \quad (2-11)$$

where

$V$  is chamber volume.

$S$  is chamber wall surface area.

$c$  is speed of light.

The term  $T_C$  is loosely referred to as the characteristic scattering time for a chamber. In a time period  $T_C$ , an average photon in the field has scattered from the walls once.

---

<sup>30</sup> Lamb reports this calculation in two concurrently published journals:  
Willis E. Lamb, Jr., “Theory of a Microwave Spectroscope,” *Physical Review*, vol. 70, no. 5 (1 September 1946) and no. 6 (15 September 1946): 308–317 (printed as one article).

The author is indebted to Theodore H. Lehman for bringing this paper to his attention.

The power received by an antenna in a reverberant field follows a 2-DOF Chi-squared  $\chi^2_2$  (exponential) statistical distribution. The statistical properties of the field are developed as it is formed and generally require about 8-to-10  $T_C$  periods.

TD technique with an A-scope display for viewing transient responses is an ideal tool for studying propagation in a space and for verifying that a proper test environment exists in a reverberation test chamber.

### 3.0 REVERBERANT FIELD BEHAVIOR AND PRIMARY MEASUREMENTS

#### 3.1 INTRODUCTION

Even though a reverberant field is always initiated with nonisotropic excitation of a space, experimental data show that wall and paddle wheel scattering processes rapidly produce an isotropic reverberant field. Geometry changes from paddle wheel or antenna motion allow the creation of an ensemble of independent but statistically equivalent reverberant field patterns from which one extracts an ensemble-averaged response.

The basic questions EMC engineers consider for the fields in a reverberant space follow:

- a. How rapidly is energy scattered from the walls of a space?
- b. How rapidly is energy lost?
- c. How rapidly does energy leak into or out of the space?<sup>31</sup>

The scattering rate ( $1/T_C$ ) is not measured directly, but is calculated from the chamber volume and surface area [see Equations (2–2) and (2–4)]. The loss and leakage rates, which are much smaller in a highly reverberant space, are calculated from the measured ensemble-averaged transient response. In a highly reverberant space, the fields are statistically uniform, and the loss and leakage rates have unique values, which can be used together with relationships based on conservation of energy to calculate insertion loss (IL), shielding effectiveness (SE), and various other quantities of interest.

Intuitively, one can form a mental picture of an initially nonisotropic field distribution driven by wall scattering to a uniform, isotropic, reverberant equilibrium state. That state can be observed using a procedure based on ensemble averaging of its transient response. If losses and leakage are small compared to the dominant scattering process, which generates and maintains the reverberant field, then it is not significantly disturbed from its equilibrium state.

Importantly, even though all measurements and analyses are performed with transient quantities, the analytical results are directly comparable to, and can be shown to be consistent with, steady state CW measurement-based results.

Peak response values are often used when performing CW measurements in reverberation chambers. However, the average steady-state CW response is well accepted and would be useful for certain calculations. The transient-based techniques described here rely on ensemble-averaged transient response. Within the stipulations placed on the rates for loss, leakage, and scattering, the ensemble average is equivalent to a spatial average and adequately describes the spatially averaged transient energy behavior in the chamber.

---

<sup>31</sup> Additionally, EMC engineers are frequently concerned about how uniform the field is within the space.

Averaging in this manner not only works with steady-state quantities, it also works for transients.

Time-domain technique offers a precise way to measure decay and leakage rates, which are required for analysis. In this section, transient measurement and analysis procedures are demonstrated to show how results are obtained and how they are related to traditional CW measurement results.

### 3.2 IDEALIZED CHAMBER RESPONSE TO DELTA FUNCTION EXCITATION

When the reverberation index of a chamber is high, the pre-reverberant phase of field formation is much shorter than the reverberant exponential decay phase. This leads to the simple and extremely useful approximation that the energy density behavior is described solely by simple exponential decay. The energy dynamics in the chamber are then set entirely by leakage and loss rate coefficients. Reverberant field (i.e., energy density) behavior suddenly becomes clear to the EMC engineer already familiar with resistance capacitance (RC) circuit behavior.

#### 3.2.1 Fundamental Differential Equation

Considering chamber response over time intervals, which are long compared with  $T_C$ , Equation (3-1) presents a simple relationship for the spatially averaged energy density  $u(t)$ :

$$u(t) = u_0 \cdot e^{-t/\tau} \quad (3-1)$$

where

$u_0$  is the initial energy density ( $\text{J/m}^3$ ).

Equation (3-1) is the solution for the differential equation posed in Equation (3-2):

$$V \dot{u}(t) = -\Lambda u(t) + \delta(t) \quad (3-2)$$

Equation (3-2) describes the rate of change of energy  $u(t) \times V$  within the chamber, which has been excited by a mathematical  $\delta$  function<sup>32</sup>.

---

<sup>32</sup> A  $\delta$  function is a short pulse. Ideally, it has infinite height and zero width with unit area. For practical chamber measurements, the pulse width should be much shorter than the chamber  $1/e$  time. Additionally, if pre-reverberant behavior is to be examined, it should be much shorter than  $T_C$ .

$V$  is retained on the left-hand side of Equation (3–2), and  $\Lambda$  is defined as the chamber wall loss rate. Power lost at the chamber walls depends on wall resistivity and on the square of the surface currents induced in the walls. Since the fields are assumed to be statistically uniform, the square of the surface current at some arbitrary point on a wall is proportional to  $u(t)$  at an arbitrary point in the chamber.<sup>33</sup> With all chamber losses lumped into  $\Lambda$ , it may be evaluated simply as  $V/\tau$ .

The energy in the  $\delta$  function is the initial energy  $W$  injected into the chamber.  $W$  is given by the product of peak pulse height ( $P_t$ ) and pulse width ( $T_p$ ). With the synthetic swept CW technique of pulse generation, which is used for the bulk of the measurements described in this report, the pulse width ( $T_p$ ) is given by  $2/BW$ , as defined in Section 2.2.1.1 and Appendix A.

The energy density within the chamber following excitation with a pulse is thus given in Equation (3–3):

$$u(t) = u_0 e^{-t/\tau} = \frac{P_t T_p}{V} e^{-t/\tau} \cdot \eta_t \quad (3-3)$$

where

$\eta_t$  is a transmitting antenna efficiency factor that includes ohmic and possibly impedance mismatch loss factors.

### 3.2.2 Insertion Loss

Ensemble-averaged power  $p_r(t)$  received by an antenna with capture area  $\lambda^2/8\pi$  in the chamber is given in Equation (3–4):

$$p_r(t) = u(t) \cdot c \cdot \frac{\lambda^2}{8\pi} \cdot \eta_r \quad (3-4)$$

where

$\eta_r$  is a receiving antenna efficiency factor.

Defining IL as the ratio of energy received to the energy transmitted into the chamber, one can integrate under a  $p_r(t)$  versus  $t$  curve, divide by  $P_t \times T_p$ , and obtain Equation (3–5):

$$IL = 10 \log \left| \frac{W_r}{W_t} \right| = 10 \log_{10} \left[ \frac{c \tau}{V} \cdot \frac{\lambda^2}{8\pi} \cdot \eta_r \eta_t \right] \quad (3-5)$$

---

<sup>33</sup>  $u$  is proportional to  $E^2$  and  $H^2$ .

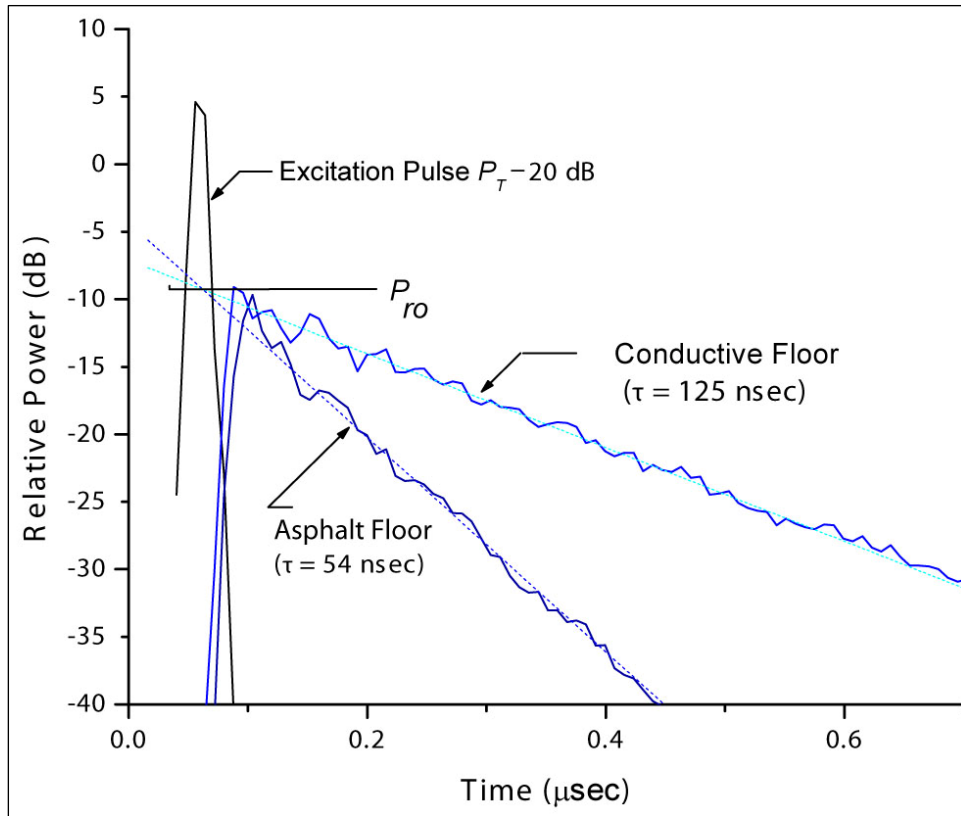
This result, in terms of received and transmitted energies, is identical to that which would be obtained as the ratio of *average* received and transmitted power with a CW measurement. CW-based and radar-based measurements of insertion loss are directly comparable and numerically equal. Operational CW measurements are often based on *peak* rather than *averaged* received power, so a peak-to-average correction must be applied when comparing results from the two techniques.

The right-hand side of Equation (3–5) shows that IL can be evaluated from measurements of  $\tau$  and chamber volume, if one has a good estimate of antenna efficiencies. A value for  $\tau$  naturally results from TD measurement, and chamber volume can usually be determined. Thus, Equation (3–5) gives an important internal consistency check on measurement results or, conversely, a measurement of antenna efficiency.

#### 3.2.2.1 Example of Received and Transmitted Energy Ratio Measurement: Tent Experiment

Figure 3–1 shows received power versus time ( $p_r(t)$ ) in a “tent” test chamber constructed from conductive cloth. The figure shows data from two averaged  $p_r(t)$  responses together with the excitation pulse obtained by disconnecting the antennas and connecting the Rx and Tx transmission lines directly together through a 20-dB calibrated attenuator. The excitation pulse for this experiment was derived from a 600-to-725-megahertz (MHz) sweep. Thus, it had a 125-MHz BW leading to a 16-nsec nominal pulse width and a center frequency of 665 MHz. The tent, basically a 12-ft cube, had a volume of 48.96 m<sup>3</sup> and a characteristic wall-scattering time ( $T_C$ ) of 8 nsec. The measurements were performed using two lightweight log-periodic dipole array antennas. The Tx antenna was tripod-mounted and fixed, while the Rx antenna was hand-held and constantly moved about the chamber during data collection, taking care not to view the Tx antenna intentionally.





Note: The transient response is shown in a conductive cloth tent with and without a conductive floor.

**Figure 3–1. Excitation Pulse and Received Power Versus Time for Antennas in a Tent Chamber**

The tent was set up in an asphalt parking lot. The experiment was performed with a bare asphalt floor and also with a conductive cloth floor. For the bare floor case, a large fraction of the EM energy escaped through the floor, which had a reflectivity of approximately 20 percent (see Sections 5.3.1 through 5.3.3). Addition of a conductive cloth floor reduced this leakage and increased the 1/e time. However, leakage of energy was still significant at unsealed seams and joints between individual cloth sheets that formed the tent walls, ceiling, and floor.

With a conductive cloth floor, the 1/e time was measured as 0.125 μsec. Substitution of these parameters into Equation (3–5), assuming unity antenna efficiency factors, yields a calculated IL of 22.04 dB and 25.68 dB for the 0.054 μsec asphalt floor case.

The initial energy density in a space immediately following the injection of a pulse has a value given by the injected energy divided by the volume. Note that the response curves from the two different floor test cases in Figure 3–1 both extrapolate back to the same value designated in Figure 3–1 as  $P_{ro}$  at  $t = 0$ . Changing the floor material of the tent does not change its volume. Both curves extrapolating back to the same point is a requirement.

In Figure 3–2, the data of Figure 3–1 are time integrated by using the SUM function available in the data analysis spreadsheet and then multiplying by the time interval between data points. For integration, data in decibel form are first converted to relative power levels using the relationship  $P = 10^{(dB/10)}$ . The vertical scales of Figures 3–1 and 3–2 are not calibrated in an absolute sense. Analysis requires the ratios of the response curve integrals to the excitation integral. This depends only on the relative position of the curves with respect to each other—not their absolute position—so an absolute calibration is not necessary. The calculations require only relative watt (W) and W-sec.

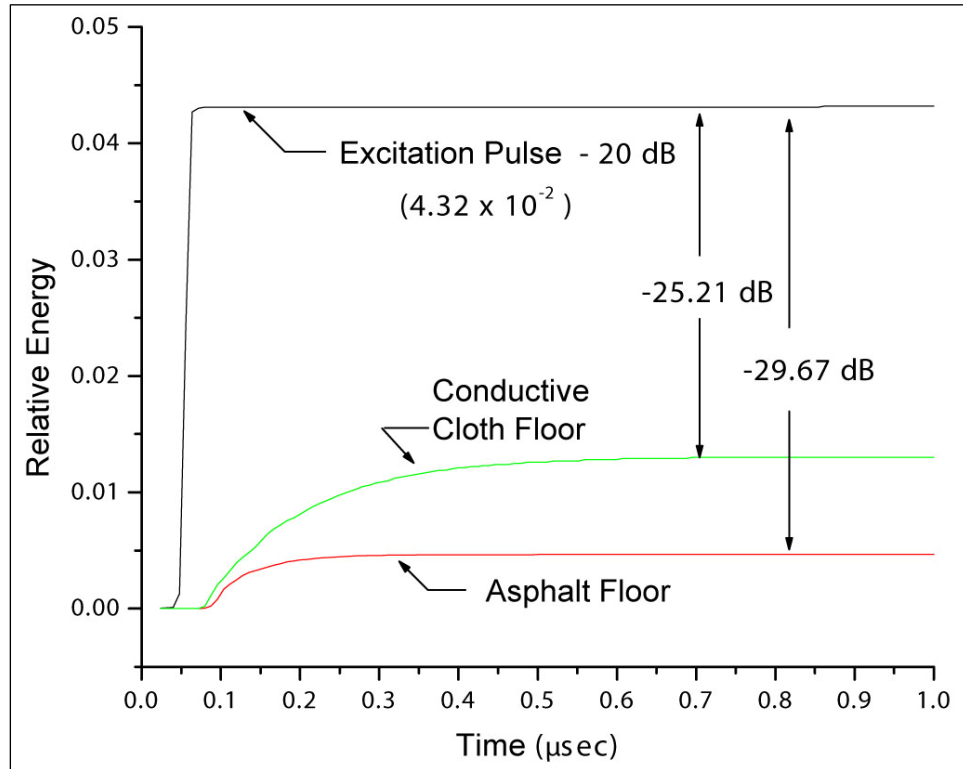


**Figure 3–2. Integrated  $P_r(t)$  Responses from Tent Chamber**

In Figure 3–2, the relative area under the excitation pulse  $4.32 \times 10^{-2}$  (relative W-sec.) is consistent with the value  $4.61 \times 10^{-2}$  obtained by multiplying the peak pulse power by the nominal 16-nsec pulse width. Taking the ratios of the pulse and response integrals in Figure 3–2, the measured insertion losses are 25.21 and 29.67 dB for the conductive and asphalt floor cases. These values are 3 to 4 dB greater than the values reported above, which were directly calculated from Equation (3–5) assuming unit antenna efficiency factors and no mismatch correction.

### 3.2.2.2 Antenna Efficiency Factor Estimate

TD measurements with their explicit (and precise) determination of  $1/e$  time provide a way of independently checking CW IL results and even for estimating antenna efficiency.

Equation (3–5) contains antenna efficiency factors that include ohmic losses in the antennas and possibly impedance mismatch factors. Typically, impedance mismatch factors add a 1-to-2-dB correction to IL measurements.

Also, with the usual orthogonal (non-LOS) antenna placement, as was used for the data of Figure 3–1, the measured response is that of the reverberant field, which is fully developed only after a few  $T_C$  periods. The energy present in the chamber for the first few  $T_C$  periods while the reverberant field is being formed is not recorded; therefore, it is missed in the measurement. In a highly reverberant space, the pre-reverberant response phase is much smaller than the reverberant phase, and its noninclusion in the measurement would normally be negligible. However, in trying to estimate an antenna efficiency factor that is nearly unity, this normally negligible factor may be important.

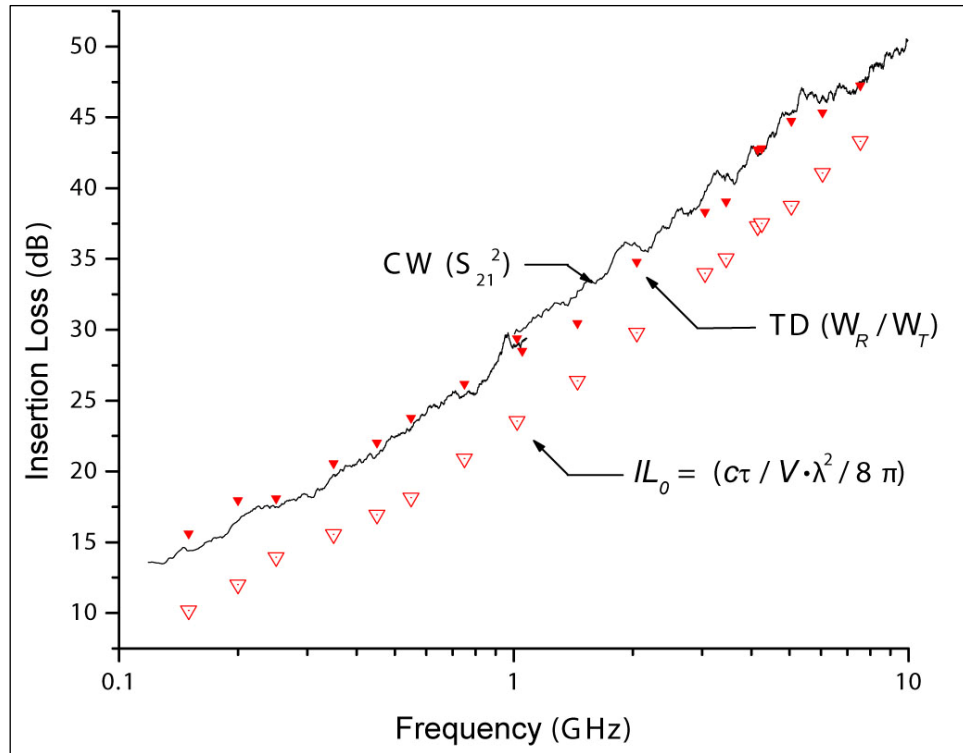
The response integrals discussed above were calculated simply as area under the received power versus time curves. The response integrals did not begin to grow until a few  $T_C$  after the excitation. An alternative way of calculating the integrals would be to integrate under the best fit exponential trend lines and, thus, begin growing the integrals at  $t = 0$ , rather than after a few  $T_C$  when the reverberant field actually builds up. This would be consistent with an idealized view of chamber response, where the assumption is that a reverberant field is formed instantaneously after excitation. Integrating under the trend lines starting at  $t = 0$  in this way adds 0.64 dB to the cloth floor and 1.64 dB to the asphalt floor integrals. The correction is smaller for the conductive cloth floor case consistent with the notion that in an ideal high-reverberation case, the reverberant field formation time is negligible in comparison with the reverberant phase of the response.<sup>34</sup>

### 3.2.2.3 Comparison of Continuous Wave (CW) and Time-Domain Insertion Loss Data

Figure 3–3 shows IL data experimentally determined from both CW-based<sup>35</sup> and time-domain-based measurements performed in the large Naval Surface Warfare Center, Dahlgren Division (NSWCDD) chamber. Log-periodic dipole array antennas were used for the Tx and Rx antennas in the frequency range between 0.1 and 1.0 GHz. Dual-ridge waveguide horns were used for measurements in the range between 1 and 10 GHz. The CW IL was measured from averaged values of  $|S_{21}|$  on a precision network analyzer connected to chamber antennas. Transmission line losses were calibrated out using standard network analyzer calibration techniques and, thus, are not at issue.

<sup>34</sup> The reverberation index for the tent with the conductive cloth floor is 15, while that for the asphalt floor case is 6.75.

<sup>35</sup> Average CW IL was measured using average received CW power, not peak power.



Note: The difference between IL and  $IL_0$  indicates antenna efficiency effects.

**Figure 3-3. Insertion Loss (IL) Measurement Results for Large NSWCDD Reverberation Chamber**

Separate measurements of  $S_{11}$  and  $S_{22}$  indicate that impedance mismatch accounts for 1-to-2 dB of the 4-to-5 dB difference between measurement data and the idealized IL calculation, denoted as  $IL_0$  in Figure 3-3 and calculated from Equation (3-5), assuming unit values for antenna efficiency. Generally,  $\tau$  can be measured accurately from the slope of a decay curve. Thus, one expects that the  $IL_0$  values in Figure 3-3 are precise.

Integration under a trend line, back to  $t = 0$ , did not produce large corrections in the TD data. The reverberation index ( $\tau/T_C$ ) for the large NSWCDD chamber is about 50.

Antenna efficiency for the log-periodic antennas used in the test is generally taken as 0.75, while efficiency for the dual-ridge horn antennas is quoted as 0.95. A value of 0.75 should produce a 2.49-dB difference between  $IL_0$  and actual measured TD and CW values. The typical 4-to-5-dB difference, which also includes a 1-to-2-dB correction for impedance mismatch, is consistent for the low-frequency data. However, if the 0.95 efficiency figure is correct for the dual-ridge antennas used between 1 to 10 GHz, the measured CW and TD data points should be about 2 dB closer to the  $IL_0$  data points. The quoted 0.95 figure may be high.

Clearly, time-domain technique offers a promising approach to the problem of antenna efficiency measurement. However, some difficulties in obtaining precise measurement

results may occur. In general, one would want to separate out the impedance mismatch correction from ohmic loss, though in practical measurements, mismatch is usually neglected. Doing mismatch correction in TD measurement is difficult with the radar. Measurement, where correction is required, would probably be most easily done by using a VNA rather than the radar. One could export  $S_{11}$  and  $S_{22}$ , as well as  $S_{21}$  parameter values, into a personal computer (PC) and perform the Fourier-transform math on corrected  $S_{21}$  values in the PC, rather than use the “canned routines” in the VNA, which operate only with  $S_{21}$  values before correction. The TD IL values shown in Figure 3–3 were calculated from the ratio of area under the response curve to area under the excitation pulse, as described for the results shown in Figure 3–2. IL calculated from TD data in this way should be exactly equivalent<sup>36</sup> to the CW data based on  $|S_{21}|^2$ . Figure 3–3 shows that the CW and TD data track closely.

The “area under a response curve” calculation to determine received energy from a TD measurement should be exactly equivalent to a CW measurement result, if the same non-LOS antenna placement is used. Ideally, the CW response does not include any direct pre-reverberant response.

Questions remain about exactly how to account for the missing portion of response while the reverberant field builds up. For example, does one integrate all the way back to  $t = 0$  (the center of the excitation pulse) or only to the point at which the excitation pulse ends? Unless the pulse is very short, some difference in the results will occur. This is a time-domain-only issue. A proper CW measurement (i.e., proper antenna orientation) yields response only from the reverberant field and, equivalently, only begins after the reverberant field has formed. All of these issues become less important if measurements are performed in a highly reflective space where the pre-reverberant phase becomes vanishingly small compared with the reverberant phase.

### 3.3 NESTED CHAMBER SHIELDING EFFECTIVENESS MEASUREMENT

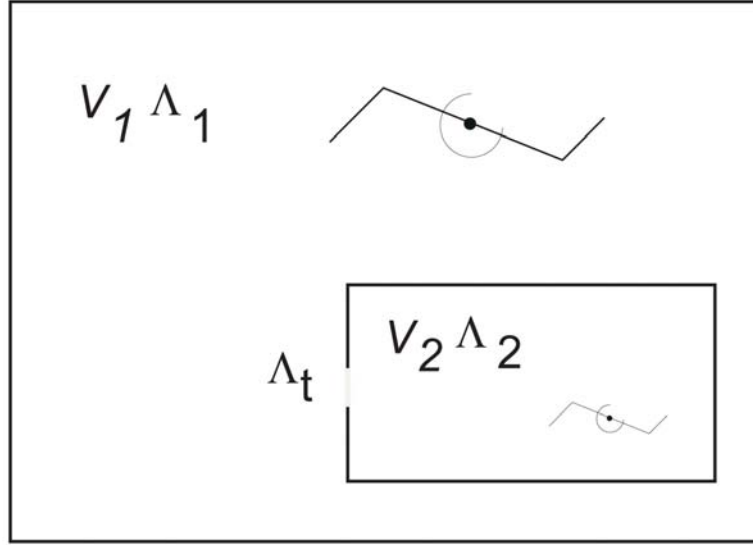
Within the limits that have been imposed about not creating situations that drive the field too far away from its equilibrium state, the picture of exponential energy density decay behavior in transient reverberation response specifically addresses the dynamics of energy loss and transfer within a cavity or between coupled cavities. It is applied here to nested chamber measurements that are used for shielding effectiveness studies of various gasket materials and are currently of interest for evaluation of advanced conductive composite materials.<sup>37</sup>

<sup>36</sup> With the same non-LOS view antenna placement, the CW data should be indicative of the reverberant field response just as the TD data are. Also, reflected power/mismatch correction was not done for the TD data.

<sup>37</sup> Christopher L. Holloway, David A. Hill, John Ladbury, Galen Koepke, and R. Garzia, “Shielding Effectiveness Measurements of Materials Using Nested Reverberation Chambers,” *IEEE Transactions on Electromagnetic Compatibility*, vol. 45, no. 2 (May 2003): n. pag.

### 3.3.1 Coupled (Nested) Cavities

Expanding on the single-cavity idea expressed in Equations (3–1) and (3–2), coupled (nested) cavities depicted in Figure 3–4 may be described with Equations (3–6) and (3–7). Each cavity is excited with a short pulse. The ensemble-averaged energy densities in it and also in the other cavity are examined. Equations (3–6) and (3–7) are written for excitation of cavity 1. The energy density  $u(t)$  is assumed to be uniform throughout each cavity, and an ensemble average is assumed to be equivalent to a spatial average.



Note: The cavity volumes are  $V_1$  and  $V_2$ , the loss coefficients are  $\Lambda_1$  and  $\Lambda_2$ , and the coupling coefficient is  $\Lambda_t$ .

**Figure 3–4. Pair of Nested Cavities**

$$V_1 \dot{u}_1(t) = -(\Lambda_1 + \Lambda_t)u_1(t) + \Lambda_t u_2(t) + \delta(t) \quad (3-6)$$

$$V_2 \dot{u}_2(t) = \Lambda_t u_1(t) - (\Lambda_2 + \Lambda_t)u_2(t) \quad (3-7)$$

where

$u_1(t)$  and  $u_2(t)$  ( $\text{J}/\text{m}^3$ ) are the ensemble and spatially averaged energy densities in each cavity following the injection of a short pulse ( $\delta(t)$ ) of EM energy.

The solution of these two equations yields Equations (3–8) and (3–9):

$$u_1(t) = \frac{U_o}{\alpha - \beta} \left[ \frac{1}{V_1} \{ \alpha e^{\alpha t} - \beta e^{\beta t} \} + \frac{\Lambda_1 + \Lambda_2}{V_1 V_2} \{ e^{\alpha t} - e^{\beta t} \} \right] \quad (3-8)$$

and

$$u_2(t) = \frac{U_o \Lambda_t}{V_1 V_2} \frac{\{ e^{\alpha t} - e^{\beta t} \}}{\alpha - \beta} \quad (3-9)$$

where the coefficients  $\alpha$  and  $\beta$  are defined according to the relationships shown in Equations (3–10) and (3–11):

$$C = \left[ \frac{\Lambda_1 \Lambda_2 + \Lambda_1 \Lambda_t + \Lambda_2 \Lambda_t}{V_1 V_2} \right] \quad B = \left[ \frac{\Lambda_2 + \Lambda_t}{V_2} + \frac{\Lambda_1 + \Lambda_t}{V_1} \right] \quad (3-10)$$

$$\alpha = \frac{-B + \sqrt{B^2 - 4C}}{2} \quad \beta = \frac{-B - \sqrt{B^2 - 4C}}{2} \quad (3-11)$$

### 3.3.2 **Definition of $\Lambda$ -Rate Coefficients and Discussion of Differential Equations for $u(t)$**

Equations (3–6) and (3–7) are based on conservation of energy. They describe the dynamics of energy loss and transfer between cavities 1 and 2 when a short pulse of energy is suddenly injected into cavity 1. Specifically, the coefficients  $\Lambda_1$  and  $\Lambda_2$  refer to the rates at which energy is lost ohmically within each cavity. The coefficient  $\Lambda_t$  describes leakage between cavities. The field in each chamber is assumed to be fully reverberant, and the leakage process is assumed to be reciprocal. That is, the leakage coefficient from chamber 1 into chamber 2 is assumed to be identical to that for chamber 2 back into chamber 1. Thus, the same value for  $\Lambda_t$  appears in both Equations (3–6) and (3–7).

The  $\Lambda$ -rate coefficients set the time scale of the dynamics. To be valid, a necessary requirement for Equations (3–6) and (3–7) is that the loss and leakage rates are much slower than the wall-scattering rate that generates and maintains the reverberant field.

According to Equation (2–5) in Section 2.5.1, power  $P_{ws}(t)$  scattered off the walls of a chamber is given by Equation (3–12):

$$P_{ws}(t) = \frac{W(t)}{T_c} = \frac{u(t) \cdot V}{T_c} \quad (3-12)$$

where

$W(t)$  is the instantaneous energy stored in the chamber.

For example, Equation (3–13) yields the power lost ohmically in the walls of chamber 1:

$$P(t)_{Loss1} = u_1(t) \cdot \Lambda_1 \quad (3-13)$$

where

$$\Lambda_1 = V_1 / \tau_1$$

When the reverberation index is high  $\tau_1$  is much greater than  $T_C$  for chamber 1. Thus, the wall-scattering rate is dominant as required.

Figure 3–5 shows plotted solutions of Equations (3–6) and (3–7) for the case:

$$V_1 = 150 \text{ m}^3 \text{ and } \tau_1 = 2.7 \text{ } \mu\text{sec}$$

$$V_2 = 0.7 \text{ m}^3 \text{ and } \tau_2 = 0.266 \text{ } \mu\text{sec}^{38}$$

with several values for  $\Lambda_t$

In this case,  $V_2$  is much smaller than  $V_1$ . Thus,  $u_1(t)$  is essentially unchanged as the coupling into the second smaller cavity is varied. However,  $u_2(t)$  varies strongly as  $\Lambda_t$  is varied.  $u_1(t)$  increases instantaneously at  $t = 0$  in response to the infinite height of the  $\delta$  function excitation in cavity 1.  $u_2(t)$  rises more slowly because  $u_1(t)$  has a finite value, and energy must leak into the second cavity through the leakage port described by  $\Lambda_t$ . The time constant for the second smaller cavity is much shorter than that for the first cavity, and after the second cavity fills,  $u_2(t)$  ultimately decreases along with  $u_1(t)$ .

The plots for the solutions of  $u_1$  and  $u_2$  have an artificially inserted delay. This delay accommodates transmission line delay when overlaying measurement data with calculated solutions in a spreadsheet or other measurement reduction software. The delay value, which was set to 125 nsec for the functions plotted in Figure 3–5, is entered into the appropriate spreadsheet cell along with the trial values for chamber volumes, time constants, and leakage coefficient.

---

<sup>38</sup> The chamber volumes and time constants were chosen because they are appropriate for a measurement setup similar to that shown in Figure 2–1.



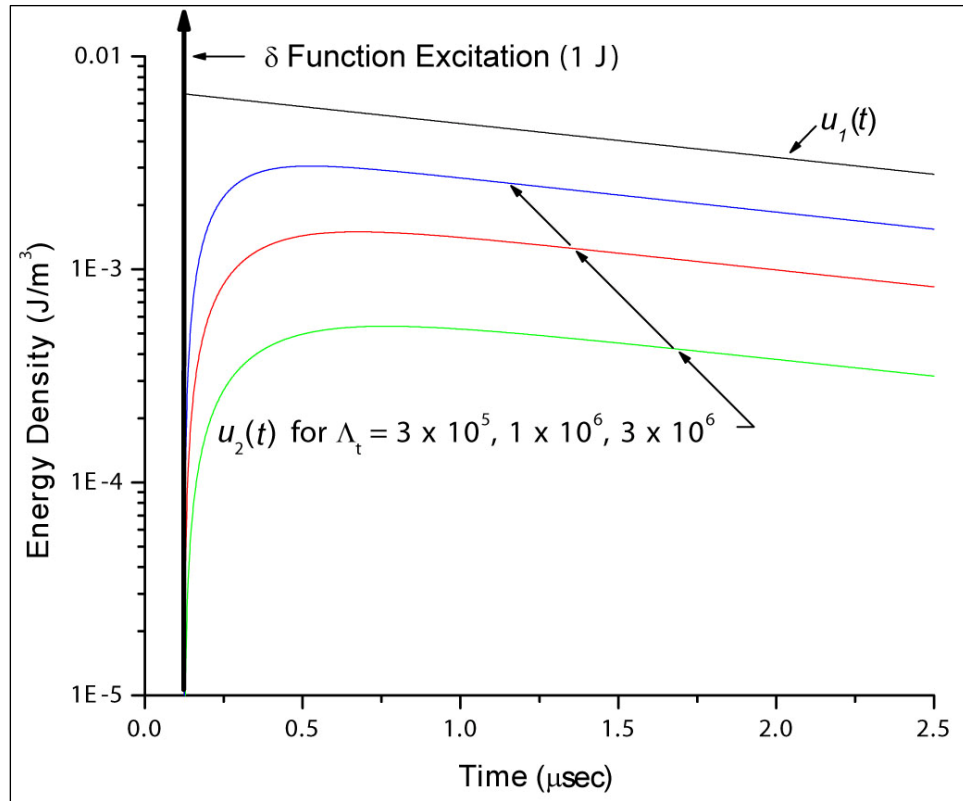


**Figure 3–5. Transient Energy Density Response in a Pair of Coupled Cavities**

### **3.3.3 Comparison of Calculations and Measurement Data for Nested Chambers**

In applying transient reverberation response analysis technique, one directly observes the solutions of the Differential Equations (3–6) and (3–7) as ensemble-averaged received power versus time on an A-scope display. Measured values for the  $\Lambda$ -rate coefficients are extracted by overlaying measurement data with calculated solutions, given by Equations (3–8) and (3–9), and performing curve-fitting operations. The coefficient values describe precisely how fast energy is decaying or leaking into or out of a cavity. As described further in Section 3.3.4, that is exactly the information that EMC engineers require to determine IL or SE.

Generally for a two-cavity experiment, four or more individual measurements are performed. One transmits in each chamber and receives in each chamber for each transmit setup. This yields four measurements to define the three rate coefficient values. Redundant measurements performed in this manner may improve accuracy or at least provide an overall accuracy estimate.

Accuracy may sometimes be improved further by performing additional experiments. Covering the leakage aperture with a conductive plate, for example, removes  $\Lambda_t$  from the experiment and isolates  $\Lambda_1$  and  $\Lambda_2$ . Such an experiment may be difficult or impossible to

conduct in a shipboard or other field test environment where the leakage port is poorly defined; however, it is usually easy in chamber experiments.

Figures 3–6 and 3–7 show plotted differential equation solutions and overlaid measurement data for comparison of energy density versus time in two chambers. The chambers for the data in Figures 3–6 and 3–7 are referred to as L (large) and S (small) and have the following parameters:<sup>39</sup>

$$V_L = 150 \text{ m}^3 \text{ and } \tau_L = 2.77 \text{ } \mu\text{sec}$$

$$V_S = 0.7 \text{ m}^3 \text{ and } \tau_S = 0.266 \text{ } \mu\text{sec}$$

$$\text{Thus, } \Lambda_L = 5.41 \times 10^7 \text{ m}^3/\text{sec and } \Lambda_S = 2.63 \times 10^6 \text{ m}^3/\text{sec}$$

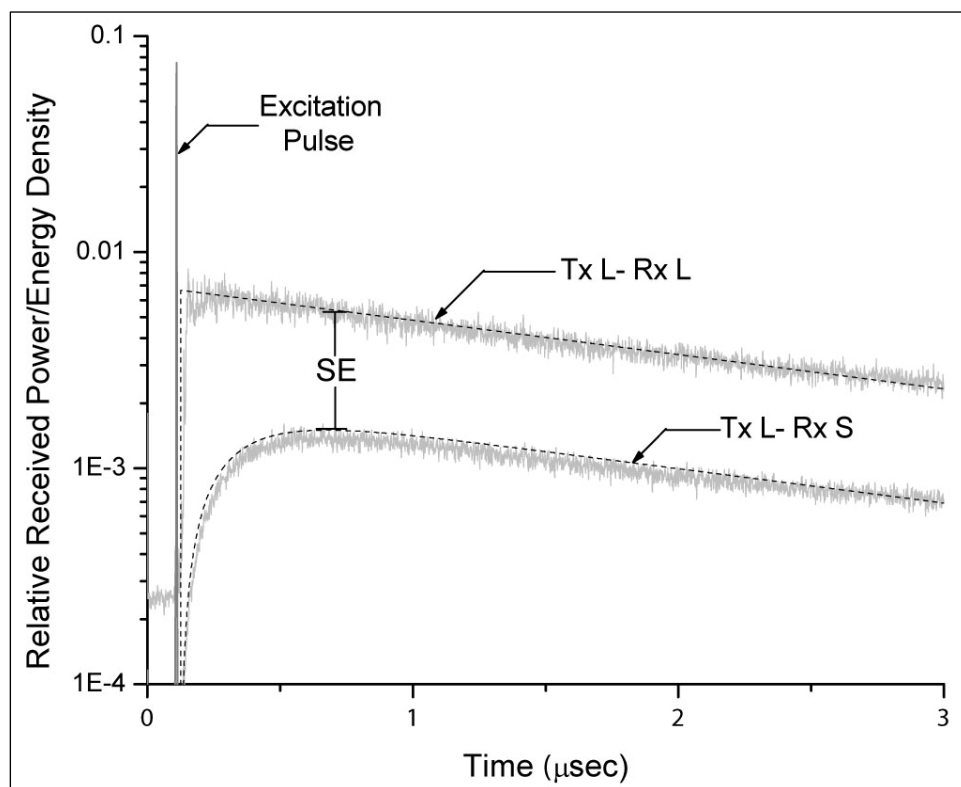


**Figure 3–6. Transient Response  $u_1(t)$  (L) and  $u_2(t)$  (S) Applying Pulse to Chamber L**

<sup>39</sup> In the notation of Equations (3–6) and (3–7), cavity 1 is excited. The notation change using  $L$  and  $S$  is done to accommodate the experimental requirement of having to excite chamber 2.

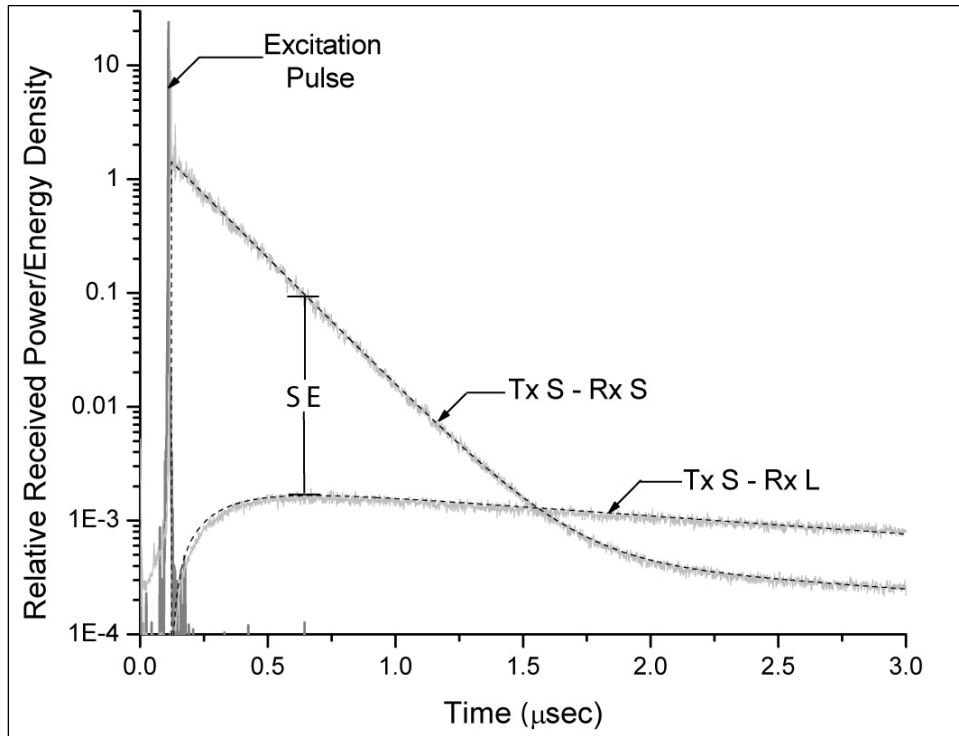


**Figure 3–7. Transient Response  $u_1(t)$  (S) and  $u_2(t)$  (L) Applying Pulse to Chamber S**

The pulse used for excitation in this measurement was derived from a 1-GHz BW sweep between 4 and 5 GHz. Thus, it had a center frequency of 4.5 GHz and a nominal 2-nsec pulse width.

The best fit of data and calculated solution yields a value for  $\Lambda_t$  of  $2.0 \times 10^6 \text{ m}^3/\text{sec}$  for this particular measurement. The overlay and curve-fitting operations described in this section were done “by eye” in a spreadsheet; however, one could use a least-squares fitting approach.

The dynamics of energy transfer in the plot of Figure 3–7 are particularly interesting. For this case, the excitation pulse is applied to the small chamber, which has a relatively short  $1/e$  time. Energy initially leaks predominantly from the small chamber into the large one. Since the small chamber has a short  $1/e$  time, the energy density there rapidly decreases due to ohmic loss. After about 1.5  $\mu\text{sec}$ , the two response curves cross. The energy density in the small chamber has dropped to a level that is below the energy density of the large chamber that it initially fed. The predominant leakage is then from the large chamber back into the smaller one.

The experiment to generate data and demonstrate the dynamics shown in Figure 3–6 and Figure 3–7 used a laboratory environment with calibrated aperture and well characterized chambers. However, energy transfer behavior shown in Figure 3–7 has been observed in real-life experiments by exciting the flight deck of a large aircraft that was positioned in a large reflective hangar. Energy from short-pulse excitation in the flight deck space

rapidly leaked out and decayed, but then was replenished by energy leaking back in from the hangar.

Explicit call-out of the leakage process by  $\Lambda_t$  in the differential equations makes it convenient to compare measurement and modeling results when a suitable leakage model exists. Hill and others have done extensive work on aperture leakage.<sup>40</sup>

The smaller chamber used in this experiment had a 5-inch (12.7-cm) diameter circular leakage aperture in its top wall. Following Hill and others, the leakage cross section ( $\sigma_t$ ) for a circular aperture is given by half of its geometric area if its diameter is greater than about 0.4 wavelength.

Thus, the leakage coefficient for the aperture is given by Equation (3–14):

$$\Lambda_t = \frac{1}{2} c \sigma_t \quad (3-14)$$

where

the extra factor of  $\frac{1}{2}$  is inserted, since energy from each cavity approaches the aperture from one side (i.e.,  $2\pi$  steradians).

Substitution of the 12.7 cm diameter value into the half geometric area relation for  $\sigma_t$  yields a leakage cross section of  $6.33 \times 10^{-3} \text{ m}^2$ . Substitution of this value in Equation (3–14) yields a  $\Lambda_t$  value of  $1.89 \times 10^6 \text{ m}^3/\text{sec}$ . This calculated value is within 0.5 dB of the measurement value derived from the measurements and overlay operation shown in Figures 3–6 and 3–7.

### 3.3.4 Nested Cavity Shielding Effectiveness in Terms of Rate Coefficients

Equations (3–6) and (3–7) were written for pulse excitation; however, they are correct for any excitation (e.g., CW) by substituting the correct driving function in place of the  $\delta$  function. The  $\Lambda$ -rate coefficients are fundamental parameters describing the basic interactions—leakage and ohmic loss—that the reverberant fields undergo. The rate coefficients are independent of excitation. Thus, coefficients that were determined from TD measurements are equally valid for CW and vice versa.

The appropriate driving function for CW excitation is simply a unit step. Further, for steady-state CW conditions, the time derivatives of  $u_1$  and  $u_2$  [i.e., ( $\dot{u}_1(t)$  and  $\dot{u}_2(t)$ )] are identically zero. With the time derivative terms removed, Equations (3–6) and (3–7) are particularly simple and easy to manipulate.

SE with CW measurement is often defined in terms of the ratio of power or energy densities inside and outside a shielded test structure, or equivalently, the difference in IL

---

<sup>40</sup> David A. Hill, Mark T. Ma, Arthur Ondrejka, Bill F. Riddle, Myron T. Crawford, and Robert T. Johnk, “Aperture Excitation of Electrically Large Lossy Cavities,” *IEEE Transactions on Electromagnetic Compatibility*, vol. 35, no. 3 (August 1994): 169–177.

$(P_{Rx}/P_{Tx})$  when moving a test antenna inside and outside the test structure. By setting the time derivatives in Equations (3–6) and (3–7) to zero and applying CW power rather than a short pulse, the ratio of  $u_2$  to  $u_1$ , while driving chamber 1, may be calculated as shown in Equation (3–15):<sup>41</sup>

$$SE = 10 \log \left| \frac{u_2}{u_1} \right| = 10 \log \left| \frac{\Lambda_t}{\Lambda_t + \Lambda_2} \right| \cong 10 \log \left| \frac{\Lambda_t}{\Lambda_2} \right| \quad (3-15)$$

Similarly, by applying Equation (3–4), transmitting CW power into either chamber 1 or 2 and considering steady-state conditions, one may define SE in terms of variation in IL.

IL<sub>11</sub> is defined as the power ratio, while receiving and transmitting in chamber 1. The definition of IL<sub>12</sub> as the power ratio receiving in chamber 2 and transmitting into chamber 1, together with some algebra, yields Equations (3–16) through (3–18):

$$IL_{11} = 10 \log \left| \frac{\lambda^2}{8\pi} \cdot \frac{c}{\Lambda_t} \right| \quad (3-16)$$

$$IL_{12} = 10 \log \left| \frac{\lambda^2}{8\pi} \cdot \frac{c}{\Lambda_1 \Lambda_2} \right| \quad (3-17)$$

$$IL_{12} = IL_{11} + 10 \log \left| \frac{\Lambda_t}{\Lambda_2} \right| = IL_{22} + 10 \log \left| \frac{\Lambda_t}{\Lambda_1} \right| \quad (3-18)$$

where

IL<sub>22</sub> is the IL transmitting and receiving in chamber 2.

Subtracting Equation (3–17) from Equation (3–16) yields Equation (3–19), which is identical to the result from Equation (3–15) that defines SE as an energy density ratio. Further manipulation yields Equation (3–20).

$$IL_{12} - IL_{11} = 10 \log \left| \frac{\Lambda_t}{\Lambda_2} \right| \quad (3-19)$$

$$IL_{12} - IL_{22} = 10 \log \left| \frac{\Lambda_t}{\Lambda_1} \right| \quad (3-20)$$

These equations show that SE or leakage rate can be determined from several different insertion loss measurement combinations. When calculating or visualizing SE, either

---

<sup>41</sup> Frequently, when the shielding effectiveness is high, the leakage coefficient is much lower than the loss coefficient, and the shielding effectiveness simply becomes equal to the ratio of leakage to loss.

from variation in IL or from relative energy density values, expression in terms of the rate coefficients gives a precise statement of exactly what is being measured.

One can interchange the coefficients  $\Lambda_1$  and  $\Lambda_2$  without changing the value of Equation (3-17). Thus,  $IL_{12}$  equals  $IL_{21}$ , satisfying reciprocity. Although the IL is identical, note that when the transmitted and received chambers are reversed, then the SE is generally different. The loss coefficients for each chamber are not necessarily equal.

SE, as it is usually defined in CW measurement ( $u_2/u_1$ ), can also be observed directly from the transient response as in Figures 3-6 and 3-7. For example, at the instant when  $\dot{u}_2(t)$  equals zero in Equation (3-7), then Equation (3-15) applies. SE can be measured as the ratio  $u_2(t) / u_1(t)$  at the instant where  $\dot{u}_2(t)$  is zero.

### 3.4 CAVITY PERTURBATION MEASUREMENTS

The TD measurements under discussion here typically yield a precise value of the cavity  $1/e$  decay time. So, this type of measurement technique is inviting to use for determining material loss factors, such as surface resistivity ( $R_s$ ), in cavity-perturbation-type experiments. This approach has been explored briefly and is described here in a series of measurements to evaluate the surface resistivity of mild steel sheeting (1010 alloy), similar to that used in construction of the large NSWCDD chamber. See Appendix E for further details.

The NSWCDD “coffin” test cavity used for this series of measurements is depicted in Figure 3-8. It was constructed of aluminum panels that were welded together. Its internal dimensions are 0.965 m by 0.596 m by 1.206 m (38 inches by 23.5 inches by 47.5 inches). The sample test plate is positioned on the top of the cavity and has a nominal active area of  $0.488 \text{ m}^2$ . Total cavity surface area is  $4.92 \text{ m}^2$ , and the volume is  $0.695 \text{ m}^3$ . The cavity is normally fitted with two dual-ridge horn antennas and a motor-driven, paddle wheel tuner for mode mixing.

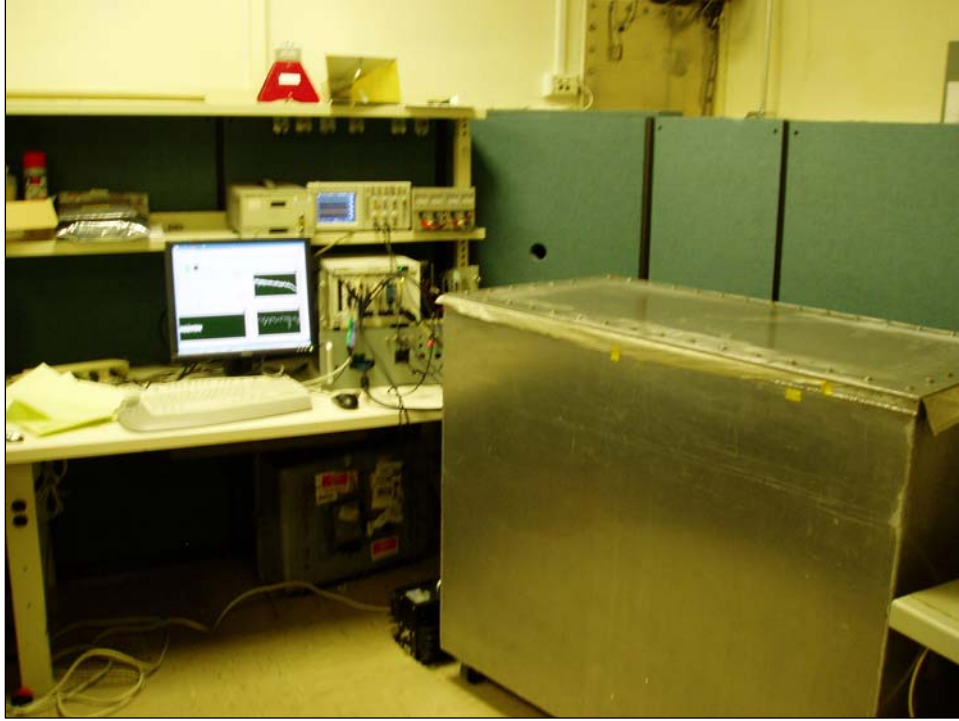


**Figure 3–8. NSWCDD “Coffin” Chamber Fitted with Removable Top Plate**

### **3.4.1 Perturbation Measurements and Losses**

Materials under examination are normally evaluated by observing small changes in the cavity loss rate when the top plate (i.e., the reference plate) is replaced by a plate made of the test material. The reference plate for the experiments reported here was made from silver-plated brass.

Equation (3–21) can be written for losses in the chamber:

$$\Lambda_{\text{meas}} = \Lambda_{\text{wall}} + \Lambda_{\text{tuner}} + 2 \cdot \Lambda_{\text{ant}} + \Lambda_{\text{gasket}} \quad (3-21)$$

where

$\Lambda$  terms on the right-hand side (RHS) of Equation (3–21) are coefficients for various loss mechanisms to be discussed below.

The measured total loss rate  $\Lambda_{\text{meas}}$  is calculated as  $V/\tau$  where  $\tau$  is the measured 1/e time.

Surface resistivity measurements are performed, first, by replacing the top wall of the cavity with an appropriately machined sample of the material to be evaluated; second, by remeasuring the  $1/e$  time; and third, by using Equation (3–22) to extract an  $R_s$  value:

$$\Delta R_s = \frac{3\mu_0 V}{4S} \cdot \Delta(1/\tau) \quad (3-22)$$

where

$S$  is the active surface area of the wall that replaced the sample to be evaluated.

Note that  $\Delta R_s$ , when evaluated in this manner, is the difference in surface resistivity between that of the reference panel and the material being evaluated.

The change in sheet resistivity is calculated from the difference in cavity loss rate with the reference and test material top plates. Thus, measuring the individual loss terms listed in Equation (3–21) is not strictly necessary. However, for maximum measurement accuracy, the other losses should be minimized or at least made stable. These losses will be studied briefly in the next several subsections, partly to show their relative significance and partly to demonstrate the power of the TD measurement technique in performing measurement diagnostics.

With the aluminum wall cavity in Figure 3–8, typically only about 10 to 20 percent of the losses occur in the cavity walls. Significant losses occur in the tuner, Rx and Tx antennas, and particularly in the interface gasket between the cavity body and top plate or reference plate.

#### 3.4.1.1 Tuner Loss

In Figure 3–9, paddle wheel tuner losses are estimated at 2.9 GHz by measuring the cavity  $1/e$  time in the usual manner: First, form a large ensemble average of transient responses using the paddle wheel for stirring; next, remove it; and last, perform a frequency-averaged response by stepping the block-start frequency so that the pulse center frequency is stepped. Regular excitation pulses were formed by using a 250-MHz BW sweep starting at 2.9 GHz, thus creating a pulse with center frequency of 3.025 GHz and a nominal width of 8 nsec. The frequency-averaged data were formed from individual responses with a block-start frequency varying from 2.8 to 3.3 GHz in 100-MHz steps. Thus, the frequency-average data are from an ensemble of only six members, rather than several hundred, and are not as smooth. The data of Figure 3–9 show clearly, however, that the time constant with the tuner removed is noticeably longer than with the tuner present.<sup>42</sup>

---

<sup>42</sup> The injected energy was slightly higher for the stepped block-start frequency measurements; thus, the curve does not have a common intersection point with the paddle-wheel-stirred data at  $t = 0$ .



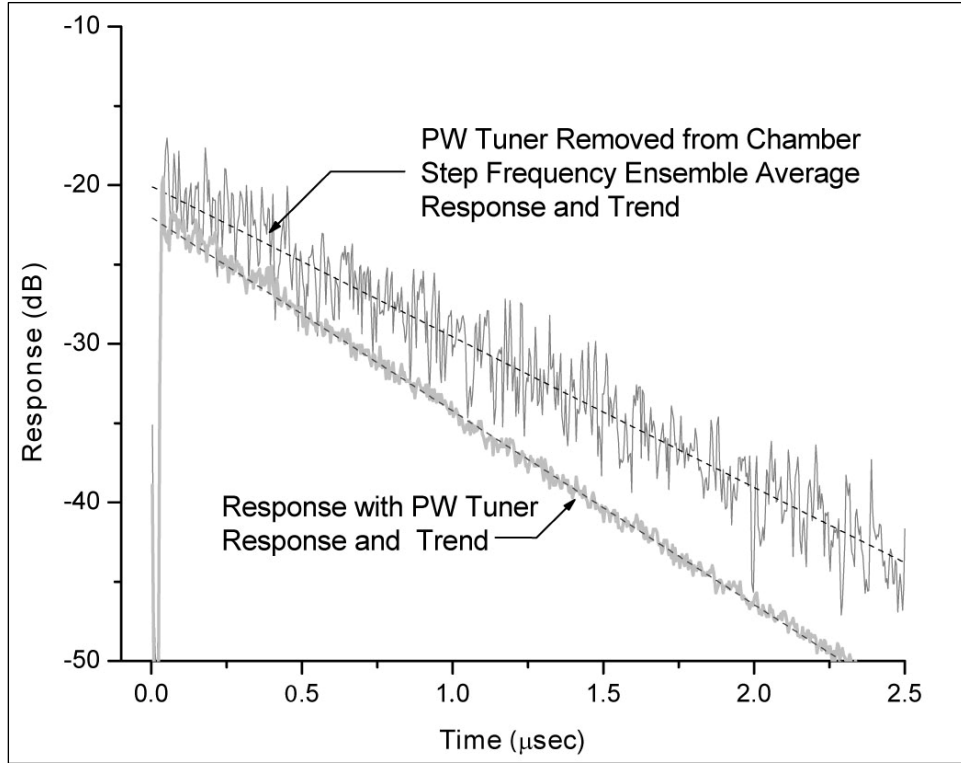


**Figure 3–9. Measured Chamber 1/e Time With and Without Tuner**

#### 3.4.1.2 Antenna Loss Coefficient $\Lambda_{\text{ant}}$

In principle, the loss rate coefficient  $\Lambda_{\text{ant}}$  due to the presence of a receiving (or for that matter, a transmitting) antenna can be calculated by considering the power it receives from the field. The effective power capture area of a properly terminated antenna in a reverberant field is given by  $\lambda^2/8\pi$ . The loss coefficient should be given by the product of  $c$  and power capture area.

However, in practice, the antenna structures, just as other structures in a chamber, introduce additional loss. Placing an unterminated antenna within a cavity introduces additional measurable loss. Thus, as stated in Equation (3–23):

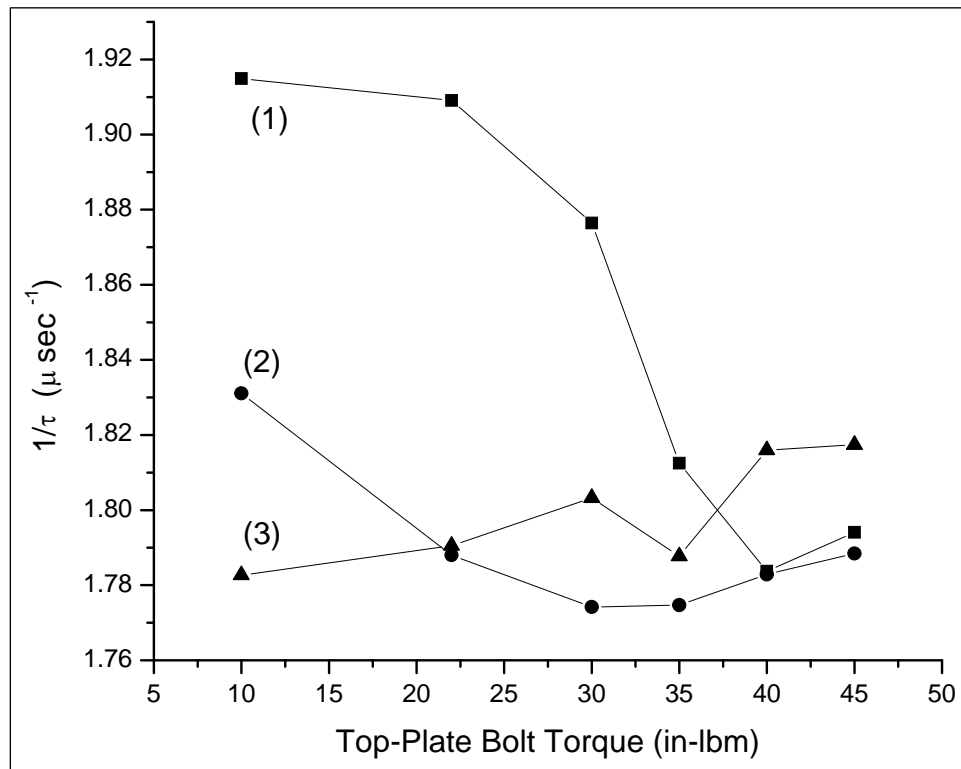
$$\Lambda_{\text{ant}} \geq c \cdot \frac{\lambda^2}{8\pi} \quad (3-23)$$

Preliminary experiments have shown that broadband dual-ridge horn antennas, which are partially constructed with dielectric material, tend to be lossier than all-aluminum designs.<sup>43</sup>

<sup>43</sup> Some horn antenna designs contain printed circuit material with slender-etched metal traces in the sidewalls.

### 3.4.1.3 Gasket Losses

Perhaps the loss due to the gasket between the cavity top plate and body is the most troublesome of all. It is both significant and unstable. Countless shielding experiments over the years by EMC engineers have shown that the pressure on a gasket and its precise seating is critical. The same is true for the loss measurements reported here. Figure 3–10 shows measured chamber inverse  $1/e$  time versus cavity top-plate-bolt torque. The gasket was made of woven stainless steel braid and covered with conductive cloth fabric. A measurement FFT block-start frequency of 2.9 GHz was used in three separate measurement sequences.



Note: Three seating sequences are displayed.

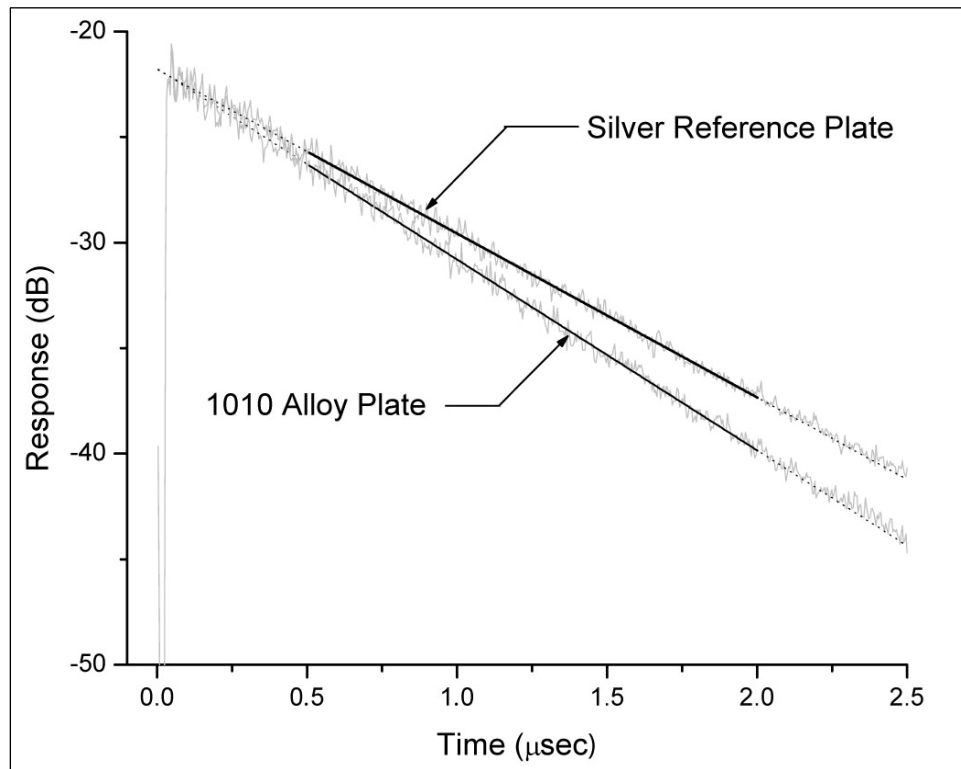
**Figure 3–10. Variation in Decay Rate ( $1/\tau$ ) as a Function of Bolt Torque**

In each sequence, the top plate was placed on the cavity flange; next, the  $1/4$ -20 nuts were tightened to a specified torque by starting at one corner and then circling the flange several times to approach the final torque gradually. After a measurement, the nuts were tightened to the next higher torque setting again with several passes around the flange. After the maximum torque [i.e., 45 inch-pounds of torque] was applied and the  $1/e$  time measurement was completed at that setting, the cover was removed and the entire sequence was repeated. The  $1/e$  time showed less variation between sequences 2 and 3 than between sequences 1 and 2, indicating some “forming” of the gasket. An ideal gasket would show no variation in  $\tau$  at a particular torque setting from one tightening sequence to the next. With bolt torque in the region of 20 to 30 inch-pounds, variation in

$1/e$  time is such that approximately  $0.04 \mu\text{sec}^{-1}$  of noise or uncertainty is introduced into the measurement. According to Equation (3-22), this leads to an estimated uncertainty in  $R_S$  of 0.054 ohm per square (ohm/sq).

### 3.4.2 Material Sheet Resistivity Evaluation

Figure 3-11 shows a comparison of responses for the silver-plated brass reference top plate and a similar mild steel (1010 alloy) plate. The  $1/e$  times for the two cases measured at a block-start frequency of 2.9 GHz (i.e., a 3.025-GHz, pulse center frequency) are 0.559286 and 0.480461  $\mu\text{sec}$ . The variation in  $1/\tau$  for these two cases is  $2.9334 \times 10^5 \text{ sec}^{-1}$ . According to Equation (3-10), this yields a  $\Delta R_S$  value of 0.394 ohm/sq. The actual value of  $R_S$  for the steel is  $\Delta R_S$  plus the sheet resistivity of the silver reference plate. The textbook value for silver  $R_S$  is  $1.38 \times 10^{-2}$  ohm/sq, which brings the actual  $R_S$  value for the steel up to 0.407 ohm/sq at 3 GHz.<sup>44</sup>



Note: Measurement center frequency is  $F = 3.025 \text{ GHz}$ .

**Figure 3-11. Measured Ensemble-Averaged Transient Response with Silver (Ag) Reference Plate and Mild (1010 Alloy) Steel Test Plate**

<sup>44</sup> Sheet resistivity was calculated according to the standard handbook definitions:  
 $R_S = 2.52 \times 10^{-7} \times F (\text{Hz})^{1/2}$ .

Figure 3–12 shows variation of  $\Delta R_S$  with frequency between 1.5 and 7.5 GHz. An approximate  $F^{1/2}$  frequency variation of  $R_S$  occurs. This is characteristic of nonmagnetic conductors.

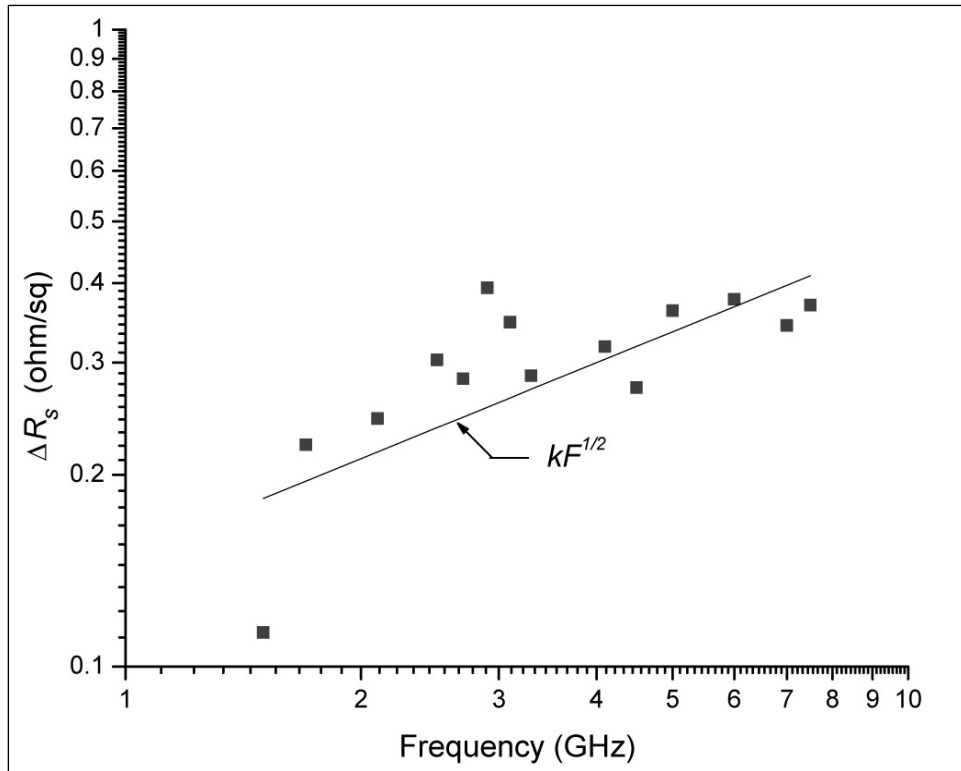


**Figure 3–12. Measured Sheet Resistivity ( $\Delta R_S$ ) for Mild (1010) Steel Versus Frequency**

### 3.4.3 Low-Frequency Measurement Limitations

The measurement value of  $R_S$  at 1.5 GHz is significantly low compared with that of the other higher frequency data. This may be due in part to gasket-seating-induced error. An estimated uncertainty of 0.054 ohm/sq exists for both the silver reference plate and the steel plate measurements. The gasket-induced error may actually be worse. Two other possible causes for concern, particularly at lower frequencies, should also be considered:

- a. Localized losses from antennas
- b. Lack of available cavity modes that ensure good random field

### 3.4.3.1 Localized Losses from Antennas

The 1.5-GHz-decay data of Figure 3–13 show a variable decay rate,<sup>45</sup> indicating that the modes present in the decay do not have a tightly peaked distribution in  $1/e$  time or the quality factor ( $Q$ ). This kind of response is occasionally noted in measurements, particularly at low frequencies. Ladbury and others have noted this kind of behavior in TD measurements. They have suggested that at lower frequencies, where antenna losses become a larger fraction of total loss, some modes may couple preferentially to the antennas. This would significantly lower the  $Q$  of these preferentially coupled modes, while leaving other modes that do not couple as tightly to the antennas less perturbed. Lowering the  $Q$  of some modes while leaving others unperturbed would have the effect of broadening an otherwise tightly peaked mode  $Q$  distribution.<sup>46</sup>

Wall losses have a slow variation with frequency ( $\sim F^{1/2}$ ). Losses due to antenna coupling vary as  $F^{-2}$  ( $\lambda^2/8\pi$ ). As frequency is decreased, antenna coupling losses eventually become dominant, as shown below:

The total loss coefficient ( $\Lambda_t$ ) in the chamber at 1.5 GHz is calculated as  $V/\tau$  with  $\tau = 0.288 \mu\text{sec}$  and numerically is  $2.42 \times 10^6 \text{ (m}^3/\text{sec)}$ .

The loss coefficient for each antenna ( $\Lambda_{\text{ant}}$ ) at 1.5 GHz is calculated as  $c \lambda^2/8\pi$  and numerically is  $4.7 \times 10^5 \text{ (m}^3/\text{sec)}$ .

The two antennas are responsible for 38 percent of the total loss in the chamber at 1.5 GHz. The antennas are localized, and intuitively, their coupling to certain modes may be somewhat greater than to others. The antennas contribute such a large portion of the total loss that the mechanism proposed by Ladbury and others is a reasonable explanation for the curvature of the data in Figure 3–13.<sup>47</sup>

---

<sup>45</sup> The measurement block-start frequency was 1.5 GHz. The pulse center frequency was 1.625 GHz.

<sup>46</sup> John M. Ladbury, Robert T Johnk, and Arthur Ondrejka, “Rapid Evaluation of Mode-Stirred Chambers Using Impulsive Waveforms,” NIST Technical Note 1381 (June 1996): n. pag.

<sup>47</sup> Ibid., n. pag.

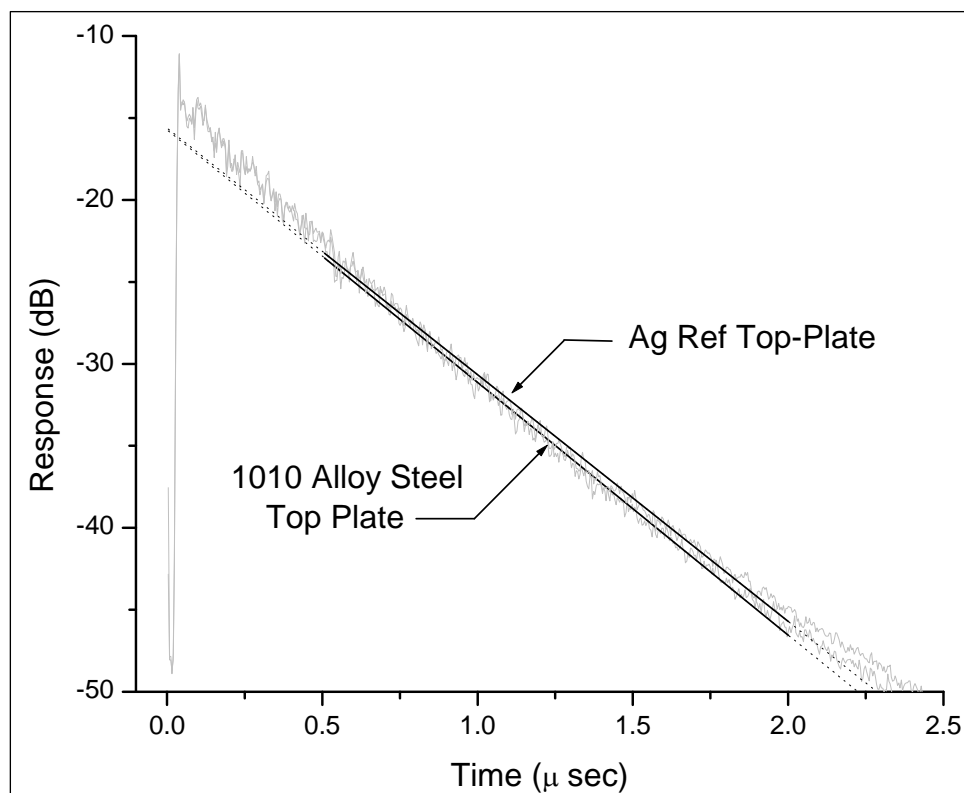


**Figure 3-13. Transient Response Comparison at 1.5 GHz**

#### 3.4.3.2 Cavity Mode Overlap Factor

The mode density overlap factor should also be considered.<sup>48</sup> The mode overlap factor or number of modes per  $Q$  bandwidth (i.e., mode line width) from the product of the Weyl mode density<sup>49</sup> is given by Equation (3-24), and the line width of a given mode is derived by Equation (3-25):

$$\frac{dN}{dF} = 8\pi V \cdot \frac{F^2}{c^3} \quad (3-24)$$

$$\Delta F = \frac{1}{2\pi\tau} \quad (3-25)$$

<sup>48</sup> The mode density overlap factor is frequently referred to as the number of modes per  $Q$  bandwidth, i.e., the FWHM mode line width.

<sup>49</sup> R. F. B. Turner, W. A. G. Voss, W. R. Tinga, and H. P. Baltes, "Eigenfrequency Distributions in Multimode Cavities," *IEE Proceedings*, vol. 132, Part H, no. 2 (April 1985): 82-88.

The product of these two expressions is given in Equation (3–26):

$$A = \frac{4 V F^2}{c^3 \tau} \quad (3-26)$$

Equation (3–26) shows that  $A$  is less than 0.5 at 1.5 GHz for the 0.695 m<sup>3</sup> cavity.

Intuitively, one expects that with excitation at a single frequency, an overlap factor of less than unity is insufficient. Actually, measurements have shown that an overlap factor of four or greater is preferred for CW measurement.<sup>50</sup> Intuitively, one expects that it may be possible to relax this requirement somewhat for pulse excitation due to the pulse bandwidth; however, this has not been demonstrated. Data at 2 GHz in Figure 3–12 are consistent with the remainder of higher frequency data, and the overlap factor at 2 GHz is only about 2.

Acoustics researchers have observed that variation in decay rate occurs not only at the low-frequency limit of chamber operation but also in poorly reverberant rooms.<sup>51</sup> The poorly reverberant acoustic spaces may have had high localized losses.

#### **3.4.4 Application of CW Technique for Cavity Perturbation Studies**

In principle, cavity perturbation measurements similar to those that have been described with time-domain technique could be done with steady-state CW technique. One would measure small variations in IL with the cavity in unloaded and loaded states. One would have difficulty quantifying IL with precision greater than about 1 dB with CW measurement. Thus, small losses, which would lead to small variations in IL, would be difficult to measure. The time-domain approach evidently gains its precision through frequency averaging, as well as ensemble averaging. A pulse has bandwidth. Presumably, accuracy similar to that available with the time-domain approach could be obtained with CW technique by using some means to increase the measurement bandwidth, such as frequency dithering, multiple measurement frequencies, or perhaps, noise modulation.

### **3.5 ADDITIONAL MEASUREMENTS AND SAMPLE CALCULATIONS**

Several additional examples are considered here to further illustrate the practicality and significance of the  $\Lambda$ -rate coefficients and other ideas contained in the time-domain-analysis technique.

---

<sup>50</sup> “Correlation Coefficient,” *IEC*, Standard 61000–4–21, Annex A: 29.

In reverberation chamber operation, the required number of samples for a given field uncertainty rises sharply for an overlap factor of less than about four. Theoreticians have insisted on factors as high as 10 to 15.

<sup>51</sup> Thomas W Bartel and Simone L. Yaniv, “Curvature of Sound Decays in Partially Reverberant Rooms,” *Journal of the Acoustical Society of America*, vol. 72, no. 6 (December 1982): n. pag.

### **3.5.1 Losses Due to People Present in a Test Chamber**

This experiment is performed basically as a cavity perturbation measurement. More detailed cavity perturbation measurements to determine the surface resistivity of conductive composite sheets that might be used for ship construction are discussed in Appendix E.

Occasionally, people are required to be present in the test area during measurements. In some cases, people would normally be present in the real-life scenario, such as in a ship compartment. Questions naturally arise about how much loss a person introduces into the space by his or her presence and whether this additional loss would cause errors in test results. Time-domain technique offers a precise answer.

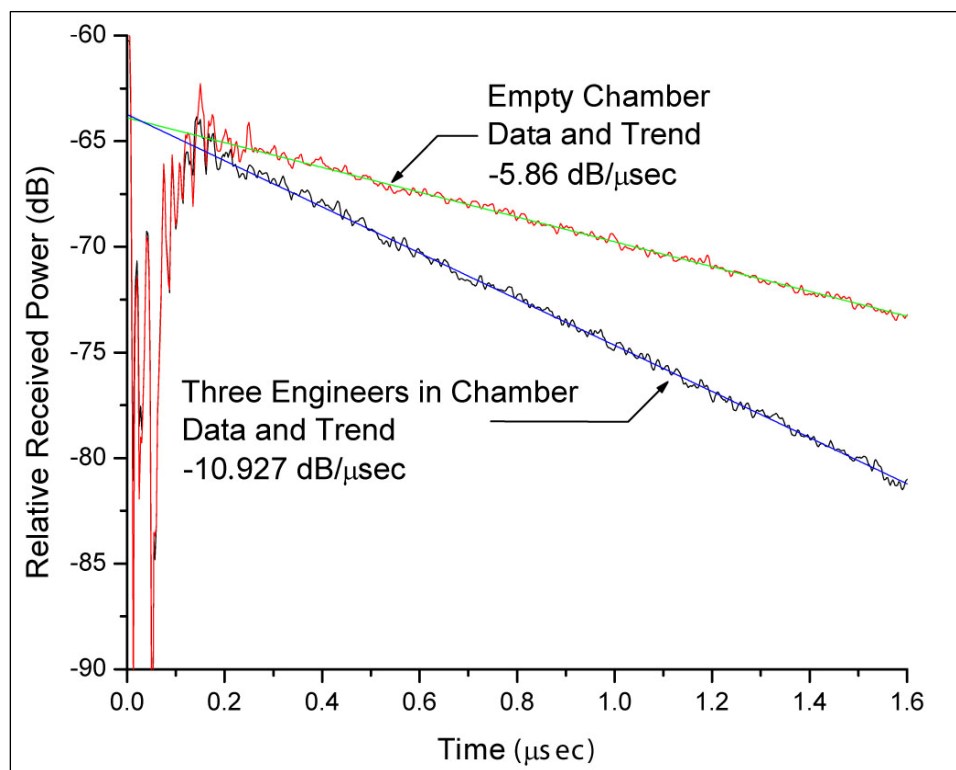
Using time-domain technique, the power absorption cross section ( $\Sigma$ ) and loss rate coefficient ( $\Lambda$ ) were determined for a medium-build, lossy EMC engineer. These factors were calculated from the increased loading and decay rate due to the presence of three engineers in a chamber. Measurements have been conducted as explained in Section 3.5.1.1.

#### **3.5.1.1 Perturbation Measurement**

Measurements of  $1/e$  time were made in the large NSWCDD chamber in an empty state, containing only the normally installed paddle wheels and test antennas. The chamber doors were closed tightly as is normal practice. A similar measurement was then made with three medium-build EMC engineers present in the chamber walking around, waving their arms, and interacting with the reverberant field.

Data from this experiment are shown in Figure 3–14. The pulse for the test had a nominal 0.5-nsec width and was derived from a 2.6-to-6.6-GHz-swept CW signal, having a 4.6-GHz center frequency and 4-GHz BW.





Note: Two measurement cases are presented:  
 (1) The large NSWCDD chamber is empty.  
 (2) The chamber is then loaded with three, medium-build EMC engineers.

**Figure 3-14. Ensemble-Averaged Chamber Response Showing Loading Effects**

Using the relationship given in Equation (3-27), empty and loaded decay rates of 5.86 and 10.927 dB/μsec yield 1/e times of 0.739 and 0.397 μsec:

$$\tau(\mu\text{sec}) = \frac{4.3429}{\text{DecayRate}(\text{dB}/\mu\text{sec})} \quad (3-27)$$

The corresponding loss coefficients for the two cases calculated as  $V/\tau$  follow:

$$\Lambda_{\text{empty}} = 3.0406 \times 10^8 \text{ m}^3/\text{sec}$$

and

$$\Lambda_{\text{loaded}} = 5.6614 \times 10^8 \text{ m}^3/\text{sec}.$$

Thus,  $\Delta\Lambda = 2.62 \times 10^8 \text{ m}^3/\text{sec}$  for three engineers

and

$$\Lambda_{\text{Eng}} = 8.73 \times 10^7 \text{ m}^3/\text{sec} \text{ for a single engineer.}$$

Determining whether the losses due to a person being present in the test space are significant can be done by comparing the loss rate of the space with that of the person.

For example, the large NSWCDD chamber used in this experiment had an empty  $1/e$  time of  $0.739 \mu\text{sec}$ , and its loss coefficient was  $\Lambda_{\text{empty}} = 3.0406 \times 10^8 \text{ m}^3/\text{sec}$ .

The loading effect of an engineer with  $\Lambda_{\text{Eng}} = 8.73 \times 10^7 \text{ m}^3/\text{sec}$  is given by  $10 \log | \Lambda_{\text{empty}} / \Lambda_{\text{empty}} + \Lambda_{\text{Eng}} |$  or -1.03 dB.

In performing measurements in a large metal pre-engineered building (PEB) (to be discussed in Section 4), the loading by a person in the test area is less important. With a volume of  $1722 \text{ m}^3$  and a  $0.05 \mu\text{sec}$  time constant, the loss rate coefficient for that building was  $3.4 \times 10^{10}$  and so, as one would guess, the additional loading by a person is negligible in a building that large.

#### 3.5.1.2 Independent Calculation of Loss Rate Coefficient for a Person in a Reverberant Field

Using some of the ideas presented in Appendix C, together with fundamental concepts from basic engineering electromagnetics textbooks, one can provide an independent estimate of the loss coefficient for a person in an isotropic field. This “back of envelope” calculation is presented below as an illustrative example.

Equation (3–28) states that the loss coefficient for an object in a chamber can be written as the product of  $c$  multiplied by the projected area of the object and an absorption factor—stated as 1 minus a reflectivity factor—to account for the percentage of incident energy that actually is absorbed.

$$\Lambda = c \Sigma (1 - R) \quad (3-28)$$

According to ideas presented in Appendix C, the projected area of a convex body in an isotropic field is 25 percent of its total surface area. Males have an average skin surface area of  $1.7 \text{ m}^2$ , so  $\Sigma$  should be on the order of  $0.425 \text{ m}^2$ . As described below, with a

simple flat plate (i.e., one-dimensional) calculation, the reflectivity ( $R$ ) of human tissue to microwave radiation is about 60 percent.

Primarily due to varying amounts of water and electrolyte content, different body tissues have various dielectric coefficients. For whole body calculations of this nature, the average dielectric constant for human tissue is often taken as  $\hat{\epsilon} = 35 \times (1 - j)$  and is numerically equal to two thirds of the value usually quoted for muscle tissue.<sup>52</sup> With an  $\hat{\epsilon}$  value of  $35(1 - j)$ , the characteristic impedance of this hypothetical average tissue can be calculated as  $49.5 + j20.5$  ohm versus the 377 ohm value for free space. The resultant power reflection coefficient  $R$  for a wave normally incident on a flat surface of this tissue is calculated as 0.591.

The resultant value for  $\Lambda$  calculated in this manner is  $5.22 \times 10^7$  m<sup>3</sup>/sec, which is 2.2 dB below the  $8.7 \times 10^7$  m<sup>3</sup>/sec value from the measurement. Since the measurement includes loss due to clothing, one can conclude that the measurement and the quick calculation presented above are roughly consistent. In addition to simply providing loss, clothing with a dielectric constant between that of air and tissue may provide impedance matching with a lower effective reflectivity  $R$  factor.

Expression of the loss for a person in terms of a loss area rather than a rate coefficient may be somewhat more meaningful in terms of everyday experience. Combining the projected area and absorption factors in Equation (3-28) yields a loss area of 0.17 m<sup>2</sup> for the 1.7 m<sup>2</sup> male. The loss area calculated from the measured loss coefficient is 0.29 m<sup>2</sup> or about 3 square feet (sq ft).

### **3.5.2 Shielding Effectiveness of an Aircraft Passenger Compartment**

Frequently, one can identify specific leakage points or apertures in a structure, which can be modeled to obtain a SE estimate or consistency check for comparison with measurement data. The aircraft shown diagrammatically in Figure 3-15 illustrates this approach. The windows are obvious leakage apertures that are considered in this analysis. Other cracks and seams in the aircraft skin for luggage compartments or landing gear stowage are not considered here; thus, this analysis is not necessarily complete. The dimensions and other numbers shown are for illustrative purposes only and do not correspond to a specific aircraft.

---

<sup>52</sup> This approximation is sometimes referred to as the “two thirds muscle model.” *Radio Frequency Radiation Dosimetry Handbook (Fourth Edition)*. U.S. Air Force, School of Aerospace Medicine, Aerospace Medical Division (AFSC), Brooks Air Force Base, Texas 78235-5301. <<http://www.brooks.af.mil/AFRL/HED/hedr/reports/handbook/>>, s.v. “Muscle Tissue.”

$L = 36 \text{ ft}$   
 $W = 7 \text{ ft}$   
 $H = 6 \text{ ft}$   
 $V = 36 \text{ m}^3$   
 $N = \text{reverberation index of 10}$   
     bounces per  $1/e$  time  
 $= \tau/T_C$   
 $T_C = 5.9 \text{ nsec}$   
 $\tau = 59 \text{ nsec}$   
 Windows:  $12 \times 2 = 24$   
 10.5-inch-diameter round aperture

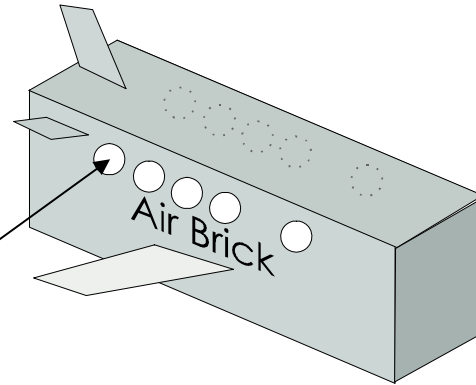


**Figure 3–15. Model for Aircraft Passenger Cabin**

With the tools that have been developed in this report, together with a few assumptions, an EMC engineer can perform a variety of calculations of interest. For example, one can estimate the power density within the cabin from excitation by an external beam. Additionally, one can estimate how rapidly power density builds up within the cabin and how much escapes out the windows from an internal emitter.

#### 3.5.2.1 Leakage Through Windows

Using polarizability theory, Hill and others have derived simplified expressions for leakage through round apertures. For a beam at normal incidence, the leakage cross section is simply given by the geometric area. For an isotropic reverberant field, where incident radiation approaches the aperture with equal probability over  $2\pi$  steradians, the cross section is given by half of the geometric area. These assumptions are appropriate for a frequency high enough so that the diameter of the aperture is  $0.41\lambda$  or greater. Hill states that resonance effects that are problematic for long slender apertures can reasonably be ignored for a nearly circular aperture.<sup>53</sup>

For lower frequencies, the leakage cross section for a single, normally incident beam is given by Equation (3–29):

$$\Sigma_{\text{beam}} = \frac{64}{27\pi} \cdot k^4 a^6 \quad (3-29)$$

where

$a = \text{aperture radius}$

$k = 2\pi/\lambda$

<sup>53</sup> Hill et al., 169–177.

Equation (3–30) gives the cross section for an isotropic reverberant field:

$$\Sigma = \frac{16}{9\pi} \cdot k^4 a^6 \quad (3-30)$$

For the isotropic field, the cross section is about 25 percent lower. These cross sections are different, which means that for the assumption of external excitation with a beam, the rates for energy leakage out the cabin window are different from those for energy leakage into the cabin from outside. This is not a violation of reciprocity, but recognition that the scattering properties of an isotropic reverberant field are different from those of a single beam.

Neglecting resonance effects, the half-geometric area and electrically small solutions intersect at a frequency near the point where  $d = 0.41\lambda$ . For a 10.5-inch-diameter window, this occurs at approximately 460 MHz. Leakage is flat above this frequency and varies as  $F^4$  below this frequency.

### 3.5.2.2 Internal Cabin Losses

Internal losses are dependent on the contents of the cabin. Measurement data from experiments conducted on several aircraft at different times have indicated that the reverberation index for an empty cabin may approach 10. Thus, a reverberation index of 10 will be assumed for the following calculations. The characteristic wall-scattering time  $T_C$  is calculated as 5.9 nsec when applying the cabin dimensions given in Figure 3–15 in Equation (2–4). The 1/e time,  $\tau$ , for the cabin is estimated by multiplying the characteristic scattering time by the reverberation index. Thus, it is 59 nsec. Equation (3–31) yields an estimated value for the cabin loss rate coefficient:

$$\Lambda_{10} = \frac{V}{\tau_0} = \frac{43 \text{ m}^3}{59 \cdot 10^{-9} \text{ sec}} = 7.3 \cdot 10^8 \text{ m}^3/\text{sec} \quad (3-31)$$

### 3.5.2.3 Losses Due to Passengers

Losses due to assumed personnel in the cabin can be estimated by Equation (3–32):

$$\Lambda_p = c \cdot \Sigma_p \cdot n \quad (3-32)$$

where

$\Sigma_p$  is given as  $0.291 \text{ m}^2$  from a previous calculation in Section 3.5.1.2.

$n$  is the number of passengers or other personnel present.

Two people present in the cabin would add an additional loss ( $\Lambda_p$ ) of  $1.74 \times 10^8 \text{ m}^3/\text{sec}$ .

#### 3.5.2.4 Losses Due to Leakage Out the Cabin Window

Reverberant energy trapped in the cabin leaks out the windows in accordance with Equation (3–33):

$$\Lambda_{t \text{ out}} = 1/2 \ c \ \Sigma \quad (3-33)$$

where

$\Sigma$  is given either  
by Equation (3–17) for frequencies below 460 MHz or  
by half the geometric area of the windows for frequencies above  
460 MHz.

For frequencies above 460 MHz, the leakage coefficient for all 24 windows is calculated by Equation (3–34):

$$\Lambda = 24 \cdot \frac{1}{2} \cdot c \ \Sigma = 1.005 \times 10^8 \text{ m}^3/\text{sec} \quad (3-34)$$

#### 3.5.2.5 Combined Internal Losses

The combined losses for the aircraft cabin are due to wall losses, personnel, and reverberant field leakage out the cabin windows. Thus, Equation (3–35) follows:

$$\Lambda_1 = \Lambda_{10} + \Lambda_p + \Lambda_{t \text{ out}} \quad (3-35)$$

With the calculation of these  $\Lambda$  loss and leakage rate coefficients in hand, estimates of power density within the cabin from either an internal or external emitter can be derived.

#### 3.5.2.6 Internal E Field and Power Emitted from an Internal Emitter Within an Aircraft Cabin

To estimate the power density within the cabin for an internal emitter, such as a cell phone, one can write Equation (3–36):

$$P_t = u \cdot (\Lambda_{10} + \Lambda_p + \Lambda_{t \text{ out}}) \quad (3-36)$$

Using the rate coefficients discussed previously (refer to Sections 3.5.2.2 through 3.5.2.5) and applying Equation (3–3) with CW excitation, average energy density ( $u$ ) in the cabin from a 1-W emitter can be calculated by Equation (3–37):

$$u = \frac{1 \text{ W}}{(7.3 \times 10^8 + 1.74 \times 10^8 + 1.005 \times 10^8) \text{ m}^3/\text{sec}} = 9.95 \times 10^{-10} \text{ J/m}^3 \quad (3-37)$$

This energy density corresponds to the following power densities and field strengths:

an isotropic power density ( $S = c u$ ) of 0.298 W/m<sup>2</sup>

or

a spatially averaged RMS E field strength of 10.61 V/m

or

an approximate 25 V/m maximum RMS at an 8-dB maximum/average ratio.

The average power escaping through the cabin windows is given simply by the product of  $u$  and  $\Lambda_{t\ out}$  and is approximately 0.1 W.

This estimate assumes that processes occur from interactions of a reverberant field with the walls and contents of the cabin. For example, these processes would apply approximately to a case where someone was moving along the center of the cabin with a cell phone, but would be in error if the cell phone was held at a window.

### **3.6 ANTENNA CROSS TALK ESTIMATE: DIRECT VERSUS REVERBERANT RESPONSE**

In Sections 2.2.1.3 through 2.2.1.4, the issue of antenna placement and direct cross talk was considered briefly. Now, with an understanding of insertion loss firmly in hand, an EMC engineer can begin to estimate the relative magnitudes of the direct and reverberant signal components that a receive antenna might deliver to a receiver. The approach is to compare the relative values of a Friis free-space calculation and an IL calculation.

#### **3.6.1 Direct and Reverberant Coupling**

Direct coupling between two antennas may be calculated from the Friis free-space relation given as Equation (3–38):

$$\frac{P_{Rx}}{P_{Tx}} = \frac{\lambda^2}{4\pi} \cdot \frac{1}{4\pi R^2} \cdot G_T G_R \quad (3-38)$$

where

$G_T$  and  $G_R$  are the gains of each antenna in the direction of the other antenna.

From the discussion in Section 3.2, the average coupling, i.e., the insertion loss, between antennas due to the reverberant field is given as Equation (3–39):

$$\frac{P_{Rx}}{P_{Tx}} = \left[ \frac{c\tau}{V} \cdot \frac{\lambda^2}{8\pi} \cdot \eta_R \eta_T \right] \quad (3-39)$$

If the chamber volume  $V$  is large or if the time constant  $\tau$  is short, then the direct coupling component is more likely to be an appreciable fraction of the total received power, where the total power is direct plus reverberant.

Assuming unit antenna efficiencies and combining Equations (3–38) and (3–39), one can solve for a value  $R_O$  given as Equation (3–40):

$$R_O = \sqrt{\frac{G_T G_R V}{2\pi c\tau}} \quad (3-40)$$

The value for  $R_O$  is actually statistical because IL given by Equation (3–39) is due to the random properties of the received power. Roughly speaking, however, for separation distances between antennas of less than  $R_O$ , the received signal is predominantly direct, while for greater distances, it is likely to be predominantly reverberant.

### **3.6.2 Implication for Digital Wireless Communication**

This result has important implications for digital wireless communication in a reverberant space. In simple experiments conducted with two computers with wireless cards (in this instance, with protocol 802.11 G), digital data could be transferred between machines in a reverberation chamber if the wireless card antennas were close to each other. If the computers were separated over a distance much greater than  $R_O$ , say  $5 R_O$ , the maximum data transfer rate was reduced, and in some cases, the machines could not communicate at all. Communication was not lost due to lack of signal. Rather, the multi-path nature of the reverberant received signals that were predominant at large separations led to an excessively high bit-error rate. Ultimately, communication was choked off between machines that had become preoccupied with error correction.

## **3.7 SUMMARY: REVERBERANT FIELD BEHAVIOR AND PRIMARY MEASUREMENTS**

In a highly reverberant space, the field is envisioned as being in an equilibrium state that is observed by analysis of an ensemble average of transient responses to short pulse excitation.

The basic questions were considered:

- a. How rapidly is energy scattered from the walls of a space?



- b. How rapidly is energy lost?
- c. How rapidly does energy leak into or out of the space?

The wall-scattering rate ( $1/T_C$ ) is not measured directly but is calculated from the chamber volume and surface area. For EMC analysis, the loss and leakage rates are usually of primary interest, and they are used to calculate SE in coupled chamber experiments.

In a highly reverberant space, the fields are statistically uniform, and the loss and leakage rates have unique values. Further, the actual scattering process that generates and maintains the reverberant field can be neglected. With this simplifying approximation, coupled first-order differential equations may be written for coupled chambers or cavities excited by a short pulse of electromagnetic energy. The equations are based on conservation of energy and may be written by inspection. The differential equations specifically include rate coefficients for ohmic loss and leakage between cavities.

The rate coefficients are evaluated by curve-fitting operations on overlaid measurement data and calculated parameterized differential equation solutions. Using this transient analysis technique, the coefficients are calculated from measurements of transient-response data, but they remain unchanged and equally valid in equations with arbitrary excitation including CW. Thus, transient TD and steady-state CW data may be readily compared.

Transient-response measurement offers a remarkably precise way of determining the loss rate of a space. This ability arises from its power to determine cavity  $1/e$  time with high accuracy solely from a measured decay slope. Thus, transient-response measurement provides a truly independent technique for verifying chamber calibration factors and IL values determined from CW test item measurements. It is also a promising approach for measurement of antenna efficiency. Further, via cavity perturbation technique, surface sheet resistivity of materials can be measured.

Explicit identification and evaluation of loss and leakage coefficients together with modeling calculations permit an EMC engineer to apply chamber measurement data in first-principle, scaling-law, and prototyping calculations.

This page is intentionally blank.

## 4.0 MEASUREMENT IN MODERATELY REVERBERANT SPACES

### 4.1 INTRODUCTION

Many spaces of interest to U.S. Navy EMC engineers have significantly less reflectivity than the reverberation chamber environments, which have been studied thus far. The differential equations and loss coefficients discussed in previous sections assume that the energy in a reverberant space obeys conservation of energy principles. If reverberation is not strong enough, the fields do not reflect from the walls enough times to become statistically uniform. Thus, for example, the field measured in a particular region is not as reliable an indicator of the field assumed to be interacting with a particular aperture at some other region in the space. Even though energy conservation still applies fundamentally, measurement results and analysis based on this principle become less certain because the average field in the space is not a unique quantity.

Although it is still useful as a paradigm in this regime, the energy conservation-based technique becomes soft. The fundamental measurement technique of observing the energy in a received pulse, including components from reflections, is still completely correct. This fundamental technique is a powerful tool to characterize propagation in any space, and it allows an EMC engineer to examine the departure of real space results from the paradigm. Results presented in this section provide a semiquantitative feel for just how large the departure is.

When the reverberation index for a space is low, the electromagnetic environment is less uniform and isotropic. Hot or cold regions may exist when excitation comes from a particular region of the space. In some cases, the questions of interest may be less about the *overall* chamber characteristics of the space and more about *particular propagation paths* within the space or between regions of coupled spaces. The radar-based measurement scheme is extremely useful for examination of these kinds of questions as well.

This section of the report presents measurement technique and examines results in a Butler-type pre-engineered building (PEB). As shown in Figure 4–1, a PEB has similar reverberation characteristics; that is, it has a similar range of reverberation index to below-deck compartmental ship spaces and aircraft compartments, which have been examined in other work. Thus, a PEB is an ideal venue in which to develop technique and examine field behavior applicable to these other spaces.

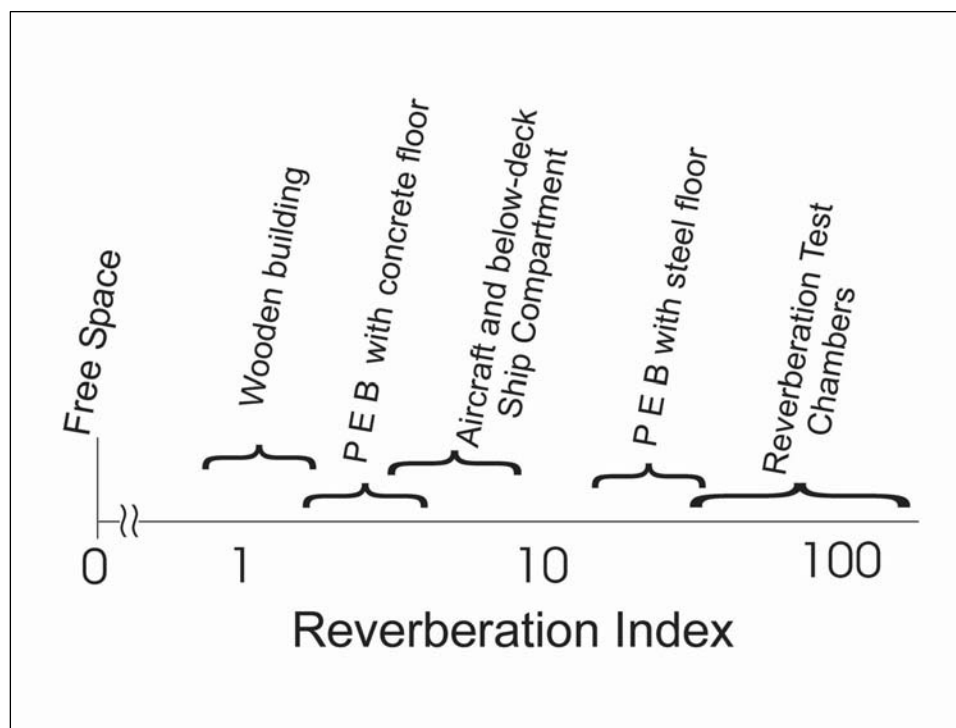


**Figure 4–1. Reflectivity of Various Spaces**

Several major application areas for these kinds of measurements exist. First, due to the proliferation of RF emitters in ship compartments, U.S. Navy EMC engineers need a reliable way of characterizing these spaces. For example, engineers need to be able to estimate how rapidly the power density in a space might build up from one or more internal emitters and how much energy might leak from one compartment to another. Loss and leakage rate measurements for the compartments under consideration—together with measurements of field uniformity—provide direct answers to these questions.

Second, an EMC engineer may wish to use a space, such as a PEB with mediocre reverberation properties as a test venue for a large test item, such as an aircraft or a portion of a ship deckhouse structure built of composite materials. The available test venue may be less than ideal for providing a uniform isotropic test field. However, if proper technique is used, then useful test data can be obtained with great cost and time savings. Hatfield has shown that surprisingly useful and accurate reverberation-chamber-type measurement results can be obtained by using “aggressive” antenna repositioning essentially forcing the excitation to be uniform.<sup>54</sup> The resultant field is apparently uniform,<sup>55</sup> and measurement data retain essential features of an isotropic uniform field readily available in a highly reverberant environment.

<sup>54</sup> Hatfield, n. pag.

<sup>55</sup> The field may be considered uniform in the sense that many different data sets are taken, and the peak values of responses that are recorded may be analyzed in a fashion similar to that which is usually applied to data from a highly reverberant space.

Finally, a PEB is a useful venue for various infrastructure elements where EM shielding from an external RF weapon threat could be at issue. Measurement technique and data in this section address all of these areas.

## **4.2 MEASUREMENT IN PRE-ENGINEERED BUILDING (PEB)**

Measurements were conducted in the NSWCDD PEB, Building 1427, to accomplish the following objectives:

- a. To demonstrate measurement technique in a poorly-to-moderately reverberant space.
- b. To examine the overall *chamber* properties of the building.
- c. To examine the typical departure of results from those expected from a highly reverberant space.
- d. To evaluate the leakage area of overhead roll-up doors typically used in PEB construction.

### **4.2.1 Building Description**

The building shown in Figure 4–2 represents a common type of PEB construction, which could be designed for use as RF-shielded facilities or RF test areas. Several measurement series were conducted in Building 1427. As shown in Figures 4–2 and 4–3, the building has aluminum siding, an internal steel skeletal structure, an aluminum roof, and a concrete floor. Building 1427 has two, 12-ft-by-12-ft, aluminum, overhead roll-up doors that are the most obvious RF-shielding leakage points. These doors provided a good opportunity to examine a shielding measurement technique. Further, the building was chosen because of its availability and relative remoteness on the base, which meant that reverberation measurements would not interfere with other base activities.



**Figure 4–2. South End of Building 1427  
Showing the West Overhead Roll-up Door**

#### **4.2.2 Basic Characterization: 1/e Time and Insertion Loss**

Fundamental parameters in characterizing a space are its wall-scattering and internal loss rates. The scattering rate is determined simply from geometry, and the loss rate can be found conveniently from a radar-based measurement of the 1/e time. Additionally, particularly for spaces that are only moderately reverberant, the field uniformity is likely to be poor. That is, if a particular region of the space is excited, the average field levels are likely to be higher near this region than at other more distant points. This so-called “field gradient,” which has been observed with CW IL measurements in aircraft compartments and other poorly reverberant spaces, can be demonstrated quite clearly and quantitatively evaluated with a TD IL measurement.

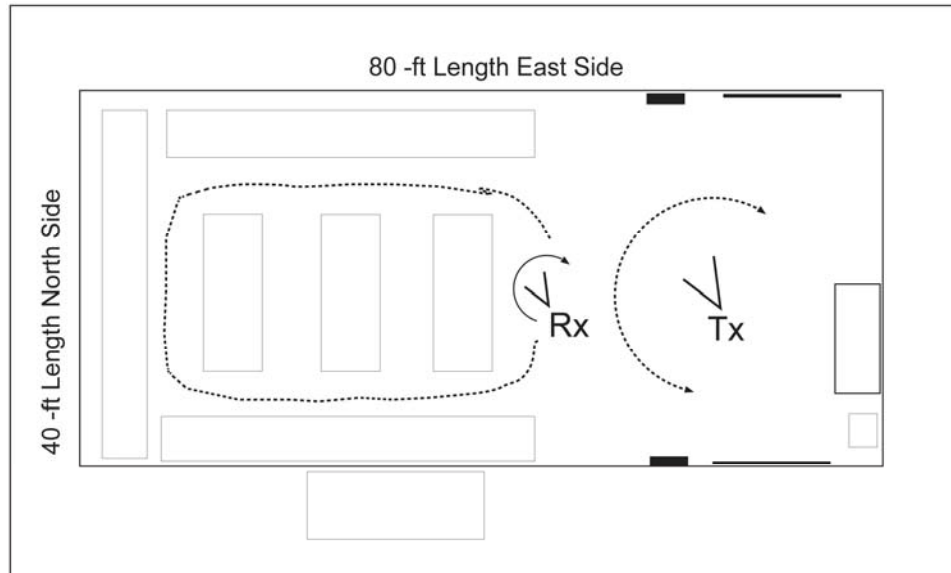


Note: The photo shows the west roll-up door and several test antennas.

**Figure 4-3. Interior of South End of Building 1427**

#### 4.2.2.1 1/e Time Measurement

Figure 4-4 is a Building 1427 floor plan showing the locus of antenna positioning for the *internal excitation* 1/e time measurements, shown in Figure 4-5. The measurements were made at several different times during 2003 and 2004. The Tx and Rx antennas were either log-periodic for 0.1-to-1.0-GHz measurements or dual-ridge-horn type for 1-to-10-GHz measurements. Also, discone antennas were used. Most measurements were made by moving the antennas to obtain an ensemble average rather than holding them stationary and using a stirring device. Limited experiments with a large, aluminum foil, stirring fan showed, however, that the fan actually worked quite well when the Tx antenna was pointed directly at it. Generally, the Tx antenna was held about 1 to 1.5 m off the floor, tilted upward slightly, and rotated about a vertical axis to irradiate the building walls and ceiling. The Rx antenna was rotated and tilted in various directions as it was carried around in the building, down the aisles, and between storage shelves. Long, flexible transmission lines were used to allow mobility of the antennas.

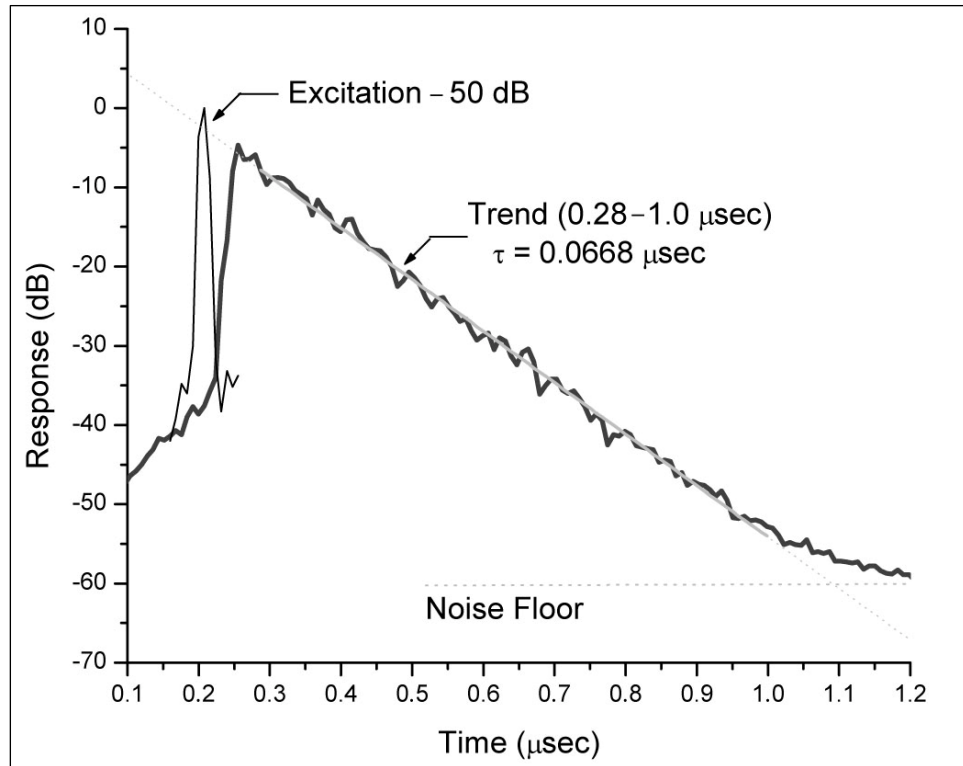


Note: For  $1/e$  time measurements, the positions and loci for Tx and Rx antennas are displayed.

**Figure 4-4. Building 1427 Floor Plan**

Figures 4-5 and 4-6 show typical response measurement data used for extracting  $1/e$  values. Most data show a single  $1/e$  value, as derived from Figure 4-5, where the received-power-versus-time data are plotted on a semilog plot appearing as a straight line.

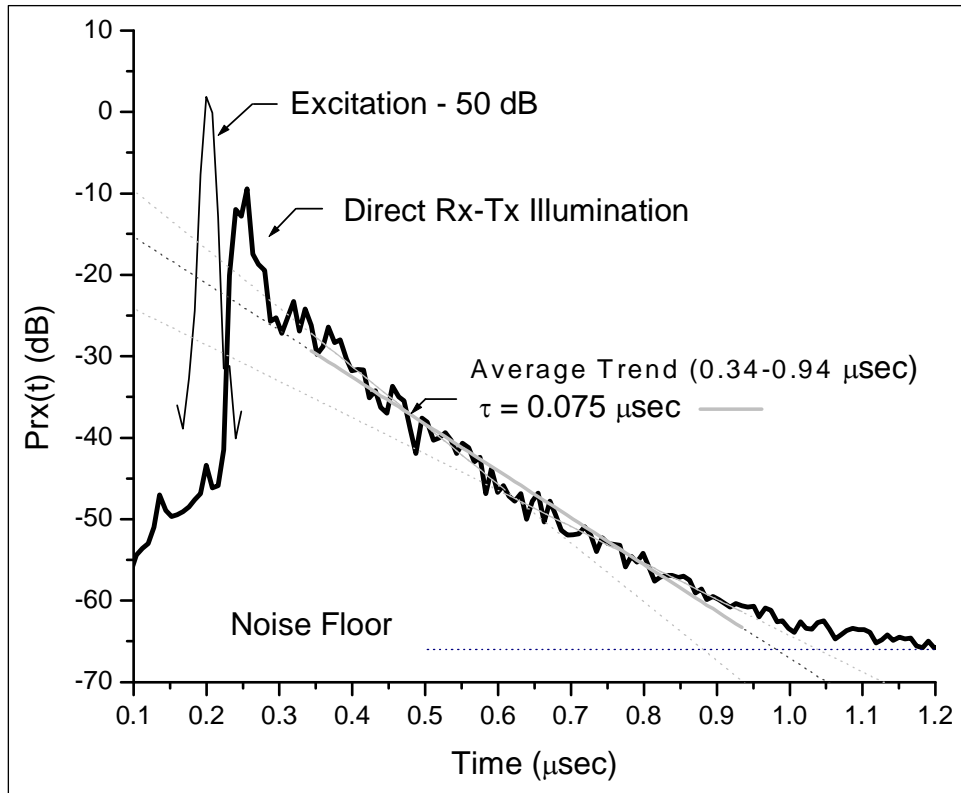




Note: Pulse Center Frequency = 600 MHz, BW = 125 MHz, and  $T_p = 16$  nsec.

**Figure 4-5. Typical Reverberant Transient Response**

The data of Figure 4-5 yield a  $1/e$  time value of  $0.0668 \mu\text{sec}$  with decay over a 50-dB range. The  $R^2$  value from the regression curve used to extract  $\tau$  was 0.995.



Note: Direct Tx-Rx illumination and range (i.e., a “spread”) in measured 1/e time values are displayed.  
Pulse Center Frequency = 400 MHz, BW = 125 MHz, and  $T_p = 16$  nsec.

**Figure 4-6. Occasional Reverberant Transient Response**

Occasionally, modes do not have a sharply peaked distribution in  $Q$ . Transient-response measurement data will occasionally show a range of  $\tau$  values, as seen in Figure 4-6 where the data plotted in a semilog plot follow a curved path.

Data taken over the roughly 30-dB-decay range between 0.34 and 0.94  $\mu\text{sec}$  yield a 1/e time of 0.075  $\mu\text{sec}$ . The regression  $R^2$  value is 0.97, in spite of the obvious curvature.

Selecting data between the time intervals of 0.34 to 0.6 and 0.6 to 0.94  $\mu\text{sec}$  yields  $\tau$  values of 0.060 and 0.097  $\mu\text{sec}$  respectively.

This response is indicative of some of the cavity modes having a much lower  $Q$  than others. This could occur from localized losses in the building. Calculation of the  $Q$  of the modes in an empty cavity with lossy walls predicts a range in  $Q$  values for modes in an interval about a frequency  $F$ . However, the straight-line response data of Figure 4-5 is far more commonly observed than a curved response, indicating that the distribution of mode  $Q$ s around a given frequency  $F$  is usually sharply peaked. The dominant Transverse Electric (TE<sub>101</sub>) mode frequency for this building is 13.75 MHz. Since 400 MHz is nearly 30 times greater, insufficient mode density is an unlikely cause. In the measurements conducted in Building 1427, the curvature was noticed at frequencies only

around 400 MHz. Currently, the curvature that is observed around only a single frequency remains unexplained. More extensive measurements may show it at other frequencies as well.

The data of Figure 4–6 also show a sharp initial peak, which is indicative of direct illumination of the Rx antenna by the Tx antenna. This occasionally happens accidentally during measurements and can be problematic with CW. In the time domain, direct illumination data points are easy to eliminate during analysis and reduction because of the “time tagging” feature of the A-scope display.

The characteristic wall-scattering time for the building was calculated as 22 nsec using the building dimensions and the relationship  $T_C = 4V/Sc$ . For  $\tau$  measurements in the range of 45 to 100 nsec, as shown in Figure 4–7, the reverberation index for the building ( $\tau/T_C$ ) varies between approximately 2.5 to 5.5.

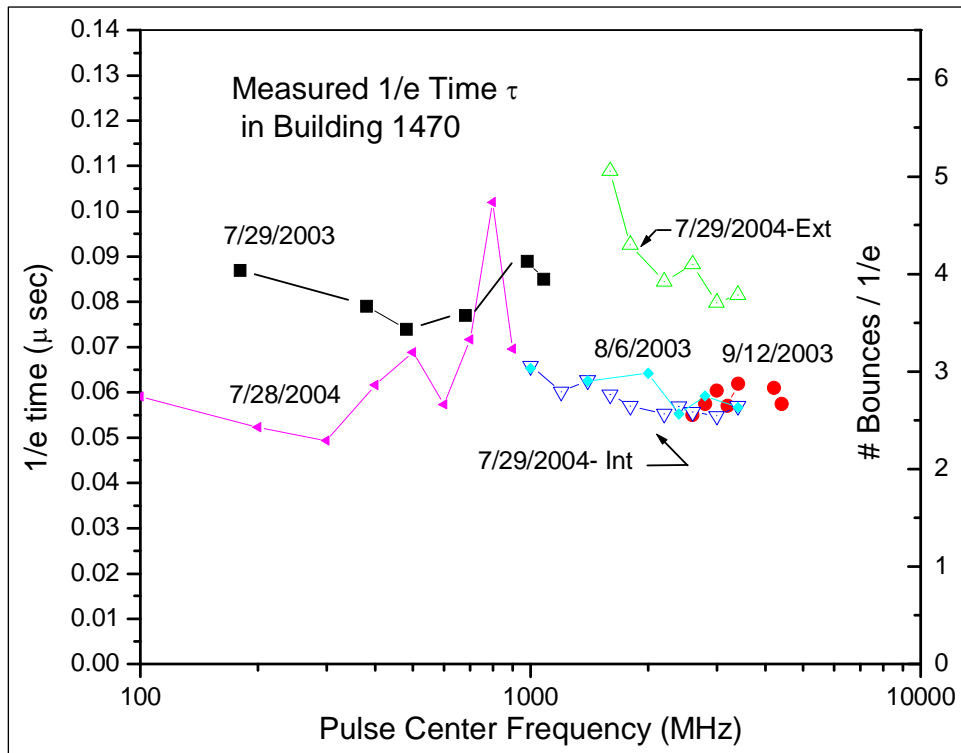


**Figure 4–7. Measured 1/e Time Versus Frequency in Building 1427**

Differences in measured 1/e time on different dates may be due in part to different loading in the building, since the amounts and types of materials stored in the building varied from time to time. Also, measurement results depend on location of the antennas. The measurement data in Figure 4–7 labeled “7/29/2004–Ext” were taken with excitation outside the building rather than inside, and the Rx antenna was located near the center of the roll-up door, to be discussed in Section 4.2.3 and Figure 4–14.

Aside from different possible loading of the building on different measurement dates, one may not be surprised that  $1/e$  times are less tightly grouped than in a highly reverberant space. Note the abnormally high  $\tau$  value at 800 MHz and the differences between internal and external excitation in the 7/29/04 data from Figure 4–7. When one obtains a good ensemble average in a highly reverberant space, it represents the response of photons that have been to all regions of the chamber with roughly equal representation. In a poorly reverberant space, one can obtain a more localized response characteristic of either a particular region of the chamber or of particular propagation modes or ray paths. The losses along different paths are likely to be different. IL data and the Fabry-Perot mode response data described in Section 4.2.2.2 illustrate this notion somewhat, but it is clearly a subject for further study.

#### 4.2.2.2 Fabry-Perot Mode

An additional type of response observed in Building 1427, as shown in Figure 4–8, was identified as a Fabry-Perot mode with waves reflecting between the two *closed* parallel overhead doors. Figure 4–9 depicts the antenna positioning for the data of Figure 4–8. The data of Figure 4–8 were taken with the Rx antenna in position A. When the Rx antenna was moved to position B, the spacing between peaks decreased by half to 38.9 nsec. Highly periodic responses of the type shown in Figure 4–8 have also been seen in large aircraft passenger cabins with waves reflecting back and forth between the sides of the aircraft.

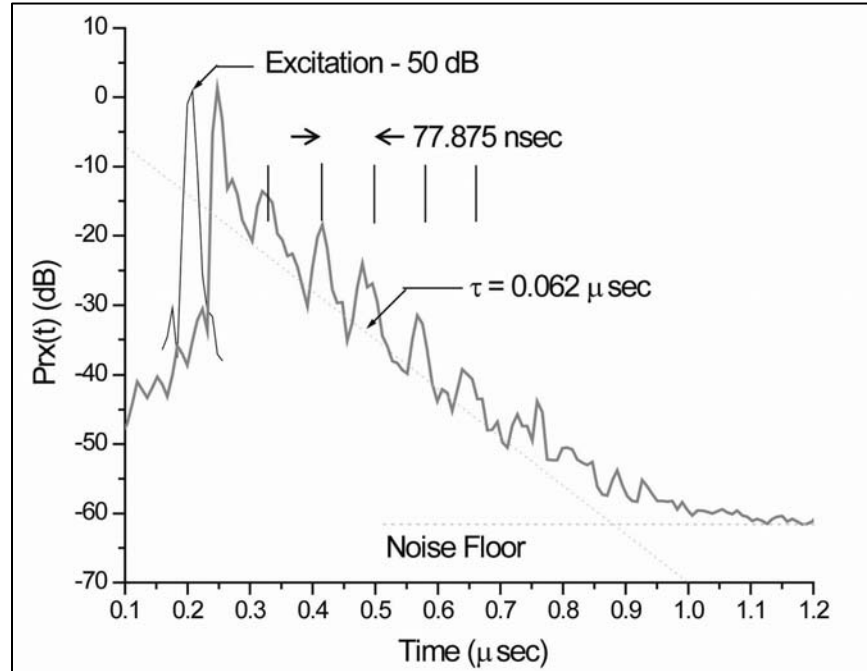


**Figure 4–8. Transient Response Showing Fabry-Perot Mode in Building 1427**

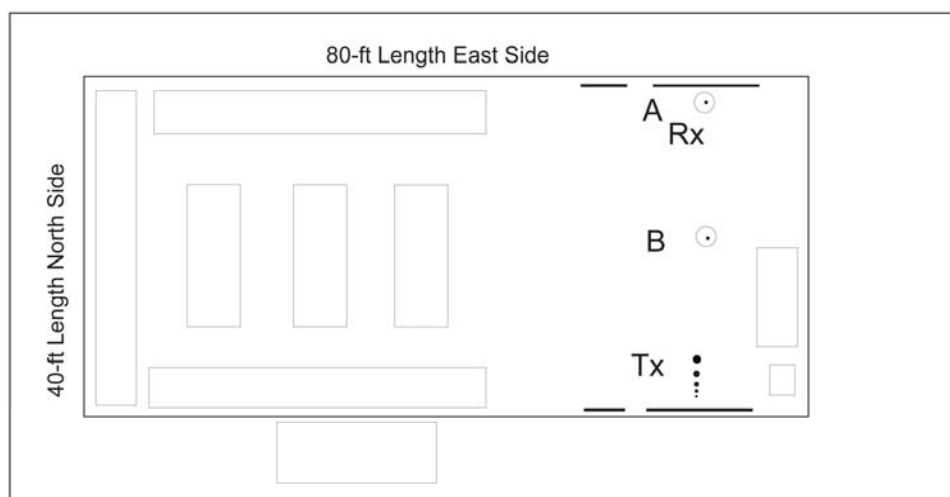


**Figure 4-9. Antenna Arrangement for Excitation of Fabry-Perot Mode in Building 1427**

#### 4.2.2.3 Insertion Loss Measurement

Figure 4-10 approximates antenna positioning in Building 1427 where IL measurements were taken. Note that this figure designates zones 1 and 3 as particular regions where the antennas were moved about for specific measurements. The CW measurements shown in Figure 4-11 were made by using a network analyzer and performing an  $S_{21}$  measurement.

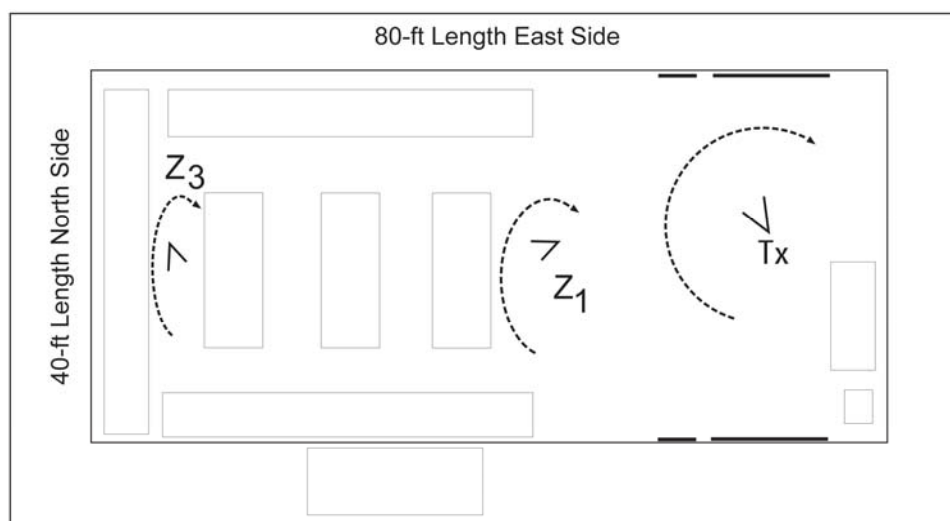


**Figure 4-10. Antenna Positioning and Movement Locus for IL Measurement**

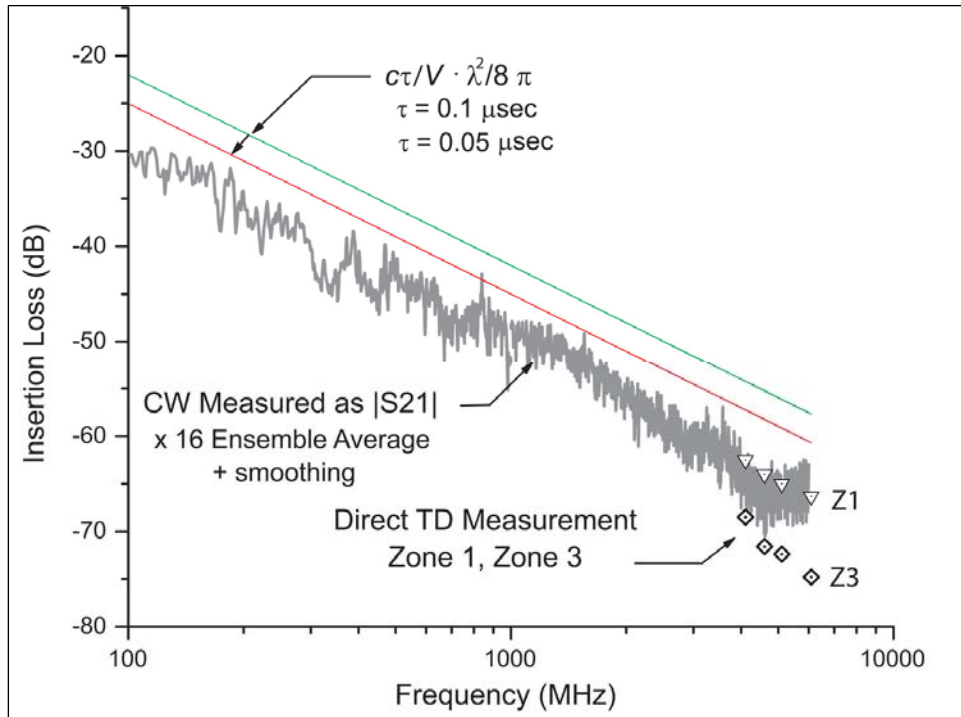


**Figure 4-11. Measured IL Versus Frequency for Building 1427**

An ensemble average of 16 different runs was made by repositioning the antennas and also by applying a small amount of smoothing, using the built-in function found on the analyzer. 801-point measurements were made between 0.1 to 1.0 and 1.0 to 6.0 GHz. Simple  $S_{21}$  measurement simulates the kind of measurement result that would normally be obtained with a sweeper and spectrum analyzer in that it does not include impedance mismatch correction at the Tx and Rx antennas. Separate measurements have shown that doing an impedance mismatch corrected measurement [i.e.,  $|S_{21}|^2 / (1 - S_{11}^2)(1 - S_{22}^2)$ ] generally reduces IL by 1 to 2 dB.<sup>56</sup>

Due to the poor reflectivity and rather large ratios of length to width or height, one might expect that fields within the space are not uniform. Another way of saying this is that energy reaches certain points in the space only through a narrow range of solid angle. The IL is not a unique quantity as it would be in a space where a nearly ideal reverberant field was maintained. The CW measurements were made with roughly the same antenna positioning as for the zone 1 TD measurements. While the general trend of CW IL values follows the ideal value given by  $c\tau/V \times \lambda^2/8\pi$ , most of the values are more negative by 6 to 10 dB.

<sup>56</sup> Frequently minimum IL obtained from a maximum-hold function on a spectrum analyzer is used. The measurement results shown in Figure 4-11 are of average rather than minimum IL.

Measurement results at 4.1 and 6.1 GHz from zones 1 and 3 are also shown in Figure 4–11. These results are discussed in more detail in Section 4.2.2.4.

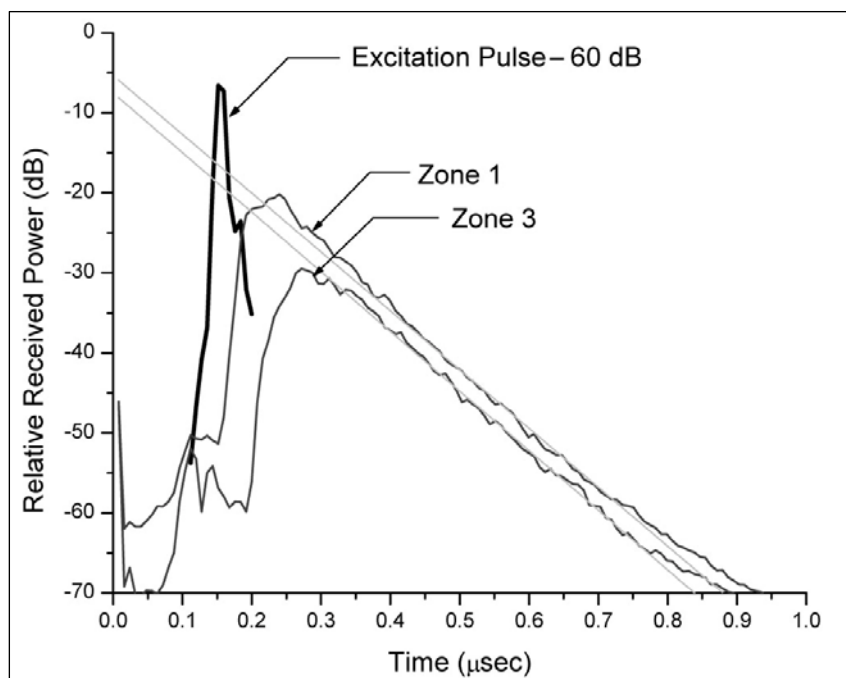
#### 4.2.2.4 Data Reduction to Extract Insertion Loss

Figures 4–12 and 4–13 show averaged and integrated 6.1-GHz, TD-response data. The excitation pulse was obtained by connecting the Rx and Tx transmission lines directly together through a 60-dB attenuator. This direct connection measurement yields time and energy reference/normalization values for calculating IL.

For the time-domain technique, IL is calculated from the ratio of received and transmitted energy instead of received and transmitted power. Energy in the excitation pulse and the response is calculated by integrating the A-scope data.

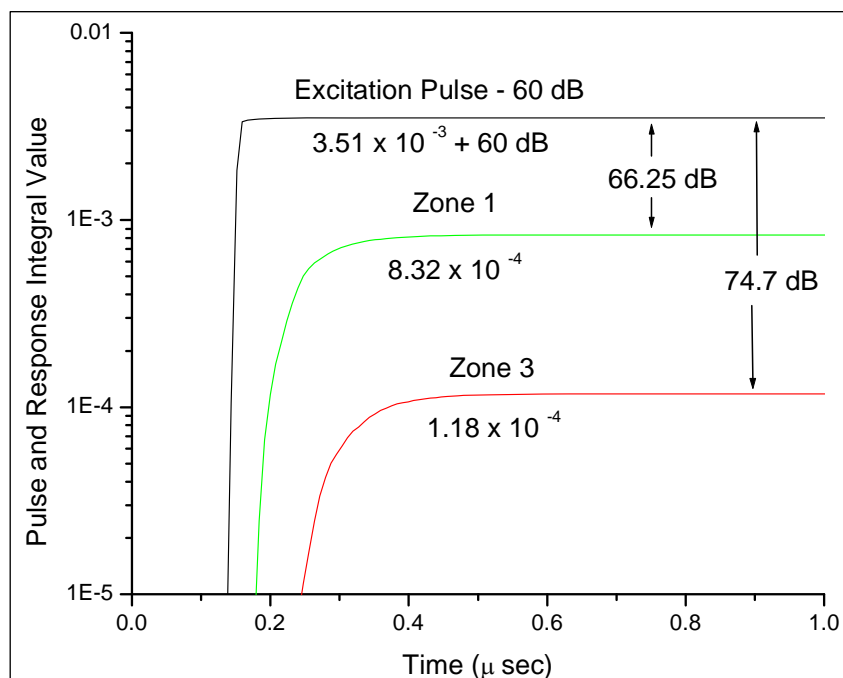
The integral values shown in Figure 4–13 are calculated from data in Figure 4–12 as follows:

- Step 1. Convert the dB values to relative power ( $10^{\text{dB}/10}$ ).
- Step 2. Multiply the relative power value by the time-step value between each data point.
- Step 3. Apply the SUM function available in the MS Excel spreadsheet to add each value from 0.1 out to 1.0  $\mu\text{sec}$ , i.e., from the beginning of the excitation out to where steady-state values of the integral have been developed.



Note: 16-nsec pulse centered at 6.1 GHz.

**Figure 4-12. Reverberation Response Measured in Zones 1 and 3**



Note: 16-nsec-pulse centered at 6.1 GHz.

**Figure 4-13. Integrated Responses from Figure 4-12**



The time-integrated value of the pulse excitation is  $3.51 \times 10^{-3} + 60$  dB (i.e., relative W-sec) from this operation. Alternatively, one can estimate the integral value by multiplying the peak value of the excitation pulse by the nominal pulse width given by  $2/BW$ . BW is the pulse bandwidth chosen by the combinations of frequency sweep rate, sample rate, and FFT block size. The pulse BW for the data of Figure 4–12 was 125 MHz yielding a nominal pulse width of 16 nsec. The peak power of the excitation pulse was -6.62 dB (+60 dB) or  $0.2177$  relative  $W \times 10^6$ . This relative power level multiplied by 16 nsec yields  $3.48 \times 10^{-3} + 60$  dB (relative W-sec), which is very close to the  $3.51 \times 10^{-3}$  value obtained from the spreadsheet integral.

In other measurements that have been conducted, comparison of the excitation energy calculated directly from the integral or from the product of peak power and pulse width (calculated as  $2/BW$ ) typically agrees to within approximately 1 to 2 dB.

The response in each zone shows nearly the same decay rate corresponding to a  $1/e$  time of 59 nsec, which is consistent with the data of Figure 4–7. However, the response in zone 3 begins about 40 nsec later, consistent with its greater distance from the transmit antenna, and then remains about 3 dB below that of the zone 1 response. As shown in Figure 4–13 and based on the area under the received power curves in Figure 4–12, the actual IL in zone 3 at this frequency is 8.4 dB greater than that in zone 1.

The 8.4-dB difference is somewhat greater than might otherwise be obtained in the building because the region around zone 3 is “shadowed” by large storage shelves in the building. Even at a height of 5 ft off the floor, a point in Zone 3 is visible from locations only near the ceiling.

Interestingly, even though the IL for zone 3 is 8.4 dB greater than that for zone 1, the two exponential decay trend lines differ by only about 3 dB. This has been observed frequently in measurements in poorly reverberant spaces. Most of the deficit in received energy leading to greater insertion loss occurs from energy arriving at the more distant point later. This effect occurs in highly reverberant spaces too, but it is less important. When reverberation is high, the time of flight for a wave to transit the length of the space becomes a small fraction of the total response time. Starting the integral a few nanoseconds later is inconsequential.

### **4.2.3 Measurement of Overhead Roll-up Door Leakage Area**

A radar-based measurement was used to determine the leakage area of the overhead door depicted in Figures 4–2 and 4–3. For this measurement, one assumes that for an externally incident beam approaching the door as in Figure 4–14, the effective leakage area would be equal to the geometric area of the door if it were open, and some reduced area if the door were closed. The final result is door leakage area expressed in decibels

below the geometric area.<sup>57</sup> Given this area, one could calculate the shielding factor for Building 1427 or for any other building, if its internal loss rate could be specified.

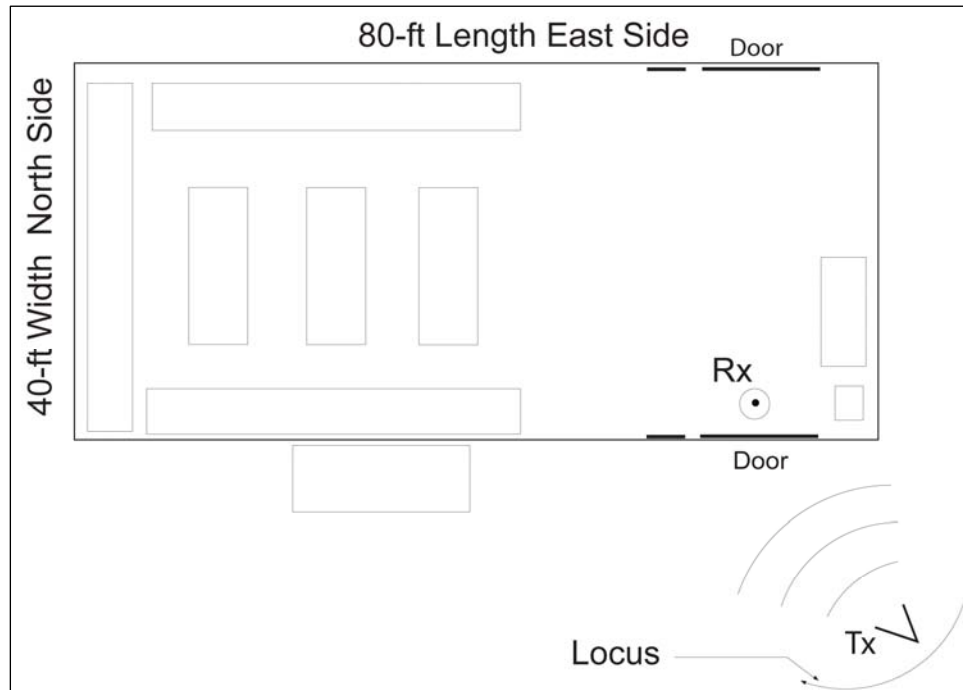


**Figure 4–14. Diagram of Antenna Positioning for Door Leakage Measurement**

#### 4.2.3.1 Excitation

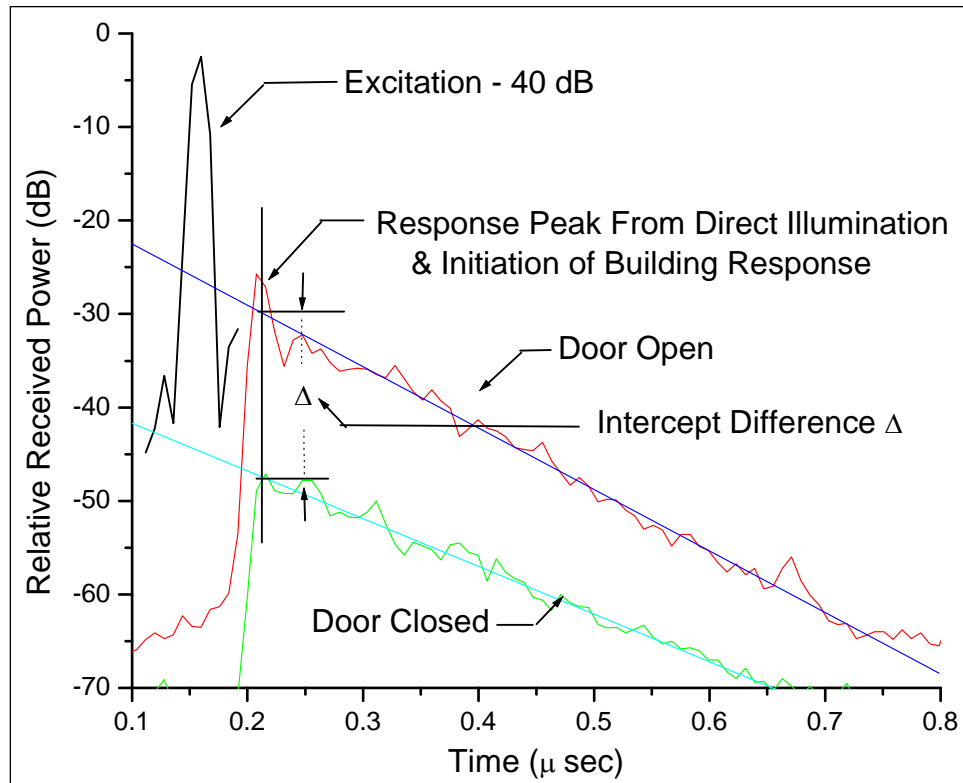
The Tx antenna was positioned as depicted in Figure 4–14 in a region near the vantage point for the photo of Figure 4–2. The Tx antenna was moved about a small locus of points as depicted in Figure 4–14 to vary the excitation and, thus, form an ensemble average. Typical incidence angle of approach was generally off-normal to minimize the effect of radiation entering the open door, striking the opposite door, and then reflecting straight back out the open door rather than being trapped within the building and developing an isotropic response.<sup>58</sup> The Rx antenna (discone) was placed about 6 ft inside the building and about 6 ft above floor-level in the center of the doorway. The transmit antenna, thus, illuminated the receive antenna directly when the door was open. With CW excitation, this antenna placement would be considered a bad or at least worrisome practice, but with an A-scope readout, as shown in Figure 4–15, Section 4.2.3.2, the direct illumination response in the received power is easily distinguishable from the reverberation response of the building.

<sup>57</sup> Area was chosen as a reference. More detailed measurements may show that door perimeter is actually a better index.

<sup>58</sup> Conceivably, in an empty building, a significant percentage of the power could still be re-radiated back out because of the retro-reflective property of the trihedral structure formed by the walls and floor.

#### 4.2.3.2 Typical Measured Response

Figure 4–15 shows a measured response sensed by the discone antenna 6 ft inside the doorway from a 16-nsec pulse centered at 2.4 GHz. A direct illumination peak in the open-door response occurs at about 0.2  $\mu$ sec, about 50 nsec after the excitation peak corresponding to the range between the Tx and Rx antennas, followed by reverberation response of the building. The open-door response trend is derived from data following, but not including, the peak.



Note: The excitation pulse has 125-MHz BW, 16-nsec pulse length, and 2.4-GHz center frequency.

**Figure 4–15. Received Power Versus Time from Discone Antenna with Open Door and Closed Door**

With the door closed, the direct illumination peak is not as prominent. Initial response, indicating initial energy density within the building with the door closed, is about 18 dB below that of the open-door case,<sup>59</sup> as indicated by the difference in intercept points ( $\Delta$ ) at the direct illumination initiation point. The response decays less rapidly with the door closed than with the door open because with the door open, leakage out the door is an additional loss mechanism. If this measurement had been performed with CW illumination rather than a short pulse, the response difference (ratio of CW steady-state

<sup>59</sup> The peak may also have moved slightly to the right a few nanoseconds, because the path between the antennas may not be through the door but around the door perimeter.

power levels) would have been about 16 dB. This corresponds to the ratio of area under the open-door and closed-door power versus time curves rather than the 18-dB difference in initial intercept. The 18-dB measurement result, along with data at other frequencies, is plotted in Figure 4–16.

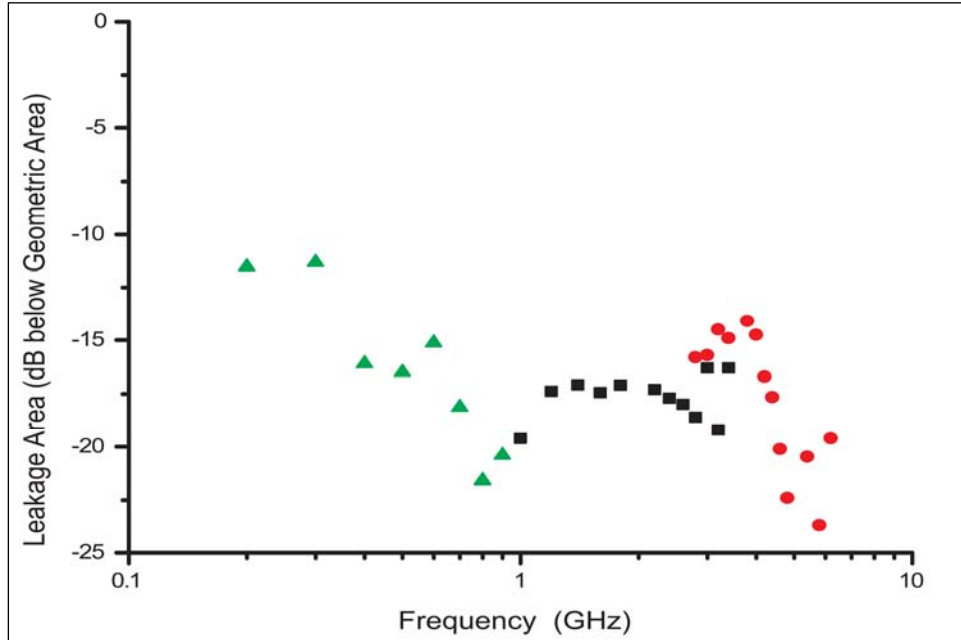


**Figure 4–16. Leakage Area of Overhead Roll-up Door**

#### 4.2.3.3 Open-Door Loss Mechanism

A prominent feature of the data in Figure 4–15 is the more rapid decay rate for fields in the open-door measurement case. Actually, the observed increase in decay rate is greater than might otherwise be expected by assuming that the fields behave as well developed isotropic fields.

For a closed door, the loss rate for fields in the building is given by  $\Lambda_{\text{closed}} = V/\tau_{\text{closed}}$ .

When the door is opened, the new 1/e time should decrease slightly, so that the new loss rate (including leakage through the door) would be greater and  $\Lambda_{\text{open}} = V/\tau_{\text{open}}$ .

Equation (4–1) gives the loss coefficient  $\Lambda_t$  due to leakage through the door:

$$\Lambda_{\text{open}} = \Lambda_{\text{closed}} + \Lambda_t \quad (4-1)$$

Hill has shown that for leakage of reverberant field power through an open aperture, the leakage cross section  $\Sigma$  can be expressed as half of the geometric area.<sup>60</sup> Further, Equation (4-2) gives the energy transfer rate coefficient  $\Lambda_t$  for this type of process:

$$\Lambda_t = 1/2 \cdot \Sigma \cdot c \quad (4-2)$$

For further discussion of leakage through an aperture, see Appendix C.

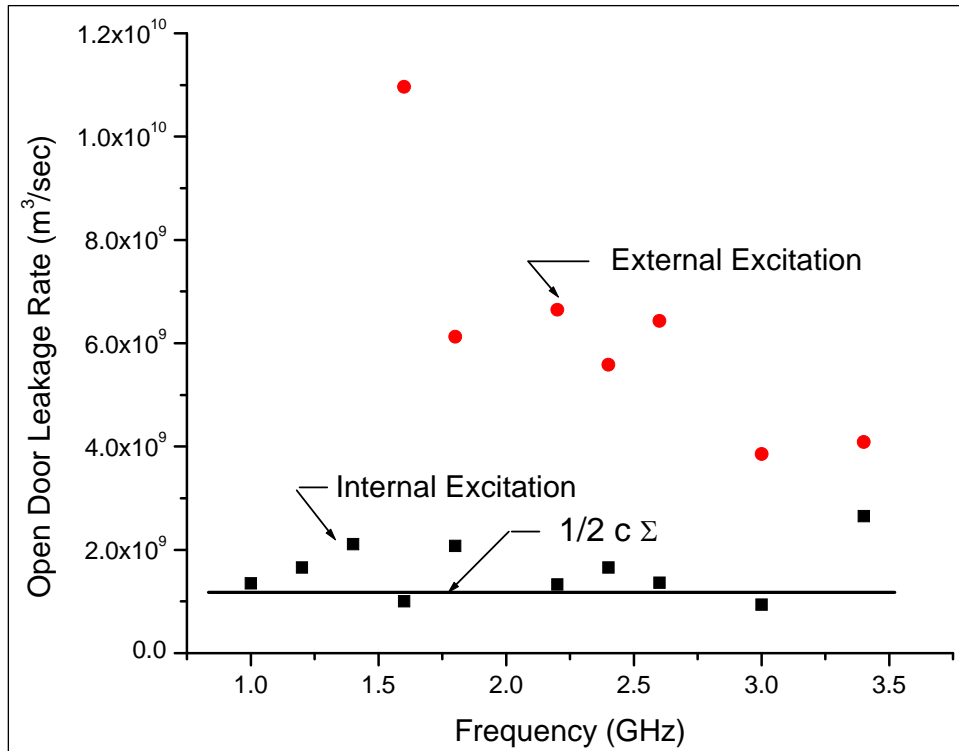
Figure 4-17 shows the difference in calculated decay rates,  $\Lambda_{\text{open}} - \Lambda_{\text{closed}}$ , for both internal excitation using excitation geometry similar to that in Figure 4-10 and for external excitation as shown in Figure 4-14. With internal excitation, the measurement data fit the theory as expressed by Equation (4-1) within a factor 2. “Error” with external excitation is much larger, indicating that a true isotropic field was not formed when external excitation was applied. These results support the notion examined by Hatfield that even though a space is not highly reverberant and, thus, does not easily support a good isotropic reverberant field, responses indicative of a good isotropic field can be obtained in the space if aggressive antenna motion is used during excitation.<sup>61</sup>

The field patterns or ray paths that were set up when external excitation was applied, apparently, favored leakage back out the door. The data in Figure 4-15 show a reasonably smooth response indicating a good average. Evidently, smoothness in the measured response is not necessarily proof of a truly isotropic field.

---

<sup>60</sup> Hill et al., 169-177.

<sup>61</sup> Hatfield, n. pag.



Note: Compared with ideal uniform isotropic case,  $\Lambda_t = \frac{1}{2} c \Sigma$ .

**Figure 4–17. Measured Open-Door Leakage Rate in Building 1427**

#### **4.2.4 General Features of Propagation in Poorly Reverberant Spaces**

The main objective in this section has been to describe technique and examine results from a series of measurements in a real space that has mediocre, but still significant, reflectivity. As a starting point, measurement data were compared with the high reverberation paradigm. Intuitively, one expects departure from the paradigm. EMC engineers should find it useful to get a semiquantitative feel for how great the departure is likely to be at a particular reverberation index.

Insertion loss is a significant parameter for analysis of propagation in a space and in chamber operation. While insertion loss in this poorly reverberant space follows the general trend that would be observed in a highly reverberant space, the data of Figures 4–11 through 4–13 show it is generally greater and its value is not necessarily unique as it must be when reverberation is high.

Figures 4–11 and 4–12, which show an apparent cold spot in zone 3 of the space, illustrate one of the more important benefits of TD measurement when reverberation is poor. An EMC engineer can inspect the measurement data quickly and see if a significant “late response” feature is present, as in the zone 3 response. Further, one can tell easily if data are contaminated from direct illumination, as is evident in the data of Figure 4–6. During measurements, inadvertent contamination of reverberant field

measurement data occurred several times. Apparently, data contamination in this way is an easy error to make. With TD data, the direct response can easily be identified and discarded if necessary. With CW measurement, one cannot tell that direct response is present in the data, except that subsequent analysis may show that the statistical properties of the data are incorrect.

The data of Figure 4–17 indicate that the leakage coefficient for the door is not necessarily unique as it would be if the fields were truly isotropic. Numbers consistent with the ideal theory result when the space is excited internally, i.e., aggressively with many Tx antenna positions and pointing directions. However, with external excitation, leakage back out the door is much more pronounced. In other words, the leakage rate is much greater than expected for an isotropic environment. This does not necessarily mean that the data are wrong. It suggests strongly that in spite of repositioning of the antenna during external excitation, as in Figure 4–14, a sufficiently isotropic field inside the building was not achieved.<sup>62</sup> Some of these data were taken on the same day and, thus, are not due to different loading in the building because of different building contents. Apparently, ray paths that exist as a result of external excitation encounter less loss.

When reverberation is high, the notion of a particular propagation path is almost meaningless, except that one might use that term to refer to a particular leakage aperture. Regardless of where energy is injected into the space, rays travel in all directions and reach all regions of the space. Equivalently, one can say that all propagation modes can exist. Each region in the space is closely coupled to other regions.

In lower reflectivity spaces, such as in the PEB, the notion of particular propagation paths starts to regain significance as it would in free space. Propagation is multi-path, but *multi* means “several,” rather than “infinite” as it does in the high reverberation limit. The radar-based measurement technique is a powerful tool in this regime because of the time-tagging feature of the A-scope display.

#### **4.2.5 Other Kinds of Measurements: Mapping Hot and Cold Regions in a Space**

In most of the measurements considered in this section, the main objective was comparison of results with those expected in a high-reverberation case. An underlying notion is that average behavior of the entire space was the measurement goal, so moving the measurement antennas by changing their location, pointing angle, and polarization is appropriate to achieve a good spatial average.

---

<sup>62</sup> Both data sets were taken with the door closed.

In some instances, however, an EMC engineer may wish to specifically examine the presence of hot or cold regions in a space when energy is injected into that space from a particular region or leakage point. In studying propagation in a ship or aircraft compartment, two questions may be posed:

- a. How much energy can propagate from one specific point or region to another in some large compartment full of equipment?
- b. What is the worst case coupling between two compartments?

Average behavior of the space is of some interest, but the most important questions may involve specific regions of the space and specific propagation paths. The apparent cold region in zone 3 from excitation in zone 1 is not necessarily a nuisance or error at all. Depending on the question, it may be the desired answer.

The first part of Appendix F discusses antenna response and illustrates how antenna gain may be an important consideration when performing “localized” measurements in a poorly reverberant space. For further study of the cold region in zone 3, one would preferably use a low-gain antenna, such as a discone, rather than the higher gain ( $\sim 10$  dB) log-periodic antennas and ridged wave-guide antennas that were used.

In a highly reverberant, truly isotropic environment, equal power arrives from all angles, so the antenna directivity makes little difference. One can easily get a good average, and the power or energy density can always be calculated by dividing the received power or energy by  $\lambda^2/8\pi$ . If the field is poorly reverberant and, consequently, less perfectly isotropic, then a high-gain antenna may incorrectly weight readings from particular angles that have abnormally high or low power density per steradian.

Appendix F illustrates how in practical situations, a useful average field reading in a particular region of a space may be obtained with as few as three<sup>63</sup> orthogonal readings by essentially using the antenna as a field probe. Antenna directivity over and above that of an ideal short dipole adds uncertainty to the measurement result. Higher directivity or any other departure from the ideal short dipole pattern adds even more uncertainty.

#### **4.2.6 Overview of Localized Field Measurements in an Automobile**

As a specific example of how hot spots in a poorly reverberant space might be of interest, the following question is posed: How large a biological nonionizing radiation dose would a person in an automobile receive, if the automobile were irradiated by a high-power microwave beam? A hypothetical scenario is illustrated briefly in Figure 4–18. While the spatial-average environment in the passenger compartment is of some interest, determining a reasonable worst case exposure—particularly at the occupant’s head, chest, and “seat-cushion level”—is essential.

---

<sup>63</sup> More readings are better.



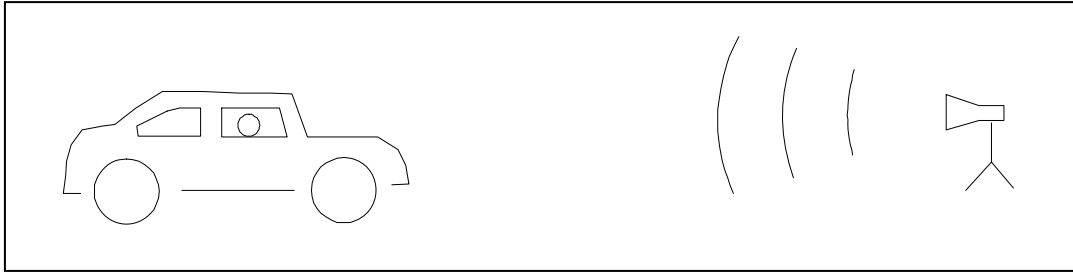


**Figure 4-18. Vehicle Irradiation Scenario**

An automotive passenger compartment is an open structure. Part of the dose that an occupant would receive would clearly be from the direct incident beam, but part could also be from reflections. Due to the random reflections, the polarization and propagation direction of the environment is random. Measurement and analysis technique must allow for these nondeterministic features.

A discone antenna may be used to measure three field components:  $\hat{x}$ ,  $\hat{y}$ , and  $\hat{z}$ .

Figure 4-19 shows three possible orthogonal antenna position arrangements to determine the environment at neck-level for a passenger. The average is orientational rather than spatial. The radiation dose to a person in that position consists of components with unknown direction of incidence and polarization. The measurement with three orthogonal orientations, as described in Appendix F, contains some uncertainty because of the nonideal pattern of the discone.<sup>64</sup> The preferred procedure would be to do additional measurements, using other orthogonal coordinate axis sets, which are rotated. More axis sets would more closely synthesize an isotropic receive pattern after averaging.

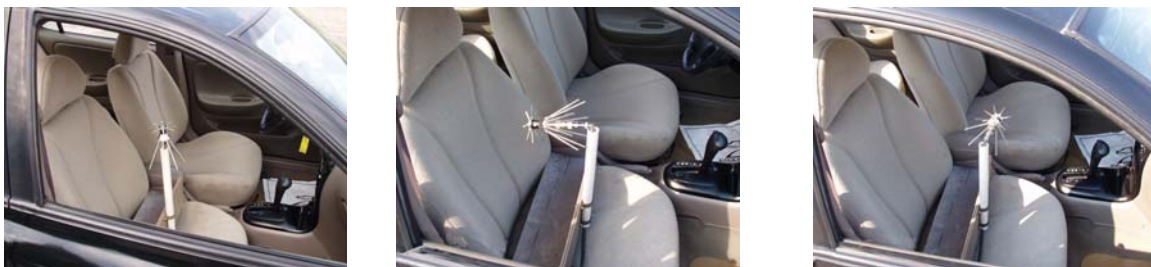


**Figure 4-19. Three Orthogonal Positions of a Discone Measurement Antenna**

Figure 4-20 shows typical data from the kind of measurement scenario under consideration. The vehicle was irradiated with a 4-nsec UHF pulse. For this particular test case, the  $\hat{x}$  measurement orientation received the highest signal component. In Figure 4-20, the received energy  $W_x$  rises sharply at  $t = 0.2 \mu\text{sec}$  and then continues to rise an additional 3 dB over the next 20 nsec. This indicates that about half of the dose is

<sup>64</sup> For the first octave above its minimum operating frequency, a discone antenna has a dipole-like pattern, which is within 2 dB of an ideal sine squared pattern.

from the direct beam, and about half is from the reverberant field that exists within the passenger compartment. The 1/e time for energy in the passenger compartment is approximately 12 nsec.

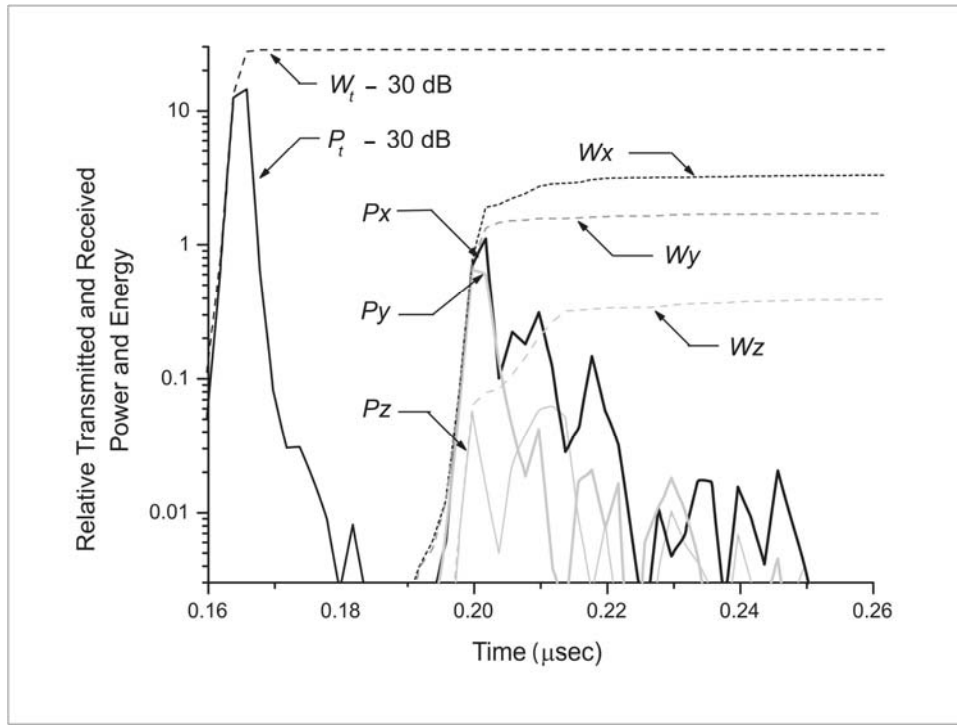


**Figure 4-20. Transmitted and Received Power and Energy in Vehicle Irradiation Experiment**

The average fluence  $\Psi$  at a point  $(x, y, z)$  (i.e., where the measurement antenna is located) is calculated by dividing the average received energy (in this case, estimated as the average of three readings) by  $\lambda^2/8\pi$ . This calculation is illustrated in Equation (4-3):

$$\Psi(x, y, z) = \frac{W_x + W_y + W_z}{3 \cdot \frac{\lambda^2}{8\pi}} \text{ J/m}^2 \quad (4-3)$$

As with power density in a reverberant space, the energy-per-unit area passing through a small sphere at the measurement point is not unidirectional as it would be from a single beam. For the case described here, the data of Figure 4-20 indicated that a little less than half of the fluence was from the reverberant response of the compartment.

How would one calculate the power density at the point for a given transmitted CW power? The ratio of average received energy to transmitted energy for the test scenario,

as depicted in Figures 4–18 and 4–19, is an insertion loss.<sup>65</sup> IL for power and energy are equivalent. For the same antenna geometries, the ratio of average received power to transmitted power would be equal to the average received energy to transmitted energy determined in the measurement.<sup>66</sup> The power density at the point  $(x, y, z)$  would be calculated by dividing the average received power by  $\lambda^2/8\pi$ .

#### 4.3 SUMMARY: MEASUREMENT IN MODERATELY REVERBERANT SPACES

This section has examined reverberant field behavior and measurement technique in a PEB, which has similar reverberation characteristics to those of ship and aircraft compartments. Measurements in an automobile passenger compartment were also reviewed briefly. The intent of the discussion was two fold:

- a. Demonstrate measurement technique and compare field behavior in a space with mediocre reflectivity to that in a highly reverberant space.
- b. Examine specialized techniques for measuring fields that have both reverberant and free-space properties.

Field behavior in a space with mediocre reflectivity has characteristics of both highly reverberant and free-space propagation. Enough reflections may be present so that free-space calculations are highly inaccurate. However, just as in free space, certain polarizations and directions of incidence may be predominant. TD measurement technique is particularly useful in this regime because of its ability to identify direct and reverberant response components.

When a space has mediocre reverberation characteristics, measurement results depart somewhat from those expected when reverberation is high. Fields within the space are not statistically uniform and are not isotropic in their direction of propagation. Insertion loss is often significantly greater than the idealized value  $IL_0$ , which is a unique function of wavelength, chamber volume, and  $1/e$  time. Hot and cold regions exist within the space, causing insertion loss values to be nonunique and highly dependent on the relative position of the Rx and Tx antennas.

Field levels can be measured in a reverberant space using an Rx antenna in a fashion similar to that which one would use with a field probe. However, when propagation is not isotropic, the measurement result will have less uncertainty if a low-gain antenna is used because directions of abnormally high or low incidence will not be significantly

---

<sup>65</sup> Clearly, the usual high-reverberation-limit paradigm would not be applicable in this case because the excitation is not transmitted from inside the passenger compartment. In this case, the insertion loss contains space loss, as well as possibly some reverberation gain.

<sup>66</sup> Differences between energy and single-frequency CW measurement results could occur because the energy measurement is averaged over the band of frequencies (i.e., BW) used to synthesize the pulse. With typical FFT windowing, the frequencies near the center of the band are weighted more heavily. See Appendix A, Figure A–15.

weighted. Ideally, the receiving pattern of the antenna should match the sine squared pattern that is characteristic of a short dipole probe. Measurement uncertainty can be reduced by taking several sets of orthogonal measurements that use several different coordinate orientations.

## 5.0 LOSS STUDY AND CHAMBER DESIGN SCALING LAWS

### 5.1 INTRODUCTION

Pre-engineered buildings (PEBs) use construction that is nearly ideal for a large semipermanent reverberation chamber facility that might be used to perform measurements on large test items.

During preparation of this report, it was possible to gain access to and perform a short series of measurements in the newly constructed NSWCDD Electric Railgun (ERG) facility building. The ERG building has extensive electrical grounding and bonding features that are important for operation of high-power electrical equipment. Thus, the empty ERG building presented an ideal case to examine microwave reverberation properties of this kind of construction without having to contend with contamination of data from losses due to internal building contents. A key construction feature for this building was aluminum flashing on the interior face of the insulation;<sup>67</sup> otherwise, no special construction for minimizing microwave leakage or internal loss was implemented.<sup>68</sup>

Two measurement objectives were designated for this test:

- a. To identify and quantify internal losses and propagation features.
- b. To develop and demonstrate scaling relationships useful for predicting the properties of similar buildings (i.e., larger or smaller) that might someday be built for use as reverberation test facilities.

The approach was to eliminate the concrete floor loss that overwhelmed all other building properties. The other loss mechanisms could then be studied in the presence of a good isotropic field.

### 5.2 BUILDING OVERVIEW

Figures 5–1 through 5–4 show general construction features of the ERG building. Many of the features are similar to those of Building 1427, studied in the previous section. Table 5–1 shows physical dimensions of the building, which are important for calculations to be presented later in this section.

---

<sup>67</sup> Aluminum-faced insulation is frequently not used in building construction because it reflects sound better than vinyl or other facing materials, leading to somewhat higher noise levels in the building, which some would find objectionable.

<sup>68</sup> The building walls were covered with fiberglass insulation. The insulation had an aluminized Kraft paper covering that appeared to have better conductivity than a steel surface.



**Figure 5–1. External View of Electric Railgun (ERG) Building**



Note: The figure shows internal construction, measurement instrumentation, and placement of conductive cloth floor covering.

**Figure 5–2. Internal View of ERG Building**





**Figure 5-3. View of Measurement Instrumentation and Bare “Walk-Around” Area**



**Figure 5-4. ERG Building Interior with Covered Floor**

**Table 5–1. ERG Building Physical Parameters Used in Scaling**

Quantity	Symbol	Value
Total Inside Surface Area	$S(m^2)$	$2.08 \times 10^3$
Volume	$V(m^3)$	$6.22 \times 10^3$
Total Floor Area	$S_F(m^2)$	518
Corrected Floor Area	$S_{FC}(m^2)$	451
Overhead Door Area	$S_{OHD}(m^2)$	104
Characteristic Scattering Time ( $4V/S$ c)	$T_C$ (nsec)	39.2

### 5.3 CAVITY PERTURBATION MEASUREMENT TECHNIQUE

The concrete floor reflectivity was measured with a cavity perturbation-type experiment, first, with the floor in its bare state, and second, covered with a special high-conductivity cloth material. Antenna positioning, pictured in Figures 5–2 through 5–4, is diagrammed in Figure 5–5.

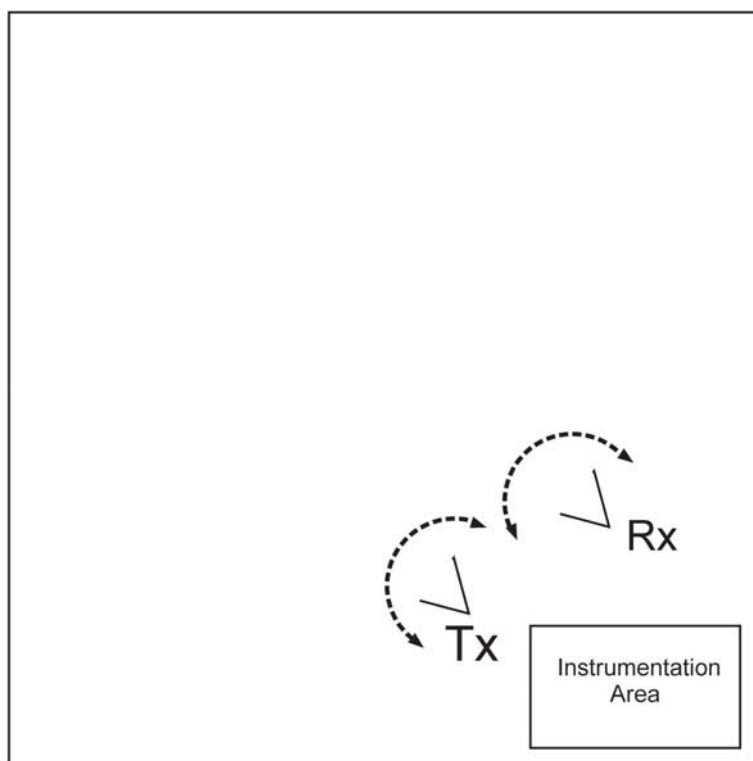


**Figure 5–5. Floor Plan and Diagram of Antenna Positioning for 1/e Time Measurements in the ERG Building**



Using short-pulse radar instrumentation, two sets of  $1/e$  time measurements were conducted:

- In the first measurement set, the concrete floor was left bare except for a 10-ft-by-50-ft section of sunken floor, equivalent to  $46.5 \text{ m}^2$ , which was covered with conductive cloth.
- In the second measurement set, the entire floor was covered with conductive cloth, including the sunken area but excluding a 12-ft-by-18-ft, “walk-around” equipment area, approximating  $20 \text{ m}^2$ . (Refer to Figure 5–3 and Figure 5–5.)

Table 5–1 refers to the difference in covered floor area in these two cases as  $S_{FC} = 451 \text{ m}^2$ .

Figure 5–6 displays typical transient-response decay curves, used to determine  $1/e$  decay time. Responses were generally characterized by straight-line decay in the semilog A-scope plots, even for the bare-floor case.<sup>69</sup> Figure 5–7 summarizes the  $1/e$  time measurement data for the two cases as a function of frequency.

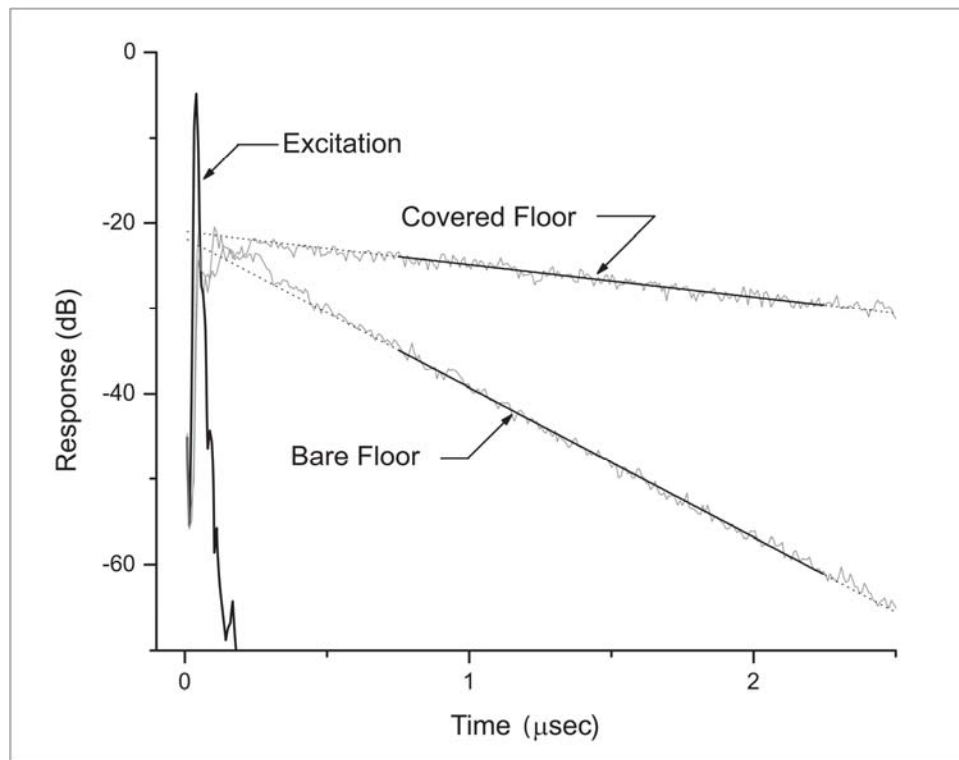


**Figure 5–6. Typical Measured Decay Responses with Bare and Conductive Cloth-Covered Floor**

<sup>69</sup> During bare-floor measurements, observing Fabry-Perot modes was possible with certain antenna orientations. These modes were more difficult to observe during covered-floor measurements, where the  $Q$  was higher.

For the bare-floor case, the 1/e time was approximately 200 nsec and was nearly independent of frequency. Covering the floor with conductive cloth increased the 1/e time to approximately 1  $\mu$ sec. This increased the reverberation index of the building from about 5 bounces per 1/e time to more than 25.

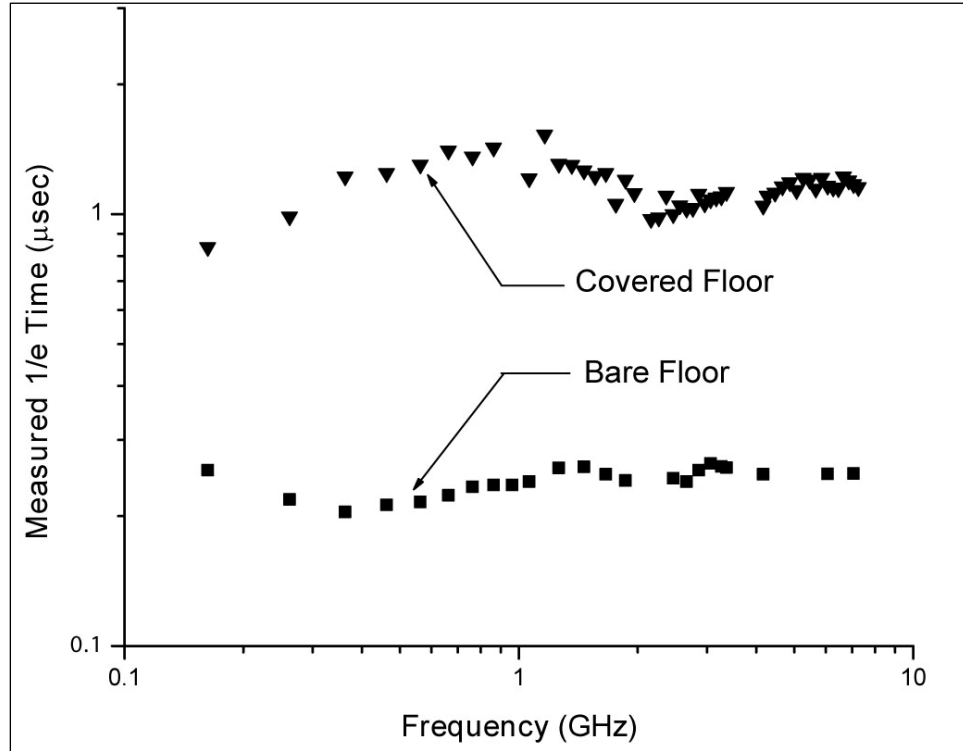


**Figure 5-7. Variation of Building 1/e Time with Bare and Cloth-Covered Floor**

Examining the concrete floor loss result *quantitatively* is instructive: First, it illustrates how to apply some of the theoretical results discussed in numerous sections; second, the final result specifically exposes issues related to performing reverberation chamber-type measurements in a poorly reverberant space.

### 5.3.1 Concrete Floor Reflectivity Calculation from Perturbation Experiment

Following Hill and others, the reverberant field loss coefficient  $\Lambda$  for a partially reflective surface in a chamber wall can be expressed as Equation (5-1):

$$\Lambda = \frac{1}{2} \cdot c \cdot \Sigma \cdot (1 - \bar{R}) \quad (5-1)$$

where

$\Sigma$  is the capture area of the surface.

$\bar{R}$  is the average power reflectivity of the surface in an isotropic field.

For further discussion of leakage through an aperture, see Appendix C.

For a surface that is large compared with wavelength,  $\Sigma$  is equal to half of the geometric area.  $\bar{R}$  is calculated by averaging the magnitude squared of the E field reflection coefficient  $\Gamma$  for both polarizations over  $\theta$  and  $\phi$ . The term  $(1 - \bar{R})$  is the fraction of power that is absorbed by the floor.

The loss rate coefficient from leakage through the floor can be calculated, as given by Equation (5-2), in terms of the difference in loss rate coefficients in a perturbation experiment with the floor bare and covered:

$$\Delta\Lambda = \frac{1}{2} \cdot c \cdot \Sigma \cdot ((1 - \bar{R}_{Bare}) - (1 - \bar{R}_{Covered})) = \frac{1}{2} \cdot c \cdot \Sigma \cdot (\bar{R}_{Covered} - \bar{R}_{Bare}) \quad (5-2)$$

The cloth has very high reflectivity. Measured sheet resistivity is less than 0.1 ohm/sq; thus, compared with  $\bar{R}_{Bare}$ ,  $\bar{R}_{Covered}$  is essentially unity, and  $\Delta\Lambda$  can be approximated as given in Equation (5-3):

$$\Delta\Lambda \cong \frac{1}{4} \cdot c \cdot S_{FC} \cdot (1 - \bar{R}_{Conc}) \quad (5-3)$$

where

$S_{FC}$  is the corrected floor area described above.

$\bar{R}_{Conc}$  is the averaged reflectivity of a concrete-dielectric half space illuminated by an isotropic field with equal energy in each polarization.

From the measurement results,  $\Delta\Lambda = V \times (\Delta 1/\tau)$  with  $\tau = 1 \mu\text{sec}$  and 200 nsec.

These results yield  $\bar{R}_{Conc} = 0.264$ . Other calculations, however, show that the reflectivity of concrete is likely to be lower than 0.264, suggesting that this perturbation measurement value is in error. This should not be surprising because, for the bare floor case, the reverberation index is only 5. Viewed another way, decreasing the reflectivity of the floor to a value of approximately 0.26 is a very large perturbation on an otherwise isotropic reverberant field.

### 5.3.2 Theoretical Estimate of Floor Reflectivity

One can get a rough estimate of the reflectivity  $\bar{R}_{Conc}$  of the concrete floor that the perturbation measurement should yield by calculating the average reflection coefficient from a single air-dielectric interface. The concrete floor in the ERG building is a slab with a thickness of approximately 7 inches that lies on a bed of stone and soil. The metal reinforcement bar grid is 16 inches on center and lies 2 inches below the surface. The grid could increase the reflectivity and may, in fact, be responsible for the slight increase

in  $\tau$  observable at the low-frequency end of the bare floor data in Figure 5–7. The overall effect of the grid is expected to be minimal, however, since the 16-inch spacing is so much greater than the wavelength over most of the measurement frequency range. The default value for earth is sometimes taken as 13, while engineering handbook values for  $\epsilon$  for concrete range between 3 and 10.<sup>70</sup> Thus, reflection from the concrete-earth interface on the bottom of the slab is generally no greater than that from the air-concrete interface at the top of the slab.

The average power reflection coefficient  $\bar{R}_{Conc}$  at the air-concrete interface is calculated as follows:

- Step 1. Calculate the E field reflection coefficients ( $\Gamma$ ) for vertical and horizontal polarization. In textbooks, these cases are referred to as E field parallel and E field perpendicular to the plane of incidence.<sup>71</sup>
- Step 2. Average the squared values of the coefficients over  $2\pi$  steradians since the reverberant field is assumed to be isotropic.
- Step 3. Calculate the average reflectivity as the sum of the averaged reflectivities for the parallel and perpendicular cases, divided by 2, since equal energy is assumed to exist in each field polarization.

For realistic dielectric constants, the reflectivity  $\bar{R}$  of the air-concrete interface calculated in this manner should be significantly lower than 0.264. Either the reflection from the reinforcement bar grid is significant, or the perturbation measurement result is erroneous, indicating that the field in the building at a reverberation index of 5 is significantly nonisotropic.

For  $\epsilon = 8 - j2$ , which is near the upper range of concrete-dielectric values,  $\bar{R}$  calculated in the manner referred to above is 0.2282. As a quick calculation check, one can determine that for normal incidence,  $\Gamma^2$  is 0.2372 at  $\epsilon = 8 - j2$ .

Depending on loss tangent assumptions, an  $\epsilon$  value of 16 to 18 is required to yield  $\bar{R} = 0.264$ . The concrete had been curing for over one month at the time of the measurement, so it was unlikely to contain a large amount of water, and the required value of 16 to 18 is unrealistically high. Even the value  $8 - j2$  is large, given the one-month cure time, so the calculated value of 0.2282 is probably higher than the true value. A realistic value for the concrete-dielectric constant is likely to be approximately 4. For  $\epsilon = 4 - j0.5$ ,  $\bar{R} = 0.188$ .

<sup>70</sup> For example, the Numerical Electromagnetic Code (NEC) method of moments (MOM) fields calculation program, uses default values  $\epsilon = 13$  and  $\sigma = 0.005$  mho/m. Above a few hundred MHz,  $\epsilon$  is the dominant parameter. Earth, which is a conductor at low frequencies, is dielectric at higher frequencies.

<sup>71</sup> The plane of incidence is the plane that contains the  $k$  vector of the incident field and a line normal to the floor surface.

### 5.3.3 Preferred Technique for Reverberation Measurement

The perturbation measurements reported here were performed for two cases: (1) The floor was completely bare except for a small sunken area, and (2) the floor was completely covered except for a small walk-around instrumentation area. A better way to have performed the experiment would have been to take additional intermediate measurement cases with various percentages of the floor covered. For example, starting with the completely covered case, 100 m<sup>2</sup> increments of the cloth covering could have been removed to see if  $\Delta 1/\tau$  followed a linear relationship with the percentage of uncovered floor. With only a small portion of the floor uncovered, the reverberation index would still have been high, leading to a measurement situation corresponding more nearly to the “ideal” assumptions about the field. (See Appendix E.)

If the experiment had been done in this way, the initial perturbations would have been likely to lead to greater changes in  $1/\tau$ . In response, a gradual trend of diminishing returns, or sublinear behavior, would have resulted as the percentage of uncovered floor increased and the reverberation index decreased. A plot of  $\Delta 1/\tau$  versus the percentage of uncovered floor would be sublinear.

## 5.4 OTHER LOSSES

By covering the floor with highly conductive material, the massive losses into the concrete are removed from consideration. The remaining losses exist in a high-reflectivity environment (i.e., registering ~ 25 bounces), where the field should approach the more ideal isotropic case.

Significant losses in addition to the simple  $J_s^2 \times R_s$  losses in the walls, ceiling, and covered floor remain. With values for  $S$  and  $V$  substituted from Table 5-1 and  $\tau = 1 \mu\text{sec}$ , application of Equation (5-4) yields a value of  $R_s = 2.8 \text{ ohm/sq}$ :

$$1/\tau = \frac{4}{3} \cdot \frac{1}{\mu_0 V} \cdot R_s \cdot S \quad (5-4)$$

For further discussion about perturbation measurements, refer to Section 3.4 and Appendix E.

$R_s$  calculated in this way is an *effective* averaged surface resistivity that includes all losses. It is much higher than the surface resistivity of the conductive floor covering or the aluminized face of the insulation on the walls and ceiling, which is less than 0.1 ohm/sq.<sup>72</sup> The existence of higher-than-expected losses, based on textbook or even

<sup>72</sup> An  $R_s$  measurement could not be obtained nondestructively from the building's insulating material, but cavity perturbation measurements, as described in Section 3.4, verified low-surface resistivity of similar material often used on heating ducts. Further, a quick qualitative continuity check with an ohmmeter indicated resistance values of 0.0 or 0.1 ohm between widely spaced measurement points on the building's inner aluminized surface.

measured values, is quite common in these kinds of measurement situations.

Equation (5-5) gives a relationship for the loss rate coefficients in the building:

$$\Lambda = \frac{V}{\tau} = \Lambda_{\text{Wall}} + \Lambda_{\text{Floor}} + \Lambda_{\text{Doors}} + \cdots \Lambda_{\text{innum}} \quad (5-5)$$

The total loss is measured with the 1/e time determination. Ideally, one should be able to specifically identify, model, and estimate values for each of these coefficients, such that all of the coefficients added together equal the combined  $V/\tau$  value. With each loss term verified in this way, developing highly accurate scaling relationships is straightforward. The scaling could be applied for estimating the properties of a new similarly constructed but differently sized building. With each loss term identified, one could make detailed decisions regarding individual construction features.

#### **5.4.1 Wall, Floor, and Ceiling Losses**

In principle, Equation (5-5) can be used to calculate losses in the building, and it can be applied with the following values from Table 5-1:

$$R_s = 0.1 \text{ ohm/sq}$$

$$S = 2.08 \times 10^3 \text{ m}^2$$

$$V = 6.22 \times 10^3 \text{ m}^3$$

This yields a 1/e time of approximately 25  $\mu\text{sec}$  for a combined loss coefficient as expressed in Equation (5-6):

$$\Lambda_{\text{Wall, Floor, Ceiling}} = 2.5 \times 10^8 \text{ m}^3/\text{sec} \quad (5-6)$$

Actual losses were much higher.

#### **5.4.2 Nonconductive Overlap in Wall Insulation**

A small leakage path occurs between the 4-ft-wide insulation blankets. As pictured in Figure 5-8, a roughly 4-inch-wide lip at the edge of each blanket covers the adjoining blanket, but the lip is nonconductive where it touches its neighbor and, thus, allows leakage. This nonconductive overlap joint can be modeled as a parallel-plate transmission line to estimate the leakage through such a path. The length of the line is about 4 inches and the width of the line is up to 40 ft.



**Figure 5–8. Noncontacting Overlap Between Insulation Sheets**

Equation (5–7) gives the characteristic impedance of a wide, closely spaced, parallel-plate transmission line:

$$Z_{0TEM} = \frac{Z_0}{\sqrt{\epsilon}} \cdot \frac{t}{w} \quad (5-7)$$

where

$w$  is the width of the parallel plates.

$t$  is the spacing.

$\epsilon$  is the relative dielectric constant of material between the plates.

For this case, the spacing is variable due to the construction, but it is estimated at 0.01 inch due to the texturized surface. The dielectric is part air and part paper and asphalt. By taking the input impedance of this parallel-plate transmission line as the characteristic impedance, one can calculate the input power  $P$  per unit length (1 meter) of overlap, as expressed in Equation (5–8):

$$P \cong \frac{1}{2} \cdot J_s^2 \cdot Z_{0TEM} \cdot 1(\text{meter}) \text{ (W/m)} \quad (5-8)$$

where

$J_s$  is the wall surface current due to fields inside the chamber.

The factor  $\frac{1}{2}$  is a polarization loss correction because the currents are omnidirectional on the surface.

Equation (5–9) expresses the  $Q$  of a chamber with wall losses given by this parallel-plate leakage model:

$$Q = \omega\tau = \frac{\omega W}{P_{Loss}} = \frac{\omega\mu_0 H_V^2 V}{\frac{1}{2} \cdot J_S^2 Z_{0TEM} L} \quad (5-9)$$

where

$L$  is the length of the overlap joint; however, this is actually the *width* of the transmission line.

Equation (5–10) gives the following relationships between fields and surface currents within the volume and at the walls:

$$J_S^2 = H_S^2 \text{ and } H_S^2 = \frac{4}{3} H_V^2 \quad (5-10)$$

Applying Equation (5–9), Equation (5–11) can be written as follows:

$$\tau = \frac{\mu_0 V}{\frac{2}{3} Z_{0TEM} 600} \quad (5-11)$$

where

the joint overlap length is assumed at approximately 600 m over the entire building walls and ceiling.

Evaluation of this equation yields a value for  $\tau$  of  $2 \times 10^{-4}$  sec, which is much greater than the 1  $\mu$ sec value observed with the conductive floor covering. Thus, calculation of  $\Lambda$  as  $V/\tau$  suggests that loss through the insulation overlap joint is apparently only about 0.5 percent of the total loss in the building with the conductive floor.

If this kind of aluminized fiberglass material and construction were to be used as the inner wall for a reverberation chamber, the proper assembly procedure would be to cover the insulation overlap joint with conductive tape that is frequently used in EMC operations. However, taping the joint is unlikely to reduce losses significantly, since the joint apparently contributes such a small fraction of the total loss.

With the cloth covering over the concrete floor in the perturbation experiment, a similar overlap joint existed between adjacent conductive cloth strips. The overlap at this joint was typically 3 inches. The cloth was conductive on both sides. Thus, the transmission line path for leakage is significantly “shorted” and should be less lossy than the insulation joint.

The transmission line model is a rough approximation to the leakage mechanism. Since the line is significantly wider than wavelength, propagation is not necessarily transverse electromagnetic (TEM) at all, but more like a transverse electric (TE) waveguide mode.



Use of the characteristic impedance of the line as its input impedance is justified for an order of magnitude argument. Voltage Standing Wave Ratio (VSWR) of an open-ended waveguide is less than 2:1.

### **5.4.3 Loss Through Overhead Doors**

When door leakage was measured in Section 4.2.3, it was done from outside to inside using a single, normally incident planewave. The door is basically a reciprocal structure, and leakage should be the same in both directions. One has only to account for the different interaction properties of the isotropic field compared with those of a single, normally incident planewave. This is described in Appendix C and also briefly in Section 3.5.2.1.

The door leakage has not been modeled in detail. The measured leakage area has simply been referred to the door area. In fact, much, if not all, of the leakage may occur at the door perimeter. Two different leakage models are presented here: (1) a semitransparent door model, which yields a lower estimate, and (2) a “leaky gap” model, which yields a slightly higher estimate. Both models consider only loss due to leakage either through or around the door. Neither model includes ohmic losses within the door structure. These losses may be significant.

### **5.4.4 Semitransparent Door**

Measurements in Building 1427 showed that effective leakage area through the overhead roll-up doors was typically about 15 dB down from the door geometric area. The ERG building has approximately 104 m<sup>2</sup> of door area. Following Hill’s aperture leakage model and subtracting 15 dB, Equation (5–12) estimates the loss coefficient  $\Lambda_{\text{door}}$  due to leakage through the door as if it were semitransparent:

$$\Lambda_{\text{door}} = \frac{1}{4} \cdot c \cdot A_{\text{door}} - 15 \text{ dB} \approx 2.5 \times 10^8 \text{ m}^3/\text{sec} \quad (5-12)$$

As described in Appendix C, the factor  $\frac{1}{4}$  in Equation (5–12) relates the efficiency of isotropic power density at leaking through an aperture to that of a single, normally incident beam. The leakage mechanism envisioned here is similar to that for the open-door leakage data presented in Figures 4–16 and 4–17 except that the door, which is actually closed, reflects most of the incident reverberant energy and transmits a small portion of it. The data of Figure 4-16 show that the leakage area is approximately 15 dB below the geometric area.

### **5.4.5 Leaky Gap Model**

Essentially nonexistent electrical contact occurs at the door perimeter where it joins the walls and the floor. Assuming that leakage at the door perimeter is driven by wall surface currents in the door and building walls, rather than directly by isotropic power

density, the factor  $\frac{1}{4}$  in Equation (5–12) must be replaced by a slightly different coefficient relating wall surface currents.

From Equation (5–10) wall surface current squared is equal to  $\frac{4}{3}$  times the squared H field component of the isotropic power density. For a more detailed discussion, see Appendix G.

When a single beam is normally incident on a highly conductive surface, a reflected wave is created such that the tangential E field at the surface is zero, and the H field at the surface is twice the incident H field. A surface current is induced in this process and is equal in magnitude to twice the incident H field. Thus, the surface current squared,  $J_s^2$ , is equal to four times the incident H field squared for a single, normally incident beam. The ratio of wall surface current squared for the isotropic field, compared to that for the single, normally incident beam, is  $\frac{4}{3}$  divided by 4 or  $\frac{1}{3}$ .<sup>73</sup>

Assuming that the doors in the ERG building have a perimeter-to-area ratio similar to those in Building 1427, the factor  $\frac{1}{4}$  in Equation (5–12) is replaced by a factor  $\frac{1}{3}$ . Thus, the two models yield estimates that differ by only 1.25 dB.

#### 5.4.6 Loss from Exposed Steel

Figures 5–2 through 5–4 show a great amount of exposed steel framework inside the building. This includes the building's skeletal structure and the mild steel shades on the electric lighting suspended from the ceiling. The estimate is approximately 780 m<sup>2</sup> of exposed steel in the building. Using Equation (5–4) and assuming that  $R_s$  for the steel is 0.4 ohm/sq, Equation (5–13) estimates the loss due to the exposed steel as follows:

$$\Lambda_{\text{Steel}} = \frac{4}{3} \frac{R_s S}{\mu_0} = 3.45 \times 10^8 \text{ (m}^3/\text{sec)} \quad (5-13)$$

This calculation does not include losses from possible lossy joints between the steel and aluminized facing on the insulation.

---

<sup>73</sup> This argument can be carried further by considering polarization effects. The isotropic-field-induced surface currents are omnidirectional on the surface, and their interaction with a single slit is reduced by a factor of 2 due to polarization, as described in Section 5.4.2. The surface current from a single planewave is unidirectional in the surface, but effectively would excite half of the total perimeter; thus, polarization effects for the two kinds of currents cancel out.

#### 5.4.7 Loss from Bare Floor Walk-Around Test Area

By neglecting the instrumentation table and other items on the bare concrete test area, Equation (5–14), using Equation (5–1), estimates the loss coefficient for the 20 m<sup>2</sup> walk-around area, assuming 20 percent reflectivity:

$$\Lambda_{BF} = \frac{1}{2} c \frac{1}{2} A_{geo} (1 - \bar{R}) = 1.2 \times 10^9 \text{ (m}^3/\text{sec)} \quad (5-14)$$

#### 5.4.8 Innumerable Losses and Loss Audit

Using approximate models and measurement results, one can estimate loss coefficients from several different mechanisms. However, as shown in Table 5–2, this approach can only account for about 10 to 20 percent of the losses which remain after covering the floor.

**Table 5–2. Audit of Losses in ERG Building with Covered Floor**

Loss Mechanism	Calculation	Value (m <sup>3</sup> /sec)	Comments
Walls, Ceiling, and Floor Total	Equation (5–6)	2.1 × 10 <sup>8</sup> 4.8 × 10 <sup>7</sup> 2.58 × 10 <sup>8</sup>	Calculated assuming $R_s = 0.1 \text{ } \Omega/\text{sq.}$
Wall Covering Overlap	Equation (5–11)	3.1 × 10 <sup>7</sup>	This is equal to 0.5 percent of measured total.
Overhead Doors	Equation (5–12)	2.5 × 10 <sup>8</sup>	This is calculated from door leakage only; losses in the door are unaccounted.
Steel Structure	Equation (5–13)	3.45 × 10 <sup>8</sup>	Loss occurs from the exposed steel in the walls and ceiling; no losses are attributed to the leaky joints.
Bare Floor under Instrumentation	Equation (5–14)	1.2 × 10 <sup>9</sup>	—
Innumerable Losses	—	—	<ul style="list-style-type: none"> <li>• Intersection between the floor perimeter and the walls</li> <li>• Lossy joint intersection of steel framework and aluminized facing on insulation</li> <li>• Unidentified mechanisms</li> </ul>
Loss Summary (not including innumerable)	—	2.08 × 10 <sup>9</sup>	Shortfall: The sum of individually modeled losses is significantly less than the measured total.
Measured Total	$V/\tau$	6.22 × 10 <sup>9</sup>	$\tau = 1 \text{ } \mu\text{sec}$ with covered floor.

Roughness and poor (lossy) contacts between the painted steel framework and aluminum facing on the wall and ceiling insulation add some additional loss, which is not accounted for by simply adding the steel loss based on its exposed area. However, explaining how these effects in the walls and ceiling can account for the large deficit in the audit is difficult.

One source of loss has not been modeled: leakage at the joint between the floor perimeter and the wall. In general, poor electrical connectivity occurred between the

conductive cloth floor covering and wall. This resulted in a possibly significant, but poorly specified, leakage aperture. By covering the floor with highly conductive cloth, the large leaky surface area was removed from consideration. On the other hand, an additional, much smaller loss mechanism, i.e., a leakage aperture around the floor perimeter, was added. The author was unable to properly specify the required parameters for evaluating the loss around the floor perimeter. However, it is difficult to see how the perimeter loss mechanism could account for all of the remaining losses that have not yet been identified.

Examination of Figures 5–2 and 5–4 show that the ceiling is cluttered with hanging light fixtures. The loss mechanism due to features such as the light fixtures involves increased scattering and possibly a smaller effective value for  $T_C$  that is normally calculated only for wall-scattering. A quantitative understanding of this mechanism is an important theoretical and measurement research goal. For example, it would assist chamber design engineers in accounting for losses in chamber paddle wheels. The time-domain-based technique with its inherent ability to measure losses precisely would be an ideal measurement approach.

The light fixtures and the skeletal steel in the walls and ceiling probably improve the isotropic nature of the field, since these features make the scattering less specular. Acoustic engineers have shown that a diffuse surface forms a reverberant field more effectively than a specular surface. The author suspects, however, that these features may add significantly to the loss. The loss due to these features may be much greater than that calculated simply by determining their exposed resistive area.

The large, innumerable, and unaccounted losses limit one's ability to assign a precise  $R_S$  value to the walls. In turn, this adds uncertainty to the  $1/e$  time (i.e., a calibration-factor estimate) in scaling calculations. EMC engineers can still make some useful estimates of prototype building characteristics, however, using effective values for resistivity, such as the 2.8 ohm/sq value that was derived from Equation (5–4).

## 5.5 SCALING CALCULATIONS FOR NEW CHAMBER DESIGN

Aside from cost, building size would be determined from trade-off studies and desired characteristics. Larger buildings would have a lower minimum operating frequency and could contain larger test items, assuming that a suitable door was part of the design. Bigger is better in this sense. However, for a given reverberation index, which has a maximum value set by construction details, larger buildings require greater transmitter power for a given test environment level. They would also have a longer  $1/e$  time, which may be critical if short-pulse-response testing is required as part of test item evaluation. If only shielding or leakage testing is required, response time is not critical. In general, the greater insertion loss inherent in a larger building is unlikely to be critical in shielding or leakage measurement, since receiving equipment can be made quite sensitive.

The ERG building represents a nearly ideal construction approach for building a large reverberation chamber facility required for testing large items. The reverberation index

would be on the order of 20 to 25. The loss measurement results described in the report allow an EMC engineer to estimate the properties of such a facility, if it were to be built using ERG building construction technique. Several calculations would show how properties vary with size or other features and would form a basis for trade-off analysis. Based on cost and desired operating characteristics, building dimensions can then be specified.

Figure 5–9 and the following text illustrate the calculation procedure for a hypothetical building. A basic assumption is that the building will be built using construction techniques similar to those of the ERG building for the walls and ceiling. Further, the building should have a steel floor with proper bonding at the wall perimeter to reduce the massive losses resulting from an ordinary concrete floor. Table 5–3 lists physical features of the building, and Table 5–4 lists assumed surface resistivity values for the walls and steel floor. The proposed building is assumed to have a 3:12 roof pitch and a typical 12-ft-by-18-ft overhead door.

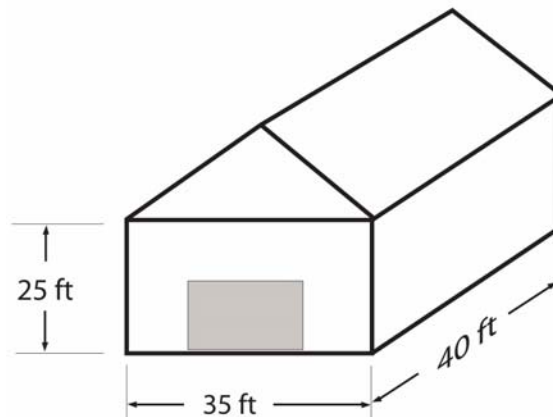


**Figure 5–9. Prototype Building: Sample Demonstrating Scaling Calculations**

**Table 5–3. Prototype Building: Physical Constants**

Parameter	Value
Wall and Ceiling Area	496.21 (m <sup>2</sup> )
Floor Area	130.13 (m <sup>2</sup> )
Volume	1.078 × 10 <sup>3</sup> (m <sup>3</sup> )
Wall-Scattering Time ( $T_C = 4V/S c$ )	22.95 (nsec)
Note: The prototype building measures 25 ft by 35 ft by 40 ft.	

**Table 5–4. Prototype Building: Inner Surface Resistivity**

Region	Value $R_s$ (ohm/sq)	Comments
Wall and Ceiling	2.61	Maximum upper-limit value
	1.0	More likely value
Steel Floor	1.0	Approximate effective value in large NSWCDD chamber

### 5.5.1 Characteristic Wall-Scattering Time

Equation (5–15) yields the characteristic wall-scattering time:

$$T_c = \frac{4V}{S_c} \quad (5-15)$$

The characteristic wall-scattering time is calculated as 22.95 nsec. (Refer to Table 5–3.)

### 5.5.2 1/e Time Estimate

The 1/e time for the building is calculated by applying Equation (5–5) for various features of the building whose losses can be identified.

#### 5.5.2.1 Wall and Floor Losses

Equation (5–16) uses parameters from Tables 5–3 and 5–4:

$$\frac{1}{\tau} = \frac{4}{3} \cdot \frac{1}{\mu_0 V} \cdot \Sigma S \cdot R_s \quad (5-16)$$

This yields  $\tau = 712$  nsec for 2.6 ohm/sq and 1.622  $\mu$ sec for 1.0 ohm/sq in the walls and ceiling. This value is uncertain because of the “wild card” nature of the apparent wall surface resistivity in the measurements described previously in Sections 5.4.1 through 5.4.8. In principle, one expects that the wall surface would be highly reflective because of the low value (i.e., less than 0.1 ohm/sq) of surface resistivity for the aluminized facing on the insulation. Unless an additional wall covering surface is anticipated, the use of aluminum-flashed-paper fiberglass insulation, rather than plastic- or paper-covered fiberglass insulation, is a significant specification for the building construction.

A highly reflective surface appropriate for reverberation chamber purposes could be realized from almost standard construction materials and practice. However, failure to properly identify and model all of the apparent losses makes it impossible to verify this important conclusion at the present time. More measurements are required.

The reflectivity of the aluminized surface with a skeletal-steel framework should be high. In any case, if vinyl or another nonconductive facing were used on the insulation, then the major wall reflection would occur from the inner surface of the mild-steel, external facing on the building. The steel would surely be more lossy and leaky. As a result, the building would be lossier and would have lower SE.

Considerable confidence exists in the 1 ohm/sq value for the steel floor. The true value is unlikely to be higher than this. This value is consistent with the effective value of the surface resistivity in the large NSWCDD chamber. It is approximately a factor 2 to 3 times higher than the perturbation measurement results for mild steel discussed in Section 3.4.2.

Additionally, the construction technique used for the building must guarantee a good RF seal at the wall and floor intersection around the floor perimeter.

A large facility dictates a large door. If overly high shielding requirements are placed on the door, its cost may become significant. If a standard overhead door is used, precautions can be taken to minimize leakage around the perimeter. In any case, the door and a paddle wheel tuner, if one is used, would contribute additional losses, slightly decreasing the 1/e time. Depending on various security-related and other issues that may dictate a high shielding effectiveness for the building, one may or may not find it necessary to use a special purpose shielded door.

#### 5.5.2.2 Overhead Door and Other Losses

Applying Equation (5-12) to a 12-foot-by-18-foot overhead door yields an estimated additional loss of  $4.76 \times 10^7 \text{ m}^3/\text{sec}$ , which would reduce a 712-nsec time constant to about 690 nsec.

Adding a large paddle wheel tuner would further reduce the 1/e time slightly. At 600 nsec/23.2 nsec, the reverberation index is 25, which should allow generation of a reasonably good isotropic field.

#### 5.5.3 Low-Frequency Operating Range Estimate

The TE<sub>101</sub> mode frequency for a 35-ft-by-45-ft rectangular chamber is 17.81 MHz. The perturbation effect of the raised ceiling is expected to increase this minimum frequency slightly. As a rule of thumb, chambers generally begin operating in a highly degraded, but possibly useful fashion, at about 3 times the first mode frequency. Thus, a minimum usable frequency of approximately 60 MHz can be estimated.

Chamber operations research has shown that a mode overlap factor or number of modes in a given  $Q$  bandwidth of approximately 4 is required for high confidence chamber operation.<sup>74</sup>

As discussed in Section 3.4.3.2, the mode overlap factor  $A$  is given by Equation (5–17):

$$A = \frac{dN}{dF} \cdot \Delta F = \frac{4 V F^2}{c^3 \tau} \quad (5-17)$$

$A$  has a value of 4 at 122 MHz for  $\tau = 600$  nsec.

As a rule of thumb, chamber designers avoid rectangular chamber dimensions that are integer multiples of each other to avoid unfavorable mode density fluctuations resulting from degenerate modes. The raised-ceiling design of the building perturbs some mode frequencies, as calculated with a rectangular design model, more than others and changes this picture somewhat. Further, use of a large paddle wheel tuner or the presence of a large test item would cause additional mode frequency changes.

Serious consideration of a building design, where lower frequency operation was an important factor, would benefit from an *eigen*-mode analysis, which is available in GEMACS.<sup>75</sup> One could also include the probable effect of walling off a separate instrumentation or anteroom area using conductive materials.

#### 5.5.4 Chamber Calibration Factor (CF) and Loading Effects

The *average* calibration factor (CF) for the building is given by Equation (5–18):

$$CF = \frac{c\tau}{V} = 0.1669 \text{ W/m}^2/\text{W} \quad (5-18)$$

With a 600-nsec 1/e time, the equation yields 7.9 volts (V)/m per root W of excitation power. Depending on the number of samples, an additional 5 to 8 dB would be added to the average field value to determine a probable maximum field. With a 600-nsec 1/e time, the large building is lossy when compared with many smaller facilities. The large NSWCDD chamber, for example, with  $\tau = 1$   $\mu$ sec and volume ( $V$ ) = 225 m<sup>3</sup> has a CF of 1.33 W/m<sup>2</sup>/W, which yields 22.3 V/m per root W.

However, the lossier building is less sensitive to loading than a smaller chamber would be. For example, measurements have shown that a typical mid-sized automobile placed within the large NSWCDD chamber loads it by approximately 3 dB. For this case,  $\Lambda_{\text{Auto}} \sim \Lambda_{\text{CH}} = (V/\tau) \sim 2.25 \times 10^8 \text{ m}^3/\text{sec}$ .

<sup>74</sup> “Correlation Coefficients,” IEC, Standard 61000–4–21 (Draft), Annex A: 13–29.

<sup>75</sup> E. L. Coffey and M. A. Coffey, GEMACS (General Electromagnetic Model for the Analysis of Complex Systems) User Manual, Version 7.1, Advanced Electromagnetics Report, AE07P001 (May 2007): n. pag.



The loss coefficient  $\Lambda$  for the building with

$$V = 1.08 \times 10^3 \text{ m}^3 \text{ and } \tau = 600 \text{ nsec}$$

yields

$$1.8 \times 10^9 \text{ m}^3/\text{sec}.$$

The same automobile placed in the building would increase the total loss to approximately  $2.025 \times 10^9$  corresponding to a 0.5-dB reduction in  $CF$ .

However, large items, such as would be tested in the facility under consideration in this report, may be much lossier. For example, consider a hypothetical structure, perhaps part of a ship deckhouse. Further, assume that the structure has  $150 \text{ m}^2$  of surface area and is constructed of graphite fiber cloth with an effective surface resistivity of 7 ohm/sq.

Application of Equation (5-4) indicates that an additional loss coefficient of  $1.1 \times 10^9 \text{ m}^3/\text{sec}$  should be added to the existing loss of  $1.8 \times 10^9 \text{ m}^3/\text{sec}$ .

For  $\tau = 600 \text{ nsec}$ , this would bring the new loaded  $\tau$  down to approximately 470 nsec and cause a corresponding decrease in the  $CF$ . In fact, the new  $\tau$  value would be somewhat less than 470 nsec because the volume of the large test item would subtract from the total available volume in the test space, reducing stored EM energy and  $Q$ .

The new reverberation index of the loaded space would still be about 20, indicating feasibility of generating a reasonably good isotropic environment. Note that the introduction of a large test item reduces the volume and increases the surface area of the space, thereby decreasing the value of  $T_C$ .

The  $CF$  tends to be lower for larger spaces indicating that high transmitter power levels for generating certain EM environments are required for active system testing. If extreme measures are taken to minimize losses and obtain an extremely high  $Q$  space, then additional issues in the environment response time may occur. Larger buildings have longer characteristic scattering time and, thus, a longer  $1/e$  time. A long  $1/e$  time would cause problems when the user is trying to generate short-pulsed EM environments.

## 5.6 SUMMARY: LOSS STUDY AND CHAMBER DESIGN SCALING LAWS

The purpose of this section has been to outline and demonstrate the use of scaling laws for calculating the properties of a prototype reverberation chamber built using PEB construction practices.

By covering the concrete floor with a conductive surface, the massive floor loss was removed, and the building was shown to be moderately reverberant with a reverberation index of about 25. However, losses remaining in the building after the floor loss had been removed from consideration were surprisingly high, and it was not possible to specifically identify the exact source of all the losses. Useful, though less detailed,

prototyping calculations were still possible to perform. An effective loss resistivity factor for the walls and ceiling was formed by combining light fixture and skeletal steel losses.

Several significant construction features for a large chamber using PEB construction techniques are noteworthy:

- a. The standard overhead door used in typical PEB construction is adequate for some purposes. Specification of high-shielding requirements for the building may require different door designs or other engineering that could be a significant cost driver.
- b. The use of aluminum flashing on the facing of the wall and ceiling insulation presents a high reflectivity surface. The resultant aluminum surface increases the building RF shielding and reduces field interaction with the lossier surface of the building's steel skin. The resulting reverberation index of the building is higher.
- c. If a PEB were to be built specifically for use as a reverberation test facility, the most significant departure from typical PEB construction would be substitution of a conductive floor—carefully bonded to the walls—instead of the ubiquitous concrete floor.

Nearly standard PEB construction techniques are ideal for building a large reverberation chamber facility for testing large items. Although the transmitter power requirements for generating high field levels for active system testing might be prohibitive, this type of space would be ideal for SE or leakage studies on large test items such as aircraft or portions of a ship deckhouse.

## 6.0 GENERAL OVERVIEW AND CONCLUSIONS

### 6.1 REVERBERANT PROPAGATION

Reverberant propagation in a space is characterized by the presence of multiple wave components traveling simultaneously in many different directions. When a space is highly reverberant, no dominant or net direction of propagation or polarization occurs. Further, energy density in the space is statistically uniform. When a space is moderately or poorly reverberant, many wave components are still present. However, one or more dominant ray paths may exist, and the energy density in a particular region of the space may be higher or lower than in other regions.

A space may be rated as to how reverberant it is by defining a reverberation index. The index is essentially the number of times an average wavefront in the space strikes the walls during a  $1/e$  energy decay time for the space. For a highly reverberant space, such as a reverberation test chamber, this index is typically between fifty and several hundred. For a typical ship compartment, the index is on the order of 5.

EM energy in a space undergoes several processes:

- a. Energy is scattered from the walls.
- b. Energy is lost ohmically.
- c. Energy leaks into or out of the space.

Additionally, engineers are often concerned with field uniformity within the space.

To understand propagation in a space, an EMC engineer should know how rapidly each of these processes occurs. When a space is highly reverberant, each rate has a unique value, and the wall-scattering rate is much greater than the other rates.

A reverberant field can be created in a space by exciting it with a single wavefront and allowing the wavefront to reflect from the walls. For a highly reverberant space, the initial wavefront undergoes many wall reflections as it expands. The resulting reverberant field consists of many wavefronts. Energy within the space decays exponentially; however, if the space is highly reverberant, the time required for decay is much greater than the initial time required for formation of the field. When this is true, individual reflections and the actual formation phase for the reverberant field can be neglected. Analysis can proceed solely on the reverberant phase. When a space is moderately or poorly reverberant, both phases may be important. Each can be analyzed separately or together.

## 6.2 GENERAL FEATURES OF TIME-DOMAIN (TD) MEASUREMENT AND ANALYSIS

A short-pulse radar is an ideal measurement tool to evaluate propagation in a space. If the space is excited with a short-pulsed wave, the reverberant field formation and subsequent decay can be viewed as a transient response. By changing the excitation or internal geometry of the space and repeating the measurement, an ensemble average of transient responses can be created. In a highly reverberant space, the ensemble-averaged transient response is equivalent to a spatially averaged response. One may note that this is a generalized interpretation of ensemble averages, which are used often in CW measurement procedure. This interpretation is relevant and accurate to the extent that the formation phase of reverberant response can be neglected in comparison with the reverberant decay phase.

By assuming conservation of energy, differential equations may be written for the energy density in a space or in coupled spaces, which could be considered to model a leakage or shielding effectiveness (SE) experiment. The differential equations are coupled first-order equations and are analogous to those written for basic RC circuit behavior. Rate coefficients from the equations describing energy loss and transfer between coupled chambers can be evaluated by overlaying measured responses displayed on a radar A-scope with parameterized differential equation solutions. This kind of analysis is a statistical mechanics procedure. It is conducted on the reverberant field as a whole (i.e., the spatially averaged energy density) rather than on individual reflected waves. It is similar to the use of gas laws that predict temperature and pressure behavior of the gas rather than the position and velocity of individual gas molecules.

If a space is poorly reverberant, propagation features take on characteristics of both reverberant and free-space behavior. Energy density within the space is not statistically uniform. The curve-fitting analysis technique used to evaluate the rate coefficients, which assume that the energy density is uniform, yields less precise answers. Because the propagation is not purely reverberant, the rate coefficients do not apply rigorously. However, the reverberant propagation picture is still a valuable paradigm, useful for designing experiments, organizing measurement results, and checking them for approximate consistency. The highly reverberant propagation paradigm becomes less applicable as the reverberation index for the space(s) is decreased.

Propagation studies in moderately or poorly reverberant spaces, such as ship and aircraft compartments, are likely to become more important in the future. By displaying measured responses on an A-scope, the EMC engineer can determine immediately the general features of propagation in a space and can see immediately how closely propagation approaches the high reverberation paradigm. Whatever the reverberation index, an engineer can perform insertion loss (IL) and field uniformity measurements by using appropriate antennas and locating them appropriately.

Even in a moderately or poorly reverberant space, measurements performed in this manner are fundamentally meaningful and correct. Measurement results do not exactly fit the high reverberation paradigm because, as the reverberation index decreases, the

fields within the space are not purely reverberant but show emergent characteristics of free-space propagation. IL measurement within a space may be specifically conducted to study a particular propagation path or to find regions of high- or low-field intensity. With radar-based measurement, the engineer has more freedom to place antennas in favorable locations than with CW measurement, because it is not necessary to prevent contamination of a reverberant-response measurement with unwanted direct response. Direct and reverberant propagation-response features may be distinguished, and unwanted portions may be discarded.

An EMC engineer is likely to perform most measurements in the context of answering questions about a steady-state CW environment. Radar-based transient-response results and CW measurement results are directly comparable. TD measurement provides information that is not directly available with steady-state CW technique. This information is frequently useful for verifying or explaining measurement results that may have been obtained with CW technique and, for some reason, are puzzling or suspect.

### 6.3 KEY FEATURES AND APPLICATION OF TD MEASUREMENT

Radar-based measurement has several of the following key features:

- a. Time-tagging feature of the A-scope display: The time-tagging feature allows the EMC engineer to distinguish between direct free-space components and reverberant components of a measured response. This allows the engineer much greater flexibility in placement of antennas and interpretation of results.
- b. Remarkable precision in measurement of response decay slope: Decay-slope measurement allows the engineer to determine loss rate of a space. With the loss rate determined solely by a response decay slope, moderate calibration errors of attenuators or directional couplers do not cause measurement error. With the decay slope technique, power or power density measurement is “traded” for a time-interval measurement. Time interval can be measured with great precision. On the scale of precision usually available with common microwave measurement, time interval is essentially absolute. Thus, TD measurements allow an independent, high-precision calibration check for steady-state CW measurement results and for calibration of hardware.

Further, the high precision inherent in the response decay slope determination allows the engineer to perform a variety of measurements that would be much more difficult to perform with CW technique. Antenna efficiency studies and most perturbation measurements require extreme precision in IL determination.

- c. Richness of available information in the A-scope display: Visualization of the reverberation response on the A-scope display immediately allows the engineer an intuitive feel for propagation in a space. Further, information in the display allows an internal self-consistency check of results.

EMC engineers frequently are tasked to perform measurements during a limited available time interval and with a limited budget. A measurement approach that allows a quick consistency check is particularly valuable in this environment since replicating the experiment at a later date may not be possible. The time-domain approach allows just such a check for IL measurement, perhaps the most ubiquitous of all the measurements that an EMC engineer makes.

As a ratio of measured power or energy, IL is subject to numerous calibration errors in test equipment. However, analytical results show that IL is determined by test-space volume, measurement frequency, and the  $1/e$  decay time. Time-domain, decay-slope measurement technique provides a near-absolute determination of  $1/e$  time. This, together with simple knowledge of the test-space volume, provides the EMC engineer with an immediate consistency check on the single-most important measurement he or she is likely to make.

## 7.0 REFERENCES

- Bartel, Thomas W. and Simone L. Yaniv. “Curvature of Sound Decays in Partially Reverberant Rooms.” *Journal of the Acoustical Society of America*, vol. 72, no. 6 (December 1982): n. pag.
- Coffey, E. L. and M. A. Coffey. *General Electromagnetic Model for the Analysis of Complex Systems (GEMACS) User Manual, Version 7.1*, Advanced Electromagnetics Report, AE07P001 (May 2007): n. pag.
- Corbett, B. L., R. E. Richardson, and T. H. Lehman. “Statistical Characterization of Reverberant Chamber Transient Response Using Common CW-Analysis Tools and Methods.” Zurich, Switzerland: Topical Meeting on Reverberation Chambers, 13–18 February 2005. EMC Zurich, [www.emczurich.ch](http://www.emczurich.ch).
- “Correlation Coefficients.” *International Electrotechnical Commission (IEC)*, Standard 61000–4–21 (Draft), Annex A.
- Dunens, E. K. and R. F. Lambert. “Impulsive Sound Response Statistics in a Reverberant Enclosure.” *Journal of the Acoustical Society of America*, vol. 6, no. 6 (June 1977): 1524–1532.
- Hatfield, M. O. *In Situ Shielding Effectiveness Measurements of a Transport Aircraft*. NSWCDD/TR–03/107.
- Hill, David A. “Section 3.3: “Probability Density Functions,” *Electromagnetic Theory of Reverberation Chambers*, National Institute of Standards and Technology (NIST) Technical Note 1506 (December 1998): 17–21.
- Hill, David A., Mark T. Ma, Arthur Ondrejka, Bill F. Riddle, Myron T. Crawford, and Robert T. Johnk. “Aperture Excitation of Electrically Large Lossy Cavities.” *IEEE Transactions on Electromagnetic Compatibility*, vol. 35, no. 3 (August 1994): 169–177.
- Holloway, Christopher L., David A. Hill, John Ladbury, Galen Koepke, and R. Garzia. “Shielding Effectiveness Measurements of Materials Using Nested Reverberation Chambers.” *IEEE Transactions on Electromagnetic Compatibility*, vol. 45, no. 2 (May 2003): n. pag.
- Holloway, Christopher L., Michael G. Cotton, and Paul McKenna. “A Model for Predicting the Power Delay Profile Characteristics Inside a Room.” *IEEE Transactions on Vehicular Technology*, vol. 48, no. 4 (July 1999): 110–120.

- Hunt, F. V. "Remarks on the Mean Free Path Problem." *Journal of the Acoustical Society of America*, vol. 36, no. 3 (March 1964): 536–534.
- Kosten, C. W. "The Mean Free Path in Room Acoustics." *Acoustica*, vol. 10 (1960): 245.
- Ladbury, John M., Robert T. Johnk, and Arthur Ondrejka. "Rapid Evaluation of Mode-Stirred Chambers Using Impulsive Waveforms." NIST Technical Note 1381 (June 1996): n. pag.
- Lamb, Jr, Willis E. "Theory of a Microwave Spectroscope." *Physical Review*, vol. 70, no. 5 (1 September 1946) and no. 6 (15 September 1946): 308–217 (printed as one article).
- Lehman, Theodore H. "A Statistical Theory of Electromagnetic Fields in Complex Cavities." U.S. Air Force, Phillips Laboratory Interaction, Note 494 (May 1993): n. pag.
- Radio Frequency Radiation Dosimetry Handbook (Fourth Edition)*. U.S. Air Force, School of Aerospace Medicine, Aerospace Medical Division (AFSC), Brooks Air Force Base, Texas 78235–5301.  
<<http://www.brooks.af.mil/AFRL/HED/hedr/reports/handbook/>>, s.v. "Muscle Tissue."
- Richardson, Robert E. "Mode-Stirred Chamber Calibration Factor, Relaxation Time and Scaling Laws." *IEEE Transactions on Instrumentation Measurement*, vol. IM-34 (December 1985): 573–580.
- Turner, R. F. B., W. A. G. Voss, W. R. Tinga, and H. P. Baltes. "Eigenfrequency Distributions in Multimode Cavities." *IEE Proceedings*, vol. 132, Part H, no. 2 (April 1985): 82–88.
- Young, Robert W. "Sabine Reverberation Equation and Sound Power Calculations." *Journal of the Acoustical Society of America*, vol. 31, no. 7 (July 1959): 912.



**APPENDIX A**  
**RADAR-BASED INSTRUMENTATION**

This page is intentionally blank.

## CONTENTS

<u>Appendix</u>	<u>Page</u>
<b>A RADAR-BASED INSTRUMENTATION</b>	
A.1 Introduction.....	A-1
A.2 Direct Time-Domain (TD Instrumentation.....	A-1
A.3 Synthetic TD Measurement and Systems .....	A-3
A.4 Vector Network Analyzer (VNA) Operation and Typical Results.....	A-13
A.5 Summary: Radar-Based Instrumentation.....	A-19
A.6 References.....	A-20

## ILLUSTRATIONS

<u>Figure</u>	<u>Page</u>
A-1 Schematic of a Simple Direct Pulse-Synthesis Short-Pulse Radar .....	A-2
A-2 Block Diagram of Frequency Modulation-(FM-CW) Radar Measurement System .....	A-4
A-3 Variations of Microwave Frequency in Reverberation Chamber over Time .....	A-4
A-4 Relationship Among Fast Fourier Transformation (FFT) Block Size, Sweep Rate, and Measurement Bandwidth .....	A-5
A-5 Time Behavior of a 3-GHz-Center Frequency Pulse with 200-MHz Bandwidth (BW).....	A-7
A-6 Simplified Schematic of a Heterodyne Swept CW Short-Pulse Radar System .....	A-9
A-7 Heterodyne Swept CW Short-Pulse System .....	A-10
A-8 Portable Two-Band Swept CW Short-Pulse Radar System.....	A-11
A-9 Simplified Low-Band Architecture of a Swept CS Short-Pulse Radar System .....	A-12
A-10 Windowed and Unwindowed Excitation Pulses .....	A-14
A-11 Vector Network Analyzer (VNA) Connection to Test Chamber.....	A-15
A-12 Raw and Corrected CW Insertion Loss (IL) for NSWCDD “Coffin” Test Chamber .....	A-16
A-13 TD-Decay Response Observed for Fields in the Test Chamber .....	A-17
A-14 Integrated Pulse and Response Calculation to Determine IL from Time-Domain (TD) Data.....	A-18
A-15 Comparison of Time and Frequency Domain-Calculated Values of IL .....	A-19

## ABBREVIATIONS AND ACRONYMS

AC	Alternating Current
A-D	Analog-to-Digital
Attn	Attenuator
BASIC	Beginner's All-Purpose Symbolic Instruction Code
BPF	Band Pass Filter
BW	Bandwidth
ctrl	Control
CW	Continuous Wave
dB	Decibel
DC	Direct Current
DRO	Dielectric Resonator Oscillators
DSO	Digital Sampling Oscilloscope
E field	Electric field component of electromagnetic wave
EM	Electromagnetic
FFT	Fast Fourier Transformation
FM	Frequency Modulation
GHz	Gigahertz
GPIB	General Purpose Instrumentation Bus
HP	Hewlett Packard
Hz	Hertz
IF	Intermediate Frequency
IL	Insertion Loss
IO	Input/Output
kHz	Kilohertz
LabVIEW <sup>®</sup>	Laboratory Virtual Instrument Engineering Workbench
LO	Local Oscillator
LPF	Low Pass Filter
m	Meter
M	Mixer
MATLAB <sup>®</sup>	Matrix Laboratory
MHz	Megahertz
Mkr	Marker
MSPS	Mega Sample per Second
mW	Milliwatt

**ABBREVIATIONS AND ACRONYMS (CONTINUED)**

NIST	National Institute of Standards and Technology
nsec	Nanosecond
NSWCDD	Naval Surface Warfare Center, Dahlgren Division
PC	Personal Computer
PCI	Peripheral Component Interconnect
PIN	P-type Intrinsic and N-type
PXI	PCI Extensions for Instrumentation
RF	Radio Frequency
Rx	Receiver
sec	Second
TD	Time Domain
trig	Trigger
TTL	Transistor-Transistor Logic
Tx	Transmitter
VEE <sup>®</sup>	Visual Engineering Environment
VNA	Vector Network Analyzer
YIG	Yttrium Iron Garnet

This page is intentionally blank.

## A.1 INTRODUCTION

Several different short-pulse radar systems were used to collect the data that have been presented in the *Reverberant Microwave Propagation* technical report. In principle, all of the data could have been collected on a modern vector network analyzer (VNA), such as a Hewlett Packard (HP)-8510 or one of its descendents with a time-domain (TD) option installed. An analyzer is convenient, of course, because of the ease in switching domains and the high available precision. However, due to budgetary and other constraints, precision analyzers were only used occasionally in collecting data for the technical report, and most of the data were collected using special improvised systems assembled from individual components borrowed from various microwave laboratories at the Naval Surface Warfare Center, Dahlgren Division (NSWCDD). Due to advances in electronic, microwave, and computer technology over the last few years, it has become easier and cheaper to construct very powerful instrumentation. Two basic approaches in equipment design were explored:

- a. Direct TD instrumentation
- b. Synthetic or equivalent TD instrumentation.

The architecture of several different systems is described in this appendix.

## A.2 DIRECT TIME-DOMAIN (TD) INSTRUMENTATION

In the direct approach, a short pulse is derived by quickly gating a signal from a continuous wave (CW) oscillator. Fast PIN (i.e., P-type Intrinsic and N-type) and varactor diode switch/modulators have been used in this approach, as diagrammed schematically in Figure A-1.

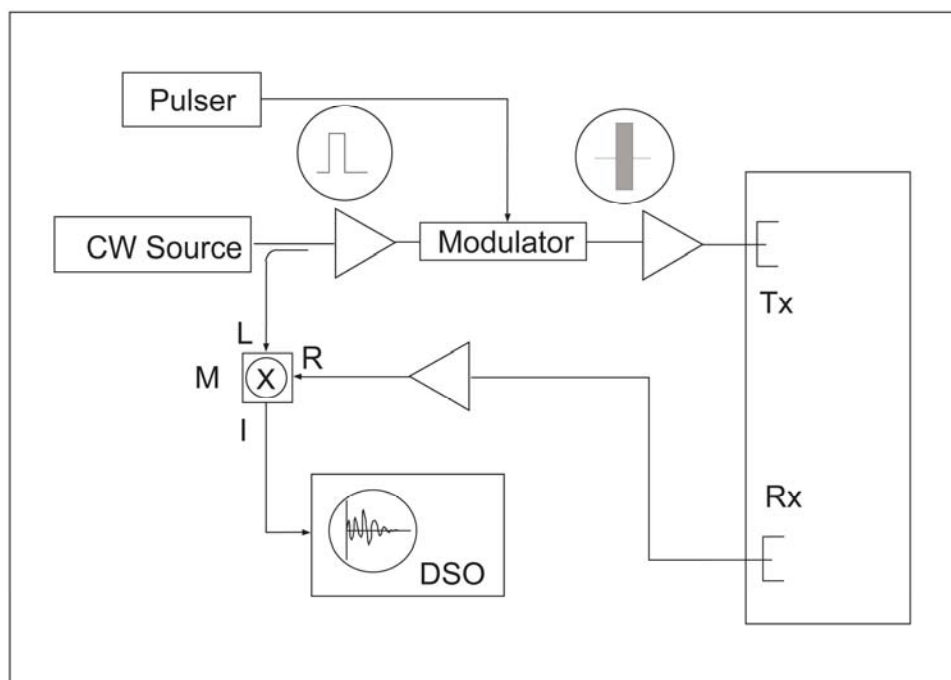


**Figure A-1. Schematic of a Simple Direct Pulse-Synthesis Short-Pulse Radar**

The signal from a CW source is switched by a PIN or varactor diode modulator and then amplified for transmission into the chamber under test. Required peak pulse power is generally only a few tens of milliwatts (mW). The CW source also acts as a local oscillator for the mixer used for detection. A fundamental requirement for the mixer is that its intermediate frequency (IF) output frequency range extends to direct current (DC). Also, the local oscillator (LO) injection and maximum radio frequency (RF) input levels must be carefully chosen, such that the mixer responds linearly to the RF input voltage. When properly embedded, the mixer IF output voltage is proportional to the E field level in the chamber, so the signal observed on the digital sampling oscilloscope (DSO) must be squared for ensemble averaging to indicate energy behavior in the chamber.

The system architecture is basically one of product detection with a mixer; this is also called homodyne detection. While detection could have been performed with a square law diode detector rather than the mixer, it was generally easier to obtain more dynamic range and greater confidence in calibration with the mixer.

With mixer operation, the IF output voltage is given by the product of the LO and RF input voltages and the cosine of the angle between them. Frequently, a DC offset voltage also occurs, resulting in some IF output level even with no RF input.

A system, such as that shown in Figure A-1, can be assembled fairly easily from equipment typically available in a microwave laboratory. Data analysis is also simple. Digital output from a low-cost “Barbie scope-type” DSO used to read the output from the mixer can be downloaded and then inserted into a spreadsheet for manipulation.



However, an important limitation of this approach is the dynamic range available with an 8-bit DSO.

Another feature of the direct system is that it is very straightforward to generate flat-topped pulses of arbitrary length simply by varying the pulse length of the pulse generator driving the modulator. All of the measurements considered in the technical report were performed with short pulses, but occasionally an EMC engineer may use a longer pulse of arbitrary length.

If higher dynamic range is required, a synthetic TD approach is more desirable. The synthetic TD approach produces mixer output signals that are much lower in frequency and, thus, permit the use of a lower frequency analog-to-digital (A-D) converter that can easily and inexpensively have more bits. The system dynamic range is then set primarily by the mixer noise floor and compression point.<sup>A-1</sup>

### A.3 SYNTHETIC TD MEASUREMENT AND SYSTEMS

The synthetic or equivalent TD technique employed for most of the measurements performed for the *Reverberant Microwave Propagation* technical report was basically a frequency modulation (FM)-CW approach together with Fast Fourier Transformation (FFT) processing to synthesize a short pulse. This subsection describes several different radar system architectures used for various experiments.

A basic system is diagrammed in Figure A-2. As shown in Figures A-2 through A-4, a linearly swept CW signal is injected into the test chamber. During the sweep interval, which typically lasts a large fraction of a second, the receiver (Rx) test antenna in the chamber samples the chamber fields that contain remnants of recently injected energy. For a linear frequency sweep, as shown in Figure A-3, the frequency difference between the outgoing signal being instantaneously injected into the chamber and the sampled remnant signal is proportional to the “time of flight,” or the reverberation time. The remnant signal, as a component of the sampled signal, has been present in the chamber, reflecting off the walls, and decaying. The time rate of chamber energy decay may be deduced, and  $\tau$  may be extracted by examining the frequency rate of roll-off from the mixer output difference frequency components. As shown in Figure A-2, the beat frequency components between the instantaneous transmitted and sampled chamber signals are determined by mixing the sampled signal with the outgoing LO signal and Fourier-transforming result.

---

<sup>A-1</sup> With an improvised system, great care must be taken to adjust the RF gain appropriately so that the mixer is correctly driven. If the mixer is driven into compression, the output signal will appear to be functioning quite well, but will actually yield incorrect  $\tau$  values.

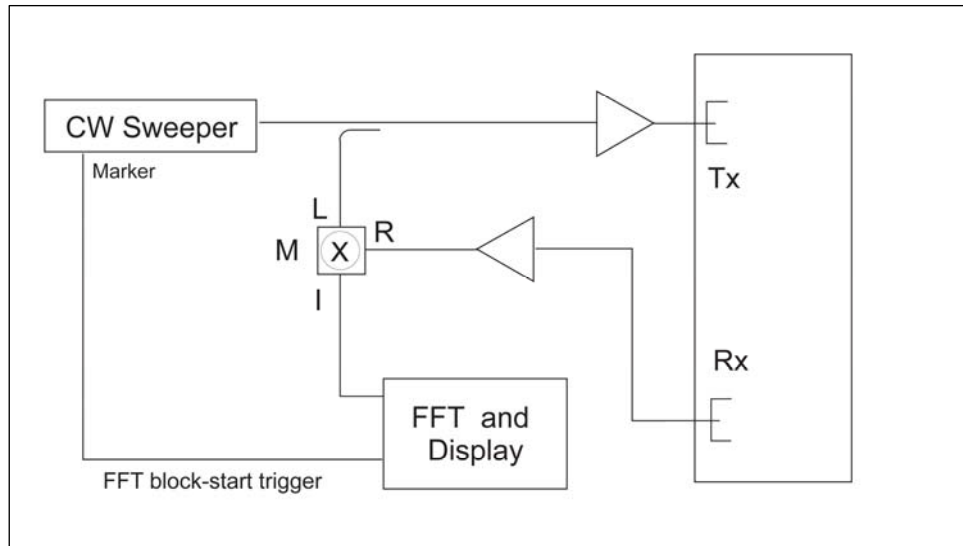


**Figure A–2. Block Diagram of Frequency Modulation–Continuous Wave (FM–CW) Radar Measurement System**

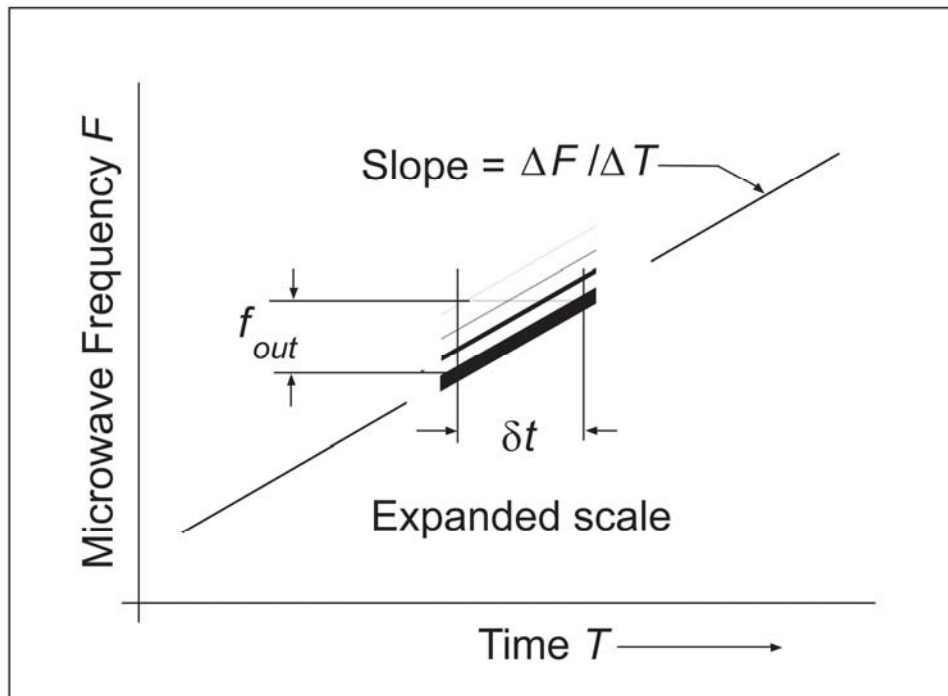


**Figure A–3. Variation of Microwave Frequency in Reverberation Chamber over Time**

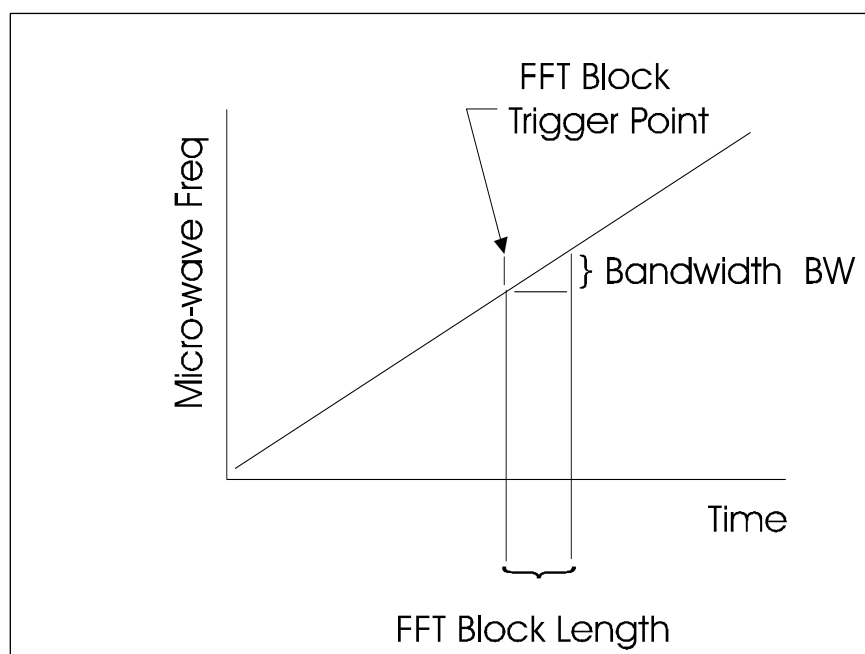


**Figure A-4. Relationship Among Fast Fourier Transformation (FFT) Block Size, Sweep Rate, and Measurement Bandwidth**

The IF output from the mixer is a burst of sinusoids. It has a continuous frequency spectrum because of the LO beating with many signal components or remnants that have been in the chamber for various lengths of time.

The mixing process is ideally a linear operation on a voltage from the antenna proportional to the chamber E field. By squaring the output from the FFT engine, one obtains an audio power density spectrum with a value ( $v^2$ ) at each frequency proportional to the energy ( $E^2$ ) remnant that has been present in the chamber for a particular amount of time [i.e.,  $\delta t$  in Equation (A-1)]. The beat frequency ( $f_{out}$ ) between the instantaneous injection frequency (i.e., LO) and a sampled chamber return signal component is given by Equation (A-1):

$$f_{out} = \frac{\Delta F}{\Delta t} \cdot \delta t \quad (\text{A-1})$$

where

$$\frac{\Delta F}{\Delta t} = \text{sweep rate of the transmitter and LO hertz/second (Hz/sec)}$$

$$\delta t = \text{time of flight or reverberation time of return signal component (sec)}$$

By careful choice of the sweep rate, one can arrive at conveniently processed mixer output frequency components for reverberation times of interest.

For example, by letting  $\Delta F/\Delta T = 5 \times 10^9$  Hz/sec [1 gigahertz (GHz)/0.2 sec], the beat frequency from a return signal component delayed by 10  $\mu$ sec is 50 kilohertz (kHz).

Signals in the 50-kHz frequency range may be conveniently A-D converted for FFT and further processing.

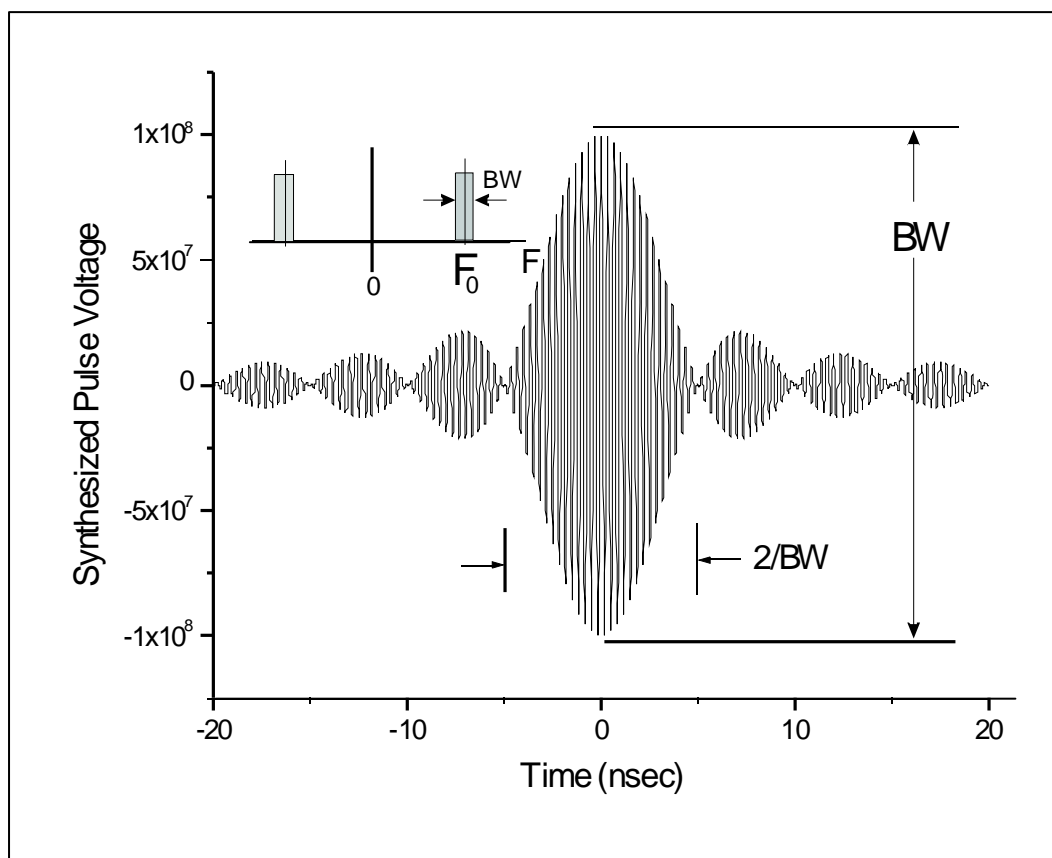
In the view just presented, the technique may be envisioned as the result of beating “old” energy signals from the chamber together with “current” LO energy. Because of loss during reverberation, the older energy is attenuated and yields smaller contributions in the FFT output. This decrease with time and resulting output audio frequency determination by the FFT allows extraction of  $\tau$  from the Fourier-transformed mixer output.

The measurement can also be envisioned as demonstrating chamber response to delta function excitation. The delta function is a short pulse with carrier frequency centered about the microwave frequency of interest. It is generated as the result of the CW sinusoids injected into the chamber for the measurement. As shown in Figure A-4, the choices of FM-CW sweep rate and FFT block size set the bandwidth (BW) of the measurement and, thereby, set the effective pulse width of the excitation. By choosing the sweep rate and block size appropriately, one may perform the measurement over any desired BW and nominal equivalent pulse width ( $2/BW$ ).<sup>A-2</sup> If a sweeper is used as the source in the system of Figure A-2, a marker output from the sweeper may be used as a trigger for the FFT engine. With this architecture the FFT block time may be only a fraction of the total sweep time.

The system of Figure A-2 produces a band-limited swept CW signal. EMC engineers are familiar with the notion that pulsing a CW signal, i.e., pulsing in the time domain, produces a  $\sin(x)/x$  pattern in the frequency domain. Similarly, band-limiting a signal in frequency domain produces a  $\sin(x)/x$  pattern in the time domain, as depicted in Figure A-5. Figure A-5 shows the time behavior of a band-limited signal with 3-GHz center frequency and uniform frequency components over a 200-megahertz (MHz) BW.

---

<sup>A-2</sup> Mischa Schwartz, *Information Transmission, Modulation and Noise*, Fourth Edition, ISBN 0-07-055909-0 (New York: McGraw-Hill Publishing Co., 1990): Ch. 2.



Note: The term “center frequency” is synonymous with the term “carrier frequency.”

**Figure A-5. Time Behavior of a 3-GHz-Center Frequency Pulse with 200-MHz Bandwidth (BW)**

The width of the central peak of the synthetic pulse signal varies inversely with BW, while the pulse height is proportional to BW. The synthesized pulse in Figure A-5 has a central peak height of  $2 \times 10^8$  volts and a width of 10 nanoseconds (nsec). At 10 nsec, most of the energy in the pulse is confined to a region in space of approximately 3 meters (m), while the amplitude is high enough to inject a useful amount of energy into the chamber. With suitable FFT processing, this kind of *synthesized* signal is available from a low-power swept CW source.

In practice, the pulse is widened slightly by windowing in the FFT process to reduce FFT side lobes, but the essential feature of spatial compactness is preserved. The pulse should be narrow in time compared to the time scale of measurement. Since most reverberation chamber 1/e times are approximately 0.1 to 1.0  $\mu$ sec, an equivalent pulse length of 0.1 to 0.02  $\mu$ sec is generally sufficient for measurement and requires BWs of 20 to 100 MHz.

As shown in Figure A-2, the measurement instrumentation consists of only a few components. A yttrium iron garnet (YIG)-based sweeper is desirable because of low phase noise and because of its inherent linearity in frequency versus control voltage. The

mixer must have an IF output that extends to DC. The frequency response of any audio amplification between the mixer output and the FFT must be flat, because it is the roll-off *rate* of mixer output frequency components from which  $\tau$  is deduced. Typically, only a few tens of milliwatts of injected power into the chamber are required, depending on how large the chamber is and how much amplification is used in front of the mixer.

The RF signal input level to the mixer RF input port is critical. This level should be kept below values that would cause compression. On the other hand, due to small imbalances in the mixer diode ring, some frequency-dependent mixer output will occur even with no RF input. Double-balanced mixer design is preferred; however, the diode ring balance is never perfect. Since the DC offset is frequency dependent, sweeping the frequency produces an alternating current (AC) noise component in the mixer output, which appears along with the desired chamber response signal. Typically, the noise from the DC offset occurs at low frequencies, and if long transmit and receive transmission lines are used in the measurement assembly, the extra cable-induced delay moves most of the desired chamber response to frequencies above where the noise is problematic. Thus, this simple single-mixer homodyne design is a surprisingly powerful instrument.

Because of the relatively low mixer output frequencies involved, one can easily use a 10- or 12-bit A-D converter, resulting in a high dynamic range for the measurement, approximately 30 to 40 dB. Higher bit capability is not useful because of overall limitations in the homodyne design. Ultimately, the mixer determines the performance limit of the system.

The FFT and display operation may be done economically with a computer plug-in A-D card and software FFT. At the NSWCDD chamber facility, this operation has also been performed with a *real-time* spectrum analyzer (i.e., often referred to as a “dynamic signal analyzer”). This type of instrument is commonly used for noise and vibration analysis and occasionally for servo system tune up. This kind of device typically performs a *hardwired* FFT operation and is very fast, allowing nearly instantaneous signal averaging and convenient operation. Typical instruments of this type have an upper frequency limit of 100 kHz, which is entirely satisfactory as shown in Equation (A-1).

The heterodyne system diagrammed in Figure A-6 uses two sweepers and circumvents some of the limitations of the homodyne system. Sweeps are triggered simultaneously, but start at a fixed distance, nominally 35 MHz apart. The operating frequency range is set by the mixer characteristics and by sweeper band-edge break points. The entire system was general purpose instrumentation bus (GPIB)-controlled by a laptop personal computer (PC) running HP-Visual Engineering Environment (VEE<sup>®</sup>). A Transistor-Transistor Logic (TTL)-sweep trigger was derived from the PC serial port. The mixers, assorted RF amplifiers, switches for multi-band operation, and a GPIB-controlled step attenuator were mounted in a chassis assembly requiring approximately 4 inches of rack space. As depicted in Figure A-7, the two sweepers, the real-time signal analyzer FFT engine, and the microwave hardware assembly are semiportable for connection to various test chambers in the laboratory.

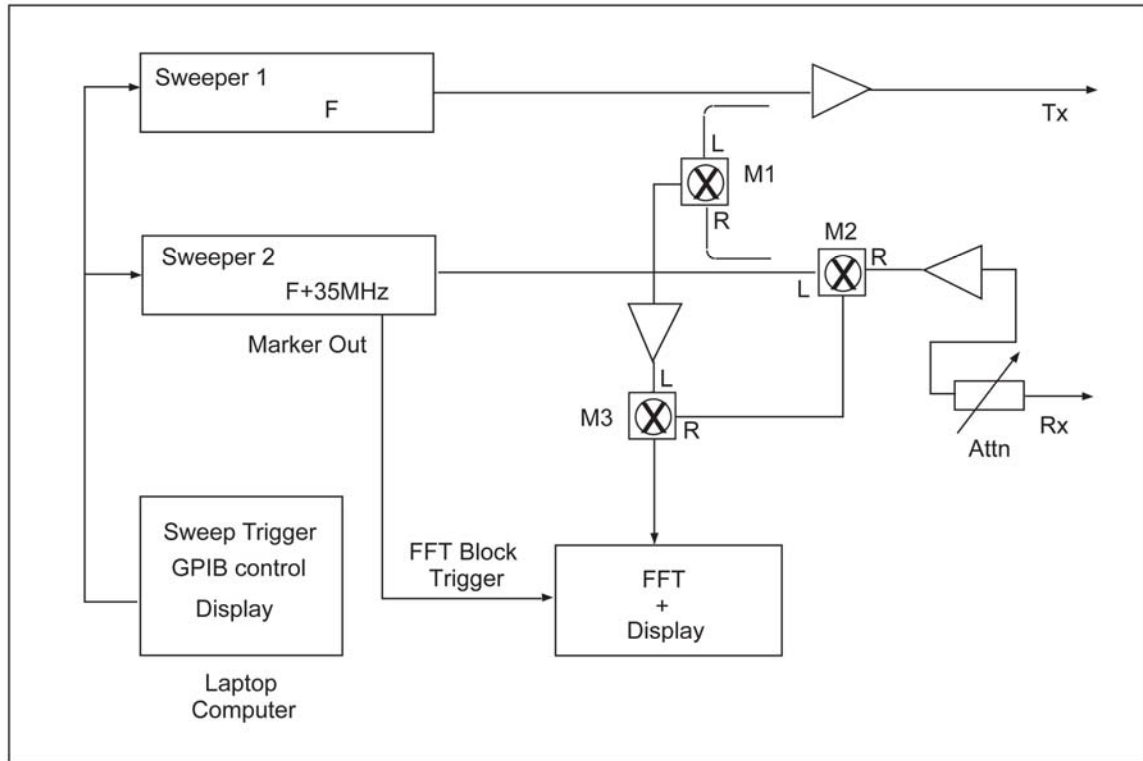


**Figure A-6. Simplified Schematic of a Heterodyne Swept CW Short-Pulse Radar System**

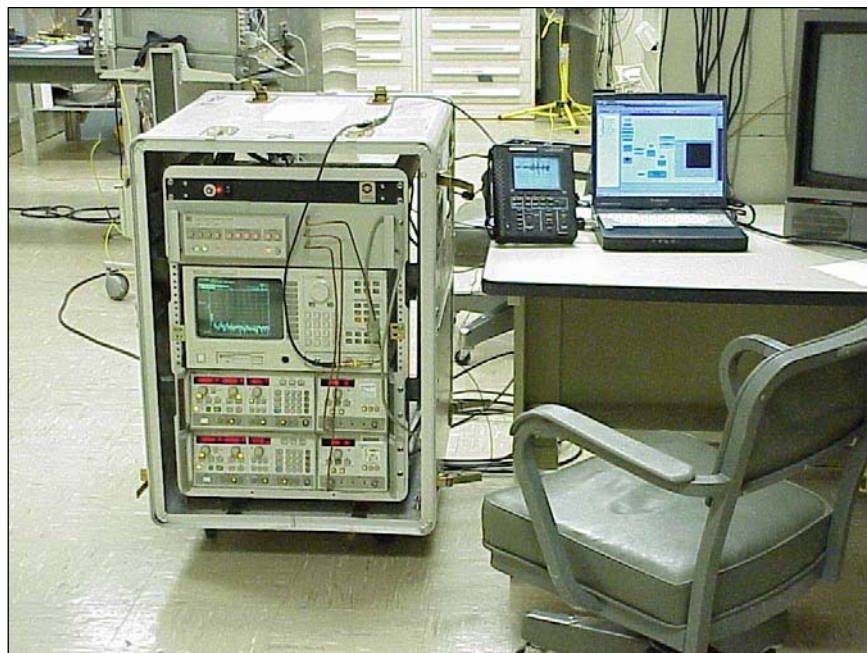


**Figure A-7. Heterodyne Swept CW Short-Pulse System**

A third system constructed for flexibility and portable operation for shipboard measurements is depicted in Figure A-8. This system was constructed around a PXI<sup>A-3</sup> computer running LabVIEW<sup>®</sup> for control of a 12-bit A-D card and a dedicated arbitrary function generator for YIG oscillator frequency control.

---

<sup>A-3</sup> Peripheral Component Interconnect (PCI) Extensions for Instrumentation (PXI)





**Figure A-8. Portable Two-Band Swept CW Short-Pulse Radar System**

The system operates on two bands: 0.05 to 3.5 GHz and 4 to 8 GHz. It was built for use in shipboard and other portable or field test operations with capabilities over a wide frequency range. The system architecture of the high-band portion is similar to that of Figure A-6 with two swept CW signals supplied by separate YIG oscillators. A simplified schematic of the low-band portion of the system is diagrammed in Figure A-9. The signal from a single YIG 4-to-8-GHz oscillator is beat together with signals from two dielectric resonator oscillators (DRO) for generation of the 0.05-to-3.5-GHz transmit and LO signals.

The system can simultaneously sweep and perform the high-speed FFT and other operations required for smooth operation and data output to a spreadsheet file for post-processing. Variable FFT block sizes ranging from 128 to 16,384 elements may be used, allowing wide flexibility trade-off between frequency and time resolution for a measurement.

The “frequency versus control voltage” relationship for YIG oscillators is usually quite linear, and a simple 555-based saw-tooth ramp generator would suffice for most applications, unless a very wide BW short pulse is required.<sup>A-4</sup> This means that a lower cost version of the system could be built around a laptop or general purpose PC running a general purpose A-D and digital input/output (IO) card. Control could be derived from any of several applications, such as LabVIEW<sup>®</sup>, VEE<sup>®</sup>, MATLAB<sup>®</sup>, or even BASIC.

---

<sup>A-4</sup> The C charging current could be derived from a suitable constant current source, such as an open collector or drain, rather than a simple resistor.

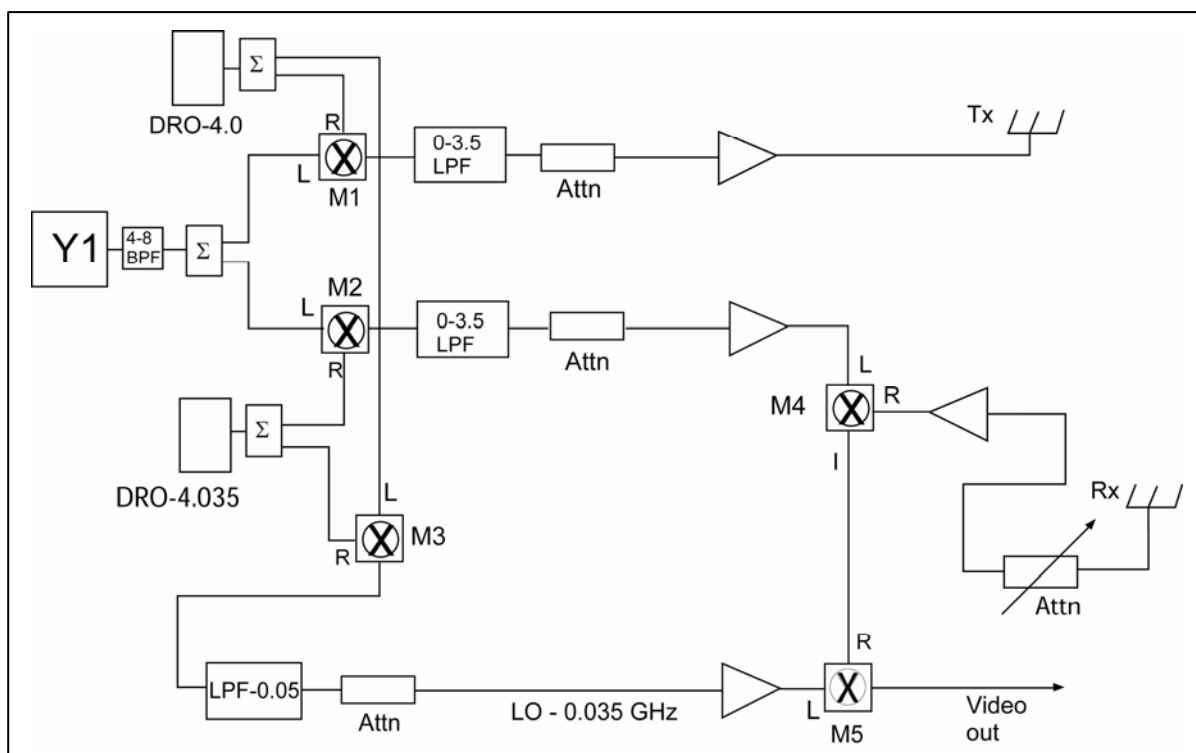


**Figure A–9. Simplified Low-Band Architecture of a Swept CW Short-Pulse Radar System**

For the current system, as shown in Figures A-8 and A-9, the video output from the mixer M5 is sampled by a 12-bit digitizing card operating at 1 mega sample per second (MSPS) after preamplification and anti-alias filtering. The anti-alias filter is a 15-pole Butterworth design with a 3-decibel (dB) point at 400 kHz. The Butterworth design was chosen over a Bessel or Tchebychev filter because of superior in-band ripple and linear phase response.<sup>A-5</sup> Measurements showed that the flat in-band response characteristic of a Butterworth design was available only after the filter was carefully terminated at both its input and output. Flat response is extremely important in this circuit because the observed roll-off rate of response signal with frequency is used to determine 1/e time.

With the single real video output signal, line spectra of different resolutions could be produced. For example, a 401-line spectral output signal could be produced by using a 1024-point FFT input block that would calculate a 512-point output block. The top 111 lines, which could contain aliased signal components from frequencies above 500 kHz, would be discarded.

The synthetic TD systems described above that use basic FFT processing yield the delta function response of a chamber to a short pulse. Although analyzers typically operate at

A-5 With the current design that operates only on the squared FFT rather than the complex FFT, linear phase is not a significant issue.

specific stepped frequencies rather than with continuous-swept chirp, this response is similar to that obtained with a VNA with a TD option. Subsection A-4 describes the operation of a HP-8510 analyzer.

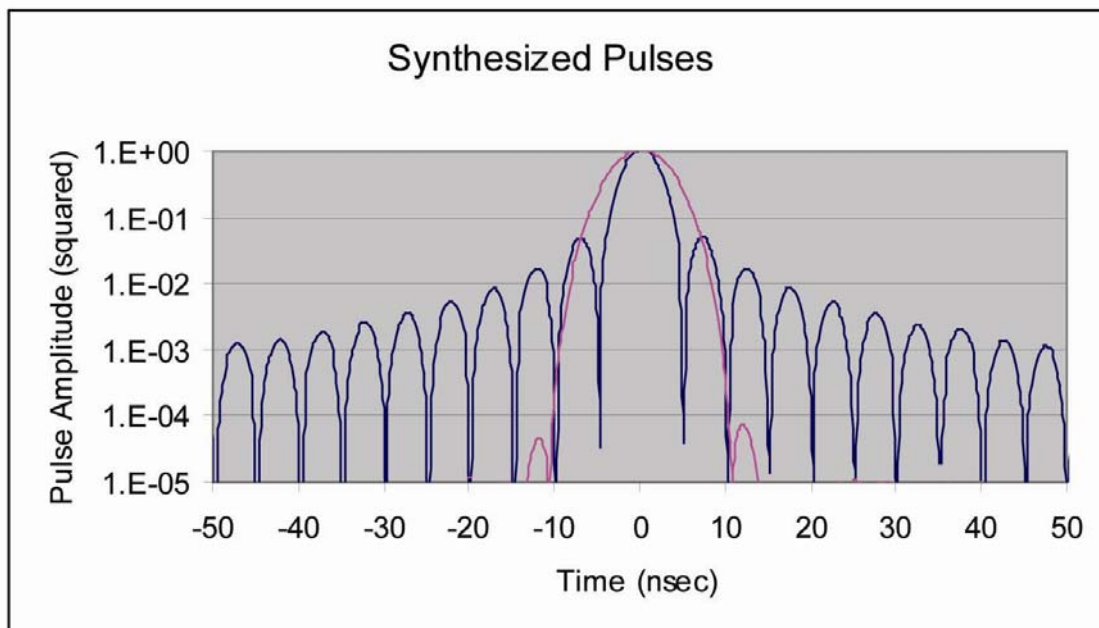
#### **A.4 VECTOR NETWORK ANALYZER (VNA) OPERATION AND TYPICAL RESULTS**

Use of a VNA with a TD option allows immediate TD measurement of reverberant space characteristics and also permits rapid switching back and forth between time and frequency domains for comparison of measurement results. Typical S parameter format of an analyzer allows natural organization of measurement data. Voltage waves in the S parameter formalism correspond naturally to incident and reflected power values with the antennas simply acting as transducers. In each domain, chamber insertion loss (IL), for example, is most naturally measured from  $S_{21}$ , while auxiliary measurements of  $S_{11}$  and  $S_{22}$  yield information about impedance mismatch losses at the Rx and transmit (Tx) antennas. Setup and operation of an HP-8510 analyzer with a TD option is described briefly below.

Synthesis of a TD pulse in the analyzer is initiated in frequency domain where the pulse-center frequency and BW are chosen. For example, setting the start and stop frequencies of a sweep between 2.9 and 3.1 GHz and then switching the analyzer to its TD band-pass state<sup>A-6</sup> causes the machine to synthesize a pulse similar to that shown in Figure A-5. The machine actually calculates an analytic pulsed signal with cosine and sine (i.e., real and imaginary) terms whose overall squared magnitude may be viewed as plotted in Figure A-10. Figure A-10 shows two pulses: One was generated with no window, and the other was generated with the default window for the analyzer. Choice of windowing is not particularly important in reverberation measurements, and the default window is excessive in its reduction of FFT side lobes, though it is satisfactory. Either a Hanning or Hamming window, which appears commonly on most FFT instrumentation such as dynamic signal analyzers, reduces FFT side lobes sufficiently without excessively broadening the pulse.

---

<sup>A-6</sup> This can be done on a HP-8510 using the following menu key sequence: Domain → Time → Bandpass.



Note: These pulses were synthesized by an HP-8510 VNA in TD mode.

**Figure A-10. Windowed and Unwindowed Excitation Pulses**

The excitation pulse, such as that shown in Figure A-10, may be viewed by directly connecting the Tx (port 1) and Rx (port 2) together and setting the analyzer start and stop times appropriately with the machine in the TD band-pass state. The rest of this subsection discusses Figures A-10 through A-15 and demonstrates the data extracted from the VNA machine by using the “Store Data” operation. Data are output as complex pairs for each S parameter at each of the 101-to-801-frequency or time steps.

A simple IL measurement is demonstrated in Figure A-11. The S parameter format calculated by the analyzer is ideal for analysis of chamber fields and propagation. The Tx and Rx antennas simply act as transducers between the chamber fields and voltage waves that are mathematically manipulated in the S parameter-based calculation scheme within the VNA. After a calibration sequence and “direct-through measurement” to produce output, such as that provided in Figure A-10, the analyzer is connected to the chamber as diagrammed in Figure A-11.

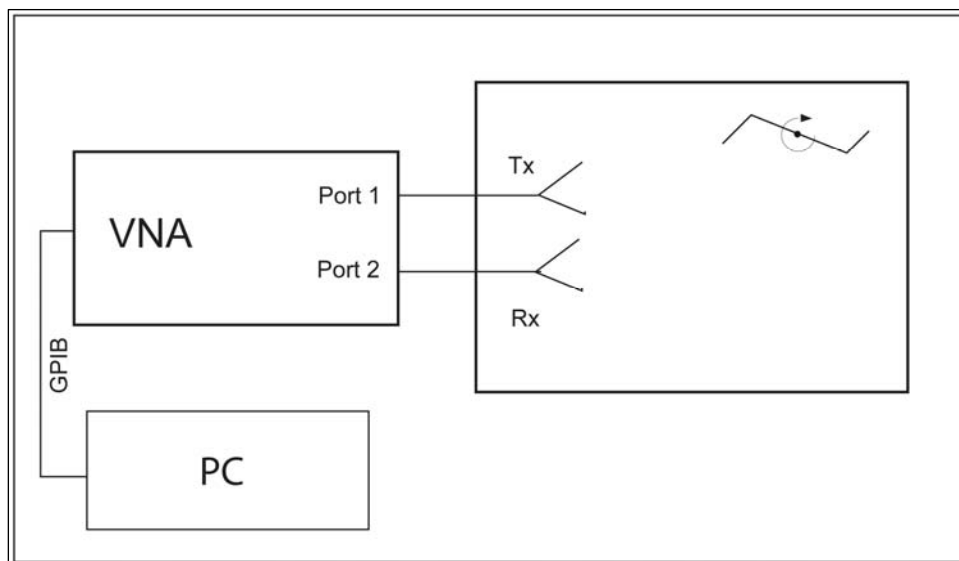


**Figure A-11. Vector Network Analyzer (VNA) Connection to Test Chamber**

Frequency domain output from a smoothed 10-times (x 10) ensemble average is shown in Figure A-12. Data plotted in Figure A-12 were taken from the 801-point 10-times ensemble average and smoothed by averaging 16 adjacent points to form a 4-MHz aperture.<sup>A-7</sup>

<sup>A-7</sup> For the data shown in the Figures A-12 through A-15, ensemble averaging of squared S parameter data was performed in Microsoft Excel. The HP-8510 calculates and outputs a complex FFT. Applying the averaging function directly in the HP-8510 tends to produce a zero result. What is really required is a mean square average rather than a phasor-type average of the HP-8510 output.

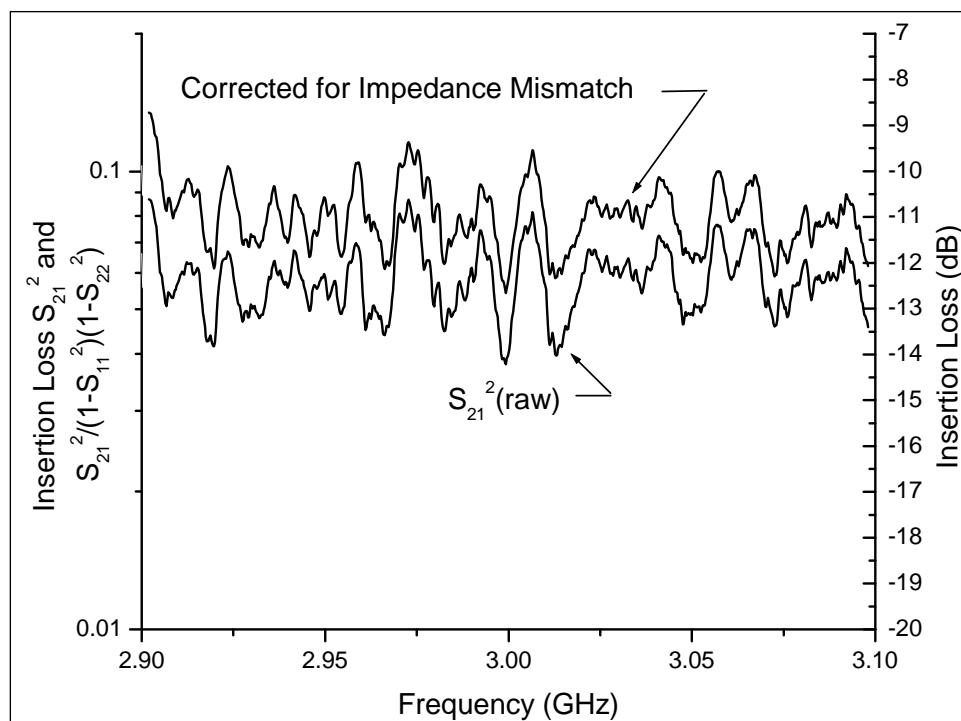


**Figure A-12. Raw and Corrected CW Insertion Loss (IL)  
for NSWCDD “Coffin” Test Chamber**

Figure A-12 shows raw IL directly ( $S_{21}^2$ ), as it is usually measured with a sweeper and spectrum analyzer. Also, corrected IL [ $S_{21}^2/(1 - S_{11}^2)(1 - S_{22}^2)$ ] is presented. As can be seen from the spacing between the two curves in Figure A-12, the corrected IL is about 1 to 2 dB less. Raw IL data provides no correction for reflections at the Rx and Tx antennas. Corrected IL, calculated as [ $S_{21}^2/(1 - S_{11}^2)(1 - S_{22}^2)$ ] is also presented. As can be seen from the spacing between the two curves in Figure A-12, the corrected IL is about 1 to 2 dB less than the uncorrected IL.

Impedance mismatch correction, which has been considered by workers at National Institute of Standards and Technology (NIST), is subtle.<sup>A-8</sup> In a chamber, reflected power from the Tx antenna consists not only of the usual  $S_{11}$  component, which would be measured in free space, but also contains a component that the Tx antenna receives from the chamber environment.

<sup>A-8</sup> John Ladbury, Galen Koepke, and Dennis Camell, “Sections 5.2 through 6.3,” *Evaluation of the NASA Langley Research Center Mode-Stirred Chamber Facility*, NIST Technical Note 1508. (Boulder, Colorado: Radio Frequency Technology Division, Electronics and Electrical Engineering Laboratory, January 1999): 69–114.

Input reflection coefficient is determined solely by  $S_{11}$  only when the Rx antenna is terminated in the system characteristic impedance (usually 50 Ohm).<sup>A-9</sup>

Correction for impedance mismatch at the Rx antenna,  $(1 - S_{22}^2)$ , is calculated from reciprocity considerations.<sup>A-10</sup>

Switching to TD and then setting the start and stop times (e.g., -0.05  $\mu\text{sec}$  and +5.0  $\mu\text{sec}$  respectively) produces output similar to that presented in Figure A-13. Figure A-13 shows 10-times ensemble-averaged chamber output.

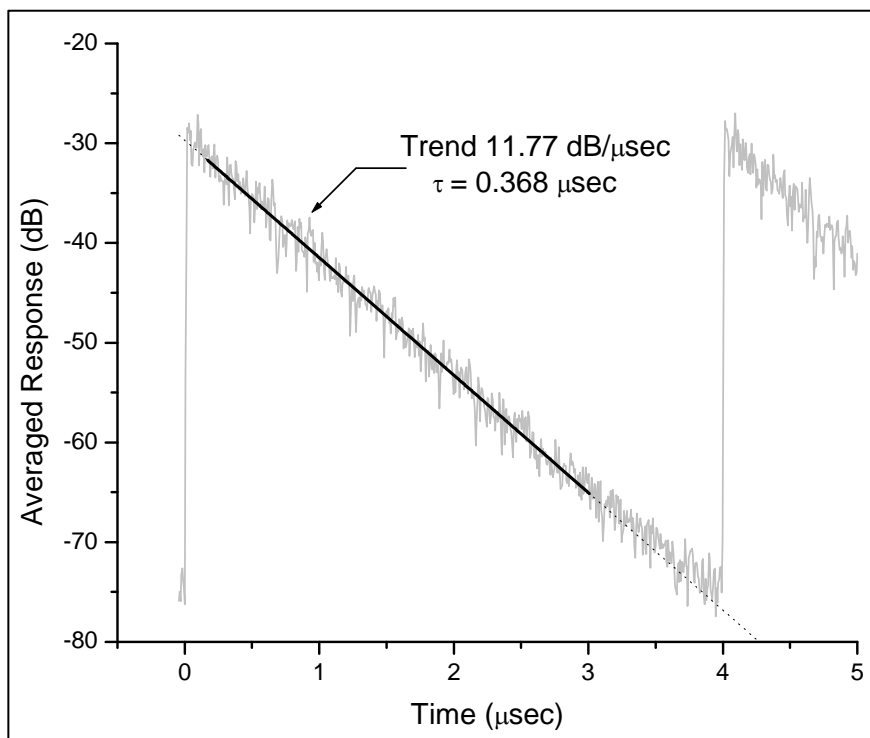


**Figure A-13. TD-Decay Response Observed for Fields in the Test Chamber**

<sup>A-9</sup> First, note that *power gain*  $G$  is referred to in this report, *Reverberant Microwave Propagation*, as “insertion loss” (IL). For the case where the receiver and transmitter are set at the characteristic impedance, the *power gain*  $G$ , is given by  $S_{21}^2/(1 - S_{11}^2)$ . This definition corrects for mismatch at the input to the chamber (i.e., the TX antenna terminal) but does not account for mismatch at the output (i.e., the Rx antenna terminal), which is present when  $S_{22}$  is nonzero. The function  $S_{21}^2/(1 - S_{11}^2)(1 - S_{22}^2)$  is identical to the maximum *unilateral power gain* calculated for networks where there is no reverse transmission. When there is no reverse transmission, the input is “unaware” of output conditions, a situation similar to that when IL is high in a chamber; *S-Parameter Techniques*, HP/Agilent Application Note 95-1, [www.agilent.com](http://www.agilent.com); *S-Parameter Design*, HP/Agilent Application Note AN-154, [www.agilent.com](http://www.agilent.com); David M. Pozar, *Microwave Engineering, Third Edition*. (N.p.: John Wiley & Sons, Inc., 2005): Section 4.3.

<sup>A-10</sup> Ladbury et al., 69.

As a result of the FFT operation performed within the VNA, response aliasing occurs at 4.0  $\mu\text{sec}$ . With 801 points in the stimulus, the 200-MHz sweep from 2.9 to 3.1 GHz has a distance ( $\Delta F$ ) of 0.25 MHz between frequency steps, which leads to the 4- $\mu\text{sec}$  alias at  $1/\Delta F$ .

Chamber 1/e time calculated from the data of Figure A-13 is 0.368  $\mu\text{sec}$ . For the measurement chamber with a volume of 0.695  $\text{m}^3$  and a pulse-center frequency of 3.0 GHz with a 0.1-m wavelength, this leads to an IL of -11.99 dB, exclusive of antenna efficiency and impedance mismatch factors.

The data of Figure A-13 can be integrated to calculate IL in the TD, as demonstrated in Figure A-14. This calculation includes the same impedance mismatch and antenna efficiency factors as the uncorrected CW IL of Figure A-12. The 12.83-dB value plotted at 3.0 GHz is within 1 dB of typical uncorrected CW values indicated in Figures A-12 and A-15.

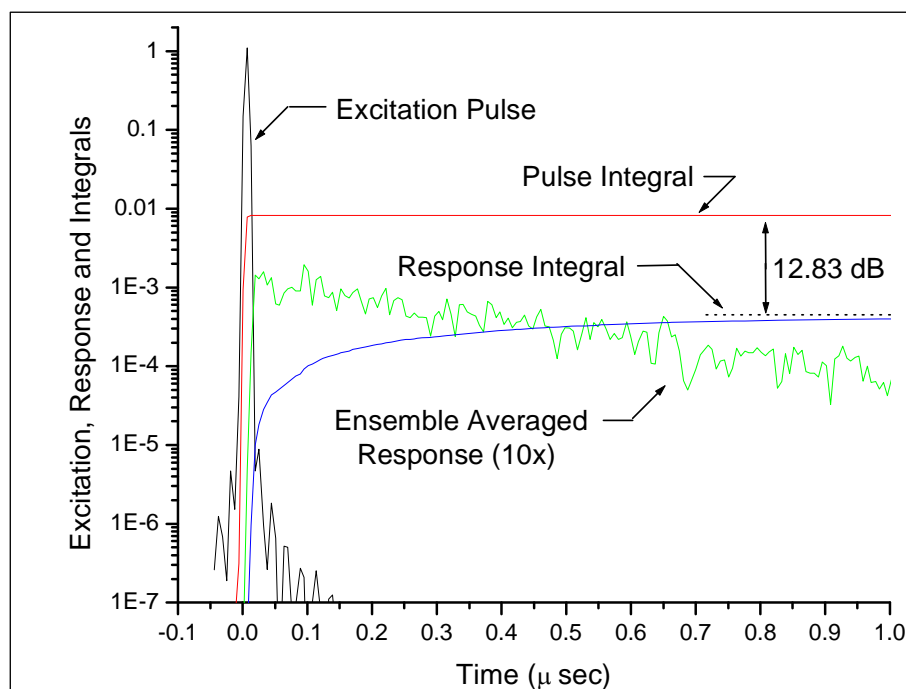


**Figure A-14. Integrated Pulse and Response Calculation to Determine IL from Time-Domain (TD) Data**



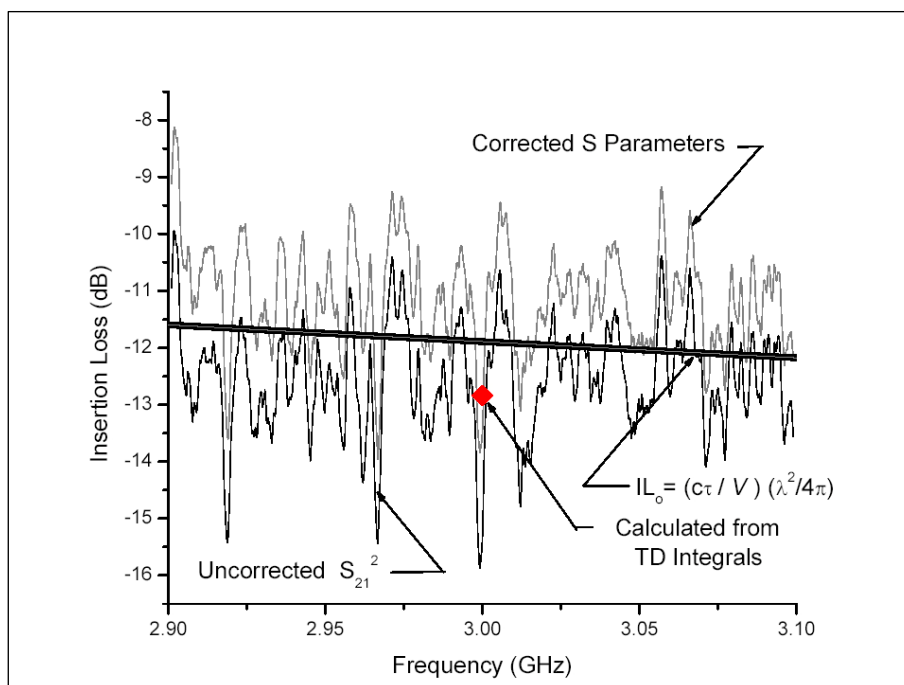


**Figure A-15. Comparison of Time and Frequency Domain-Calculated Values of IL**

Figure A-15 also displays a frequency-dependent  $IL_0$  value, using the  $0.368 \mu\text{sec}$   $1/e$  time extracted from Figure A-13.

With suitable attention to maintaining stable losses at connectors, this kind of experiment provides a promising approach for determination of antenna efficiency. The key piece of information that allows this is the measurement of the true loss factor for the cavity calculated from the  $1/e$  time. For a known cavity volume and  $1/e$  time, the spatially averaged power density is established.

## A.5 SUMMARY: RADAR-BASED INSTRUMENTATION

The fundamental measurement instrument in the TD measurement approach is a short-pulse radar that injects short pulses of electromagnetic (EM) energy into a test space and then records the transient field response.

An ideal measurement instrument is, thus, a precision VNA that contains firmware for TD measurement. Extremely useful low-cost instrumentation can be built, however, which may be more appropriate for shipboard or other field measurement venues.

## A.6 REFERENCES

- Ladbury, John, Galen Koepke, and Dennis Camell. "Sections 5.2 through 6.3," *Evaluation of the NASA Langley Research Center Mode-Stirred Chamber Facility*, NIST Technical Note 1508. Boulder, Colorado: Radio Frequency Technology Division, Electronics and Electrical Engineering Laboratory, January 1999: 69–114.
- Pozar, David M. *Microwave Engineering, Third Edition*. Hoboken, New Jersey: John Wiley & Sons, Inc., 2005: Section 4.3.
- S-Parameter Design*. HP/Agilent Application Note AN-154. 20 June 2006. [www.agilent.com](http://www.agilent.com).
- S-Parameter Techniques*. HP/Agilent Application Note 95-1. 1 February 1967. [www.agilent.com](http://www.agilent.com).
- Schwartz, Mischa. *Information Transmission, Modulation and Noise, Fourth Edition*. ISBN 0-07-055909-0. New York: McGraw-Hill Publishing Co., 1990: Ch. 2.

**APPENDIX B**

**EQUIVALENT REVERBERATION CHAMBER  
FROM THE METHOD OF IMAGES**

This page is intentionally blank.

## CONTENTS

<u>Appendix</u>	<u>Page</u>
<b>B    EQUIVALENT REVERBERATION CHAMBER FROM THE METHOD OF IMAGES</b>	
B.1   Introduction.....	B-1
B.2   Application of Image Method.....	B-1
B.3   Fields Within Chamber.....	B-2
B.4   Wall Reflections and Losses.....	B-4
B.5   Summary: Equivalent Reverberation Chamber from the Method of Images .....	B-4
B.6   References.....	B-5

## ILLUSTRATION

<u>Appendix</u>	<u>Page</u>
B-1    Two-Dimensional Representation of a Three-Dimensional Lattice of Image Sources.....	B-2

## ABBREVIATIONS AND ACRONYMS

n. pag.	No pagination (used with references)
no.	Number (issue number used with references)
vol.	Volume (used with references)

This page is intentionally blank.

## B.1 INTRODUCTION

As a reverberant field is developed, the energy contained in an initial expanding spherical wave from a source inside the chamber is transformed into a large number of individual wavefronts that are created from reflections off the chamber walls, paddle wheels, and other internal objects. Insight into the creation and properties of the reverberant field can be gained by considering an analysis based on the method of images. This technique has been used in the past by physicists to study electromagnetic,<sup>B-1</sup> as well as acoustic reflections.

## B.2 APPLICATION OF IMAGE METHOD

The antenna that emits the initial spherical wave is enclosed on all sides by conducting walls. In applying the method of images, as shown in Figure B-1, the walls are removed and replaced by a three-dimensional lattice containing an infinite number of image sources located at integer multiples of chamber dimensions. No more walls exist, only sources. At the inner surface of the original conductive walls and within the original chamber region, the fields from the image sources are equivalent to those from reflections off the original conductive walls. Correct application of the image analysis technique requires that an infinite number of sources be employed so that field boundary conditions at the original conductive walls are satisfied. Fields from the image sources are considered only after they have entered the original chamber region.

---

<sup>B-1</sup> Two references document this method of images technique for electromagnetics:  
 William H. Hayt, Jr., *Engineering Electromagnetics, Fourth Edition* (New York: McGraw-Hill Book Co., 1981): 140-141;  
 Robert E. Collin, *Field Theory of Guided Waves* (New York: McGraw-Hill Book Co., 1960): 523-525.

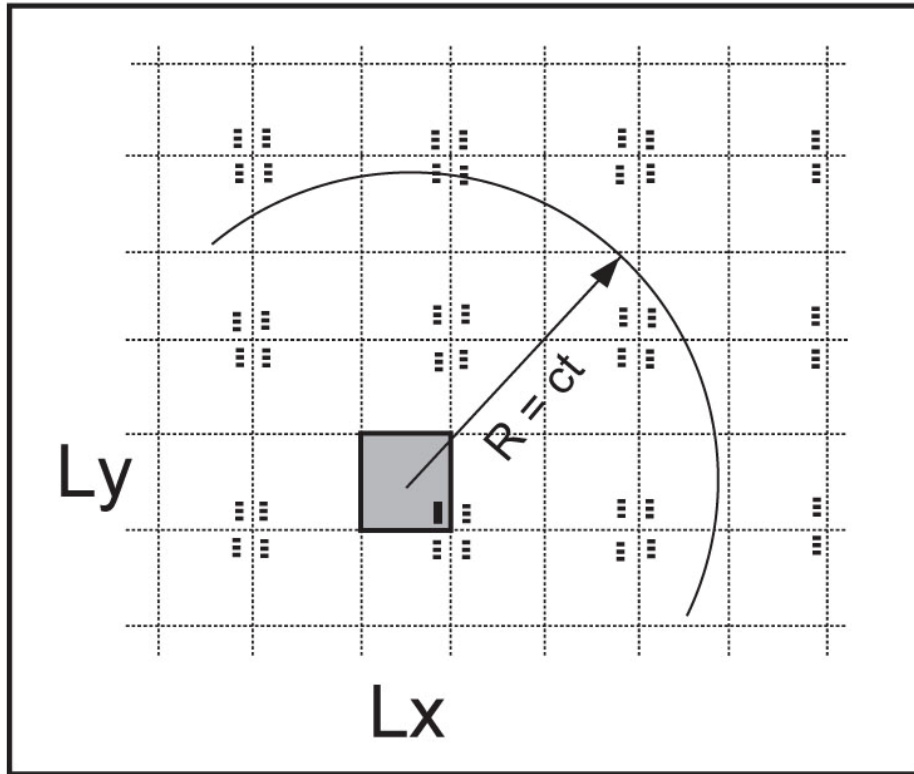


**Figure B-1. Two-Dimensional Representation of a Three-Dimensional Lattice of Image Sources**

In spite of an infinite number of sources that exist in the new problem that replaced a single source and six walls, many researchers find that the “bookkeeping” from this approach is much easier to visualize than accounting for properties of individual reflections from the original walls. The number of individual wavefronts reflected from the walls also would eventually become infinite. As applied here, the technique is for a single source within an empty chamber with planar walls. Paddle wheels and other objects within the chamber are not considered because of additional complexities. Nevertheless, this calculation—for chamber walls only—shows key features of the reverberation response.

### **B.3 FIELDS WITHIN CHAMBER**

The fields within the chamber may be calculated at any time  $t$  as the resultant of the fields from each image source, which is assumed to emit a short spherical wave pulse at time  $t = 0$ . At any given time  $t$  following excitation, the fields within the original chamber region are those resulting from the image sources in the vicinity of the surface of an expanding sphere with radius  $ct$ . The pulsed radiation field from each source is a single



expanding spherical wave with the electric field  $E$  and power density  $S$  at any point on the wavefront, as given by Equations (B-1) and (B-2):

$$E = E_0/r \quad (\text{B-1})$$

$$S = E_0^2 / 377 \times 1/r^2 \quad (\text{B-2})$$

where

$$r = ct$$

Neglecting losses for a moment, the image calculation model predicts a constant energy density within the chamber region. With  $r = ct$ , the denominator of  $S$  varies as  $t^2$ , so the energy density of a spherical wavefront varies as  $t^{-2}$ . However, from the image lattice construction, the number of image-source terms contributing to the fields within the chamber at time  $t$  comes from a thin shell at the sphere surface with expanding radius  $ct$ . The surface area of a sphere grows as the square of its radius grows; thus, the number of individual sources contributing to the field within the chamber at  $t$  grows as  $t^{+2}$ .

Thus, after excitation with a short pulse, the chamber region becomes filled with an increasingly greater ( $t^2$ ) number of weaker ( $t^{-2}$ ) pulsed-field wavefronts from more distant image sources. Subjectively, the term “diffuse,” used to describe acoustic reverberant fields, appears particularly descriptive. The terms “uniform” and “isotropic,” which are commonly used in the reverberation chamber community, refer to the essential features of the fields for chamber operational test and measurement purposes.

Experimental data have shown that a good reverberant field is formed in a space after 8-to-10 characteristic wall-scattering times ( $T_C$ ).

Using the construction of Figure B-1, one can show that at  $t = 10 \times T_C$ , there are more than 300 wavefronts present within the chamber. Reasoning proceeds as follows:

- a. The number of wavefronts in the chamber at  $t = 10 \times T_C$  equals the number of sources within a shell of radius  $R = 10 \times L_C$  and thickness  $\Delta R = L_C$ .
- b. The volume of the shell is  $4\pi \times R^2 \times \Delta R = 4\pi \times 100 \times L_C^3$ .
- c. The characteristic wall-scattering length  $L_C$  of the chamber is given as  $T_C \times c$  and is usually approximately equal to a minimum chamber dimension. For a cubic chamber,  $L_C = 0.666 \times a$ , where  $a$  is the length of a chamber wall.<sup>B-2</sup>
- d. Each volume element of volume  $L_C^3$  contains approximately  $0.666^3 = 0.296$  sources that establish wavefronts in the chamber.

---

<sup>B-2</sup> In Figure B-1,  $L_x = L_y = L_z = a$ .

Hence, the number of sources from the shell of radius  $10 L_C$  and thickness  $L_C$  is given as follows:

$$4\pi \times 100 \times 0.296 = 372$$

#### B.4 WALL REFLECTIONS AND LOSSES

Wall losses are inserted into this model as an energy loss per lattice wall crossing (i.e.,  $1 - \Gamma^2$  per wall reflection where  $\Gamma$  is an averaged field reflection coefficient). Losses appearing in this manner lead to simple exponential decay of the reverberant fields as was described by Sabine for acoustic fields early in the 20<sup>th</sup> century.<sup>B-3</sup> Energy loss at each crossing implies that “far out” image sources diminish in their importance to the field contribution. If losses are too great, then the overall response is dominated by a few “close-in” early sources. The result is a loss of isotropic probability of direction of wavefront arrival and true random polarization on a chamber test item.

In normal chamber operation, reverberation is high. These problems are further mitigated by clever use of paddle wheels, which form an ensemble of statistically equivalent chambers, and proper processing of measurement results. In a poorly reverberant space, particularly if antennas with significant directivity are used, one expects intuitively that an isotropic field is not well generated from a single antenna arrangement. However, this can be partially offset by aggressive stirring and/or motion of the antennas so that all values of  $\theta, \phi$  are represented in a good ensemble average.

#### B.5 SUMMARY: EQUIVALENT REVERBERATION CHAMBER FROM THE METHOD OF IMAGES

Calculations based on the method of images show that after excitation with a short pulse, the chamber region quickly becomes filled with an increasingly great number of wavefronts. In the limiting case of no losses, the number of individual wavefronts grows as  $t^2$ , while the strength of any given wavefront varies as  $t^{-2}$ . Subjectively, the term “diffuse,” used in the acoustic community to describe reverberant fields, appears particularly descriptive.

---

<sup>B-3</sup> Exponential decay for acoustic fields was discussed in the following sources:  
W.C. Sabine, *Collected Papers on Acoustics* (New York: Dover, 1964): n. pag;  
Robert W. Young, “Sabine Reverberation Equation and Sound Power Calculation,” *Journal of the Acoustical Society of America*, vol. 31, no. 7 (July 1959): 912–921.

## **B.6 REFERENCES**

Collin, Robert E. *Field Theory of Guided Waves*. New York: McGraw-Hill Book Co., 1960.

Hayt, Jr., William H. *Engineering Electromagnetics, Fourth Edition*. New York: McGraw-Hill Book Co., 1981.

Sabine, W.C. *Collected Papers on Acoustics*. New York: Dover, 1964.

Young, Robert W. "Sabine Reverberation Equation and Sound Power Calculation," *Journal of the Acoustical Society of America*, vol. 31, no. 7 (July 1959): 912.

This page is intentionally blank.

**APPENDIX C**

**SCATTERING PROPERTIES OF A REVERBERANT FIELD**

This page is intentionally blank.

## CONTENTS

<u>Appendix</u>	<u>Page</u>
<b>C SCATTERING PROPERTIES OF A REVERBERANT FIELD</b>	
C.1 Introduction.....	C-1
C.2 Scalar Power Density .....	C-1
C.3 Leakage and Scattering at a Chamber Wall.....	C-2
C.4 Scattering from Objects Within a Chamber.....	C-4
C.4.1 Projected Area .....	C-4
C.4.2 Scattering, Diffraction, and the Extinction Paradox.....	C-5
C.4.3 Wall Leakage Calculations.....	C-7
C.5 Summary: Scattering Properties of a Reverberant Field .....	C-7
C.6 References.....	C-7

## ILLUSTRATION

<u>Figure</u>	<u>Page</u>
C-1 Diffraction Pattern Observed for a Conductive Strip at Two Ranges .....	C-5

## ABBREVIATIONS AND ACRONYMS

dB	Decibel
GHz	Gigahertz
m	Meter
no.	Number (issue number used with references)
NSWCDD	Naval Surface Warfare Center, Dahlgren Division
$Q$	Quality Factor
vol.	Volume (used with references)

This page is intentionally blank.



## C.1 INTRODUCTION

Due to its isotropic nature, a reverberant field interacts with objects in a manner different from that of a single planewave field or beam. Calculation results are similar to those for a randomly oriented, also called “tumble-averaged,” object in a single beam. Differences between isotropic and single-planewave interactions generally appear as innocuous factors of  $\frac{1}{2}$  or  $\frac{1}{4}$  in equations containing scalar power density ( $S$ ), but sometimes these differences lead to more puzzling results, such as the apparent loss of antenna directivity in a reverberant field.<sup>C-1</sup> This section presents some simple derivations and discussion to provide insight into reverberant field interactions.

In particular, one can determine the rate at which energy either passes through a small aperture in a wall or scatters from an object, such as a paddle wheel within a chamber. In these calculations, one assumes that the equilibrium isotropic state of the field is undisturbed. Energy passing through a wall aperture is lost to the field, so the aperture must not be too large. Evidently, no restriction on maximum size of a lossless scattering plate or other object within a chamber is required, as long as the field may otherwise be assumed to retain its isotropic nature.

## C.2 SCALAR POWER DENSITY

An ideal isotropic reverberant field has equal energy density propagating in all directions. Scalar power density  $S$  of a field with energy density  $u$  ( $\text{J}/\text{m}^3$ ) may be written as Equation (C-1):

$$S = c u \text{ (W/m}^2\text{)} \quad (\text{C-1})$$

where

$c$  is the speed of light.

Further, one may define  $\hat{S} = S/4\pi$  [ $\text{W}/(\text{m}^2 \times \text{steradian})$ ], as the power density propagating in a particular direction  $(\theta, \phi)$  per unit solid angle  $\Omega$ .  $\hat{S}$  may be referred to as the scalar power density per steradian. For an isotropic field,  $\hat{S}$  is a constant independent of  $\theta$  and  $\phi$ .  $\hat{S}$  has the same units as  $S$  because steradian is dimensionless. However,  $\hat{S}$  specifically refers to this notion in an isotropic field: *Equal energy propagates in any direction*. This may be stated even more precisely as follows: *Equal energy propagates in any direction per unit solid angle*.

---

<sup>C-1</sup> For more detail, refer to “Antenna Response and Field Measurements in a Reverberant Space,” appearing as Appendix F in this technical report, *Reverberant Microwave Propagation*.

When considering simple interactions of a field with apertures or scattering objects within a chamber, the definition of  $\hat{S}$  allows a precise way of describing the field, and most calculations are performed with simple integrals over  $\theta$  and  $\phi$ .

### C.3 LEAKAGE AND SCATTERING AT A CHAMBER WALL

The power transmitted ( $P_t$ ) through a small aperture  $A$  is given by Equation (C-2):

$$P_t = \frac{cU}{4\pi V} \cdot A \cdot \int_0^{2\pi} \int_0^{\pi} \sin(\theta) \cdot \cos(\theta) d\theta d\phi \quad (\text{C-2})$$

The quantity  $cU/4\pi V$  is  $\hat{S}$ , the scalar power density per steradian. Power escaping through  $A$  is given by the area  $A$  times the power density per unit solid angle integrated over  $2\pi$  steradians, which is one side (i.e., the inside) of the chamber wall that contains  $A$ . The integral over  $2\pi$  results by integrating  $\theta$  from 0 to  $\pi/2$ .

The  $\cos(\theta)$  term is an obliquity factor describing the projected area of  $A$  to rays that approach  $A$  at  $\theta$  angles off normal incidence.

The  $\sin(\theta)$  term is the usual spherical coordinate weighting factor describing a small elemental surface area on a unit sphere.

Carrying through the integral, one obtains Equation (C-3):

$$P_t = \frac{cU}{V} \cdot A \cdot \frac{1}{4} \quad (\text{C-3})$$

The factor  $\frac{1}{4}$  arises from the product of two factors of  $\frac{1}{2}$ . The first is from the obliquity factor  $\langle \cos(\theta) \rangle$ , which has an average value of  $\frac{1}{2}$  when integrated over  $2\pi$  steradians. The second factor of  $\frac{1}{2}$  is from the integral being taken over  $2\pi$  while the energy in  $S$  is actually spread out over  $4\pi$ .

The energy in an isotropic field can be viewed as traveling along rays. For the field to be isotropic, the rays are distributed uniformly in direction with a uniform number of rays per unit solid angle. There is no net direction of propagation, and equal amounts of energy travel in each direction along the ray, thus leading to a factor of  $\frac{1}{2}$  for a  $2\pi$  integral.

The result in Equation (C-3) is consistent with Lamb's calculation in which he calculated the  $Q$  of a large chamber with photons leaking through a small aperture of area  $A$ .<sup>C-2</sup> Hill also calculated similar results.<sup>3</sup> To calculate the power transmitted through an aperture, as in Equation (C-2) using Hill's notation, one would write Equation (C-4):

$$Pt = S \cdot \langle \sigma_t \rangle \cdot \frac{1}{2} \quad (\text{C-4})$$

where

$$\langle \sigma_t \rangle = A/2$$

The explicit factor  $\frac{1}{2}$  in Equation (C-4) is from  $2\pi$  versus  $4\pi$  illumination since the hole is in the wall. The obliquity factor of  $\frac{1}{2}$  is contained within the definition of  $\sigma$ .

When considering scattering rather than leakage effects, one can relax the constraint about the maximum size of  $A$ . This is because the scattered power is returned to the isotropic field rather than being lost and disturbing the equilibrium of the isotropic field state.

If  $A$  is allowed to be the entire chamber wall area, then the *wall-scattered* power  $P_{ws}$  is given by Equation (C-5):

$$P_{ws} = U \cdot c \cdot \frac{A}{4V} = U \cdot \frac{cA}{4V} = \frac{U}{T_C} \quad (\text{C-5})$$

where

$$T_C \text{ is the characteristic wall-scattering time } \frac{4V}{cA}.$$

The term  $1/T_C$  is the collision frequency for an isotropic field that has been derived by early acoustics researchers.<sup>C-3</sup>

Power approaches the wall only from the inside of the chamber, so the shadowing effect factor of  $\frac{1}{2}$  is retained, along with the factor of  $\frac{1}{2}$  from obliquity, leading to a factor 4 rather than 2 in the denominator.

---

<sup>C-2</sup> Lamb reports this calculation in two successively published journals:  
Willis E. Lamb, Jr., "Theory of a Microwave Spectroscope," *Physical Review*, vol. 70, no. 5 (1 September 1946) and no. 6 (15 September 1946): 308–317 (reprinted as one article).

Additionally, this calculation was recollected in private communications between the author and Theodore H. Lehman of T. H. Lehman Consultants (2005).

<sup>C-3</sup> David A. Hill, Mark T. Ma, Arthur Ondrejka, Bill F. Riddle, Myron T. Crawford, and Robert T. Johnk, "Aperture Excitation of Electrically Large Lossy Cavities," *IEEE Transactions on Electromagnetic Compatibility*, vol. 35, no. 3 (August 1994): 169–177.

## C.4 SCATTERING FROM OBJECTS WITHIN A CHAMBER

Scattered power from an object in a reverberant field is proportional to the average projected area of the object in the field and to the solid angle at which rays approach it. Further, even for large objects, one must also consider diffraction if the total scattered power is to be calculated.

### C.4.1 Projected Area

The average projected area of an aperture in a chamber wall is  $\frac{1}{4}$  of its geometric area. The factor of  $\frac{1}{4}$  results from an obliquity factor of  $\frac{1}{2}$  and a shadowing effect factor of  $\frac{1}{2}$  since power approaches it from only one side.

The projected area of a disc within a chamber may be calculated in terms of its one-sided area, an obliquity factor of  $\frac{1}{2}$ , and a shadowing effect factor of 1, since one may assume that power approaches the one-sided area from  $4\pi$  steradians. Conversely, one may use the two-sided area of the disc, an obliquity factor of  $\frac{1}{2}$ , and a shadowing effect factor of  $\frac{1}{2}$  since power approaches each side from  $2\pi$  steradians. The projected area of the disc within the chamber is given by  $\frac{1}{4}$  of its total two-sided area and is twice that of an equal one-sided area aperture in the wall.

A sphere of radius  $R$  has a projected area of  $\pi R^2$ , independent of the incidence angle of approaching rays. Viewed in this way, the obliquity factor and shadowing effect factor are each 1. The projected area of a sphere is twice that of a disc with the same radius.

These results are consistent with a theorem published in Van De Hulst's book, *Light Scattering by Small Particles*, which states that the tumble average geometrical cross section for any convex body with random orientation is equal to  $\frac{1}{4}$  of its total surface area.<sup>C-4</sup>

A common paddle wheel design for reverberation chamber operation is the so-called Z-fold design. The Z-fold contains nonconvex regions so the elegant  $A/4$  rule, relating projected area and geometric area, does not apply. Rays cannot approach a concave region in a surface from a full  $2\pi$  steradians, so the shadowing effect factor is less than  $\frac{1}{2}$ .

---

<sup>C-4</sup> H. C. Van De Hulst, *Light Scattering by Small Particles*, LOC#57-5936 (New York: John Wiley and Sons, 1957): Ch. 8.

#### C.4.2 Scattering, Diffraction, and the Extinction Paradox

When calculating total scattered power from objects within a chamber, one must consider diffraction effects even for large objects.<sup>C-5</sup>

Consider the interaction of an object with a single planewave or beam. This beam could be any one of the infinite number of beams that make up the reverberant field. The total scattering cross section for an object in a beam accounts for all of the energy removed from the beam. In the scattering process, energy is removed from the beam by diffraction around the object, as well as from the much more obvious process of reflection, which leads to the geometric shadow. Figure C-1 show the diffraction pattern from a 1-meter (m)-wide conductive strip, illuminated by a 3-gigahertz (GHz) unit intensity beam.<sup>C-6</sup>

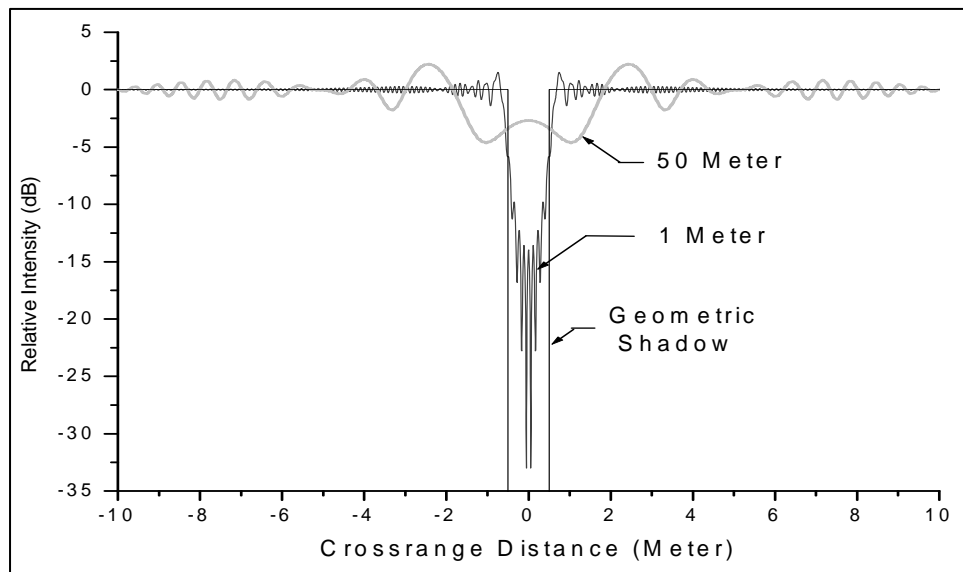


**Figure C-1. Diffraction Pattern Observed for a Conductive Strip at Two Ranges**

The patterns shown are those that would be observed at distances of 1 and 50 m behind the strip.

- At 1 m, the shadow is well defined with intensity reduced approximately 15 decibels (dB) near the center.
- At 50 m, the “shadow” is much wider than the geometric shadow and not as deep. Note that the diffraction pattern actually has a bright region in its center.

<sup>C-5</sup> The author is greatly indebted to Dr. Barton Billard [Naval Surface Warfare Center, Dahlgren Division (NSWCDD), Q23] for insightful description and discussions of diffraction effects (April 2007).

<sup>C-6</sup> At 3 GHz,  $\lambda = 0.1$  m.

- c. At greater range, the effect of the strip extends over a wider region of space, but is less pronounced in such a way that the total power in the diffraction pattern remains constant.

The waves that form a diffraction pattern are spherical.<sup>C-7</sup> They have  $1/R^2$  variation with distance away from the scattering object. The power in these waves is no longer in the original parallel beam/planewave, which means that the diffraction effect must be included in the total scattering cross section. Diffraction removes power from the original beam. More detailed calculations show that the power in the waves forming the diffraction pattern is equal in magnitude to the power that is intercepted from the beam by its geometric cross section. This is important: If the shadowing object were removed and replaced by a radiating object with intensity at its surface equal to that of the incident beam, the diffraction pattern would vanish.

The total cross section of an object in the beam is given, thus, by twice its geometric area because of the two processes, shadowing and diffraction, which operate on the beam. The notion that one must use twice the geometric area of an object to calculate the total cross section in a beam, rather than simply 1 times the geometrical area, is counterintuitive and is referred to in optics as the *extinction paradox*. The factor 2 in relating the total scattering cross section to the geometric area of a large object is called the *extinction efficiency*.<sup>C-8</sup>

The above discussion in this subsection applies for an object in a single planewave beam. An isotropic field consists of an infinite number of single planewave beams. In an isotropic reverberant field, one would calculate the scattering cross section from the tumble-averaged projected area with an additional factor of 2 because of diffraction.

In everyday experience, people normally observe geometric shadowing by an object illuminated by a light beam and do not sense the diffraction effects, which only become apparent at a long distance from a shadowing object. However, waves travel a great distance in a good chamber. For example, in a chamber with a 10-foot characteristic scattering length ( $L = 4V/A_c$ ) and a reverberation index of 200,<sup>C-9</sup> waves travel 2000 feet in a chamber  $1/e$  time. Obviously, a diffraction pattern would not be directly observable in a chamber. However, the waves that would normally form a diffraction pattern strike the chamber walls and, subsequently, reilluminate the paddle wheels and walls at different angles than they would if they were still in the original beam.<sup>C-10</sup>

Due to diffraction, the scattering cross section of an object, such as a paddle wheel, is calculated by tumble averaging the projected area over  $4\pi$  and then multiplying the result by 2.

---

<sup>C-7</sup> Notice that the waves appearing in Figure C-1 are actually cylindrical for the one-dimensional strip.

<sup>C-8</sup> The factor 2 is a limiting case for large objects. Resonance effects are observed at  $D/\lambda$  even as high as 10, which cause some departure from the limiting case.  $D$  is a characteristic dimension of the object.

<sup>C-9</sup> These are approximate values for the Lindgren Chamber at NSWCDD.

<sup>C-10</sup> The reverberant field consists of an infinite number of planewave beams.

### C.4.3 Wall Leakage Calculations

A thoughtful reader might ask, “Why is it unnecessary to multiply the average projected area of a wall leakage aperture by a factor of 2 to correctly calculate the leakage?” The leakage calculation is correct with 1 times the projected area. According to Babinet’s principle, the leakage problem is complementary to the scattering problem described in Figure C–1. In a complementary geometry, a scattering object would be replaced by an equal-area aperture in a screen. In the case of Figure C–1, the aperture would be a slit. The power passing through the aperture would be calculated as the product of intensity and 1 times the aperture geometrical area.

## C.5 SUMMARY: SCATTERING PROPERTIES OF A REVERBERANT FIELD

Due to its isotropic rather than unidirectional nature, an isotropic field interacts with objects differently from the manner in which a single planewave interacts. A quantity  $\hat{S}$ , which is the scalar power density per steradian, has been defined. Power scattered from an object or transmitted through an aperture is calculated as the product of the cross section or projected area and  $\hat{S}$  integrated over  $2\pi$  or  $4\pi$  steradians. Factors of  $\frac{1}{2}$  or  $\frac{1}{4}$  emerge in the calculation results due to obliquity effects from rays approaching an aperture at off-normal incidence and due to shadowing effects where rays approach an object from only one side. Diffraction effects, which are often ignored when calculating the properties of objects that are large compared with wavelength, must be considered when calculating the scattering cross section of objects within a chamber.

## C.6 REFERENCES

- Billard, Barton. NSWCDD, Q23. Private communications with the author. April 2007.
- Hill, David A., Mark T. Ma, Arthur Ondrejka, Bill F. Riddle, Myron T. Crawford, and Robert T. Johnk. “Aperture Excitation of Electrically Large Lossy Cavities,” *IEEE Transactions on Electromagnetic Compatibility*, vol. 35, no. 3 (August 1994): 169–177.
- Lamb, Jr., Willis E. “Theory of a Microwave Spectroscope,” *Physical Review*, vol. 70, no. 5 (1 September 1946) and no. 6 (15 September 1946): 308–317 (printed as one article).
- Lehman, Theodore H. (T. H. Lehman Consultants). Private communications with the author. 2005.
- Van De Hulst, H. C. *Light Scattering by Small Particles*. LOC#57-5936. New York: John Wiley and Sons, 1957: Ch. 8.

This page is intentionally blank.



**APPENDIX D**

**WIRE CURRENT IN A REVERBERANT FIELD**

This page is intentionally blank.

## CONTENTS

<u>Appendix</u>	<u>Page</u>
<b>D WIRE CURRENT IN A REVERBERANT FIELD</b>	
D.1 Introduction.....	D-1
D.2 Dipole in a Planewave Field .....	D-1
D.3 Application of the Dipole Model in a Stochastic Field .....	D-2
D.4 Experimental Results .....	D-3
D.5 Discussion.....	D-5
D.6 Summary: Wire Current in a Reverberant Field.....	D-6
D.7 References.....	D-6

## ILLUSTRATIONS

<u>Figure</u>	<u>Page</u>
D-1 Equivalent Circuits for a Dipole Receiving Antenna and a Dipole Element Scatterer .....	D-2
D-2 Current in Wires Placed in 10 Volts/Meter (V/m) (Peak) Field in a Reverberation Chamber .....	D-4

## ABBREVIATIONS AND ACRONYMS

dB	Decibel
E field	Electric field component of electromagnetic wave
EED	Electro-Explosive Device
EMC	Electromagnetic Compatibility
ft	Foot (feet)
GHz	Gigahertz
HERO	Hazards of Electromagnetic Radiation to Ordnance
IEEE	Institute of Electrical & Electronics Engineers
m	Meter(s)
ma	Milliampere
MAX	Maximum
MHz	Megahertz
n. pag.	No pagination (used with references)
NIST	National Institute of Standards & Technology
NSWCDD	Naval Surface Warfare Center, Dahlgren Division
OATS	Open Air Test Site
V	Volt(s)

## D.1 INTRODUCTION

An Electromagnetic Compatibility (EMC) engineer frequently needs to be able to estimate the maximum current in a wire when it is in a reverberant field. An example situation involves evaluating currents for Hazards of Electromagnetic Radiation to Ordnance (HERO) problems. This can be done using familiar models and constants. As a reasonable worst case estimate, the current in the center of a half-wave dipole is calculated in a two-step process:

- Step 1. Calculate the current in the center of the dipole when it is placed in a planewave environment and aligned with the incident E field.
- Step 2. Relate the single planewave E field to an equivalent reverberant E field.

## D.2 DIPOLE IN A PLANEWAVE FIELD

The capture area of a dipole receiver in a planewave field is given as Equation (D-1):

$$A_o = \frac{\lambda^2}{4\pi} G_{Di} \quad (\text{D-1})$$

Additionally, the power received by a matched 73-ohm receiver at the center of the dipole is given by Equation (D-2):

$$P_{Rx} = I^2 \cdot 73 = \frac{E^2}{377} \cdot A_o \quad (\text{D-2})$$

Experimental results and more detailed calculations show that the optimal impedance for maximum power transfer to a receiver at the center of the dipole is 73 ohm. The dipole is displayed as an equivalent circuit in Figure D-1.

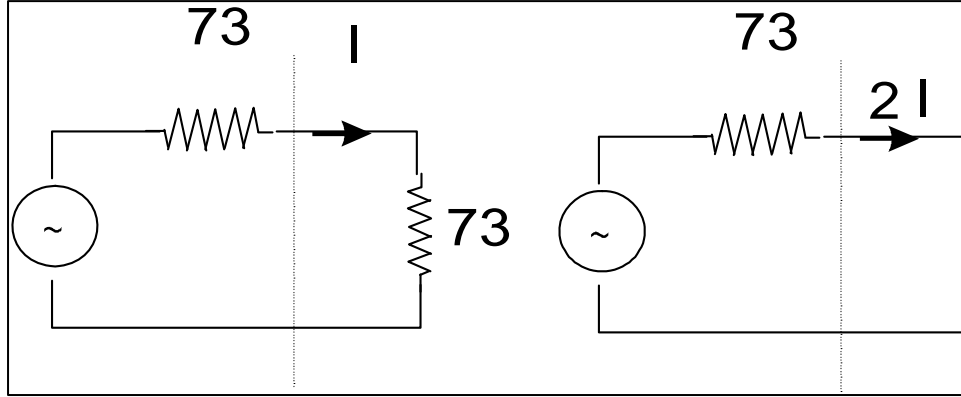


**Figure D-1. Equivalent Circuits for a Dipole Receiving Antenna and a Dipole Element Scatterer**

The dipole center is a voltage source with 73-ohm internal impedance. Normally, if the dipole is used as a receiving antenna, a 73-ohm receiver is connected. If the dipole is not used as a receiving antenna, but simply as a scatterer or an electro-explosive device (EED) bridge wire, the 73-ohm load is removed and the current  $I$  will double. This model assumes that the bridge wire resistance is zero. From manipulating Equations (D-1) and (D-2), one can write Equation (D-3):

$$\hat{I} = E \cdot \sqrt{\frac{\lambda^2 G_{Di}}{4\pi 377 73}} \cdot 2 \quad (\text{D-3})$$

where

$\hat{I}$  is the current in the center of the half-wave dipole scatterer.

The current  $\hat{I}$  is a maximum current; additionally, it is the maximum current in the standing-wave current pattern induced in the dipole under optimal alignment and polarization conditions. Further, Equation (D-3) assumes that the wire is resonant.

### D.3 APPLICATION OF THE DIPOLE MODEL IN A STOCHASTIC FIELD

The field in a reverberant environment may be specified in terms of its mean square value  $\langle E^2 \rangle$ .

$\langle E^2 \rangle$  has three equal components:  $\langle E^2 \rangle = \langle E_x^2 \rangle + \langle E_y^2 \rangle + \langle E_z^2 \rangle$ .

Any single component of the field,  $\langle E_x^2 \rangle$  for example, is given by  $\langle E_x^2 \rangle = \langle E^2 \rangle / 3$ .

By squaring Equation (D-3) to obtain  $\hat{I}^2$  and assuming that the dipole remains aligned with a single component of the field, one can rewrite Equation (D-3) as Equation (D-4):

$$\hat{I}^2 = \frac{\langle E^2 \rangle}{3} \cdot \frac{\lambda^2 G_{Di}}{4\pi} \cdot \frac{1}{377 \cdot 73} \cdot 4 \quad (\text{D-4})$$

where

$\langle E^2 \rangle$  is the mean square E field in the reverberant space.

Arbitrarily, the dipole gain factor  $G_{Di}$  is retained. For a half-wave dipole at resonance,  $G_{Di}$  is equal to 2.14 decibels (dB). Optimal alignment with  $\sqrt{E_x^2}$ , a single component of  $E^2$  is assumed, and all other field components are ignored. Although  $\sqrt{E_x^2}$  is perfectly aligned with the antenna, the  $k$  vectors for the individual wavelets that make up  $\sqrt{E_x^2}$  are distributed over  $4\pi$  steradians.

#### D.4 EXPERIMENTAL RESULTS

The data displayed in Figure D-2 were obtained by placing 6-foot (ft), 3-ft, and 1-ft wires in a reverberation chamber with a 10 volt/meter (V/m) peak field.<sup>D-1</sup> An instrumented EED bridge wire was placed in the center of each wire to record the induced current as excitation frequency was stepped. Measured currents are compared with the theoretical model represented by Equation (D-4).

---

<sup>D-1</sup> S. D. Pierce and R. E. Richardson, *Half-Wave Dipole Model and Induced Current in Long Wires in Overmoded Cavities*, Paper presented at Reverberation Chamber, Anechoic Chamber, and Open Air Test Site (OATS) Conference, User Group Meeting, Austin, Texas, 30 April 2003: N. pag.

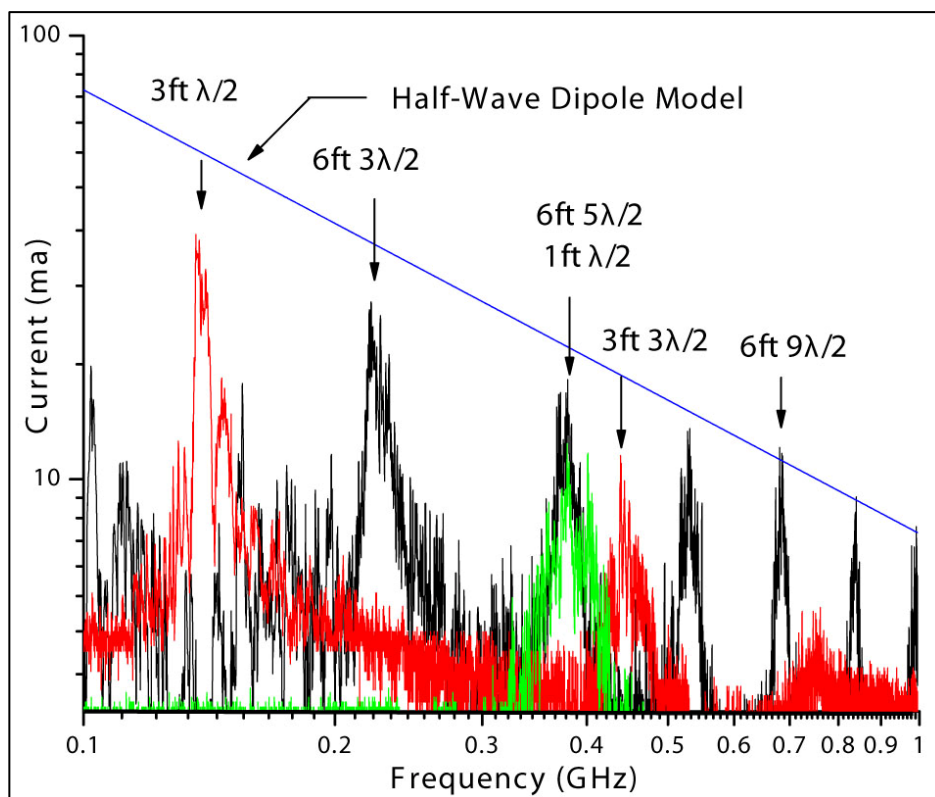


**Figure D-2. Current in Wires Placed in 10 Volts/Meter (V/m) (Peak) Field in a Reverberation Chamber**

The dipole model for calculating current assumes that the antenna is resonant and that the current is measured at a maximum current point on the wire. Data in Figure D-2 demonstrate that the wires go in and out of resonance as the frequency is stepped.

The 3-ft wire shows a major response at approximately 150 megahertz (MHz), at which it exhibits half-wave resonance and again at 450 MHz, approximately 3 times the first response frequency. A major response at 300 MHz is not registered because the instrumented EED probe is at the center of the wire. The standing wave pattern at the frequency at which the wire is one wavelength long has a current null at the wire center. The response of the 6-ft wire at approximately 230 MHz is actually a third-order response, corresponding to the 450-MHz response noted for the 3-ft wire. Higher order responses (such as 5, 7, 9, 11, or 13) for the 6-ft wire may be observed at 525, 680, 850, and 1000+ MHz.



## D.5 DISCUSSION

The half-wave dipole model specified by Equation (D-4) provides an approximate worst-case envelope for the maximum currents in the wires as they go through resonance. However, agreement between measured data and the half-wave dipole model response is only approximate. Application of the simple dipole model exposes an interesting issue regarding gain or directivity and its effect (or lack thereof) on wire current response in a reverberant field.

The decrease in maximum current with increasing frequency in the Figure D-2 data actually appears to be somewhat less rapid than  $1/F^2$  as dictated by  $\lambda^2$  in Equation (D-4). The use of  $G_{Di}$  in Equation (D-4) is arbitrary and controversial since gain is thought *not* to apply in an isotropic environment. Conversely, if one were to apply the 2.14-dB-gain figure for half-wave response, why would one not apply successively higher gain factors for higher order responses? For example, the directivity of an antenna that is 9 half-wavelengths long is 6.67 dB.<sup>D-2</sup> Gradually increasing directivity with frequency, as is characteristic of wire response in a planewave field, would decrease the slope of the model calculation line from Equation (D-4), displayed in Figure D-2. Decreasing the slope slightly would make it appear to follow the measurement data more closely.

Arguments that lead to unity gain with 3-dB-polarization loss for wire antenna response describe *average* rather than peak response. For example, the simple discussion in Appendix F.3<sup>D-3</sup> and other more sophisticated calculations<sup>D-4</sup> involve an integral over  $4\pi$  steradians and imply *ensemble-averaged response* rather than peak response. While these calculations clearly show that gain does not apply on average, they do *not* show that gain cannot affect peak response.

On the other hand, a body of experimental data indicates that the statistical behavior of received power response from moderate gain antennas is similar to that from low-gain antennas.<sup>D-5</sup> Intuitively, one would think that if antenna gain or directivity is a significant factor in determining antenna peak response in a reverberant field, then it should cause the statistical behavior of received power data from a high-gain antenna to be different from that of a low-gain antenna. However, since the statistical behavior of response from low- and high-gain antennas is virtually identical, antenna gain or directivity, apparently, has little or no effect on peak response.

<sup>D-2</sup> Ronald W. P. King, *The Theory of Linear Antennas* (Cambridge, Massachusetts: Harvard University Press, 1956): 563.

<sup>D-3</sup> For more detail, refer to “Antenna Response and Field Measurements in a Reverberant Space,” appearing as Appendix F in this technical report, *Reverberant Microwave Propagation*.

<sup>D-4</sup> David A. Hill, “Linear Dipole Response in a Reverberation Chamber,” *IEEE Transactions on Electromagnetic Compatibility*, vol. 41, no. 4 (November 1999): 365–368.

<sup>D-5</sup> The author is indebted to Theodore H. Lehman, John Ladbury, and Blaise L. Corbett for several thoughtful discussions about statistical behavior, August 2007.

Inclusion of gain or increasing gain with increasing frequency, as is characteristic of wire antenna behavior in free space, may be useful for engineering calculations, particularly where a worst case safety margin is often desired. However, presently there are no other compelling experimental or theoretical reasons for its inclusion.

## **D.6 SUMMARY: WIRE CURRENT IN A REVERBERANT FIELD**

Wire current in a reverberant field is calculated using a half-wave dipole model and compared with measurement data taken with several different wires suspended in a 10 V/m (peak) reverberant field. The dipole model calculates a near-worst case value for the maximum current induced at some point in the wire when it becomes resonant.

The approximate agreement between the dipole model and measurement data demonstrates that the model is useful for engineering estimates.

## **D.7 REFERENCES**

- Corbett, Blaise L. (NSWCDD, Q51). Private communications with the author. August 2007.
- Hill, David A. "Linear Dipole Response in a Reverberation Chamber," *IEEE Transactions on Electromagnetic Compatibility*, vol. 41, no. 4 (November 1999): 365–368.
- King, Ronald W. P. *The Theory of Linear Antennas* (Cambridge, Massachusetts: Harvard University Press, 1956): 563.
- Ladbury, John (NIST, 818.02). Private communications with the author. August 2007.
- Lehman, Theodore H. (T. H. Lehman Consulting). Private communications with the author. August 2007.
- Pierce, S. D. and R. E. Richardson. *Half-Wave Dipole Model and Induced Current in Long Wires in Overmoded Cavities*. Paper presented at Reverberation Chamber, Anechoic Chamber, and Open Air Test Site (OATS) Conference, User Group Meeting; Austin, Texas. 30 April 2003.

**APPENDIX E**  
**CAVITY PERTURBATION MEASUREMENTS**

This page is intentionally blank.

## CONTENTS

<u>Appendix</u>	<u>Page</u>
<b>E CAVITY PERTURBATION MEASUREMENTS</b>	
E.1 Introduction.....	E-1
E.2 Wall Surface Resistivity .....	E-1
E.2.1 Relationship Between Cavity Energy and Wall Losses .....	E-2
E.2.2 Cavity $Q$ and $1/e$ Time in Terms of Wall Surface Resistivity.....	E-2
E.2.3 Prototype Panel Surface Resistivity Measurement .....	E-3
E.3 Summary: Cavity Perturbation Measurements .....	E-5

## ILLUSTRATIONS

<u>Figure</u>	<u>Page</u>
E-1 Time Constant Decrease due to Chamber Loading with a 4-ft by 8-ft Panel .....	E-4
E-2 Increase in Reverberation Chamber $1/t$ with Increased Loading Panel Area.....	E-5

## ABBREVIATIONS AND ACRONYMS

E field	Electric field component of electromagnetic wave
ft	Foot (feet)
GHz	Gigahertz
H field	Magnetic field component of electromagnetic wave
NSWCDD	Naval Surface Warfare Center, Dahlgren Division
ohm/sq	Ohms per square
$Q$	Quality Factor

This page is intentionally blank.

## E.1 INTRODUCTION

Cavity perturbation measurements are commonly performed using small laboratory test cavities operating in a single mode for evaluation of conductive or dielectric properties of samples of material. Test samples are placed either within the cavity or as a cavity replacement wall in a position such that the mode E field or H field interacts with it in a known way. Changes in the resonant frequency and  $Q$  are observed due to the insertion of the test sample (or substitution of the wall sample). The electrical properties of the test sample are extracted from energy conservation relationships and from the general principle that at resonance, the magnetic and electric energies are equal. Real dielectric constant or magnetic permeability values are derived from mode resonant frequency variations. Loss-related factors, such as loss tangent or resistivity, are derived from changes in cavity  $Q$ . Data extraction relationships are derived with the understanding that the perturbation is not so large as to change the basic nature of the fields from their unperturbed state.

Mode resonant frequency changes are not practical to measure in a reverberation chamber, so real dielectric constant values are not available. However, the sensitivity of radar-based technique to  $Q$  (i.e.,  $1/e$  time) variation indicates that the technique should be a powerful tool for determination of loss properties, such as sheet resistivity of a test sample.

## E.2 WALL SURFACE RESISTIVITY

With a test sample positioned as a wall of a cavity, the analytical portion of the measurement is to develop a relationship between the energy in the cavity and the losses in the cavity wall. This relationship can be established with the following assumptions:

- a. The fields within the cavity are expressible in terms of the usual rectangular modes.
- b. Due to the random nature of the problem, all of these modes are equally probable.
- c. Also due to the random nature of the problem, there are no preferred x, y, or z directions in the test cavity.

### E.2.1 Relationship Between Cavity Energy and Wall Losses

In general, cavity  $Q$  can be written as shown in Equation (E-1):

$$Q = \frac{\omega U}{P_{diss}} = \omega \tau \quad (\text{E-1})$$

where

$\omega$  is  $2\pi$  times the resonant frequency.

$U$  is the stored energy in the cavity fields.

$P_{diss}$  is the average dissipated power.

$\tau$  is the 1/e time.

Additionally,  $U$  is equal to the maximum electric energy, given as  $\epsilon_0 \cdot \overline{E_v^2} \cdot V$ , where  $\epsilon_0$  is free-space permeability;  $V$  is the cavity volume; and  $\overline{E_v^2}$  is the temporal peak value of  $E$ , spatially averaged over the cavity volume. For a cavity at resonance, the electric and magnetic energies are equal; thus,  $\mu_0 \cdot \overline{H_v^2} = \epsilon_0 \cdot \overline{E_v^2}$ , where  $H$  is similarly averaged over the cavity volume. Further, by conducting a similar average over the cavity walls, one can show that for  $H$ ,  $\overline{H_s^2} = 4/3 \cdot \overline{H_v^2}$ .<sup>E-1</sup>

Power dissipated in the walls is given by  $J_s^2 \cdot R_s \cdot S$ , where  $J_s$  is the surface current density at the cavity wall;  $R_s$  is the surface resistivity; and  $S$  is the wall surface area. At each point on the walls,  $|J| = |H|$ .  $J_s$  is perpendicular to  $H_s$  but is equal in magnitude.

### E.2.2 Cavity $Q$ and 1/e Time in Terms of Wall Surface Resistivity

From Section E.2.1,  $\overline{H_s^2} = 4/3 \cdot \epsilon_0 / \mu_0 \cdot \overline{E_v^2}$  and  $Q$  may be written as Equation (E-2):

$$Q = \omega \tau = \frac{3}{4} \cdot \frac{\omega V \mu_0}{R_s S} \quad (\text{E-2})$$

$R_s$  may be written as  $1/\delta\sigma$ , where  $\sigma$  is conductivity and  $\delta$  is skin depth given by Equation (E-3):

$$\delta = \sqrt{\frac{2}{\omega \mu_0 \sigma}} \quad (\text{E-3})$$

---

<sup>E-1</sup> This equation is described briefly in “Fields at Chamber Walls,” appearing as Appendix G in this technical report, *Reverberant Microwave Propagation*.



Substituting for  $R_S$  above yields Equation (E-4):

$$Q = \frac{3}{2} \cdot \frac{V}{S \delta} \quad (\text{E-4})$$

Equation (E-4) is a well known general relation and, thus, provides a check on Equation (E-2).

Further manipulation of Equation (E-2) yields Equation (E-5):

$$\frac{1}{\tau_0} = \frac{4/3}{\mu_0 V} \cdot S R_S \quad (\text{E-5})$$

The variation in  $1/\tau$  due to variation in  $R_S$  of a wall surface area  $S$  is given by Equation (E-6):

$$\Delta(1/\tau) = \frac{4}{3\mu_0 V} \cdot \Delta(S R_S) \quad (\text{E-6})$$

### **E.2.3 Prototype Panel Surface Resistivity Measurement**

The relationship in Equation (E-6) has been used to determine the surface resistivity of some prototype composite test panels that were measured in the large Naval Surface Warfare Center, Dahlgren Division (NSWCDD) reverberation chamber.

The increase in  $1/\tau$  due to placement of a 4-foot (ft) by 8-ft panel in the large NSWCDD reverberation chamber can be seen as a slightly increased decay rate or a steeper slope in the data of Figure E-1.

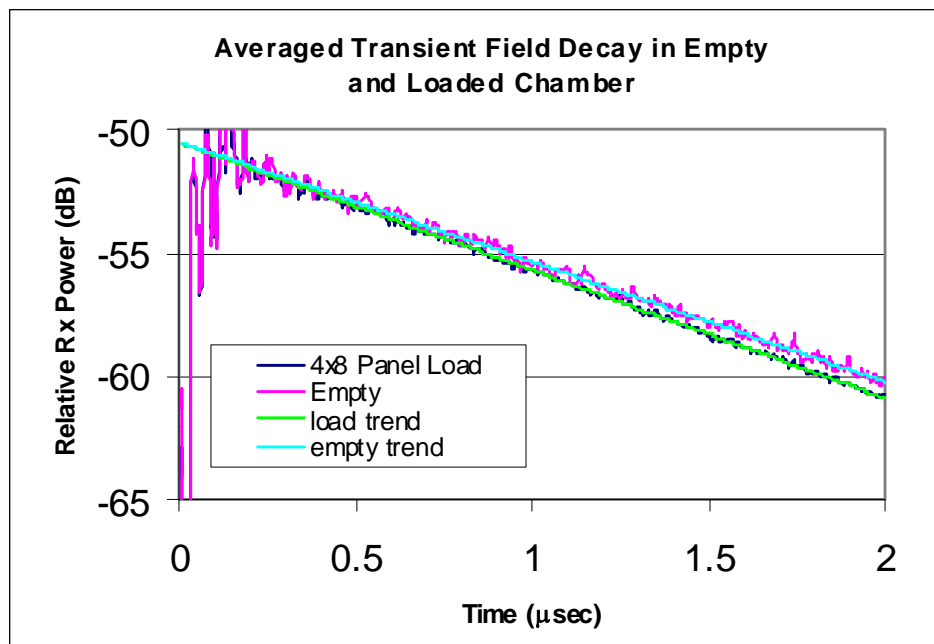


**Figure E-1. Time Constant Decrease due to Chamber Loading with a 4-ft by 8-ft Panel**

This measurement was performed as a TD measurement with a short microwave pulse, centered at 3.5 gigahertz (GHz). Additional data with a 2-ft by 4-ft panel and both a 2-ft by 4-ft and 4-ft by 8-ft panel placed in the chamber show the behavior indicated in Figure E-2. The perturbation (i.e., the increase in  $1/\tau$ ) is proportional to the panel surface area, as Equation (E-1) states that it should be. Thus, the data are consistent with the requirement: The perturbation must be *small* for the perturbation response to be *linear*.

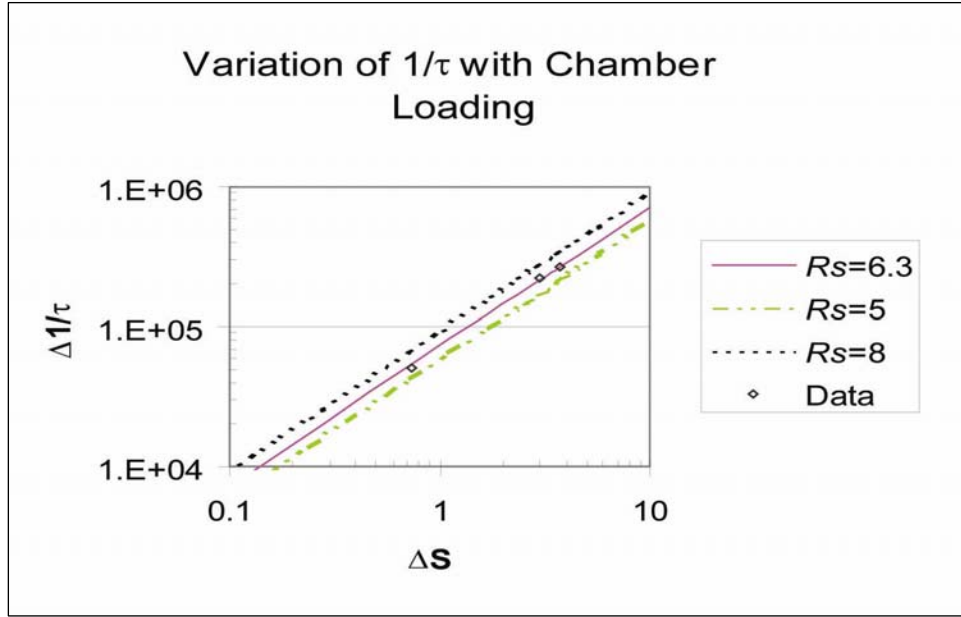


**Figure E-2. Increase in Reverberation Chamber  $1/\tau$  with Increased Loading Panel Area**

The data of Figure E-2 fit a value of 6.3 ohm/square (ohm/sq). This represents an increase in surface resistivity over that of the steel chamber floor, which has an effective value of approximately 1 ohm/sq. The resultant measured value of 7.3 ohm/sq is consistent with a design value of 7 ohm/sq for the test panels.

### **E.3 SUMMARY: CAVITY PERTURBATION MEASUREMENTS**

Because of the high precision available in time domain based measurement of loss rate in a reverberation chamber, this technique may be used for determination of loss factors of various materials. The perturbation measurement results described here clearly demonstrate the utility of a reverberation chamber-based measurement to verify the properties of composite materials and structures that could be used for ship construction.

This page is intentionally blank.

**APPENDIX F**

**ANTENNA RESPONSE AND FIELD MEASUREMENTS  
IN A REVERBERANT SPACE**

This page is intentionally blank.

## CONTENTS

<u>Appendix</u>	<u>Page</u>
<b>F ANTENNA RESPONSE AND FIELD MEASUREMENTS IN A REVERBERANT SPACE</b>	
F.1 Introduction.....	F-1
F.2 Localized Measurements in a Poorly Reverberant Space.....	F-1
F.3 Apparent Antenna Gain in a Highly Reverberant Field .....	F-5
F.4 Summary: Antenna Response and Field Measurements in a Reverberant Space .....	F-7
F.5 References.....	F-7

## ILLUSTRATION

<u>Figure</u>	<u>Page</u>
F-1 Incident Electric Field on Three Orthogonally Placed Dipole Antennas .....	F-2

## TABLE

<u>Table</u>	<u>Page</u>
F-1 Directivity Factors for Short Dipole (SD) and Half-Wave Dipole (HWD)...	F-3

## ABBREVIATIONS AND ACRONYMS

CW	Continuous Wave
dB	Decibel(s)
E field	Electric field component of electromagnetic wave
EMC	Electromagnetic Capability
HWD	Half-Wave Dipole
IEEE	Institute of Electrical & Electronics Engineers
J	Joule(s)
m	Meter(s)
N. p.	No place (used with references)
n. pag.	No pagination (used with references)
no.	Number (issue number used with references)
<i>PD</i>	Power Density
SD	Short Dipole
vol.	Volume (used with references)
W	Watt(s)



## F.1 INTRODUCTION

Although field probes are occasionally used, most measurements that an Electromagnetic Compatibility (EMC) engineer makes in reverberant spaces will be performed with antennas. Since the field in a reverberant space is, by definition, never a single planewave field, the usual free-space relationships used for reducing data acquired from an antenna in a reverberant space must be modified. Specifically, the effective gain of an antenna is of primary importance. This appendix describes how the power density (PD) in a space may be deduced, even though the incidence direction and polarization of the fields may be unknown or random. The following discussion addresses directivity and polarization issues. The antennas are assumed to be efficient and well matched.

## F.2 LOCALIZED MEASUREMENTS IN A POORLY REVERBERANT SPACE

Hill has shown that the effective area  $A_0$  of a matched dipole in a reverberation chamber is given by Equation (F-1):<sup>F-1</sup>

$$A_0 = \frac{\lambda^2}{8\pi} \quad (\text{F-1})$$

$A_0$  has half the area of a matched isotropic receiver. The 3-decibel (dB) difference is attributed to polarization loss.

In general, the isotropic PD in a space can be inferred from an ensemble average of received power values formed by placing the receiving antenna in the space and taking a number of random readings. The PD value is calculated by dividing the average received power by the effective area  $A_0$ , given in Equation (F-1). The readings can be randomized by either using multiple paddle wheel positions or multiple antenna locations. Further, if PD at a particular point in a test space is required, multiple antenna orientations could be employed.

Equation (F-1) is true for any antenna, regardless of its gain when the field is highly reverberant—meaning *isotropic*—and a good ensemble average is obtained. Additionally, it is approximately true for a low-gain low-directivity antenna, if the ensemble average is formed from three orthogonal measurements in a manner similar to that where one might use a single-axis E field probe to measure three components of an E field at a specific location. An understanding of antenna pattern effects and insight as to how the 3-dB-polarization loss arises can be gained by examining the results of a simple measurement sequence one would use to obtain a *three-orthogonal-measurement average*.

---

<sup>F-1</sup> David A. Hill, “Linear Dipole Response in a Reverberation Chamber,” *IEEE Transactions on Electromagnetic Compatibility*, vol. 41, no. 4 (November 1999): n. pag.

At any given test point in a measurement space, three received power readings ( $P_x$ ,  $P_y$ , and  $P_z$ ) may be taken with the antenna oriented along three orthogonal axes. The  $PD$  is calculated from Equation (F-2):

$$PD = \frac{(P_x + P_y + P_z)}{3} \cdot \frac{1}{\lambda^2 / 8\pi} \quad (\text{F-2})$$

To calculate power density, the average received power,  $(P_x + P_y + P_z)/3$ , is divided by  $\lambda^2/8\pi$ .

Figure F-1 depicts a wave with E field  $E_i$  and propagation vector  $k_i$  approaching dipole antennas at the origin. For this case,  $E_i$  and  $k_i$  are in the x-z plane so  $\phi = 0$ . The propagation vector  $k_i$  approaches the origin at an angle  $\theta$ .

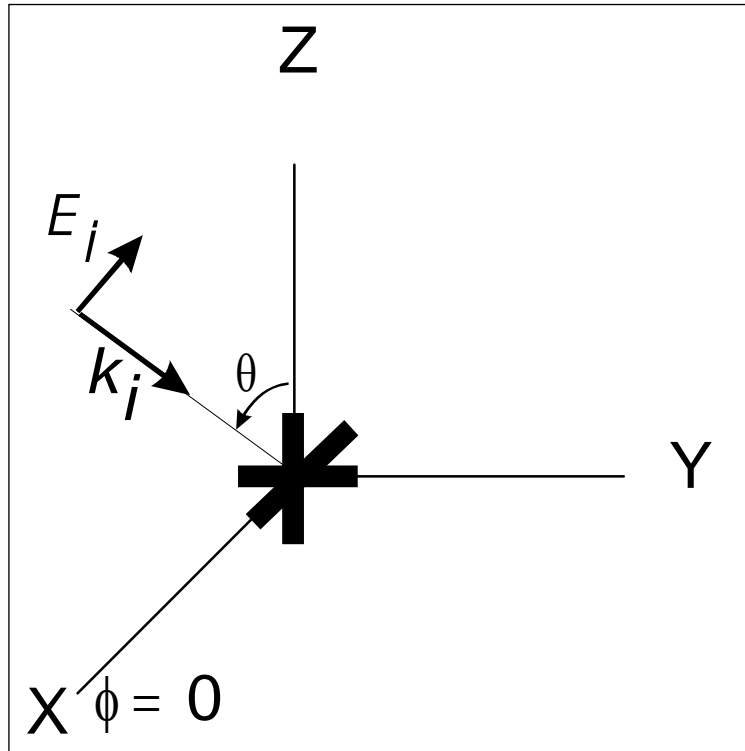


**Figure F-1. Incident Electric Field on Three Orthogonally Placed Dipole Antennas**

For any field component incident with its  $k$  vector at some angle  $\theta$  to the antenna axis, the received power is calculated from the product of incident  $PD$ , antenna directivity  $D(\theta)$ , and an additional polarization factor ( $\Pi$ ). For the linear polarization case considered here, the polarization factor is calculated as the cosine squared of the angle between the

incident E field and the  $\theta$  component of the E field that the test antenna would radiate if it were transmitting.<sup>F-2</sup>

The directivity of a half-wave dipole (HWD) and a short dipole (SD) are given respectively by Equations (F-3) and (F-4):

$$D_{HWD} = 1.64 \cdot \left[ \frac{\cos(\pi/2 \cdot \cos(\theta))}{\sin \theta} \right]^2 \quad (\text{F-3})$$

and

$$D_{SD} = 1.5 \cdot \sin^2(\theta) \quad (\text{F-4})$$

Values at  $\theta = 0$  (end-on), 45 degrees (diagonal), and 90 degrees (broadside) are provided in Table F-1.

**Table F-1. Directivity Factors for Short Dipole (SD) and Half-Wave Dipole (HWD)**

Antenna Directivity Factor D( $\theta$ )			
Type	End-on	Diagonal	Broadside
$\theta$	0	45	90
SD	0	0.75	1.5
HWD	0	0.6469	1.6506

As an example, consider a wave with  $E$  and  $k$  in the x-z plane as depicted in Figure F-1. The  $PD$  of the wave is given by  $E^2/377$ .

According to free-space ideas, the power  $Pr$  received by the antenna would be given by Equation (F-5):

$$Pr = \frac{\lambda^2}{4\pi} \cdot D(\theta, \phi) \cdot \Pi \cdot PD \quad (\text{F-5})$$

<sup>F-2</sup> The polarization factor is established in two sources:  
 Warren L. Stutzman and Gary A. Thiele, *Antenna Theory and Design, Second Edition*, ISBN 0-471-04458-X (New York: John Wiley & Sons, 1998): 396-400;  
 Robert E. Collin, *Antennas and Radiowave Propagation*, ISBN 0-07-011808-6 (N.p: McGraw-Hill Book Co., circa 1960): 300-303.

With  $E$  parallel to the  $z$  axis and  $k$  parallel to the  $x$  axis (i.e.,  $\theta = 90$  degrees), a short-matched dipole antenna oriented successively along the  $x$ ,  $y$ , and  $z$  axes would receive the following power levels designated in Equation (F-6):

$$Pr = 0 + 0 + PD \cdot \frac{\lambda^2}{4\pi} \cdot 1.5 \quad (\text{F-6})$$

For the antenna aligned with the  $x$  axis,  $\Pi$  and  $D$  are both zero.

For the antenna aligned with the  $y$  axis,  $\Pi$  is zero.

For the antenna aligned with the  $z$  axis,  $\Pi$  is unity and  $D$  is 1.5.

Thus, for this case the  $z$ -axis-oriented antenna has a nonzero contribution to  $Pr$ .

Using the relationship from the Equation (F-2), the calculated  $PD$  from this series of three measurements is given by Equation (F-7):

$$PD = \frac{(Pr)}{3 \cdot \lambda^2 / 8\pi} = PD \cdot \frac{2}{3} \cdot 1.5 \quad (\text{F-7})$$

Equation (F-7) is identically correct.

If the  $k$  vector for the wave were at  $\theta = 45$  degrees, the received power would yield Equation (F-8):

$$Pr = PD \cdot \frac{\lambda^2}{4\pi} \cdot (0.75 + 0 + 0.75) \quad (\text{F-8})$$

Using Equation (F-2), Equation (F-8) would yield an identically correct result.

On the other hand, if an HWD rather than an ideal SD is used, Equations (F-6) and (F-8) become Equation (F-9):

$$Pr = 0 + 0 + PD \cdot \frac{\lambda^2}{4\pi} \cdot 1.6406 \quad (\text{F-9})$$

For the case of  $\theta = 90$  degrees, Equation (F-9) together with Equation (F-2) yields an answer that is 0.389 dB high.

For the case of 45 degrees, Equation (F-10) together with Equation (F-2) yields a result that is 0.64-dB low:

$$Pr = PD \cdot \frac{\lambda^2}{4\pi} \cdot D \cdot (0.6469 + 0 + 0.6469) \quad (\text{F-10})$$

The errors incurred in these cases would be greater if an antenna with higher directivity were to be used. The results obtained with the ideal SD were identically correct because the ideal short antenna has the same directivity as a field probe.<sup>F-3</sup>

A HWD or other test antenna, such as a discone that typically has an HWD-like pattern, introduces some additional but possibly acceptable error in this measurement, where three orthogonal readings rather than many readings are taken with the antenna oriented in many directions.<sup>F-4</sup>

When continuous wave (CW) measurements are performed, the standing wave nature of the field patterns in the reflective space introduces wide variation in the received power readings with small displacement of the antenna; thus, multiple measurements should be performed over a region of wavelength or more dimensions. The wide variation in readings is less pronounced if radar-based measurements are performed using a pulsed signal because of the pulse bandwidth and inherent frequency averaging.<sup>F-5</sup>

A three-measurement average with a low-gain antenna is useful from a practical standpoint. Essentially, the antenna is used as an E field probe. Suppose an EMC engineer has the measurement task of studying specific hot and cold regions in a space rather than simply finding a grand ensemble average by stirring the fields with paddle wheels or aggressively moving the antenna. Such a measurement would be required when characterizing a reverberation chamber for field uniformity.<sup>F-6</sup>

This kind of measurement might also be performed to show hot and cold regions in a reflective but poorly reverberant space, such as a passenger car or an aircraft flight deck illuminated by a single beam. Because of the nonisotropic excitation and highly localized losses and leakages, one would expect the fields to be nonuniform and nonisotropic.

### F.3 APPARENT ANTENNA GAIN IN A HIGHLY REVERBERANT FIELD

EMC engineers have observed that antenna gain in a reverberant field does not appear to apply as it usually does in a free-space planewave field. Actually, gain is maintained.<sup>F-7</sup> The apparent independence of received power from an antenna (as its aim point is varied) is due to the isotropic nature of the reverberant field. Further, as one replaces a low- or

---

<sup>F-3</sup> A probe is designed to not accept appreciable power from the field being measured. That is, it has a small power capture area. An antenna has a capture area of  $G \lambda^2 / 4\pi$ .

<sup>F-4</sup> Typically, the pattern is most dipole-like at frequencies within an octave of the antenna's lowest usable frequency.

<sup>F-5</sup> Results should be based on the integral of the response, as discussed in the insertion loss calculation procedure in Section 3.2.2 of this technical report, *Reverberant Microwave Propagation*.

<sup>F-6</sup> Generally, a probe is used for this task.

<sup>F-7</sup> Antenna gain applies very clearly when observing transient field buildup, as shown in the data of Figures 2–3 and 2–4 of this technical report, *Reverberant Microwave Propagation*.

medium-gain antenna with a high-gain antenna in a test setup, the ensemble-averaged received power remains constant. This can be demonstrated by calculating the response of a high-gain antenna in an isotropic field as an integral over the spherical angles  $\theta, \phi$ .

An isotropic reverberant field has equal energy density propagating in all directions. Scalar power density  $S$  of a field with energy density  $u$  (joule/meter<sup>3</sup>) (J/m<sup>3</sup>) may be written as Equation (F-11):

$$S = c u \text{ (W/m}^2\text{)} \quad (\text{F-11})$$

where

$c$  is the speed of light.

For a field with scalar power density  $S$  (watts/meter<sup>2</sup>) (W/m<sup>2</sup>), the quantity  $\hat{S}$  can be defined as  $\hat{S} = S/4\pi$  (W/(m<sup>2</sup> · steradian)).  $\hat{S}$  is the power density propagating in a particular direction ( $\theta, \phi$ ) per unit solid angle  $\Omega$ . For an isotropic field,  $\hat{S}$  is a constant independent of  $\theta$  and  $\phi$ .

Next, consider an ideal pencil-beam antenna with no side or back lobes in its receiving pattern. Antenna gain is derived from directivity in that it transmits or receives energy only through a limited solid angle  $\Delta\Omega$  around some direction  $\theta_0, \phi_0$ . Over the small region  $\Delta\Omega$  (i.e.,  $\sin(\theta_0) \Delta\theta \Delta\phi$ ) where it does receive or transmit energy, its directivity is enhanced by the factor  $4\pi/\Delta\Omega$  and is zero elsewhere. The effective area  $A$  (m<sup>2</sup>) of this antenna is given by Equation (F-12):

$$A = \frac{\lambda^2}{4\pi} \cdot G = \frac{\lambda^2}{4\pi} \cdot \frac{4\pi}{\Delta\Omega} \text{ (inside } \Delta\Omega\text{) and } A = 0 \text{ (outside } \Delta\Omega\text{)} \quad (\text{F-12})$$

The power  $P_R$  received by the antenna in the field is computed by integrating the product of  $\hat{S}$  and  $A$  over angles  $\theta, \phi$ . Due to the idealized antenna pattern, the product is nonzero only in the directions in the region  $\Delta\Omega$  around  $\theta_0, \phi_0$ , where the antenna directivity is given as  $4\pi/\Delta\Omega$ . The received power is calculated in Equation (F-13):

$$P_R = \frac{1}{2} \cdot \iint_{\Delta\Omega} A \cdot \hat{S} \cdot d\Omega = \frac{1}{2} \cdot \frac{\lambda^2}{4\pi} \cdot \iint_{\Delta\Omega} \frac{S}{4\pi} \cdot \frac{4\pi}{\Delta\Omega} \cdot d\Omega = \frac{1}{2} \cdot \frac{\lambda^2}{4\pi} \cdot \frac{S}{4\pi} \cdot \frac{4\pi}{\Delta\Omega} \cdot \Delta\Omega = \frac{1}{2} \cdot S \cdot \frac{\lambda^2}{4\pi} \quad (\text{F-13})$$

The power received is independent of the antenna gain because the product of  $A$  and  $\hat{S}$  is nonzero over a smaller value of  $\Delta\Omega$  for higher-gain antennas. The higher-gain antenna accepts power over a smaller range of solid angle, and the  $\Delta\Omega$  in the numerator and denominator exactly cancel.

The extra factor of  $\frac{1}{2}$  in the result is due to polarization mismatch as discussed in Section F.2.

This calculation shows that received power in an isotropic field is independent of antenna gain or directivity. An earlier calculation showed clearly that if the antenna had directivity other than the ideal  $\sin^2\theta$  behavior of the ideal matched SD, uncertainty would be introduced in the power density estimate. The nonideal-directivity-induced uncertainty in the earlier calculation arose from replacement of a true  $4\pi$   $\theta, \phi$  average with three measurements along arbitrarily chosen orthogonal axes. The integrals over  $4\pi$  are equivalent to a good ensemble average.

#### **F.4 SUMMARY: ANTENNA RESPONSE AND FIELD MEASUREMENTS IN A REVERBERANT SPACE**

The effective power capture area  $A_0$  of an antenna in a highly reverberant field is given by the following relation:

$$A_0 = \lambda^2/8\pi$$

This is half the area of a matched isotropic receiver. The 3-dB loss in area arises from polarization mismatch. The apparent independence of capture area on antenna gain or directivity is due to the isotropic nature of the reverberant field. If the field is truly isotropic, there are no preferred antenna pointing directions to receive power.

#### **F.5 REFERENCES**

- Collin, Robert E. *Antennas and Radiowave Propagation*. ISBN 0-07-011808-6.  
N. p.: McGraw-Hill Book Co., circa 1960.
- Hill, David A. "Linear Dipole Response in a Reverberation Chamber,"  
*IEEE Transactions on Electromagnetic Compatibility*, vol. 41, no. 4  
(November 1999): n. pag.
- Stutzman, Warren L. and Gary A. Thiele. *Antenna Theory and Design, Second Edition*.  
ISBN 0-471-04458-X. New York: John Wiley & Sons, 1998.

This page is intentionally blank.



**APPENDIX G**  
**FIELDS AT CHAMBER WALLS**

This page is intentionally blank.

## CONTENTS

<u>Appendix</u>	<u>Page</u>
<b>G    FIELDS AT CHAMBER WALLS</b>	
G.1 Introduction.....	G-1
G.2 Fields in Terms of Chamber Modes .....	G-1
G.3 Volume Integrals.....	G-2
G.4 Surface Integrals and Averaging.....	G-2
G.5 Summary: Fields at Chamber Walls .....	G-4
G.6 References.....	G-4

## ABBREVIATIONS AND ACRONYMS

E field	Electric field component of electromagnetic wave
H field	Magnetic field component of electromagnetic wave
no.	Number (issue number used with references)
$Q$	Quality Factor
TE	Transverse Electric
V	Volt(s)
vol.	Volume (used with references)

This page is intentionally blank.

## G.1 INTRODUCTION

In this appendix, the relationship between fields within the volume of a chamber and those at the chamber walls is briefly examined. Generally, in reverberation chamber operations, great care is taken to avoid placing a test item and field probes or antennas near the chamber walls. The volume and wall fields do bear a definite relationship to each other. For instrumentation purposes, there is no specific reason why chamber fields could not be measured with wall-mounted field probes, provided suitable allowance is made for the wall boundary conditions. Further, general knowledge of the relationship between volume and wall fields is required in development of perturbation relations or other studies of chamber  $Q$  and losses.

## G.2 FIELDS IN TERMS OF CHAMBER MODES

Consider the electric field for a transverse electric (TE)  $mnp$  mode in a chamber with wall dimensions  $a$ ,  $b$ , and  $d$ . As is shown in many electromagnetics text books, the fields  $E_x$  and  $E_y$  for a cavity mode that is TE to the  $z$  direction may be written as Equations (G-1) and (G-2):<sup>G-1</sup>

$$E_x = \frac{j\omega\mu C}{k_c^2} \cdot \left(\frac{n\pi}{b}\right) \cdot \cos\left(\frac{m\pi x}{a}\right) \sin\left(\frac{n\pi y}{b}\right) \sin\left(\frac{p\pi z}{d}\right) \quad (\text{G-1})$$

$$E_y = \frac{-j\omega\mu C}{k_c^2} \cdot \left(\frac{m\pi}{a}\right) \cdot \sin\left(\frac{m\pi x}{a}\right) \cos\left(\frac{n\pi y}{b}\right) \sin\left(\frac{p\pi z}{d}\right) \quad (\text{G-2})$$

where

$C$  is an arbitrary constant proportional to the cavity  $H$  field.

$$k_c^2 = \left(\frac{m\pi}{a}\right)^2 + \left(\frac{n\pi}{b}\right)^2$$

---

<sup>G-1</sup> Simon Ramo and John R. Whinnery, *Fields and Waves in Modern Radio* (New York: John Wiley and Sons, Inc., July 1962): 55–66.

### G.3 VOLUME INTEGRALS

The ratio between the average value of  $E^2$  within the cavity volume  $\overline{E_v^2}$  and at the cavity walls  $\overline{E_s^2}$  is calculated by performing the appropriate integrals over the chamber volume ( $V$ ) and at the walls or surface ( $S$ ). Further, the wall surface integrals are averaged by adding them and dividing by 3.

The average value of  $E^2$  within the volume is calculated generally as expressed in Equation (G-3):

$$\overline{E_v^2} = \frac{\iiint E^2 dv}{V} \quad (\text{G-3})$$

For the specific modes described in Equations (G-1) and (G-2), the integral may be written as shown in Equation (G-4):

$$\begin{aligned} \overline{E_v^2} = \frac{\omega^2 \mu^2 C^2}{abd k_c^4} \cdot \left[ \left( \frac{n^2 \pi^2}{b^2} \right) \cdot \left( \iiint \cos^2 \left( \frac{n\pi x}{a} \right) \sin^2 \left( \frac{m\pi y}{b} \right) \sin^2 \left( \frac{p\pi z}{d} \right) dx dy dz \right) + \right. \\ \left. \left( \frac{m^2 \pi^2}{a^2} \right) \cdot \left( \iiint \sin^2 \left( \frac{n\pi x}{a} \right) \cos^2 \left( \frac{m\pi y}{b} \right) \sin^2 \left( \frac{p\pi z}{d} \right) dx dy dz \right) \right] \quad (\text{G-4}) \end{aligned}$$

Over the volume, each of the  $\sin^2$  and  $\cos^2$  terms in Equation (G-4) integrates to a value of  $\frac{1}{2}$  of  $a$ ,  $b$ , or  $d$ .

Thus  $\overline{E_v^2}$  reduces to the expression in Equation (G-5):

$$\overline{E_v^2} = \frac{\omega^2 \mu^2 C^2}{k_c^2} \cdot \frac{1}{8} \quad (\text{G-5})$$

### G.4 SURFACE INTEGRALS AND AVERAGING

The surface integral is performed over each of three surfaces— $ab$ ,  $ad$ , and  $bd$ —that are perpendicular to the  $x$ ,  $y$ , and  $z$  axes. No axes or coordinate directions are preferred, and in general, the fields could be TE to any of the axes.

The surface integral values are averaged by adding them and dividing by 3, as expressed in Equation (G-6):

$$\overline{E_s^2} = \frac{\iint E_x^2 dy dz + \iint E_y^2 dx dz + 0}{3} \quad (\text{G-6})$$

The  $\sin^2$  and  $\cos^2$  terms integrate to  $\frac{1}{2} a$  or  $\frac{1}{2} b$ , and the integrals over the planes  $ad$  and  $bd$  reduce to the values given in Equations (G-7) and (G-8):

$$\overline{E_{sad}^2} = \frac{\omega^2 \mu^2 C^2}{k_c^4} \left( \frac{m\pi}{a} \right)^2 \cdot \frac{1}{4} \quad (\text{G-7})$$

$$\overline{E_{sbd}^2} = \frac{\omega^2 \mu^2 C^2}{k_c^4} \left( \frac{n\pi}{b} \right)^2 \cdot \frac{1}{4} \quad (\text{G-8})$$

As expressed in Equation (G-6), the average value of the surface integrals is calculated as the sum of Equations (G-7) and (G-8) divided by 3. The averaged surface integral value is displayed in Equation (G-9):

$$\overline{E_s^2} = \frac{1}{3} \cdot \frac{1}{4} \cdot \frac{\omega^2 \mu^2 C^2}{k_c^2} \quad (\text{G-9})$$

The ratio of the average value of  $E^2$  within the volume to that at the surface is given in Equation (G-10):

$$\frac{\overline{E_v^2}}{\overline{E_s^2}} = \frac{3}{2} \quad (\text{G-10})$$

The average value of  $E^2$  measured within a chamber volume is equal to the average value of  $E^2$  measured at the chamber walls. Dunn obtained a similar result by assuming that the chamber fields consist of a planewave spectrum rather than a sum of cavity modes.<sup>G-2</sup>

Using similar integration procedures for mode  $H$  fields, one can show that the corresponding relationship for  $\overline{H^2}$  within the chamber volume and at the chamber walls is that given in Equation (G-11):

$$\frac{\overline{H_v^2}}{\overline{H_s^2}} = \frac{3}{4} \quad (\text{G-11})$$

---

<sup>G-2</sup> John M. Dunn, "Local, High-Frequency Analysis of the Fields in a Mode-Stirred Chamber," *IEEE Transactions on Electromagnetic Compatibility*, vol. 32, no. 1 (February 1990): 53–58.

The different ratio for the E field and H field quantities arises from the nature of the conductive wall boundary conditions.  $E$  is normal to the wall at the wall, and  $H$  is tangential.

## G.5 SUMMARY: FIELDS AT CHAMBER WALLS

The ratio of spatially averaged mean-square field values within a chamber volume and at the chamber walls is given by the following relations:

$$\frac{\overline{E_v^2}}{\overline{E_s^2}} = \frac{3}{2}$$

and

$$\frac{\overline{H_v^2}}{\overline{H_s^2}} = \frac{3}{4}$$

These ratios are required for developing expressions for cavity  $Q$  and losses in perturbation experiments. Further, since a definite relationship exists between volume and wall fields, field levels within the volume of a chamber could be determined from wall measurements if a suitable field probe were used.

## G.6 REFERENCES

- Dunn, John M. "Local, High-Frequency Analysis of the Fields in a Mode-Stirred Chamber," *IEEE Transactions on Electromagnetic Compatibility*, vol. 32, no. 1 (February 1990): 53–58.
- Ramo, Simon and John R. Whinnery. *Fields and Waves in Modern Radio*. New York: John Wiley and Sons, Inc., July 1962.



**DISTRIBUTION**

	<u>Copies</u> <u>Paper/CD(s)</u>		<u>Copies</u> <u>Paper/CD(s)</u>
<b>DOD ACTIVITIES (CONUS)</b>		SPAWAR SYSTEMS CENTER-PACIFIC	
COMMANDING OFFICER		ATTN DAVID SOUTHWORTH	0/6
CSSDD NSWC		PL-MR CODE 55420	
ATTN CODE A76	0/1	53560 HULL ST	
(TECHNICAL LIBRARY)		SAN DIEGO CA 92152-5001	
6703 W HIGHWAY 98			
PANAMA CITY FL 32407-7001		<b>NON DOD ACTIVITIES (CONUS)</b>	
		THE CNA CORPORATION	
DEFENSE TECHNICAL INFO CENTER		ATTN DOCUMENT CENTER	0/1
8725 JOHN J KINGMAN RD – STE 0944		825 MARK CENTER DR	
FT BELVOIR VA 22060-6218	1/1	ALEXANDRIA VA 22311-1850	
NAVAL AIR WARFARE CENTER		GOVERNMENT DOCUMENTS SECTION	
AIRCRAFT DIVISION (NAWCAD)		LIBRARY OF CONGRESS	
ATTN DIANE KEMPF	0/1	ATTN JOHN CHIN	2/2
48298 SHAW RD – BLDG 1461		101 INDEPENDENCE AVE SE	
PATUXENT RIVER MD 20670		WASHINGTON DC 20540-4172	
NAVAL RESEARCH LABORATORY		APPLIED RESEARCH ASSOCIATES INC	
ATTN LAWRENCE COHEN	0/1	ATTN DR EDGAR L COFFEY	0/1
CODE 5348		4694 MILLENNIUM DR – STE 100	
4555 OVERLOOK AVE SW		BELCAMP MD 21017	
WASHINGTON DC 20375			
		BEAVER AEROSPACE AND	
NAVAL SEA SYSTEMS COMMAND		DEFENSE INC	
ATTN DAVID MARK JOHNSON	0/1	ATTN STEVE DEPEN	0/1
F1 1W RM 1W-3127		11850 MAYFIELD	
BLDG 197		LIVONIA MI 48150	
WASHINGTON DC 20375			
		BOEING	
NAVAL UNDERSEA WARFARE CENTER		ATTN TERRI HE	0/1
E3 BRANCH CODE 3431		1156 ½ E 10TH ST	
ATTN CRAIG F DEREWIANY		LONG BEACH CA 90813	
ATTN MICHAEL J CARPENTER	0/2		
1176 HOWELL ST		BOEING	
NEWPORT RI 02841-1707		ATTN DENNIS LEWIS	0/5
		MC 19-LL	
SPACE AND NAVAL WARFARE		POB 3707	
SYSTEMS CENTER-CHARLESTON		SEATTLE WA 98124	
ATTN WAYNE LUTZEN			
ATTN CHRIS DILAY	0/2	BOEING	
CODE 56170		ATTN DON SHULTZ	0/1
POB 190022		MC 03-CM	
NORTH CHARLESTON SC 29419-9044		3003 WEST CASINO RD	
		EVERETT WA 98204	

**DISTRIBUTION (CONTINUED)**

	<u>Copies</u> <u>Paper/CD(s)</u>		<u>Copies</u> <u>Paper/CD(s)</u>
CESSNA (TEXTRON) ATTN BILLY M MARTIN 1207 ARMSTRONG AVE DERBY KS 67037	0/1	LAWRENCE LIVERMORE NATIONAL LABORATORY UNIVERSITY OF CALIFORNIA ATTN STEPHEN E SAMPAYAN PHD POB 808 LIVERMORE CA 94551	0/1
CESSNA AIRCRAFT EMS LAB ATTN ANDREW NGUYEN 2060 S KESSLER ST – BLDG 2 WICHITA KS 67213	0/1	LOCKHEED MARTIN ATTN DOROTHY SUMMERS 16539 COMMERCE DR – STE 10 KING GEORGE VA 22485-5847	0/2
CPI MPP DIVISION MANUFACTURING ENGINEERING ATTN PAUL KRZEMINSKI 607 HANSEN WAY PALO ALTO CA 94304	0/1	NASA LANGLEY RESEARCH CENTER ATTN TRUONG NGUYEN 1 S WRIGHT STREET MS 130 HAMPTON VA 23681-0001	0/1
ECLIPSE AVIATION CORPORATION ATTN HECTOR DEL AGUILA 2503 CLARK CARR LOOP SE ALBUQUERQUE NM 87105	0/1	NASA ATTN NOEL SARGENT MC 500-AOS 21000 BROOKPARK RD CLEVELAND OH 44135	0/1
G. J. F. ASSOCIATES ATTN G FREYER 20045 CAPELLA DR MONUMENT CO 80132	0/1	NATIONAL INSTITUTE OF STANDARDS & TECHNOLOGY (NIST) RF FIELD GROUP ATTN PERRY E WILSON MC 818.02 ELECTROMAGNETICS 325 BROADWAY BOULDER CO 80305	0/6
GENERAL MOTORS MILFORD PROVING GROUND ATTN JANALEE GRAHAM MC 483-340-111 3300 GENERAL MOTORS RD MILFORD MI 48380-3726	0/1	NORTHROP GRUMMAN ATTN WALTER J SCOTT PE 8211 TERMINAL RD – STE 1000 LORTON VA 22079	0/1
JACOBS ENGINEERING GROUP ATTN ROBERT P NELSON MC 483-340-145 3300 GENERAL MOTORS RD MILFORD MI 48380	0/1	OKLAHOMA STATE UNIVERSITY ATTN CHARLES F BUNTING PHD 202 ENGINEERING SOUTH STILLWATER OK 74078	0/1
INSTITUTE FOR TELECOMMUNICATION SCIENCES ATTN BOB JOHNK PROJECT LEADER MS ITS T 325 BROADWAY BOULDER CO 80305	0/1	RAYTHEON ATTN THOMAS FAGAN TU MO2 MS T17 1151 E HERMANS RD TUCSON AZ 85706	0/1

**DISTRIBUTION (CONTINUED)**

	<u>Copies</u> <u>Paper/CD(s)</u>		<u>Copies</u> <u>Paper/CD(s)</u>
SANDIA NATIONAL LABORATORIES		<b>INTERNAL</b>	
ATTN DR MATTHEW B HIGGINS	0/5		
MS 1152		Z31 BOZICEVICH	1/1
PO BOX 5800		Z31 (TECHNICAL LIBRARY)	1/1
ALBUQUERQUE NM 87185-1152		Q (V S HUDSON)	2/2
		Q50 (EMAC LIBRARY)	1/1
WELCH ALLYN		Q50 (R RICHARDSON)	10/3
ATTN SEAN EMERSON	0/1	Q52 (M SLOCUM)	1/1
8500 SW CREEKSIDE PL			
BEAVERTON OR 97008-7107			

This page is intentionally blank.



